The Effect of Combined Environmental and Service Loads on Bridge Piers Using Non-Linear Finite Element Analysis

By

Sepideh Zaghian

Thesis submitted in partial fulfillment of the requirements for the degree of

DOCTOR OF PHILOSOPHY

in Civil Engineering

Department of Civil Engineering
Faculty of Engineering
University of Ottawa

Abstract

Corrosion of reinforcing steel has been identified as the leading cause of deterioration in North America's reinforced concrete (RC) infrastructure. Global warming accelerates both reinforcement corrosion initiation and propagation. Furthermore, global warming could lead to higher freeze-thaw cycle (FTC) frequency in cold regions, affecting the structural performance and service life of aging RC infrastructures. There is a scarcity of numerical research on the effects of FTCs or the combined effects of corrosion and FTCs on the structural performance of real-scale columns/piers. The present study develops a numerical framework to analyse deteriorated RC bridge piers by adopting comprehensive corrosion and frost damage models from the literature. Comparisons with available test data from the literature assess the adopted damage models. Corroded columns and frost-damaged beams from the literature were selected and simulated by incorporating the adopted damage models. A stage-based damage framework during the service life of a bridge is proposed, and it is illustrated for a bridge located in Montreal, Canada. First, the detrimental effects of corrosion on the pier's structural performance are studied. The stage-based analysis is then conducted to study the combined effects of corrosion and freeze-thaw cycles over 60 years of the bridge's service life. The present study assumes three combined corrosion-frost damage levels. At level 1, it is assumed that all the reinforcement, core concrete, and the bond-slip response in the splashing zone are affected by stage 1 corrosion, and the cover concrete is degraded under 22 FTCs after ten years. At level 2, the steel rebars and the bond-slip response are affected by stage 2 corrosion, and the cover concrete and corrosion-induced damaged core concrete are assumed to degrade under 113 FTCs after 40 years. Level 3, the worst-case scenario, corresponds to extensive corrosion of rebars (stage 3), spalling of the cover concrete, and frost-induced damage penetration towards the core concrete (splashing zone) after 60 years of service. Three-dimensional nonlinear

finite element analyses using the finite element program, DIANA, are conducted to evaluate the structural performance of the RC bridge pier under service loading and subjected to corrosion alone and to corrosion combined with FTCs after ten, forty, and sixty years. From analysis of the numerical results, it is observed that a significant decrease in the pier's ultimate axial and flexural capacity, rigidity, and deformability shows the importance of periodic inspection and investigation in the first ten years and rehabilitation planning in the first 40 years of the bridge's service life. Comparing the structural performance of the pier deteriorated by frost damage only and a combination of corrosion and frost damage shows the intensifying effects of corrosion in the degradation process. The present modelling framework can also successfully capture the failure pattern of the damaged RC pier. A simplified sectional nonlinear analysis is also conducted to evaluate the validity of the proposed quantitative evaluation approach and propose an efficient assessment approach to approximately estimate the remaining capacity of aging piers.

Acknowledgments

I would like to express my sincere gratitude to my supervisor, Prof. Beatriz Martin-Perez, for her unconditional support and continuous encouragement throughout my Ph.D. study. Also, I wish to express my highest appreciation to my co-supervisor, Dr. Husham Almansour, for his endless inspiration and technical support through the ups and downs of this journey. Beyond any doubt, this study would have been impossible without their invaluable knowledge and guidance.

Financial support provided by the National Research Council of Canada under the CRBCPI-Resilient Highway Bridges project and the Natural Sciences and Engineering Research Council of Canada is gratefully acknowledged. I would also like to thank the National Research Council of Canada for access to its computational facilities and resources.

My special thanks go to my husband, Rouzbeh, for his everlasting support, love, patience, and motivation. My son, Araz, gave me the strength and motivation to finish this journey.

I am forever grateful to my beloved parents and sister for their endless love, support and sacrifice. I am also profoundly grateful to my in-laws for their support and encouragement.

Table of Contents

List of Figures

List of Tables

Notation List

α_s	normal strength concrete coefficient in Mander et al. (1989)
$\alpha_y, \alpha_u, \alpha_1$	empirical coefficients in Cairns et al. (2005)
γ	empirical parameters dependent on temperature range and specimen size in Berto et al. (2015)
δ	degradation parameter in Lin and Zhao (2016)
$\Delta D(t)$	corroding reinforcement diameter loss in millimetres in Val (2007)
$\Delta V'_{ICE}$	ice-induced volume increase causing damage in Gong and Maekawa (2018)
ΔV_{ICE}	the original ice-induced volume increase in Gong and Maekawa (2018)
ε_{01}	strain at the peak for unconfined concrete in Saatcioglu and Razvi (1992)
ε_1	• strain at peak for confined concrete in Saatcioglu and Razvi (1992) • the average tensile strain of cracked cover concrete in the direction perpendicular to the applied compression in Vecchio and Collins (1986)
ε_{085}	strain corresponding to 85% of peak stress for unconfined concrete in Saatcioglu and Razvi (1992)
ε_{85}	strain corresponding to 85% of peak stress for confined concrete in Saatcioglu and Razvi (1992)
$\varepsilon_{ut,cor}$	the degraded ultimate tensile strain in Cairns et al. (2005)
ε_{ut}	the ultimate tensile strain of un-corroded rebar in Cairns et al. (2005)
$\varepsilon_{ut,cor}$	ultimate tensile strain of corroded rebar in Kashani et al. (2013)
ε_{ut}	uncorroded rebar ultimate strain
$\varepsilon_{ut,cor}$	corroded rebar ultimate strain
ε_t	bending-induced strain

η_s	mass loss percentage in Lin and Zhao (2016)
η_2	variables defined in Model Code 2010 (Fib 2013)
η	non-dimensional stress and strain in Kashani et al. (2013)
$\lambda_{p,cor}$	non-dimensional buckling parameter of corroded rebars in Kashani et al. (2013)
ν	the ratio of rust volume to steel volume in bond-corrosion model by Lundgren (2002)
ν_{rs}	the ratio of the volume of corroded and uncorroded rebar
ξ	non-dimensional stress and strain in Kashani et al. (2013)
ρ_{cc}	the ratio of the area of longitudinal reinforcement to the area of the core of the section in Mander et al. (1989)
ρ_s	the transverse reinforcing bar ratio in Mander et al. (1989)
$\rho(t)$	the cross-sectional loss rate of corroding rebar subjected to uniform corrosion in Deng et al. (2018)
$\sigma_{ij,b-cr}$, $\sigma_{ij,a-cr}$	the internal stresses of the porous matrix before and after cracking in Gong and Maekawa (2018)
$\sigma_{ij}{}^{*}$	effective stress tensor in Gong and Maekawa (2018)
$\sigma_{cr,corr}$	critical stress of corroded rebar
τ_b	bond stress in the Model Code 2010
$\tau_{b\max}$	maximum bond strength in the Model Code 2010
τ_{bf}	residual bond stress in the Model Code 2010
$\tau_{bu,spilit,red}$	reduced bond strength of corroded specimens in Blomfors st al. (2018)
$\tau_{\max}{}^{d}$	frost-damaged bond tension in Petersen et al. (2007)
$\tau_{res,\mathrm{mod}}(K_{tr})$	reduced residual bond capacity of corroded specimens in Blomfors st al. (2018)
χ	empirical parameters dependent on temperature range and specimen size in Berto et al. (2015)

A_e	area of the effectively confined concrete core in Mander et al. (1989)
A_c	area of the concrete core enclosed by the center line of the perimeter spiral or hoop in Mander et al. (1989)
A_s	tie leg cross-sectional area in Saatcioglu and Razvi (1992)
$A_p(t)$	the cross-sectional area of a pit in Val and Melchers (1997)
A_{st}	tie's cross-section in Xin et al. (2019)
d(t)	time-dependent diameter of the corroded rebar in Deng et al. (2018)
d_b	un-corroded rebar diameter
$d_{b,corr}$	corroded rebar diameter
D	Relative reduction in modulus of elasticity of frost-damaged concrete
E_r	reduced modulus of elasticity of rebars in Xin et al. (2019)
E_p	hardening modulus of steel rebar in Xin et al. (2019)
$E_c{}^d$	modulus of elasticity of frost-damaged concrete
f'_{cc}	maximum compressive strength of a square confined concrete in Mander et al. (1989)
f_c	compressive strength of unconfined concrete
f_{yt}	yield strength of the transverse reinforcement
f_{le}	equivalent lateral confinement pressure in Saatcioglu and Razvi (1992)
f_l	lateral confinement pressure in Saatcioglu and Razvi (1992)
F	Faraday's constant
$f_{yt,cor}$	the degraded tensile yield stress in Cairns et al. (2005)
$f_{ut,cor}$	the degraded ultimate tensile stress in Cairns et al. (2005)
f_{yt}	the tensile yield stress of un-corroded rebar in Cairns et al. (2005)
f_{ut}	the ultimate tensile stress of un-corroded rebar in Cairns et al. (2005)
$f_{yc,cor}$	compressive yield stress of corroded rebar in Kashani et al. (2013)

$f_{yt,cor}$	tensile yield stress of corroded rebar in Kashani et al. (2013)
$f_{ut,cor}$	ultimate tensile stress of corroded rebar in Kashani et al. (2013)
$f_{c,cor}$	the compressive strength of cracked concrete (corrosion-induced)
f_c^d and f_t^d	frost-damaged compressive and tensile strength of concrete
f_{cr}	concrete cracking strength
f_y	uncorroded rebar yield strength
f_u	uncorroded rebar ultimate strength
$I_{current}$	current
i_{corr}	current density
k_e	confinement effectiveness coefficient in Mander et al. (1989)
k_1	Saatcioglu and Razvi's model empirical parameter
	stiffness parameter in Xin et al. (2019)
k_{in}	interpolation factor introduced by Lundgren et al. (2009)
K_{cor}	regression parameters in Lundgren (2002)
k_m , k_{tr}	variables defined in Model Code 2010 (Fib 2013)
l_i	unit directional vector normal to a crack plane in Gong and Maekawa (2018)
m_s	corroded rebar mass loss in Faraday’s law
n_{bars}	the number of rebars undergoing corrosion in Coronelli and Gambarova (2004)
M	the atomic weight of the metal in Faraday’s law
N_{eq}	equivalent number of FTCs
N	number of FTCs
p	regression parameters in Lundgren (2002)
P_{hydrau} , P_{cryst} , P_{cryo}	the hydraulic pressure, crystallization pressure, and cryo-suction pressure in Gong and Maekawa (2018)

R_τ	the ratio of corroded to un-corroded bond strength
R	the ratio between the maximum depth of the pit to the average depth of the pit in Val (2007)
r	corrosion rate (in mm/year) in Deng et al. (2018)
$RDME$	relative dynamic modulus of elasticity
S_{ICE}	the ice saturation level in Gong and Maekawa (2018)
S_{CR}	critical degree of saturation of concrete
t_n	normal stress in bond-corrosion model by Lundgren (2002)
T_0	corrosion initiation time in Deng et al. (2018)
t	rebar expansion in Molina et al. (1993)
u_{nbond}	relative normal displacement in the layer corresponding to the bond mode in bond-corrosion model by Lundgren (2002)
u_{tbond}	slip corresponding to the bond model in bond-corrosion model by Lundgren (2002)
u_{icorr}	the opening of each single radial crack in Molina et al. (1993)
W_{cr}	total crack width in Molina et al. (1993)
x_t	corroded rebar diameter reduction in Faraday's law
X_{corr}	corrosion level (percentage)
z	the iron oxidation induced valence of iron in Faraday's law

Chapter 1: Introduction

1.1 General

Climate change in the past decades has been of interest to many researchers. Recently, there have been some investigations to evaluate the effect of climate change on the service life and the ultimate capacity of infrastructures, especially in countries located in cold regions such as Canada (Nasr et al. 2020). Corrosion of rebars in reinforced concrete (RC) infrastructure is one of the most concerning factors affecting its serviceability and ultimate capacity (Sæther and Sand 2016; Tahershamsi 2016). Over the past decades, the risk of carbonation-induced corrosion in RC structures has increased due to the increase of atmospheric CO_2 due to greenhouse emissions (Talakokula et al. 2016). In many cold regions, such as Canada, the heavy use of de-icing salts during the winter increases the potential risk of chloride-induced corrosion, which could be combined with carbonation-induced corrosion and accelerate the corrosion process. Global warming is known as an accelerating factor in reinforcement corrosion initiation and propagation by increasing the rate of chemical reaction (Roberge 2010). Furthermore, it has been observed that the annual frequency of freeze-thaw cycles (FTCs) is higher in cold regions due to global warming, affecting the structural performance and service life of ageing (and corroding) RC infrastructure (Pakkala et al. 2015). Available studies in the literature have mainly focused on the deteriorating effects of either corrosion or FTCs on the mechanical properties of rebars and concrete in RC structures. Berra et al. (2003), Melchers et al. (2006), Sæther and Sand (2016), Xia et al. (2016), Deng et al. (2018), and Xin et al. (2019) have studied the instantaneous degrading effects of pitting and uniform corrosion on the material properties of steel and concrete. Compressive strength degradation of concrete within the cover zone and a portion of confined concrete due to rust formation-induced cracks, rebar cross-section reduction due to uniform and pitting corrosion (longitudinal and stirrups), rebar ductility degradation due to pitting corrosion, buckling of compressive longitudinal reinforcing bars due to rebar cross-section reduction and confinement degradation, and degradation of the bond-slip response induced by concrete cracking or spalling were considered as the main deteriorating factors. It was observed that these damage mechanisms occurring at the critical flexural or shear zones could lead to severe structural performance deterioration. Other researchers have conducted experimental and numerical studies on the effect of FTCs on the mechanical properties and structural performance of RC structures (Hasan et al. 2004, Hanjari et al. 2013, Hayashida et al. 2014, Berto et al. 2015, Qin et al. 2017, Gong and Maekawa 2018, Liu et al. 2019).

The Ontario Structure Inspection Manual (OSIM) proposes regular detailed visual inspections of bridges to ensure public safety and convenience, to prolong the bridges' useful life, and to set out a structure management system for maintenance and rehabilitation (Ontario Ministry of Transportation 2008). Such inspections determine the severity of corrosion damage as follows:

- Light: appearance of a light rust stain on the surface
- Medium: rebar's cross-section loss of less than 10% and exposed rebar with uniform light rust
- Severe: rebar's cross-section loss of 10%-20% and exposed rebar with heavy rusting and localized pit
- Very severe: rebar's cross-section loss of over 20% and exposed rebar with very heavy rusting and localized pit

Visual inspections also determine the severity of the freeze-thaw-induced scaling as follows (Ontario Ministry of Transportation 2008):

- Light: loss of surface mortar to a maximum of 5 mm without exposure of coarse aggregate
- Medium: loss of surface mortar to a maximum of 6 to 10 mm with exposure of some coarse aggregates
- Severe: loss of surface mortar to a maximum of 11 to 20 mm with some aggregates standing out

from the concrete and some of them completely lost

- Very severe: loss of mortar and aggregates to a depth greater than 20 mm

These guidelines provide a reasonable qualitative assessment approach. However, in view of the increase in traffic volume, environmentally-induced deterioration, and backlog of severely deficient bridges (CIRC 2019), relying on a quantitative assessment approach to assess the residual capacity and performance of aging bridges, especially their piers, is crucial (Mohammed 2014). The stability and ability of the piers to provide adequate support to the superstructure should be closely monitored and assessed thoroughly. It is crucial to monitor the possibility of any vertical, longitudinal or transverse translations or rotations (Ministry of Transportation 2008).

Only a few experimental studies have focused on the synergistic effects of environmental exposure (FTCs and corrosion) and mechanical loading on the mechanical behaviour and structural performance of ageing structural members (Diao et al. 2011; Wu et al. 2018). There is still a scarcity of studies on the structural performance of real-scale bridge piers subjected to combined deterioration effects during their service life.

1.2 Objectives of the present study

The present study's main objectives are:

a) Investigating the impact of reinforcement corrosion on the mechanical behaviour and ultimate capacity of RC bridge piers subjected to stage-based corrosion scenario through three-dimensional non-linear finite element analysis (3D-NLFEA) using the commercially finite element program DIANA (Diana 2019).

b) Investigating the impact of reinforcement corrosion and frost damage on the mechanical behaviour and ultimate capacity of RC bridge piers subjected to stage-based combined damage scenario through three-dimensional non-linear finite element analysis (3D-NLFEA) using the commercially finite element program DIANA (Diana 2019).

1.3 Scopes of the present study

The main scope of the present study are summarized as follows:

a) Comprehensive State-of-the-Art (analytical, numerical, and experimental) on the mechanical properties and the structural behaviour of RC beam-columns damaged by corrosion, frost damage, combined/coupled action of reinforcement corrosion and concrete frost damage.

b) Adoption of a comprehensive corrosion damage model based on available models in the literature to account for the effects of pitting and uniform corrosion on the material properties of reinforcing steel and concrete, such as strength degradation of concrete within the cover zone and a portion of confined concrete due to corrosion-induced cracking, rebar cross section reduction due to uniform and pitting corrosion (longitudinal and stirrups), steel's ductility degradation due to pitting corrosion, buckling of compressive reinforcement due to cross section reduction and confinement degradation, and bond-slip response degradation.

c) Evaluation of the accuracy of the adopted corrosion damage model under task (b) by simulating previously tested corroded columns from the literature in the commercially finite element program DIANA (release 10.3).

d) Adoption of a comprehensive frost damage model based on available models in the literature to account for FTCs-induced deterioration, such as degradation in concrete compressive strength and peak compressive strain, concrete modulus of elasticity, concrete tensile strength, and fracture energy.

e) Evaluation of the accuracy of the adopted frost damage model under task (d) by simulating tested frost-damaged RC members from the literature in the commercially finite element program DIANA (release 10.4).

f) Design of a multi-column bent of an ageing bridge according to the loading combination of the superstructure and based on CSA S6:19 (Canadian Highway and Bridge Design-CHBDC, CSA 2019) recommendations.

g) Proposal of a stage-based corrosion damage scenario and a combined stage-based progressive corrosion/frost damage scenario over the bridge service life.

h) 3D-NLFEA using the commercially available finite element program DIANA (release 10.4) at the member level to evaluate the structural performance of the bridge pier subjected to a progressive corrosion damage scenario and a combined action scenario by incorporating the adopted damage models under task (b), (d), and (g) as a stage-based analysis.

i) Evaluation of the trend and effectiveness of the proposed model by generating the interaction diagrams of the damaged piers based on the present model and nonlinear sectional analysis.

1.4 Research significance

The present study's outcome contributes to a comprehensive insight into the staged deteriorating effects of corrosion, FTCs, and the combination of corrosion and FTCs on the ultimate axial and flexural capacity, rigidity, and deformability of RC bridge piers subjected to traffic load during their service life. The present model successfully captures the failure modes of the aging piers. A comparison between the results based on the present methodology and those based on experimental tests from the literature demonstrates the reliability of the present study. The interaction diagrams of the damaged piers based on the present model and nonlinear sectional analysis are generated and compared for further verification of the validity of the present study.

1.5 Thesis format and organization

This thesis is prepared in a "paper format," including six chapters. Each chapter is presented with its own bibliography. The chapters are as follows:

Chapter 1 provides an introduction and a description of the objectives and scope of the thesis.

Chapter 2 presents a comprehensive state-of-the-art on the deteriorating effects of reinforcement corrosion and FTCs on the concrete and rebars' mechanical and geometrical properties, as well as the structural performance of the deteriorated RC members. Chapter 2 will be submitted as a review paper to an international journal.

Chapter 3 develops a nonlinear finite element analysis of the impact of reinforcement corrosion on bridge piers under concentric loads. This chapter introduces a comprehensive adopted corrosion damage model and then verifies it by simulating previously tested corroded columns subjected to concentric loading from the literature. A stage-based corrosion damage model is introduced, and an RC bridge pier is designed and simulated in DIANA. The corrosion damage model is incorporated into the finite element model to assess the structural performance of the corroded RC pier subjected to a progressive corrosion scenario and concentric load over the bridge service life. Chapter 3 has been published as Zaghian et al. (2022).

Chapter 4 presents the finite element modelling of bridge piers subjected to eccentric load combined with reinforcement corrosion. The axial-flexural responses of the corroded pier under different eccentricities are studied. The accuracy of the adopted damage model and the proposed 3D-NLFEA is verified by simulating two corroded RC columns from the literature. The adopted corrosion damage model is then incorporated into the model as a stage-based analysis to evaluate the structural performance of the corroded RC pier under eccentric load. The corroded RC pier's interaction diagram at each damage stage is then generated and discussed. This chapter has been published as Zaghian et al. (2023a).

Chapter 5 uses 3D-NLFEA to evaluate the structural performance of an RC bridge pier subjected to the combination of corrosion, FTCs, and service load. The corrosion damage model is briefly reviewed, and the adopted frost damage model is introduced. The adopted frost damage model is then verified by simulating the experimental tests of frost-damaged beams reported in the literature. A comprehensive combined damage model is proposed as a stage-based scenario. The combined scenario is incorporated into the model to evaluate the structural performance of the RC pier damaged by the progressive combined action of corrosion and FTCs over the bridge's service life. This chapter has been published as Zaghian et al. (2023b).

Chapter 6 summarizes the major conclusions of each technical paper and suggests a reliable evaluation approach for affected RC bridge piers based on nonlinear sectional analysis.

1.6 References

Berra, M., Castellani, A., Coronelli, D., Zanni, S., and Zhang, G. (2003). “Steel-concrete bond deterioration due to corrosion: finite-element analysis for different confinement levels.” Magazine of Concrete Research, 55(3), 237–247.

Berto, L., Saetta, A., and Talledo, D. (2015). “Constitutive model of concrete damaged by freeze-thaw action for evaluation of structural performance of RC elements.” Construction and Building Materials, Elsevier Ltd, 98, 559–569.

CIRC. (2019). “Canada Infrastructure Report Card 2019.” Canadian Infrastructure, 1–56.

CSA (2019) CSA S6:19 Canadian Highway Bridge Design Code, CSA Group, Toronto, Ontario.

Diana. (2019). “DIANA Finite Element Analysis, User’s Manual, Release 10.” TNO Building and Construction Research, Delft, Netherlands.

Melchers, R. E., Li, C. Q., and Lawanwisut, W. (2006). “Modelling deterioration of structural behaviour of reinforced concrete beams under saline environment corrosion.” Magazine of Concrete Research, 58(9), 575–587.

Ministry of Transportation. (2008). Ontario Structure Inspection Manual (OSIM), Policy, planning & Standards division engineering standards branch bridge office;

Mohammed, A. M. (2014). “Semi-Quantitative Assessment Framework for Corrosion Damaged Slab-on-Girder Bridge Columns Using Simplified Nonlinear Finite Element Analysis, Ph.D. Thesis.” University of Ottawa.

Nasr, A., Kjellström, E., Björnsson, I., Honfi, D., Ivanov, O. L., and Johansson, J. (2020). “Bridges in a changing climate: a study of the potential impacts of climate change on bridges and their possible adaptations.” Structure and Infrastructure Engineering, Taylor & Francis, 16(4), 738–749.

Pakkala, T. A., Köliö, A., Lahdensivu, J., and Pentti, M. (2015). “The effect of climate change on freeze-thaw cycles in nordic climate C. Andrade, J. Gulikers, and R. Polder, eds., Springer Cham,.” Durability of Reinforced Concrete from Composition to Protection, C. Andrade, J. Gulikers, and R. Polder, eds., ed., Springer Cham, 145–154.

Roberge, P. R. (2010). “Impact of climate change on corrosion risks.” Corrosion Engineering Science and Technology, 45(1), 27–33.

Sæther, I., and Sand, S. (2016). “FEM simulations of reinforced concrete beams attacked by corrosion.” Nordic Concrete Research, 39, 15–32, (June), 15–32.

Tahershamsi, M. (2016). “Structural Effects of Reinforcement Corrosion in Concrete Structures,.” Doctoral Dissertation, Chalmers University of Technology, Sweden.

Talakokula, V., Bhalla, S., Ball, R. J., Bowen, C. R., Pesce, G. L., Kurchania, R., Bhattacharjee, B., Gupta, A., and Paine, K. (2016). “Diagnosis of carbonation induced corrosion initiation and progression in reinforced concrete structures using piezo-impedance transducers.” Sensors and Actuators, A: Physical, Elsevier B.V., 242, 79–91.

Xia, J., Jin, W., and Li, L. (2016). “Performance of Corroded Reinforced Concrete Columns under the Action of Eccentric Loads.” Journal of Materials in Civil Engineering, 28(1), 04015087.

Xin, J., Zhou, J., Zhou, F., Yang, S. X., and Zhou, Y. (2018). “Bearing capacity model of corroded RC eccentric compression columns based on hermite interpolation and fourier fitting.” Applied Sciences (Switzerland), 9(1).

Zaghian, S., Martín-Pérez, B., and Almansour, H. (2022). “Nonlinear Finite Element Modeling of the Impact of Reinforcement Corrosion on Bridge Piers under Concentric Loads.” Structural Concrete, 23(1), 138-153 https://doi.org/10.1002/suco.202100254.

Zaghian, S., Martín-Pérez, B., and Almansour, H. (2023a). “Finite element modelling of bridge piers subjected to eccentric load combined with reinforcement corrosion.” Engineering Structures, 283, 115822. https://doi.org/10.1016/j.engstruct.2023.115822

Zaghian, S., Martín-Pérez, B., Almansour, H., and Shirkhani, H. (2023b). “Nonlinear finite element modelling of bridge piers under the combined effect of corrosion, freeze-thaw cycles, and service load.” Structural Concrete, Published online ahead of print February 28th, 2023. https://doi.org/10.1002/suco.202200370

Chapter 2: Literature Review on Reinforcement Corrosion and Frost Damage and Gap in the State-of-the-Art

2.1 Introduction

Reinforcement corrosion has been known as a primary cause of deterioration in RC infrastructures. Corrosion of reinforcing steel is an electrochemical reaction triggered by either carbonation of the concrete cover or accumulation of a sufficient amount of chloride ions at the steel surface. When either of these mechanisms occurs, the passivity afforded by the alkali environment around the rebars breaks down, and corrosion initiates. Corrosion appears as rust staining on the concrete surface, followed by cracking and delamination of the concrete cover at advanced stages (Ontario Ministry of Transportation 2008). Concrete frost damage induced by freezing and thawing cycles (FTCs) is another deleterious phenomenon in RC structures, especially in cold regions. Two types of frost damage are widely distinguished: internal damage and surface scaling. Water freezing inside the concrete pore system causes the first damage type, whereas the latter damage type is caused by weakening of the exposed concrete surface in contact with a saline solution (Berto et al. 2015).

A comprehensive state-of-the-art literature survey (analytical, numerical, and experimental studies) on the destructive effects of corrosion, FTCs, and a combination of corrosion and FTCs on the material properties and structural performance of RC members is presented in this chapter. Available studies are categorized as (i) studies on the deteriorating effects of corrosion and FTCs on the mechanical properties of concrete, rebars, and the bond-slip response, and (ii) studies on the deteriorating effects of corrosion and FTCs on the structural performance of RC structures. The sections in the present chapter are summarised in Figure 2-1.

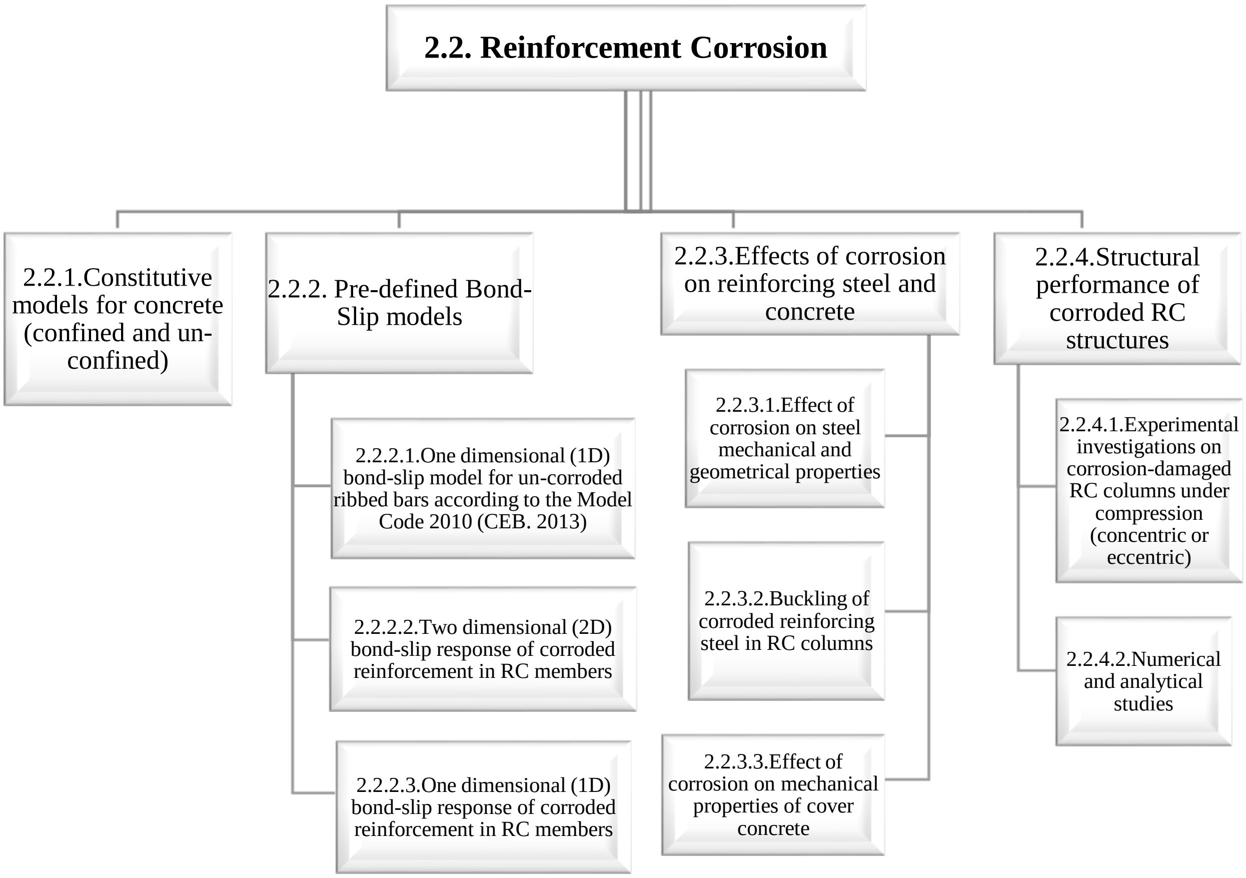

2.2. Reinforcement Corrosion
2.2.1.Constitutive models for concrete (confined and un-confined)
2.2.2. Pre-defined Bond-Slip models
2.2.2.1.One dimensional (1D) bond-slip model for un-corroded ribbed bars according to the Model Code 2010 (CEB. 2013)
2.2.2.2.Two dimensional (2D) bond-slip response of corroded reinforcement in RC members
2.2.2.3.One dimensional (1D) bond-slip response of corroded reinforcement in RC members
2.2.3.Effects of corrosion on reinforcing steel and concrete
2.2.3.1.Effect of corrosion on steel mechanical and geometrical properties
2.2.3.2.Buckling of corroded reinforcing steel in RC columns
2.2.3.3.Effect of corrosion on mechanical properties of cover concrete
2.2.4.Structural performance of corroded RC structures
2.2.4.1.Experimental investigations on corrosion-damaged RC columns under compression (concentric or eccentric)
2.2.4.2.Numerical and analytical studies

(a)

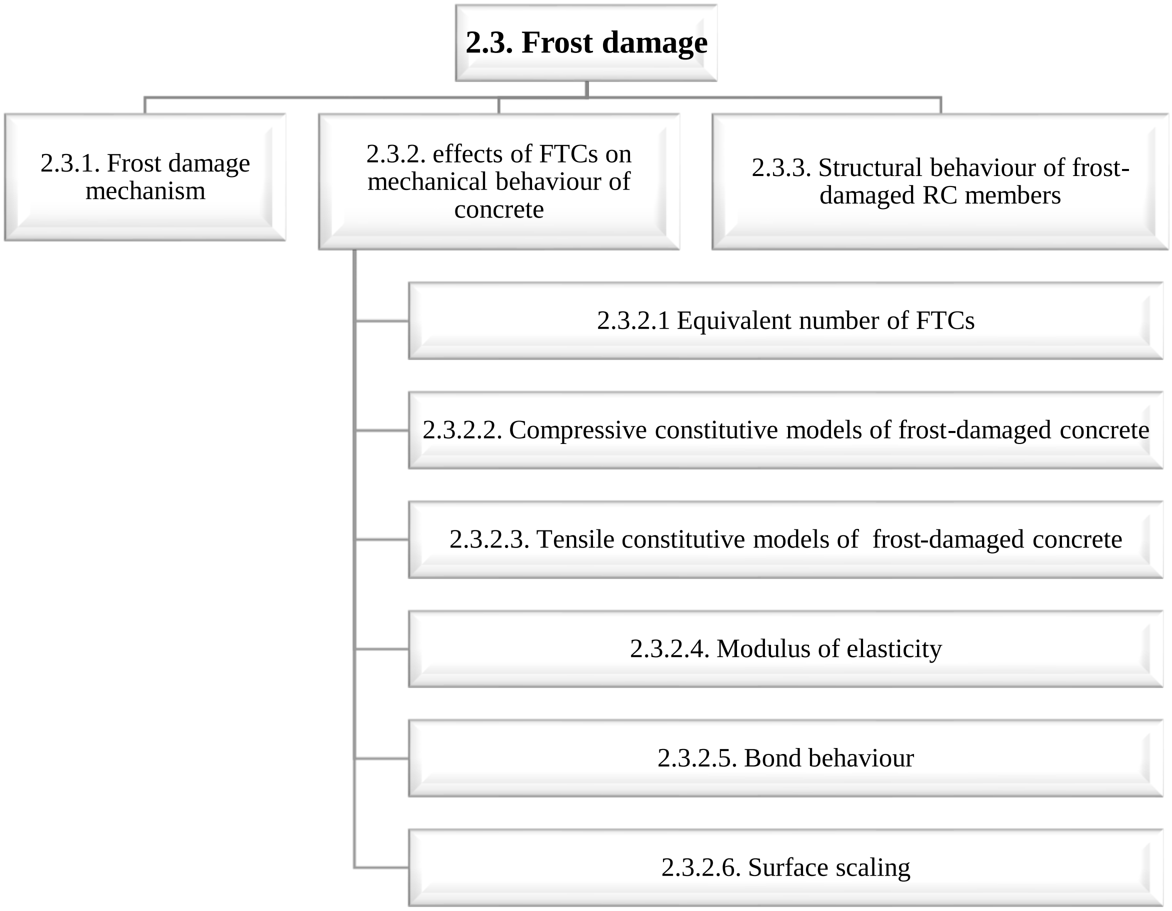

(b)

Figure 2-1 A summary of the state-of-the-art presented in Chapter 2

2.2 Constitutive models for concrete (confined and un-confined)

According to many studies reviewed in this section, the stress-strain response of concrete and rebars follows a non-linear trend. Hognestad (1951) is the most well-known model used by many researchers among many developed concrete constitutive models in compression. In this model, the compressive stress-strain response of concrete follows a second-order trend (parabola) up to the ultimate stress. The descending branch (relatively significant decrease in strain) follows a linear trend up to failure (Figure 2-2, a). Mander et al. (1989) conducted a theoretical study to investigate the effect of transverse reinforcement (spiral or rectangular hoops) on the stress-strain model of the concrete under uniaxial compression. The model is also valid for the case of cyclic loading and strain rate. In Mander's model, the maximum compressive strength of a square confined concrete (f'_{cc}) is calculated as:

$$f'_{cc} = f_c\left(-1.254 + 2.254\sqrt{1 + 7.94\alpha_s \frac{f_l}{f_c}} - 2\alpha_s \frac{f_l}{f_c}\right) \tag{2.1}$$

$$f_l = \frac{1}{2}k_e\rho_s f_{yt} \;\; ; \;\; k_e = \frac{A_e}{A_{cc}}; \; A_{cc} = A_c\left(1-\rho_{cc}\right) \tag{2.2}$$

in which f_c is the compressive strength of unconfined concrete; $f_l^{'}$ is the maximum lateral pressure induced by the transverse reinforcement; α_s is the normal strength concrete coefficient; k_e is the confinement effectiveness coefficient; A_e is the area of the effectively confined concrete core; ρ_{cc} is the ratio of the area of longitudinal reinforcement to the area of the core of section; A_c is the area of the concrete core enclosed by the center line of the perimeter spiral or hoop; ρ_s is the transverse reinforcing bar ratio, and f_{yt} is the yield strength of the transverse reinforcement.

Another well-known compressive model for concrete is the model proposed by Thorenfeldt et al. (1987) who made modifications to the Popovics (1973) model to adjust the descending branch of the stress-strain response. Thorenfeldt's model is presented in Figure 2-2 (b).

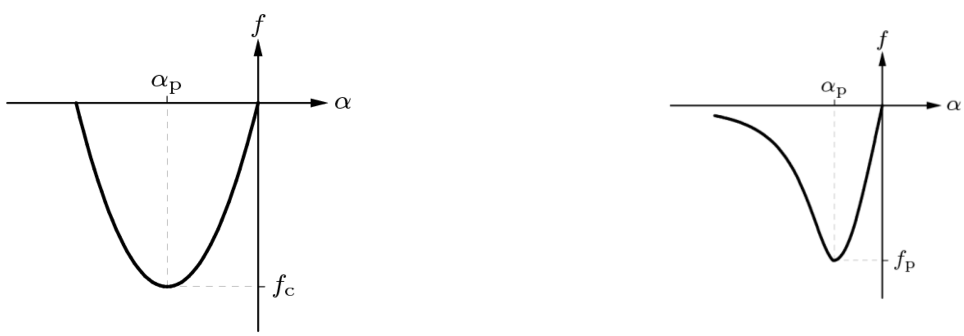

(a) (b)

Figure 2-2 Concrete compressive stress-strain responses reproduced from DIANA (Diana 2019) (a) Hognestad model, (b) Thorenfeldt model

Saatcioglu and Razvi (1992) conducted an analytical study to conduct the compressive constitutive model for confined concrete. In this model, the authors constructed the descending branch according to 85% of peak stress and assumed constant residual strength beyond the descending branch equivalent to 20% of peak stress. Adopting various test data, the authors developed an empirical relationship for the stress-strain of confined concrete in compression. Accounting for confinement pressure induced by spiral and rectilinear reinforcement, it was proven that both strength and ductility of confined concrete significantly improve. Saatcioglu and Razvi (1992) proposed the confined compressive strength of concrete as:

$$f'_{cc} = f_c + k_1 f_{le} \tag{2.3}$$

where f'_{cc} and f_c are the confined strength of concrete and unconfined in-place strength of concrete in structural members, respectively. The f_{le} is the equivalent lateral confinement pressure and is introduced as $f_{le} = k_2 f_l$ at which f_l is the lateral confinement pressure (Eq. 2.5), $k_2 = 0.15\sqrt{\frac{b_c}{s}\frac{b_c}{s_l}} \leq 1.0$ for rectilinear reinforcement (b_c, s ,and s_l are the section width, transverse reinforcement spacing, and spacing of laterally supported longitudinal reinforcement respectively) and $k_2 = 1.0$ for spiral reinforcement. The coefficient k_1 is an empirical parameter, and according to the test data regression analysis, Saatcioglu and Razvi (1992) proposed the variation of the coefficient k_1 as a function of f_{le} (Eq. 2.4). The variables f_l, ε_1, and ε_{85} were calibrated as Eqs. 2.5 , 2.6, and 2.7, respectively.

$$k_1 = 6.7\left(f_{le}\right)^{-0.17} \tag{2.4}$$

$$f_l = \frac{\sum_{i=1}^{q}\left(A_s f_{yt} \sin\alpha\right)_i}{s b_c} \tag{2.5}$$

$$\varepsilon_1 = \varepsilon_{01}\left(1+5K\right) \;; \qquad K = \frac{k_1 f_{le}}{f_{co}^{'}} \tag{2.6}$$

$$\varepsilon_{85} = 260\rho\varepsilon_1 + \varepsilon_{085} \quad ; \qquad \varepsilon_1 = \varepsilon_{01}\left(1+5K\right) \tag{2.7}$$

in which A_s is the tie leg cross sectional area; f_{yt} is the yield strength of tie; q is the number of tie legs that cross the side of core concrete for which the average lateral pressure, f_l, is computed; ε_{01}, ε_1, ε_{085}, ε_{85} are the strain at the peak and strain corresponding to 85% of peak stress for the unconfined and confined concrete, respectively.

Gilbert and Warner (1978) used a layered discrete element method to investigate the short-term behaviour of RC slabs considering the effects of tension stiffening. The authors proposed a linear ascending branch for the concrete in tension up to the first crack with a tensile modulus equal to the initial modulus of concrete in compression and a linear post-crack descending branch considering tension stiffening. Gilbert and Warner (1978) also assumed a simplified bilinear stress-strain relationship for the steel in both tension and compression.

2.3 Reinforcement corrosion

Depending on the type of corrosion (pitting or uniform), corrosion of rebars in RC members could have deteriorating effects in different aspects such as rebar cross-sectional loss (Faraday's law), rebar's pit-induced ductility degradation (Cairns et al. 2005), the possibility of elastic and inelastic buckling of corroded rebars due to the rebar's cross-sectional reduction and confinement degradation (Rodriguez et al. 1995 and Kashani et al. 2013), reduction in cover concrete compressive strength due to possible cracking and spalling (Coronelli and Gambarova 2004), loss of partial confinement, and bond-slip response degradation (Lundgren et al. 2012).

This chapter critically reviews the studies conducted on the effects of corrosion on the mechanical properties and structural performance of RC structural members. The main scope of the present state-of-the-art is presented in Figure 2-1(a).

2.3.1 Pre-defined bond-slip models

2.3.1.1 One dimensional (1D) bond-slip model for un-corroded ribbed bars according to the Model Code 2010 (CEB. 2013)

The bond mechanism in RC members appears as three components, i.e., (1) chemical adhesion, (2) mechanical interface interlock, and (3) active friction (fib 2013). The chemical adhesion strength between rebar and concrete is reported to be around 0.1 MPa, according to the Model Code 2010 (fib 2013). The loss of this type of bond leads to the appearance of micro-cracks around the rebar (Tahershamsi 2016). The interface interlock is induced by the restraining force between embossments and indentations of the steel profile, and it is highly dependent on the shape and size of the ribs (fib 2013). The lowest bond strength among the mentioned three components is active friction around 0.003 MPa. Still, it cannot be neglected because of its contribution to the shear strength and its development all over the interface.

The 1D bond-slip relationship for monotonic loading introduced in the Model Code 2010 (fib 2013) depends on different parameters such as rebar geometry, concrete cover, location of rebar, and boundary conditions (Eq. 2.8). The bond-slip curve (pull-out case) consists of four different sections, i.e., (1) the small slip that causes micro cracking and local crushing, (2) the straight part which occurs for the well-confined cases and the crushing between the ribs occur, (3) descending branch of the bond-slip curve due to splitting cracks, and (4) the residual bond stress, which is dependent on the degree of integrity caused by the transverse reinforcement (Figure 2-3).

$$
\begin{aligned}
&\tau_b = \tau_{b\max}(s/s_1)^{\alpha} && \textit{for} \quad 0 \le s \le s_1 \\
&\tau_b = \tau_{b\max} && \textit{for} \quad s_1 \le s \le s_2 \\
&\tau_b = \tau_{b\max} - \left(\tau_{b\max} - \tau_{bf}\right)(s - s_2)/(s_3 - s_2) && \textit{for} \quad s_2 \le s \le s_3 \\
&\tau_b = \tau_{bf} && \textit{for} \quad s_3 < s
\end{aligned}
\qquad 2.8
$$

where τ_b is the bond stress; $\tau_{b\max}$ is the maximum bond strength; τ_{bf} is the residual bond stress.

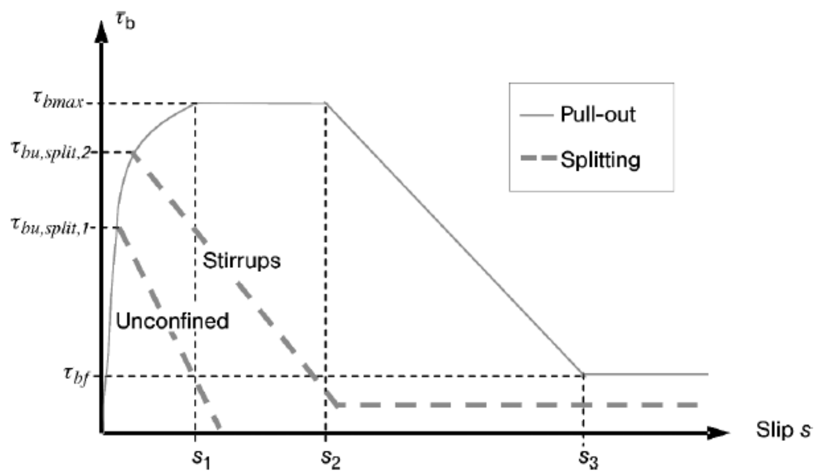

Figure 2-3 1D bond-slip relationship (reproduced from CEB-fib 2010)

Lundgren et al. (2009) conducted an interpolation between the extreme cases of the Model Code 1990 bond-slip model, which is the pull-out failure (confined) and splitting failure (un-confined), by introducing an interpolation factor k_{in} to define a more practical model in real-life structures (Eq. 2.9).

$$\tau_b = k_{in}.\tau_{b,conf} + \left(1 - k_{in}\right).\tau_{b,unconf} \qquad 2.9$$

$$k_{in} = \max\begin{cases} k_{c/d} \\ k_{Asw} \end{cases}$$

The interpolation factor was defined as a cover-to-bar diameter ratio (c/d) or the amount of transverse reinforcement corresponding to the pull-out failure, i.e., the ratio between the transverse reinforcement area to the transverse reinforcement spacing (A_{sw}/s).

2.3.1.2 Two-dimensional (2D) bond-slip response of corroded rebars in RC members

Over the past few decades, many studies have been conducted on the effects of corrosion on the bond-slip behaviour of RC structural members. Higher corrosion product volume than the original material results in splitting stresses, cover cracking or delamination. The corrosion product expansion also adversely affects the interaction between steel and concrete (Lundgren 2002). Ignoring the flow of corrosion products into the cracks, Lundgren (2002) developed a combined model of bond-corrosion. In this study, the frictional bond model developed by Lundgren (1999), considering the effect of splitting stress, bond stress, longitudinal slip between concrete and rebar, and the radial deformation around the rebar, was adopted. The bond model was combined with the corrosion model, which includes the effect of voluminous corrosion product expansion. For the bond model, considering elastoplastic theory, the relationship between the stresses and deformations was defined as Eq. 2.10.

$$\begin{bmatrix} t_n \\ t_t \end{bmatrix} = \begin{bmatrix} D_{11} & \dfrac{|u_{tbond}|}{u_{tbond}} D_{12} \\ 0 & D_{22} \end{bmatrix} \begin{bmatrix} u_{nbond} \\ t_{tbond} \end{bmatrix} \qquad 2.10$$

where t_n is the normal stress; t_t is the bond stress; u_{nbond} is the relative normal displacement in the layer corresponding to the bond mode; u_{tbond} is the slip corresponding to the bond model (Figure 2-4).

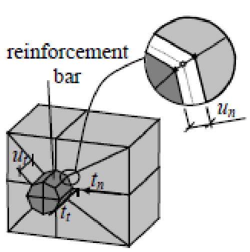

$$\mathbf{t} = \begin{bmatrix} t_n \\ t_t \end{bmatrix} = \begin{bmatrix} \text{normal splitting stress} \\ \text{bond stress} \end{bmatrix}$$

$$\mathbf{u} = \begin{bmatrix} u_n \\ u_t \end{bmatrix} = \begin{bmatrix} \text{relative normal displacement at the layer} \\ \text{slip} \end{bmatrix}$$

Figure 2-4 Stress and deformation definition in the bond model defined by Lundgren (1999) (reproduced from Lundgren 1999)

Lundgren (2002) also developed a corrosion model considering the voluminous corrosion product expansion. The ratio between the volume of corrosion products to the volume of corroded steel (stripped area), ν, was introduced as an essential factor. Assuming incompressibility of corrosion products, the free increase of radius based on Lundgren's model was introduced as:

$$a = -r + \sqrt{r^2 + (\nu - 1).(2rx - x^2)} \tag{2.11}$$

in which ν is the ratio of rust volume to steel volume, and x is the corrosion penetration depth.

The free increase of radius corresponds to the zero normal stress in the rebar. Lundgren (2002) suggested the normal strain corresponding to the volume expansion of corrosion products and corresponding normal stress of rust at loading as Eqs. 2.12 and 2.13, respectively:

$$\varepsilon_{cor} = \frac{u_{ncor} - a}{x + a} \tag{2.12}$$

$$t_n = K_{cor}.\varepsilon_{cor}^{p} \tag{2.13}$$

in which parameters K_{cor} and p are regression parameters (according to the previous test results such as Andrade et al. 1993).

The bond model developed by Lundgren (1999) was modified by the author in a subsequence study (Lundgren 2005). The modified model introduces a third component, which prevents the bar from rotating around its axis. Within the past two decades, the corrosion/bond damage model developed by Lundgren (2002) has been used by many researchers conducting 3D FEA on the structural behaviour of corroding RC members using DIANA software. The corrosion and bond layers were modelled using 2D interface elements at the surface between rebars and concrete, both modelled by 3D solid elements. Lundgren (2002) integrated two separate layers into one layer to reduce the node numbers and consequently increase the computational efficiency of the solution. Lundgren (2002) assumed that the bond and corrosion layers' traction is equal due to equilibrium. The displacement relationship within the single interface element layer was introduced as Eq. (2.14).

$$u_n = u_{ncor} + u_{nbond}$$
$$u_t = u_{tbond}, u_{tcor} = 0 \qquad 2.14$$

Tahershamsi (2016) used the bond/corrosion model developed by Lundgren (2002) to conduct a numerical study investigating the effects of natural corrosion on the structural behaviour of corroding RC beams. In this study, Lundgren's bond/corrosion model was implemented into the commercial DIANA 9.5 software through 2D interface elements to introduce the swelling effect of corrosion products in addition to the friction bond. In this model, the corrosion penetration was used as a function of time, and a time step analysis was conducted as the corrosion propagation. Hussain and Miteva (2018) also followed the elastoplastic bond/corrosion model developed by Lundgren (2002) to model the structural behaviour of naturally corroded beams in DIANA 10.2 software.

2.3.1.3 One dimensional (1D) bond-slip response of corroded reinforcement in RC members

The effects of crack development along the radial direction around the rebar and the bond-slip response of un-corroded and corroded RC members have been of interest to many numerical studies (Schlune 2006). Schlune (2006) conducted a numerical study using DIANA software to investigate the effects of corrosion on the bond-slip response of corroded RC members. It was observed that cracking mode is independent of the source of cracking, i.e., corrosion and slip. Many researchers conducted numerical and analytical studies to develop the bond-slip curve of corroded RC members, named slave curve, by modifying the bond-slip relationship developed by the Model Code 1990 (CEB. 1993), named master curve. Shifting the master curve along the slip axis (Schlune 2006) or the bond axes (Tørlen and Horrigmoe 1998) was a reliable method.

Schlune (2006) showed that by shifting the bond-slip curve of the Model Code 1990 (CEB. 1993) to the left side, the bond-slip curve for the corroded RC member could be achieved, assuming the corrosion application before the pull-out application. Two reasons could explain this, i.e., (1) dependency of bond stress on the radial stress around the rebar, (2) dependency of radial deformation caused by corrosion and radial deformation caused by slip. In Schlune (2006), the master curve was first shifted along the slip axes by $\Delta s = -fx$ where x was defined as corrosion penetration depth in millimetres and f was defined as a factor to relate the effect of corrosion on cracking to the effect of slip on cracking. The corroded bond-slip curve was then described by Schlune (2006) as Eqs. 2.15 to 2.18 (Figure 2-5). Schlune's model does not include the change of failure mode due to corrosion.

$$\tau = \tau_{\max}\left(\frac{s}{s_1}\right)^{\alpha} \quad for \quad 0 \le s \le s_1 \tag{2.15}$$

$$\tau = \tau_{\max} \quad for \quad s_{1shifted} \le s \le s_{2shifted} \tag{2.16}$$

$$\tau = \tau_{\max} - \left(\tau_{\max} - \tau_f\right)\left(\frac{s - s_{2shifted}}{s_{3shifted} - s_{2shifted}}\right) \quad for \quad s_{2shifted} \le s \le s_{3shifted} \tag{2.17}$$

$$\tau = \tau_f \quad for \quad s_{3shifted} < s \tag{2.18}$$

in which all the parameters with subscript "shifted" are the initial values of the Model Code 1990 (CEB. 1993) shifted by Δs along the slip axes.

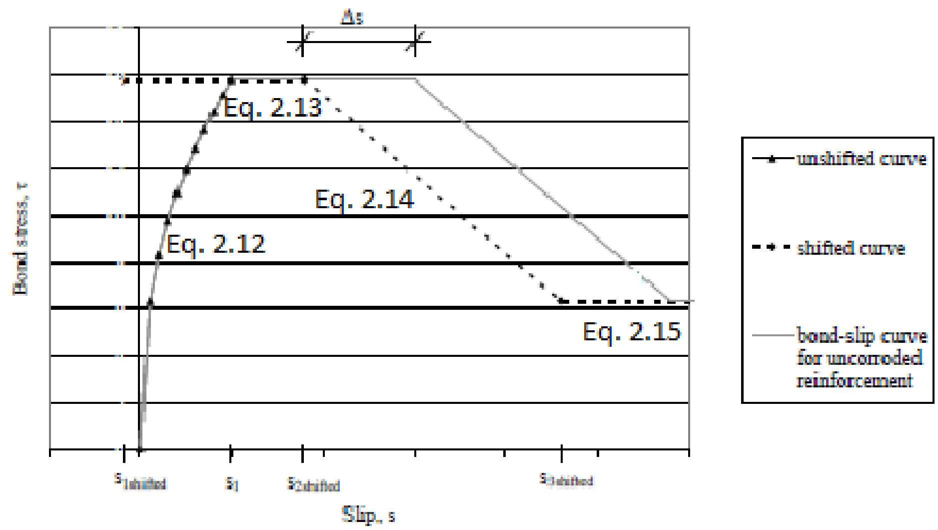

Δs
Eq. 2.13
Eq. 2.14
Eq. 2.12
Eq. 2.15
Bond stress, τ
Slip, s
unshifted curve
shifted curve
bond-slip curve for uncorroded reinforcement

(a)

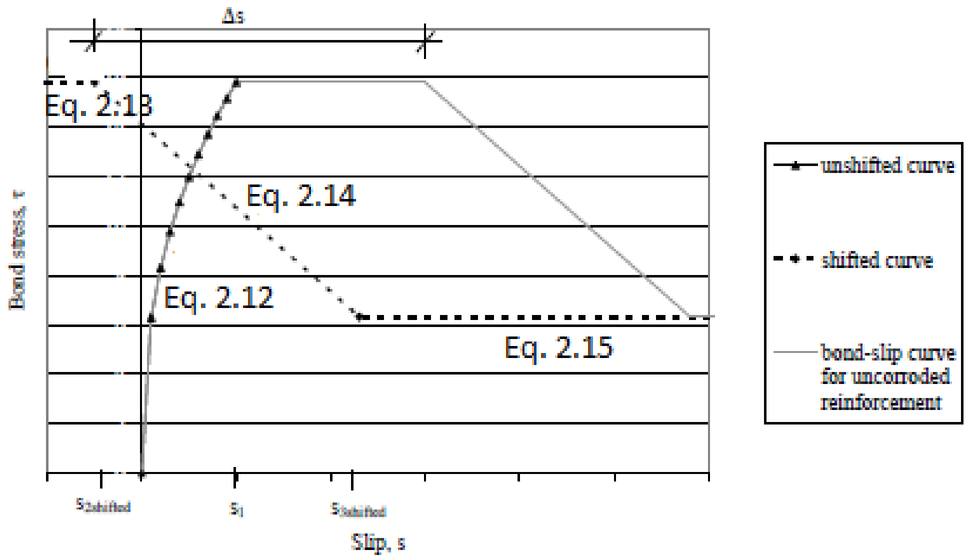

Δs
Eq. 2.13
Eq. 2.14
Eq. 2.12
Eq. 2.15
Bond stress, τ
Slip, s
unshifted curve
shifted curve
bond-slip curve for uncorroded reinforcement

(b)

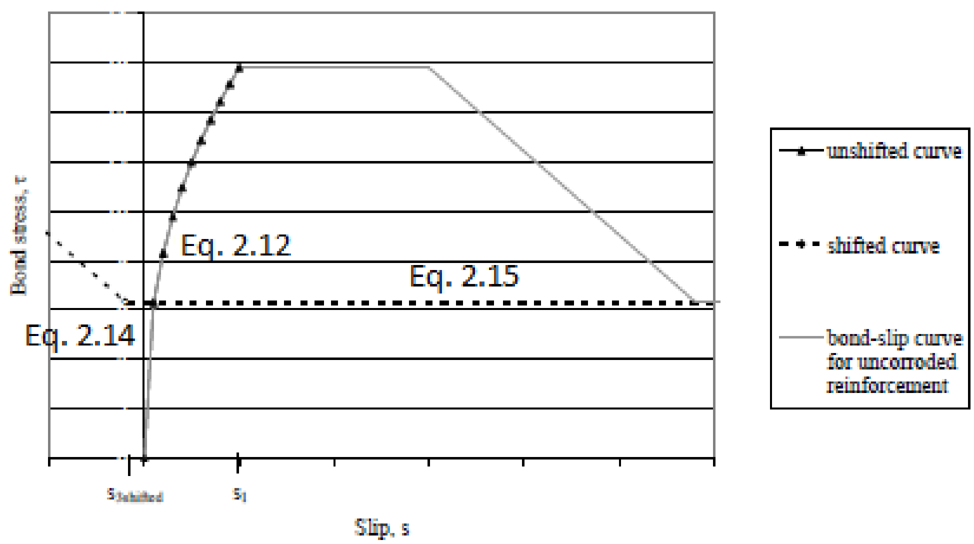

(c)

Figure 2-5 Corroded Bond-slip curve developed by Schlune (2006), (a) $0 \leq s_1 \leq s_{2shifted}$, (b) $s_{2shifted} \leq s_1 \leq s_{3shifted}$, (c) $s_{3shifted} < s_1$

In corroded RC members, transverse reinforcement is crucial in avoiding brittle splitting failure. Lack of sufficient confinement in the corroded RC members results in the change of failure from ductile pull out to brittle splitting failure (Lundgren et al. 2009). In a subsequent study, Lundgren et al. (2009) followed Schlune's method to develop a plasticity formulation based on Model Code 1990 (CEB. 1993) to make it applicable for corroded rebars as well as reversed and cyclic loading conditions. In this model, the bond stress was assumed to follow an elastoplastic behaviour defined as $\tau = D(s - s_P)$; $|\tau| \leq \tau_b(\kappa)$. Parameters D and s_P were defined as the bond stiffness and plastic slip, respectively; τ , τ_b , and s are the bond stress, bond strength as a function of un-corroded hardening parameters, κ, and slip, respectively. In the modified bond strength model, only the first part of the bond strength curve was reformulated slightly to interpolate an initial finite stiffness; however, the remaining parts of the equations follow the model by the Model

Code 1990 (CEB. 1993). Equation. 2.19 describes the modified elastoplastic bond strength curve for un-corroded reinforcement.

$$\begin{aligned}
&\tau_b(\kappa)=\left(1-\left(1-2\frac{\kappa}{s_1}\right)^2\right).\tau_{\max}, && 0\le\kappa\le\frac{s_1}{2}\\
&\tau_b(\kappa)=\tau_{\max}, && \frac{s_1}{2}\le\kappa\le s_2-\frac{s_1}{2}\\
&\tau_b(\kappa)=\tau_{\max}-\left(\tau_{\max}-\tau_f\right)\left(\frac{\kappa-s_2+\frac{s_1}{2}}{s_3-\frac{\tau_f}{D}-s_2+\frac{s_1}{2}}\right), && s_2-\frac{s_1}{2}\le\kappa\le s_3-\frac{\tau_f}{D}\\
&\tau_b(\kappa)=\tau_f, && s_3-\frac{\tau_f}{D}\le\kappa
\end{aligned} \qquad 2.19$$

in which all the parameters are defined in the Model Code 1990 (CEB. 1993). The bond stiffness and hardening parameter were defined as $D=\frac{2\tau_{\max}}{s_1}$ and $\kappa=s_p$, respectively.

Lundgren et al. (2009) introduced a new hardening parameter as a function of plastic slip and corrosion penetration depth, ignoring the possibility of cover spalling (Eq. 2.20).

$$\kappa=s_p+ax \qquad 2.20$$

where x is the corrosion penetration depth, a was defined as a coefficient according to Schlune (2006). Equation 2.20 does not account for the change of failure mode of corroded longitudinal reinforcing bars from ductile pull out to brittle splitting in case of no or low amount of transverse reinforcement. To incorporate the effect of cracking-induced failure mode change into the equations, Lundgren et al. (2009) introduced an interpolation factor k_{cor}, which is a function of the ratio between the corrosion penetration depth (x) to the corrosion penetration that causes cover cracking (x_{cr}, Eq.2.22). The bond strength for the corroded reinforcement was presented as an interpolation between the critical cases, i.e., confined and un-confined (Eq. 2.21).

$$\tau_b = k_{cor}.\tau_{b,conf} + (1-k_{cor}).\tau_{b,unconf} \quad 2.21$$

$$x_{cr} = 11.\left(\frac{f_{cc}}{40}\right)^{0.8}.\left(\frac{c}{d}\right)^{1.5}.\left(\frac{d}{16}\right)^{0.5} \quad 2.22$$

where x_{cr} is the corrosion level which cracks the concrete cover (μm), c is the concrete cover in mm, d is the rebar diameter in mm, and f_{cc} is the concrete cylindrical compressive strength in *MPa*.

According to Lundgren et al. (2009), the deterioration in bond-slip is a sequence of bond-slip shifting along the slip axis (Schlune 2006) plus the effect of k_{cor}, which defines the change of failure mode in corroded members (Figure 2-6).

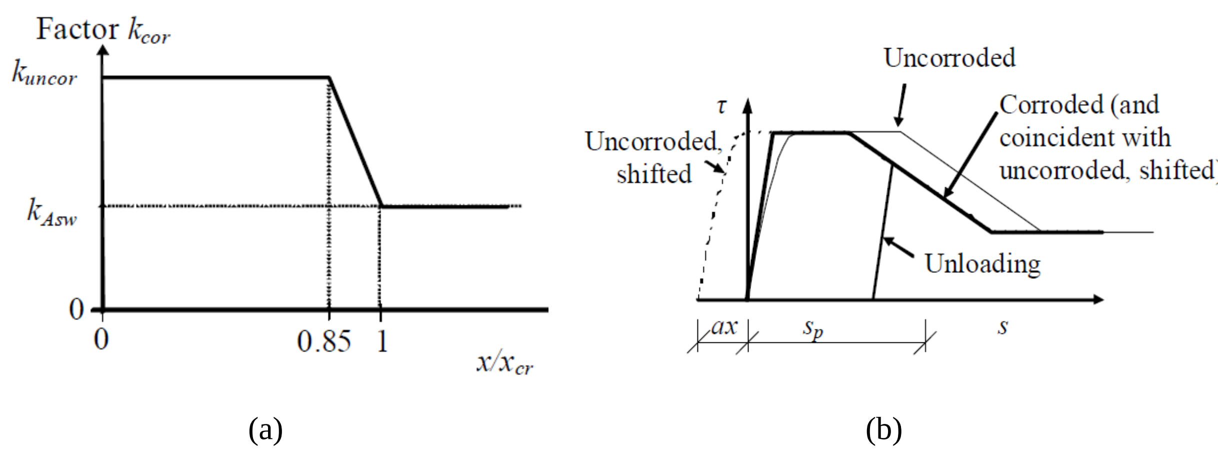

Figure 2-6- (a) Interpolation factor for corroded reinforcement (change of failure mode), (b) Corroded bond-slip curve (Reproduced from Lundgren et al. 2009)

In all of the studies reviewed earlier, the effect of cover spalling and stirrup corrosion due to the high level of corrosion was not considered. Zandi (2015) interpolated the effect of cover spalling into the bond-slip model developed by Lundgren et al. 2009 (Eq. 2.21) by introducing a new coefficient which is a function of confinement parameters. Zandi (2015) develop the local bond-slip curve at cover spalling for good bond condition (Figure 2-7).

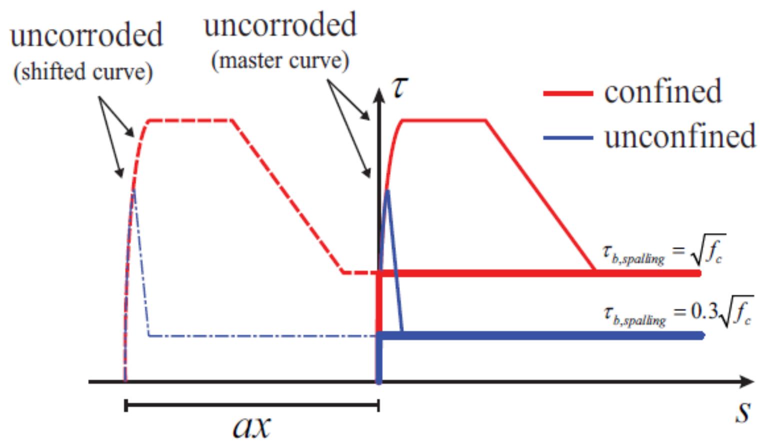

Figure 2-7 The local bond-slip curve at cover spalling for good bond condition (Reproduced from Zandi 2015)

There are also numerous experimental studies on the effects of corrosion on the bond-slip response. Almusallam et al. (1996), Al−Sulaimani et al. (1990), and Berra et al. (1997) suggested that at the initial stages of corrosion and formation of oxide around the steel rebar, the corrosion products adhere tightly to the rebar and decrease the porosity of the concrete close to reinforcement. The corrosion-induced pressure was observed to increase the bond strength before cracking initiation. However, the corrosion level-bond strength relationship after cracking was observed to be dependent on various parameters such as concrete cover, confinement level, and skin reinforcement. As shown in Figure 2-8(c), the ascending branch continues even after cracking in the presence of transverse and skin reinforcement. According to Almusallam et al. (1996), lack of confinement and sufficient concrete cover results in bond deterioration. In case of sufficient confinement, even in the absence of skin reinforcement, the residual bond strength remains above the bond strength of non-corroded RC members (Al−Sulaimani et al 1990).

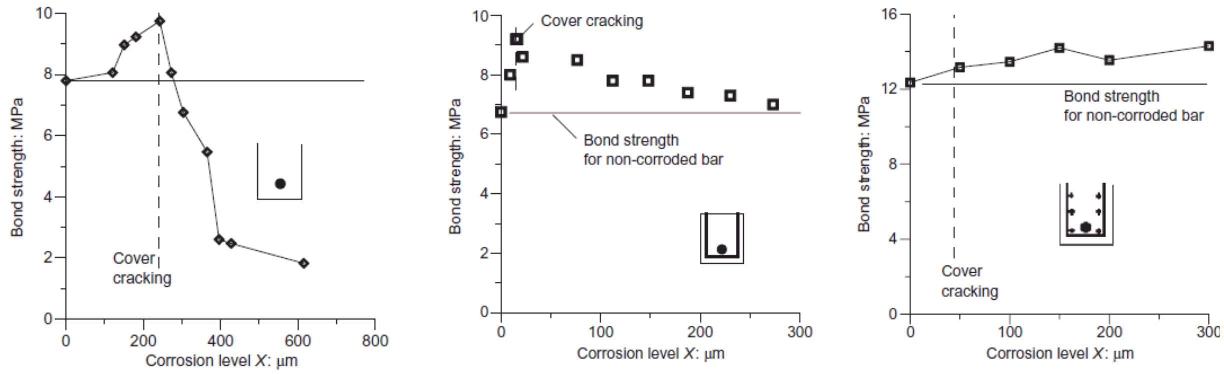

(a) (b) (c)

Figure 2-8 Bond strength versus corrosion level relationship for the cases (a) without transverse reinforcement (reproduced from Almusallam et al. 1996), (b) with transverse reinforcement (reproduced from Al−Sulaimani et al 1990), (c) with transverse and skin reinforcement (reproduced from Berra et al. 1997)

Many researchers have also numerically studied the bond strength deterioration of corroded RC structural members. Tørlen and Horrigmoe (1998) adopted the bond model by the Model Code 1990 (Figure 2-9) and proposed a new degraded bond-slip response (Figure 2-10,a). Tørlen and Horrigmoe's model (for confined concrete) can be described as a reduction of bond stresses by a scale factor and approximately no change in the slip values. Residual bond stress in Tørlen and Horrigmoe's model was obtained according to the test data conducted by Rodriguez et al. (1994). Castellani and Coronelli (1999) constructed another corrosion-induced bond-slip deterioration model based on the Model Code 1990 (CEB. 1993) (Figure 2-10, b). In this model, ascending branch of deteriorated bond-slip model follows the Model Code 1990 (CEB. 1993) up to the maximum corroded bond stress ($\tau^{c}_{\max}$), which was defined according to Rodriguez et al. (1994) experimental data.

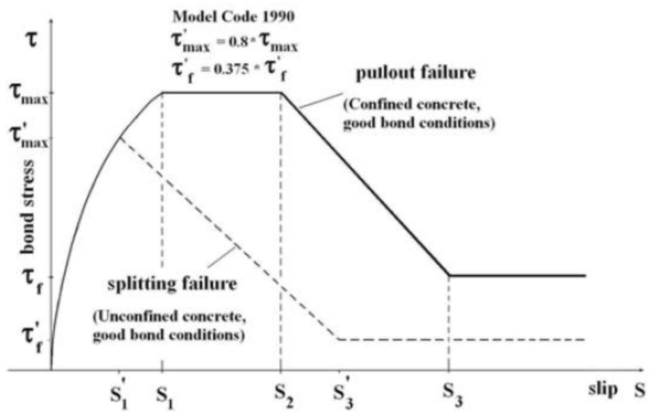

Figure 2-9 Bond-slip diagram for monotonic loading based on the Model Code 1990 (reproduced from CEB. 1993)

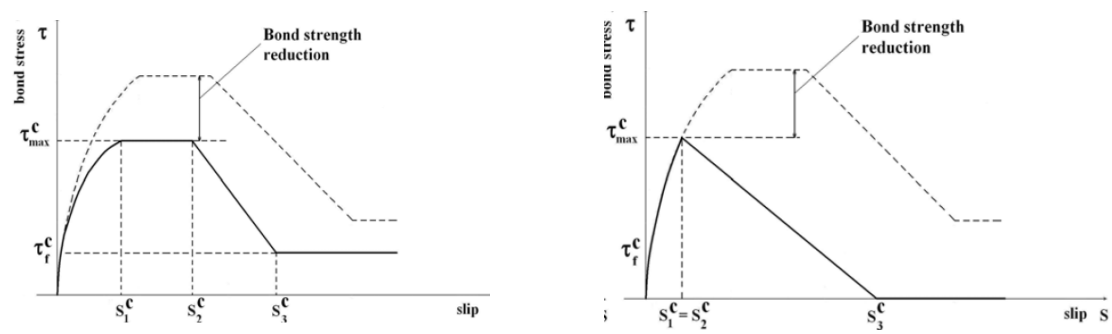

(a) (b)

Figure 2-10 Bond-slip deterioration model proposed by (a) Tørlen and Horrigmoe (1998) and (b) Castellani and Coronelli (1999)

Berra et al. (2003) numerically studied the effect of confinement on the corrosion-induced bond deterioration of corroded members. In this study, a 3D axisymmetric finite element analysis was conducted. The residual bond strength between corroded longitudinal reinforcing bars and concrete was compared to that based on experimental results reported by Berra et al. (1997) and Rodriguez et al. (1994). In the ABAQUS finite element simulation, a ribbed bar surrounded by concrete was modelled using axisymmetric elements. The smeared cracking model was adopted with an elastic-plastic theory for the compressive response and an elastic theory for the pre-cracking tensile response. The fracture energy of the material was modelled using a linear softening behaviour. An elastic-plastic constitutive model was adopted for the rebar, considering the experimental material properties of the steel. The authors assumed two types of steel-concrete bond in this study. In the first model, all the interaction nodes between steel and concrete were assumed to be compatible, and in the second model, the compatibility was assumed only for the nodes between the compressed concrete and inclined ribs. Two types of confinements were modelled in this study, i.e., type 1 which is transverse steel confinement simulated by springs and type 2 which is embedded stirrups in concrete and skin reinforcement modeled by shell elements. Orthotropic thermal expansion properties were imposed into the model to consider the radial expansion of corrosion products. Adopting and modifying the previous test results, the relationship between the thickness of corrosion product, thermal strain, corrosion level, and total crack width was then established and the thermal strain in ABAQUS increased to impose a corrosion level of 400 μm. It was observed that confinement significantly decreases the bond deterioration and also increases the bond strength in case of adequate amount of stirrups. It was also observed that the presence of skin reinforcement in addition to the stirrups contributes to enhancement of positive effects of confinement.

Lin and Zhao (2016) developed an empirical model for corrosion-induced bond degradation. The authors conducted an experimental study to evaluate the effect of confinement and corrosion rate on the bond deterioration of corroded reinforcing steel in RC members. A “wetting-drying-cycle” method was used to simulate the real corrosion process up to 15% mass loss with a current density of 400 $\mu A/cm^2$. The bond degradation model proposed by Lin and Zhao (2016) is:

$$R_\tau = \begin{cases} 1 & \eta_s \le 1.5\% \\ e^{-\delta(\eta_s - 1.5\%)} & \eta_s > 1.5\% \end{cases} \qquad 2.23$$

where R_τ is the relative bond strength (the ratio of corroded to un-corroded bond strength), η_s is the mass loss percentage and δ is a degradation parameter which is a function of concrete cover to rebar diameter ratio (c/d) and stirrup confinement. The coefficient δ was defined empirically as Eq.2.24.

$$\delta = \begin{cases} \dfrac{k_1 + k_2\left(c/d\right)}{k_4\xi_{st} + 1} & i_{corr} \le 200 \;\; \mu A/cm^2 \\ \dfrac{k_1 + k_2\left(c/d\right)}{k_4\xi_{st} + 1}\left[k_3 \ln\left(\dfrac{i_{corr}}{200}\right) + 1.0\right] & i_{corr} > 200 \;\; \mu A/cm^2 \end{cases} \tag{2.24}$$

in which i_{corr} is the corrosion current density ($\mu A/cm^2$), ξ_{st} is the stirrup index, coefficients k_1 , k_2 , k_3 , and k_4 are empirical parameters which are dependent on the corrosion test condition, specimen geometry, stirrup index and bar position, respectively.

Sæther and Sand (2016) also conducted a numerical finite element analysis and experimental study on corroded RC beams. In this study, the commercial finite element software DIANA was used to simulate the corroded RC beams tested by Rodriguez et al. (1995) and Rodriguez et al. (1996) and investigate the effects of corrosion-induced steel rebar cross-section loss and steel-concrete bond degradation on the mechanical response of corroded RC beams. In this model, it was assumed that the bond strength of corroded beams experiences 65% or alternatively 80% loss.

Deng et al. (2018) studied the corrosion effects on the seismic performance of multi-span-simply-supported bridges (MSSS). In this study, the authors developed a bond-slip deterioration model considering the strain penetration for two cases, i.e., straight rebar embedded in a concrete member (column-footing connection) and straight rebar with a hook embedded in a concrete member. Deng et al. (2018) used the Bond_SP01 material and Zero Length element in OpenSees and then modified four input parameters of the Bond_SP01 material according to the corrosion level, i.e., yield and ultimate tensile stresses of longitudinal rebar ($f_{yt,cor}$ and $f_{ut,cor}$) and corresponding yield and ultimate slip values (s_y and s_u).

Maaddawy et al. (2005) developed a 1D model for the bond strength of corroded longitudinal reinforcing bars. One of the most important advantages of this model compared to the other developed bond models is accounting for the contribution of stirrups and concrete individually, meaning that the corrosion of flexural reinforcement doesn't affect the contribution of stirrups (in case of no corrosion on the stirrups) in bond strength. In this model, the bond stress-slip model based on the Model Code 1990 (CEB. 1993) was adopted and modified for corrosion effects. The maximum bond strength of corroded reinforcement was described as Eq. (2.25).

$$\begin{aligned} &\tau_{\max C} = R\left(0.55 + 0.24\frac{C_c}{d_b}\right)\sqrt{f_c} + 0.191\frac{A_v f_{yt}}{Sd_b} \\ &R = \left(A_1 + A_2 m_l\right) \end{aligned} \qquad 2.25$$

in which R is an empirical coefficient that defines the corrosion-induced deterioration of bond strength, m_l is the corrosion-induced mass loss percentage, C_c is the smaller of concrete cover and half of reinforcing bar spacing, d_b is the diameter of un-corroded reinforcing bar, f_{yt} is the yield strength of transverse reinforcement, S is the spacing of the stirrups, and A_v is the cross-sectional area of transverse reinforcement. Vu et al. (2016) adopted Eq. 2.25 and substituted it into the bond-slip model based on the Model Code 1990 (CEB. 1993) in their numerical study to account for the bond-slip deterioration as one of the deteriorating effects of corrosion on the strength and drift capacity of corroded RC columns.

Blomfors et al. (2018) proposed a new engineering bond model for corroded reinforcement. The local bond stress-slip relationship of the Model Code 2010 (fib 2013) was adopted and modified to account for the deteriorating effects of corrosion by introducing equivalent slip and change of failure mode to splitting failure due to corrosion-induced cover cracking and spalling. The maximum splitting strength and residual bond stress defined in the Model Code 2010 (fib 2013) for splitting failure have been modified in case of low stirrup content. According to the model Schlune (2006) proposed, the local bond stress-slip curve was first shifted in the slip direction by equivalent slip (s_{eq}) to account for the effect of corrosion. In the next step, the influence of corrosion-induced cracking was implemented into the splitting strength equation by reducing the concrete cover-related factor to 1 (Eq. 2.26). Finally, the reduced residual bond capacity of corroded specimens with low stirrup content was modified according to the reduced bond strength (Eq.2.27).

$$\tau_{bu,spilit,red} = \eta_2 .6.5.\left(\frac{f_c}{25}\right)^{0.25}\left(\frac{25}{d_b}\right)^{0.25}\left(1+k_m .k_{tr}\right) \qquad 2.26$$

$$\tau_{res,\mathrm{mod}}\left(K_{tr}\right) = \begin{cases}\left(0.16+12K_{tr}\right).\tau_{bu,spilit,red} & for \quad 0 \le K_{tr} \le 0.02 \\ 0.4\tau_{bu,spilit,red} & for \quad 0.02 < K_{tr}\end{cases} \qquad 2.27$$

in which variables η_2, k_m, and k_{tr} were chosen as described in the Model Code 2010 (Fib 2013). Variables f_c and d_b are the cylindrical compressive strength of concrete and rebar diameter, respectively. Variables $\tau_{bu,spilit,red}$ and $\tau_{res,\mathrm{mod}}\left(K_{tr}\right)$ are the reduced bond strength and reduced residual bond capacity of corroded specimens, respectively.

2.3.2 Effects of corrosion on reinforcing steel and concrete

By exceeding the level of chloride ions around the longitudinal reinforcing bars in RC members, chloride-induced corrosion initiates and propagates over time and negatively affects the rebars and concrete. The corrosion propagation weakens the concrete cover and core concrete, resulting in confinement loss and the potential risk of buckling in the compressive longitudinal rebars. The following sections briefly summarize some of the studies conducted on pitting (localized) and uniform (general) corrosion effects on the degradation of concrete and rebar's mechanical and geometrical properties.

2.3.2.1Effect of corrosion on rebar mechanical and geometrical properties

Faraday's law estimates the mass loss of the rebars (m_s) and rebar diameter reduction (x_t) as Eqs. 2.28 and 2.29, respectively.

$$m_s = \frac{MI_{current}t}{zF} \tag{2.28}$$

$$x_t = 0.0116 i_{corr} t \tag{2.29}$$

in which M is the atomic weight of metal ($55.85\, g/mol$ for iron), z is the iron oxidation induced valence of iron ($z = 2 \;\; for \;\; Fe \rightarrow Fe^{2+} + 2e^{-}$), F is Faraday's constant ($F = 96,485\, C/mol$), $I_{current}$ is current (A), t is the time (in seconds in Eq. 2.28 and in years in Eq. 2.29), and i_{corr} is the current density $\left(\mu A/cm^2 \right)$.

Val (2007) studied the effects of pitting and uniform corrosion on the reliability of corroded beams. In the case of uniform corrosion, the corrosion current density can be related directly to the mass loss of the rebars through Faraday's law. Assuming a constant corrosion rate and uniform corrosion penetration all around the perimeter of the rebar, Val (2007) adopted the estimated corroded rebar diameter reduction (Eq.2.29) to introduce the cross-section of a group of n identical corroded rebars, $A_s\left(t\right)$, as:

$$\Delta D\left(t\right) = 2 \times 0.0116 i_{corr} t \tag{2.30}$$

$$A_s\left(t\right) = n\frac{\pi\left[d_b - \Delta D\left(t\right)\right]^2}{4} \geq 0 \tag{2.31}$$

where $\Delta D(t)$ is corroding reinforcement diameter loss in millimetres, i_{corr} is corrosion current density $\left(\mu A/cm^2\right)$ and d_b is un-corroded rebar diameter. According to the corroded rebar diameter reduction, Faraday's law (Eq.2.29), the depth of a pit in case of pitting corrosion can be estimated as:

$$p(t) = 0.0116 i_{corr} t R \qquad 2.32$$

where R is the ratio between the maximum penetration of pitting to the average penetration depth and was defined by Tuutti (1982) as 4 and 10 for 5 and 10 mm of 150-300 mm-length reinforcing bar. According to a hemispherical model of a pit suggested by Val and Melchers (1997), the cross-sectional area of a pit, $A_p(t)$, was suggested as Eq. 2.33 and Figure 2-11.

$$A_p(t) = \begin{cases} A_1 + A_2 & p(t) \le \dfrac{D_0}{\sqrt{2}} \\ \dfrac{\pi D_0{}^2}{4} - A_1 + A_2 & \dfrac{D_0}{\sqrt{2}} \le p(t) \le D_0 \\ \dfrac{\pi D_0{}^2}{4} & p(t) > D_0 \end{cases} \qquad 2.33$$

$$A_1 = \frac{1}{2}\left[\theta_1\left(\frac{D_0}{2}\right)^2 - a\left|\frac{D_0}{2} - \frac{p(t)^2}{D_0}\right|\right] \quad , \quad A_2 = \frac{1}{2}\left[\theta_2 p(t)^2 - a\frac{p(t)^2}{D_0}\right] \quad ,$$

$$a = 2p(t)\sqrt{1 - \left[\frac{p(t)}{D_0}\right]^2} \quad , \quad \theta_1 = 2\arcsin\left(\frac{a}{D_0}\right) \quad , \quad \theta_2 = 2\arcsin\left(\frac{a}{2p(t)}\right)$$

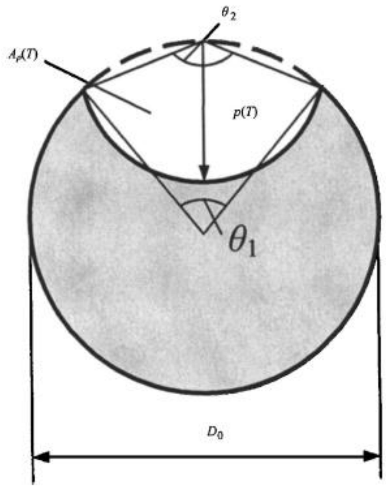

Figure 2-11 Pit configuration defined by Val and Melchers (1997)

In a more recent study by Deng et al. (2018), assuming varying corrosion rates due to different exposure conditions and binder types (Andrade and Alonso 2001), the cross-sectional loss rate of corroding rebar subjected to uniform corrosion, $\rho(t)$, was estimated as:

$$\rho(t)=\begin{cases} 0 & t \le T_0 \\ 1-\left(\dfrac{d(t)}{d_b}\right)^2 & T_0 \le t \le \quad T_0+d_b/r \\ 1 & t > T_0+d_b/r \end{cases} \qquad 2.34$$

where T_0 is corrosion initiation time, $d(t)$ is the time-dependent diameter of the corroded rebar and was defined as $d(t)=d_b-r(t-T_0)$, and r is the corrosion rate (in mm/year). According to experimental investigations by Almusallam (2001) and Du et al. (2005), the cross-sectional loss of rebar due to uniform corrosion was observed to affect the nominal strength of the steel, and pitting corrosion was observed to degrade the ductility. Based on such observations, Cairns et al. (2005) expressed the degraded tensile yield stress ($f_{yt,cor}$) , ultimate tensile stress ($f_{ut,cor}$) and ultimate tensile strain ($\varepsilon_{ut,cor}$) of corroded rebar as:

$$f_{yt,cor}=\left[1.0-100\times\alpha_y.\rho(t)\right]f_{yt} \qquad 2.35$$

$$f_{ut,cor} = \left[1.0 - 100 \times \alpha_u . \rho(t)\right] f_{ut} \quad 2.36$$

$$\varepsilon_{ut,cor} = \left[1.0 - 100 \times \alpha_1 . \rho(t)\right] \varepsilon_{ut} \quad 2.37$$

where f_{yt}, f_{ut}, and ε_{ut} are the tensile yield stress, ultimate tensile stress, and ultimate tensile strain of un-corroded rebar, and the variable $\rho(t)$ is the cross-section loss rate. The calibrated values of the empirical coefficients in Eqs. 2.35-2.37 have been reported as $\alpha_y = 0.01, \alpha_u = 0.01$, and $\alpha_1 = 0.035$ (Cairns et al. 2005). Figure 2-12 shows the uniaxial constitutive model for corroded longitudinal reinforcing bars used in Deng et al. (2018).

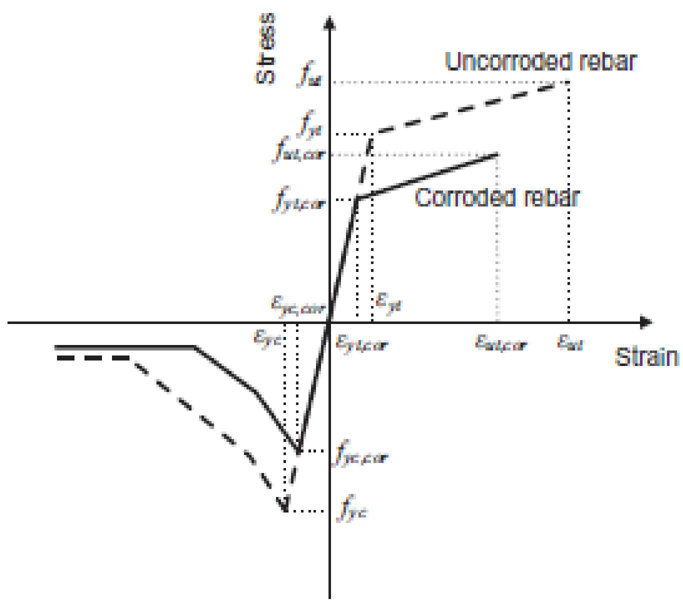

Figure 2-12 Uniaxial constitutive model for corroding rebar used in Deng et al. (2018)

2.3.2.2Buckling of corroded longitudinal reinforcing bars in RC columns

Corrosion of transverse reinforcement followed by loss of confinement and rebar cross-section loss increases the potential risk of longitudinal rebar buckling. Inelastic buckling of the corroded longitudinal rebars under compression is another vital limit state which needs to be studied, especially in the seismic design of structures in earthquake zones. Kashani et al. (2013) developed a degraded stress-strain response in tension and compression based on the Dhakal–Maekawa buckling model, as shown in Figure 2-14 (a) (Dhaka and Maekawa 2002) and evaluated the effect of different corrosion levels on the inelastic buckling behaviour of the compressive longitudinal reinforcing bars (Figure 2-14, b). The authors observed an unsymmetrical buckling mechanism in corroded rebars with either single or multiple intermediate plastic hinges (Figure 2-13).

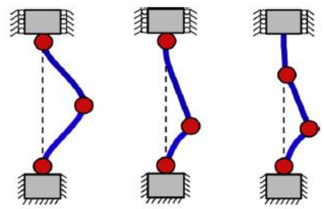

(a) (b) (c)

Figure 2-13 Inelastic buckling mechanism after Kashani et al. (2013) for (a) un-corroded rebar (a symmetrical mechanism), (b) and (c) corroded rebar (an un-symmetrical mechanism)

Equation 2.38 shows the degraded compressive stress-strain envelope proposed by Kashani et al. (2013) .

$$\eta = \sigma / f_{yc,cor} = \begin{cases} \xi = \varepsilon / \varepsilon_{yc,cor} & \xi \le 1 \\ \dfrac{\eta_2 - 1}{\xi_2 - 1}(\xi - 1) + 1 & 1 < \xi \le 2 \\ \eta_2 - 0.02(\xi - \xi_2) & \xi_2 \le \xi \;\&\; \eta \ge 0.2 \\ 0.2 & otherwise \end{cases} \quad ; \quad \begin{aligned} &\xi_2 = \max\{55 - 2.3\lambda_{p,cor}; 7\} \\ &\eta_2 = \max\{\alpha(1.1 - 0.016\lambda_{p,cor})\eta^*_2; 0.2\} \\ &\lambda_{p,cor} = \sqrt{\frac{f_{yc,cor}}{100}}\frac{s}{d_b - 2x_{cp}} \end{aligned}$$

$$f_{yc,cor} = f_{yc}\left[1 - 100 \times \beta . \rho(t)\right] \quad ; \quad \beta = \begin{cases} 0.005 & s/d_b \le 5 \\ 0.0065 & 5 < s/d_b \le 10 \\ 0.0125 & s/d_b > 10 \end{cases}$$

2.38

in which η and ξ are the non-dimensional stress and strain, respectively; s is the transverse reinforcement spacing and d_b is the un-corroded rebar diameter; α is the softening coefficient and is considered as 1 for the case of $s/d_b < 10$ and is considered as 0.75 for the case of $s/d_b > 10$; η^*_2 is the non-dimensional stress corresponding to ξ_2 (in case of no buckling); $f_{yc,cor}$ is the compressive strength of corroded rebar; $\lambda_{p,cor}$ is the non-dimensional buckling parameters of corroded rebar; x_{cp} is the corrosion penetration depth; $\rho(t)$ is the cross-sectional loss rate; and β is a regression analysis coefficient.

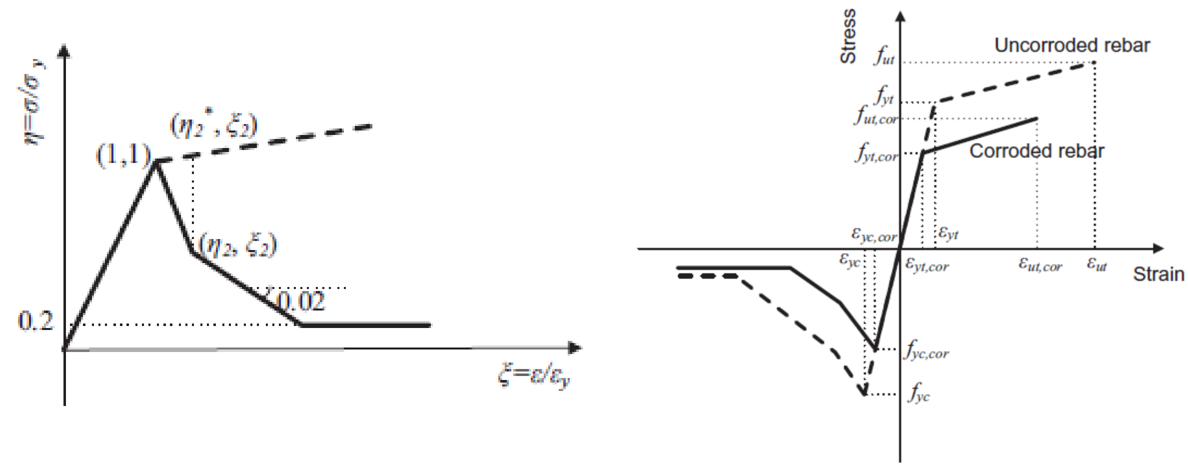

(a) (b)

Figure 2-14- Buckling model for (a) un-corroded reinforcing steel proposed by Dhaka and Maekawa (2002) and (b) for corroded reinforcing steel proposed by Kashani et al. (2013)

Xin et al. (2019) introduced the critical stress of compressive longitudinal reinforcement in corroded RC columns (Eq. 2.39) by adopting the model developed by Giamundo et al. (2014) for non-corroded reinforcement. In this model, the maximum allowable stress of corroded compressive longitudinal reinforcing bars was assumed as the minimum amount of yield strength (f_y) and critical stress (σ_{cr}). A new yield stress attenuation coefficient β , i.e., the ratio of critical stress and yield stress of compressive longitudinal rebar, was used. The inelastic critical stress proposed by Xin et al. (2019) for corroded compressive rebar is:

$$\sigma_{cr} = \frac{3.46\sqrt{E_r I k_1}}{A_{all}} \qquad 2.39$$

in which

$$E_r = \frac{4E_s E_p}{\left(\sqrt{E_s}+\sqrt{E_p}\right)^2} = \frac{4E_s\beta_1}{\left(1+\sqrt{\beta_1}\right)^2} \quad ; \; I = \frac{\pi\varphi_1^4}{64} \; ; \begin{cases} \beta_1 = 1 & \text{elastic range} \\ \beta_1 = 0.03 & \text{yielding stage} \end{cases}$$

$$\begin{cases} k_1 = \sqrt{2}\,\dfrac{E_p A_{st}}{bs} & \text{for corner bar} \\ k_1 = \dfrac{48 E_p I_{st}}{s_1^3 s} & \text{for a mid-face bar} \end{cases}$$

in which E_r is the reduced modulus of elasticity; E_p is the hardening modulus of steel rebar, i.e., $E_p = \beta_1 E_s$; A_{all} is the area of longitudinal compressive reinforcement; k_1 is the stiffness parameter which is different for corner and mid-face bars; A_{st} is the tie's cross section; I_{st} is the tie's moment of inertia; s_1 is the lateral spacing of longitudinal rebars; and s is the transverse reinforcement spacing.

2.3.2.3Effect of corrosion on mechanical properties of cover concrete

Berra et al. (2003) adopted the corrosion-induced concrete crack width model developed by Molina et al. (1993) as described in Eq. 2.40, assuming the incompressibility of corrosion products. The model was then modified, considering corrosion products' tendency to penetrate (Eq. 2.41).

$$W_{cr} = \sum_i u_{i\,corr} = 2\pi t \quad , \quad t = \left(\upsilon_{rs} - 1\right) X \tag{2.40}$$

$$t = \frac{d_b \left(\nu_{rs} - 1\right)}{d_b + c} X \tag{2.41}$$

where W_{cr}, $u_{i\,corr}$, t, υ_{rs}, and X are the total crack width, the opening of each single radial crack, rebar expansion, the ratio of the volume of corroded and un-corroded rebar, and corrosion penetration depth (rebar thickness reduction), respectively. Variables d_b and c are the bar diameter and crack extension within the cover.

According to a model developed by Vecchio and Collins (1986), cracking and spalling of the concrete cover in the compression zone was described as a reduction in compressive strength of the concrete cover by adopting a brittle post-peak behaviour (Eq. 2.42). In this equation, the reduction of compressive strength followed by longitudinal micro cracks was introduced as a function of the average strain in the transverse direction:

$$f_{c,cor} = \frac{f_c}{1 + K\varepsilon_1 / \varepsilon_{C0}} \tag{2.42}$$

in which $f_{c,cor}$ and f_c are the compressive strength of cracked and sound concrete, respectively, K is the coefficient related to the properties of rebar, ε_{c0} is the un-corroded compressive peak strain, and ε_1 is the average tensile strain of cracked cover concrete in the direction perpendicular to the applied compression. Coronelli and Gambarova (2004) adopted the equation developed by Vecchio and Collins (1986) and modified it for the compressive strength reduction in the concrete cover of corroded RC members. Coronelli and Gambarova (2004) introduced ε_1 as:

$$\varepsilon_1 = \left(b_f - b_0\right) / b_0 \quad ; \quad b_f - b_0 = n_{bars}.w_{cr} \tag{2.43}$$

in which b_f and b_0 are the width of the corroded and un-corroded sections, n_{bars} is the number of rebars undergoing corrosion, and W_{cr} is the total crack width as suggested by Molina et al. (1993) (Eq. 2.40). Many researchers have used Eq. 2.42 for modelling the deteriorated cover concrete in corroded RC members (Vu et al. 2016 and Deng et al. 2018).

2.3.3 Structural performance of corroded RC columns

The post-peak response of flexural columns is reported to be affected significantly by the geometrical nonlinearity besides the material nonlinearity (Dhakal and Maekawa 2001). This effect is insignificant in the columns where shear-induced diagonal cracks govern the failure. The combination of second-order effects (P-delta effect) and the local nonlinearity effects due to inelastic material behaviour, such as buckling of longitudinal reinforcements in compression and concrete cover spalling, affect the failure mode and post-peak response of flexural columns, i.e.

slender columns and eccentrically-loaded columns, significantly. One of RC bridge piers' most common failure modes, especially under seismic loading, was reported as core concrete crushing along with vertical reinforcement buckling (Kashani et al. 2019). Such effects become more critical and significant in the case of corrosion in which the constitutive model of concrete and reinforcing steel are adversely affected, and the concrete cover at some sections spall off. The adverse effect of corrosion on the strength and ductility of the corroded RC columns also depends on the initial degree of confinement. It would be more pronounced in case of inadequate confinement (Joshi et al. 2015). This section reviews experimental, analytical and numerical investigations on the structural performance of corroded RC members under pure axial, lateral, and combined axial-lateral loading.

2.3.3.1Experimental investigations

Rodriguez et al. (1996a) conducted an experimental study to establish a relationship between the corrosion level and the structural performance of corroded columns. Three types of columns with different longitudinal rebars and link arrangements were fabricated. Some specimens were cast using 3% calcium chloride, and all the columns were cast and cured in indoor conditions for 28 days. The columns with calcium chloride underwent the accelerated corrosion procedure for 100-200 days, using a constant current density of 100 $\mu A/cm^2$. The columns were then axially loaded. It was observed that the ultimate capacity, strain at this load, and the compressive stiffness at service load in corroded columns decrease significantly. Concrete cover cracking and spalling due to corrosion was introduced as the most relevant form of deterioration. Corrosion-induced mechanical eccentricity and premature buckling of the main longitudinal reinforcing bars due to the link’s cross-sectional loss were observed as other relevant forms of deterioration.

Saito et al. (2007) conducted an experimental study to evaluate the structural performance of corroded short RC columns under uniaxial compression. The cross-section of the tested specimens was 180 mm by 180 mm, and the height was 660 mm with a corrosion region of 200 mm (mid-height). The main variables of this test were the location of corrosion (one side, two sides, or all the sides), corrosion simulation method (electrolytic corrosion, scrapped bar, and small-size round bar), and corrosion level (20% to 80%). It was also assumed that in case of stirrup corrosion, it occurs in 4 stirrups within the corroded region. The specimens were then tested under uni-axial compression. It was observed that corrosion of the main longitudinal reinforcing bars results in strength reduction, and the stirrups' corrosion contributes to strain softening behaviour in the post-peak region.

Wang and Liang (2008) conducted an experimental study to evaluate the structural performance of eccentrically loaded RC columns with partial length corrosion. The corrosion was performed by adding calcium chloride to the mixing water and applying the external impressed current method. The variables of this test were the column corroded side (tensile or compressive) and eccentricity. It was observed that corrosion changes the failure mode of the column to a more brittle pattern. For the corroded column subjected to a larger eccentricity, it was observed that corrosion on the tensile side significantly degrades the structural performance. On the other hand, for the columns under smaller eccentricity, corrosion of the compressive was observed to have a more pronounced effect on the load capacity. The relatively shorter corrosion partial length located on the tensile or compressive side was observed to cause longitudinal cracks and reduction of confinement effects.

Xia et al. (2016) conducted an experimental study to quantitatively estimate the residual strength of corroded RC columns under eccentric loading. A total of 24 RC columns were tested, including 20 corroded columns (using a combined electro-migration process and wet and dry cycles to simulate chloride-induced pitting corrosion) and four un-corroded columns. The main variables of this study were the stirrup spacing (100 mm and 200 mm), the loading eccentricity (50 and 90 mm), and the corrosion level. The cross-sectional loss of rebars, the corrosion-induced crack width in the concrete cover, and the loss of bond between steel and concrete were reported as significant factors in reducing the bearing capacity of corroded RC columns. During the corrosion propagation, it was observed that the cracks propagate approximately parallel to the longitudinal reinforcing bars. The maximum crack width was observed to have a linear relationship with the average crack width. By increasing the corrosion level, the ultimate compressive strength and the initial stiffness were significantly reduced. The reduction rate of compressive strength was observed to increase by increasing the load eccentricity and decreasing the stirrup spacing. The appearance of corrosion-induced cracks in the concrete cover followed by spalling and delamination was noted as an important factor in increasing the load eccentricity, which tends to accelerate the structural failure of the RC column.

Vu et al. (2017) investigated the adverse effect of transverse reinforcement corrosion on the nonlinear behaviour of confined concrete through several experimental tests. The authors considered the effect of corrosion level of transverse reinforcement, arrangement of confinement, and cross-sectional shape of confined concrete as the main variables of the study. By increasing the mass loss ratio of confining reinforcement (more than 10%), the strength and ductility of the confined concrete decreased significantly. The post-peak branch of the stress-strain curve was observed to become steeper, leading to a change of failure mode of confined concrete from ductile to brittle. In this study, the stress-strain model for the confined concrete developed by Mander et al. (1989) was modified to account for the effect of corrosion. The model was verified by comparing the results to those based on the experiments (for both square and circular specimens).

2.3.3.2Numerical and analytical studies

Mohammed (2014) developed simplified nonlinear static and dynamic finite element analysis approaches to study the effects of corrosion on the structural performance and serviceability of corroded bridge columns. A simplified nonlinear sectional analysis (NLSA), simplified nonlinear finite element analysis (NLFEA) approach, simplified hybrid linear/nonlinear dynamic finite element analysis (SHDFEA) approach, and simplified non-linear seismic analysis (SNLSA) approach were conducted to evaluate the ultimate and seismic capacity and serviceability of corroded columns. In one of the case studies carried out in this work, two large-scale bridge columns (6 m height) with different load-over-capacity ratios were modelled (column A with load over capacity ratio (LOCR) of 40% and column B with a load-over-capacity ratio (LOCR) of 50%). The time-dependent corrosion process for these two columns was simulated as 5% rebar cross-section reduction resulting in cover cracking, 15% cross-section reduction resulting in spalling, 20% cross-section reduction resulting in one tie failure, and 30% cross-section reduction resulting in two ties failure. The integrity of the proposed model was then verified through different case studies by comparing the results based on the proposed model and available experimental and analytical results.

Sæther and Sand (2016) conducted a numerical finite element analysis and experimental study on corroded reinforced concrete beams. In this study, the commercial finite element software DIANA was used to simulate the corroded RC beams tested by Rodriguez et al. (1995) and Rodriguez et al. (1996). This study investigates the effects of corrosion-induced steel rebar cross-sectional loss and steel-concrete bond degradation on the mechanical response of corroded RC beams. Among a total of thirty-one reinforced concrete beams tested by Rodriguez et al. (1996), only two beams were selected as un-corroded, and one beam was selected as the corroded RC beam. The concrete, rebars, and bond-slip were modelled by eight-node quadrilateral CQ16M plane stress elements, discrete truss CL6TR elements, and the interface elements IP33 CL12I, respectively. Two types of smeared crack models, the total strain fixed crack model and the rotating crack model, were used to investigate the effects of smeared models on the flexural response of RC corroded beams. It was observed that the result based on the latter type is the best fit to the experimental data. In this numerical approach, it was assumed that one of the tensile reinforcements is attacked by the average level of corrosion and the maximum level attacks another one to investigate the effect of corrosion level on the load-bearing capacity of corroded RC beams. This study adopted two types of compressive constitutive models: elastic-ideally plastic and parabolic stress-strain curve. A bilinear interaction was proposed as the tensile constitutive model with fracture energy according to the Model Code 1990 (CEB. 1993). In this study, the bond-slip response for the reference beam was adopted from the Model Code 1990 (CEB. 1993), and the bond-slip degradation was assumed due to a lack of experimental data. The material properties of corroded and un-corroded samples were adopted based on the Norwegian Code for Design of Concrete Structures NS 3473, assumptions, DIANA library, or previously published test data. It was observed that bond degradation is not as effective as steel bar cross-section loss on the load-center deflection response of corroded beams.

Over the past few decades, many studies have been conducted on corroded RC structures in the serviceability limit state (Plizzari et al. 2005) and ultimate limit state (Mohammed 2014). In all of them, artificially corroded structures have been studied to investigate the effect of corrosion on stiffness loss (serviceability limit state), ultimate capacity, and ductility degradation (ultimate limit state). Tahershamsi (2016) conducted a study to evaluate the effect of corrosion (in natural conditions) on the bond behaviour of RC members in the anchorage zone and the consequent degradation of structural behaviour. In this study, naturally corroded beams from the 32-year-old Stallbacka Bridge were taken and studied experimentally and numerically. In the first phase of this study, the anchorage capacity of corroded beams was tested, and splitting-induced pull-out failure was observed in all the specimens. It was also observed that the bond stress and concrete compressive strength of corroded beams with splitting-induced cracks and cover spalling are lower than those of the uncorroded beams. Tahershamsi (2016) found that the compressive strength of concrete in naturally corroded beams was lower than that of identical beams under the same amount of artificially-induced corrosion due to the possible effect of frost damage in addition to corrosion in real-life structures. In the next phase of the study, the corroded beams' corrosion level was evaluated through gravimetric measurements and advanced 3D optical scanning. The correlation between the corrosion level, splitting-induced crack width and anchorage capacity of corroded beams was then examined experimentally. In the last phase of Tahershamsi's study, two types of numerical studies were conducted under the commercial DIANA 9.5 software, i.e., (1) a three-dimensional (3D) non-linear finite element analysis (NLFEA) including frictional bond model and corrosion model considering the effects of bond and splitting stress formulated by Lundgren (2005) and explained in the previous section, and (2) a more simplified FEA using 1D bond-slip model based on the local bond-slip model defined in the fib Model Code (1990). In the first approach, a 3D NLFEA was conducted by modelling the concrete and reinforcing bars with (3D) tetrahedral elements (TE12L) and the interface layer with (2D) interface elements (IF6L). Concrete was modelled using a total strain-based smeared crack model. The 3D NLFEA was conducted in three steps: corrosion, self-weight, and mechanical loading. In the second approach, only the concrete was modelled using solid elements. The rebars were modelled by embedded reinforcement, and the interaction between steel and concrete was modelled using the modified bond-slip response developed by Lundgren et al. (2009). It was observed that the former computationally expensive FEA predicts the overall structural behaviour of corroded beams very well in terms of residual capacity, end-slip behaviour, and cracking pattern compared to the experiments. The latter approach was proved to overestimate the capacity of corroded beams compared to the experimental results since the splitting action was ignored. Still, it was quicker and computationally more effective.

Di Carlo et al. (2017) conducted a 3D FEA using code TNO Diana (2005) to evaluate the corrosion effects on the cyclic behaviour of ageing RC columns. Deterioration of concrete properties, steel ductility, bond behaviour, and rebar buckling was considered the consequences of corrosion and was implemented in the software according to the previously published empirical relationships. It is worth noting that in this study, the stirrups were assumed to be protected against corrosion. A horizontal loading history was imposed, and numerical analysis in displacement control was conducted. The numerical results were then verified through a comparison with those based on the experimental tests on medium-scale RC columns conducted at the University of Bergamo by Meda et al. (2014). It was found that for low levels of corrosion, even in the case of reduction in steel ductility, the failure of the RC column is governed by concrete crushing. However, by increasing the corrosion level to 20%, the maximum load decreased to 26%, and the maximum displacement was found to reduce to 50% of the initial value (non-corroded). In such a case, the risk of rebar buckling increased, and the premature failure of the RC member tended to occur.

One of the highly damaged beams of the Stallbacka Bridge was studied numerically by Hussain and Miteva (2018) to describe the anchorage failure of the naturally corroded beam tested earlier by Tahershamsi (2016). Hussain and Miteva (2018) conducted a 3D NLFEA using Diana 10.2 software. The concrete and bottom reinforcements of the beam were modelled using 3D solid elements, while the top and middle reinforcements were modelled by embedded steel reinforcement. Two nodes merged bottom reinforcement bars to introduce a bundle. A non-linear fracture-based constitutive model was used for the concrete, and the Von Mises plasticity criterion was used for the reinforcement. The bond (friction) and corrosion models were implemented into the software using two-layer interface elements around the rebar (Lundgren, 2005). The simply-supported beam was then meshed using 3D tetrahedral elements (TE12L) for the concrete and bottom reinforcement bars. The interface elements were modelled by Interface elements (T18IF), and the loading plates were meshed by triangular prism elements (TP18L) and (HX24L). In the experiments (Tahershamsi 2016), different levels of corrosion were observed for all the rebars; however, for simplicity, Hussain and Miteva (2018) assumed identical average corrosion for the rebars. The combined non-linear analysis was conducted in two phases: (1) corrosion using a time-step analysis and (2) mechanical displacement-controlled loading. The spalling cracks induced by the first phase of 3D-

NLFEA followed the same pattern as the experimental results. The bond loss in both the experimental and numerical approaches shows anchorage failure. The load-deflection curves based on both methods were observed to agree reasonably, although the 3D-NLFEA showed an overestimation for the maximum load due to the fact that the average corrosion was applied to all the rebars instead of the actual corrosion level for each bar.

Kashani et al. (2017) developed a numerical model and conducted an experimental investigation to simulate the non-linear flexural response of corroded RC bridge piers. A displacement-based beam-column element was employed in the simulation. The corrosion-induced cover cracking and corrosion-induced transverse reinforcement damage were implemented by reducing the cover concrete strength (Coronelli and Gambarova 2004) and core confined concrete strength, respectively. In Kashani et al. (2017) simulation, the effect of corrosion, inelastic buckling of corroded rebars, and low-cycle fatigue degradation were incorporated into the material model for reinforcing rebars developed earlier by Kashani et al. (2015). The bond strength of rebars below the foundation level (anchorage zone) was the same as the bond strength of the un-corroded rebar. According to the experimental results, it was observed that the corrosion affects the bond strength of corroded rebars above the foundation level; however, the bond failure was observed not to govern the failure of the RC bridge piers. Therefore, the bond strength degradation of the corroded rebars was ignored in Kashani et al. (2017). Assuming the plane section remains plane and neglects the interaction effects of direct and shear stress, a computational model for the non-linear response of corroded RC bridge piers was developed. Based on the numerical results for both un-corroded and corroded cases, it was observed that ignoring the buckling effect, the failure mode of the RC column is governed by fracture of tensile bars, whereas, assuming the effect of inelastic buckling, crushing of the compressed core concrete governs the failure. By considering the effect of inelastic buckling in a corroded column, it was observed that the impact of the applied axial force is more obvious on the column's non-linear response. A series of moment-curvature analyses were conducted for the corroded columns in case of 10%, 25%, and 50% mass loss to demonstrate the capacity reduction due to corrosion (Figure 2-15, a). The axial force-moment interaction diagrams of the corroded RC column for 10%, 20%, 30%, and 50% mass loss were also conducted (Figure 2-15, b). The numerical model was then verified by testing the same corroded column in the lab under lateral cyclic loading. Kashani et al. (2017) showed that corrosion induced material degradation has a significant deteriorating effect on the non-linear response of the RC column at the section-level, member-level, and bridge system-level.

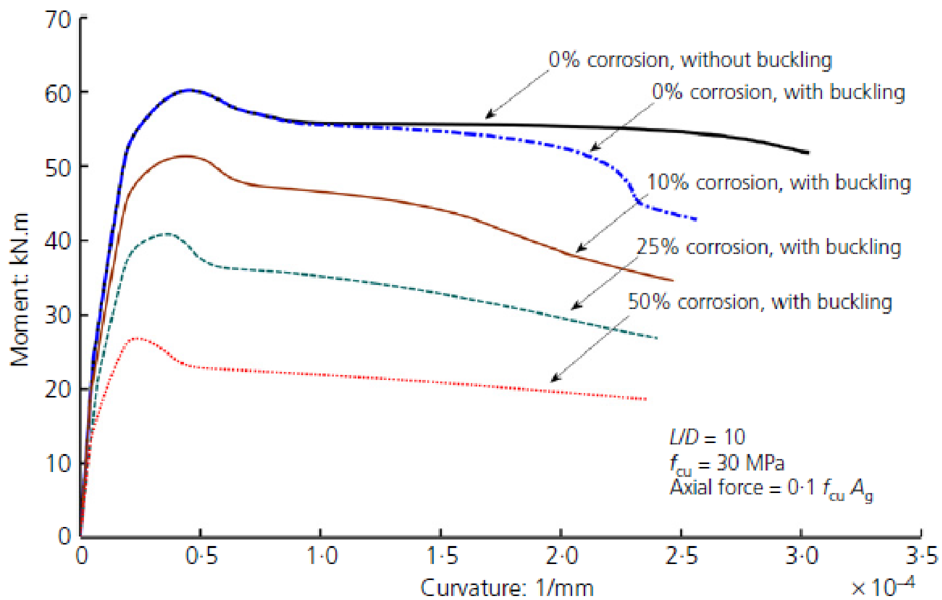

(a)

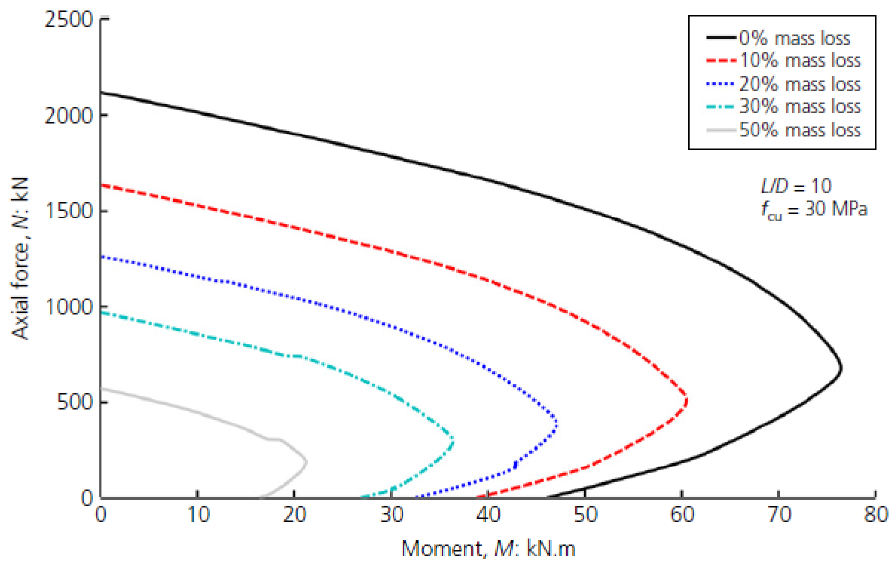

(b)

Figure 2-15 -(a) moment-curvature response for the un-corroded and corroded RC column developed by Kashani et al. (2017), (b) comparison between the interaction diagram of un-corroded RC column and different level corroded RC column (reproduced from Kashani et al. 2017)

Deng et al. (2018) verified the developed corrosion damage model (as described earlier) through a 3D FEA using the OpenSees software. A multi-span simply supported (MSSS) bridge was selected (Figure 2-16) and the corrosion model was implemented into the software to investigate the time-dependent seismic fragility of corroded RC bridges. This study assumed that corrosion is only effective on the piers and bents, and the superstructure is not damaged under seismic loading. In FEA, the girder and deck were modelled by elastic beam-column elements, and displacement-based beam-column elements modelled the piers and bents. The core concrete and steel rebars were modelled using Concrete04 and uniaxial hysteretic material, respectively. High-type bearings (fixed and rocker bearings) were modelled by a combination of bilinear materials and hysteretic material. The abutment-deck interaction was simulated by a bilinear spring, including energy dissipation. The longitudinal abutment-soil interaction was introduced as a spring, and the transverse interaction between abutment and soil was neglected. The time-dependent corrosion damage model was implemented into the software to evaluate the capacity of the MSSS bridge under different intensity level earthquakes. It was observed that the corrosion affects the bridge's capacity under earthquake loads with large PGA intensities, while it is not very deteriorating under small-intensity earthquakes. It was also revealed that the deteriorating effect of corrosion on the strain penetration effect and rebar mechanical properties is more influential on the seismic fragility of the MSSS bridge compared to the other parameters.

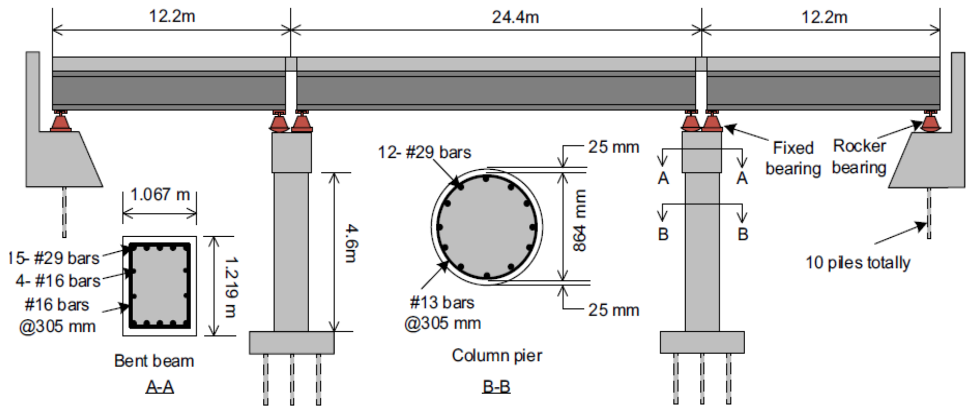

(a)

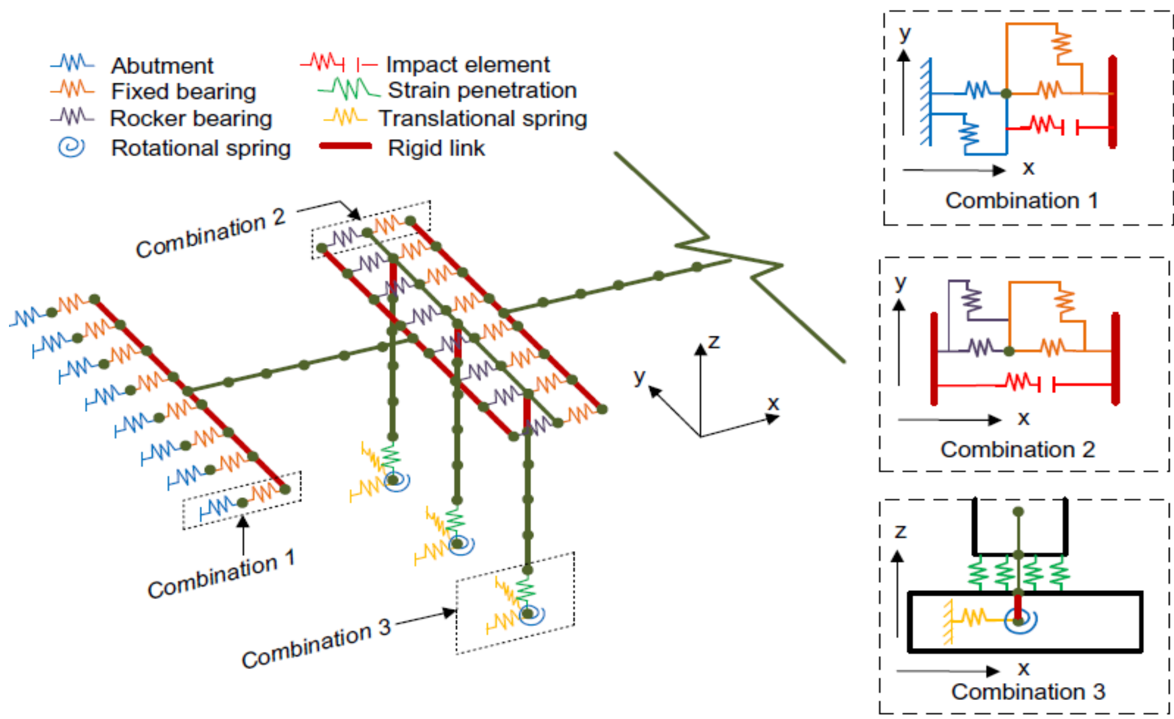

(b)

Figure 2-16 (a) Configuration of selected MSSS bridge, (b) OpenSees model of MSSS bridge (reproduced from Deng et al. 2018)

Xin et al. (2019) developed a bearing capacity model for corroded RC columns under eccentric loading to establish the relationship between the corrosion rate and bearing capacity degradation (Figure 2-17). In this study, the cross-section of the corroded RC column was divided into four parts: cracked unconfined concrete cover, cracked confined concrete, uncracked confined concrete, and longitudinal reinforcement area (considering buckling effects). The corrosion effects, such as steel properties degradation, steel-concrete bond deterioration, and concrete cracking on the three main points of the moment-axial force curve, i.e., the axial compression point, the pure bending point and the balanced failure point, were evaluated. The interpolation points were then determined through piecewise cubic Hermite interpolating polynomials. The curve fitting was conducted through the trigonometric Fourier series model. The results based on the proposed model and the experimental data were then compared to verify the accuracy of the proposed model.

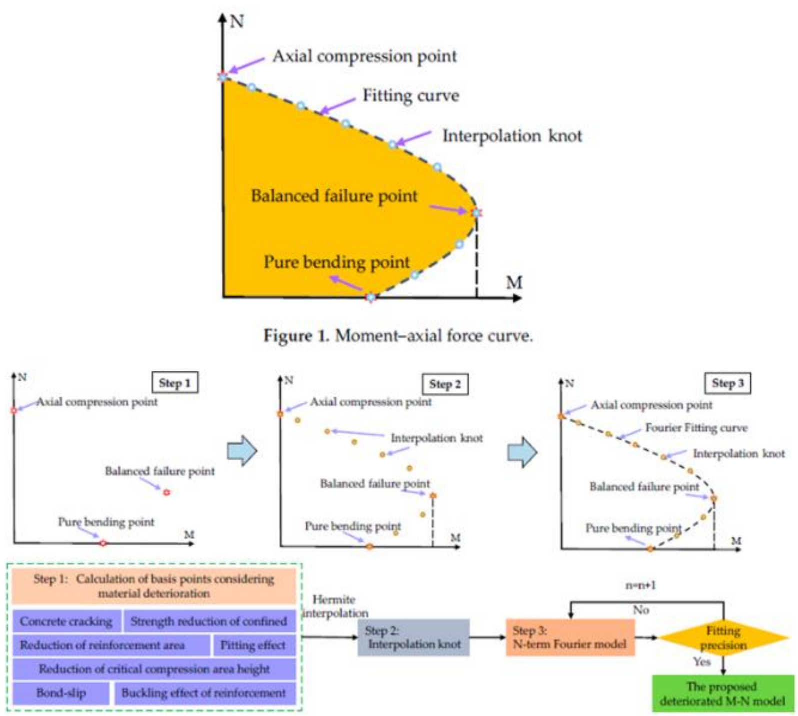

Figure 2-17 Analytical model flowchart conducted by Xin et al. (2019)

2.4 Frost damage

This section presents a comprehensive state-of-the-art on the basic mechanism of frost damage and structural and mechanical damages induced by freeze-thaw cycles (FTCs). In many cold region countries such as Canada, the use of de-icing salt during the winter increases the potential risk of chloride-induced corrosion along with the damage caused by freezing and thawing cycles. Global warming, known as an acceleration factor in corrosion initiation and propagation and a critical reason for higher FTCs frequency, has been of interest in many studies in the last decades. To the best of the author's knowledge, only a few studies investigated the combined/coupled effect of corrosion and FTCs on the structural performance and residual service life of ageing infrastructures. In this chapter, the basic mechanism of freeze-thaw (FT) (Section 2.4.1), studies conducted on the effect of FTCs on the mechanical properties of concrete (Section 2.4.2), studies conducted on the effects of FTCs on the structural performance of RC members (section 2.4.3), and finally the combined/coupled effect of FTCs and corrosion on RC members are presented.

2.4.1 Frost damage mechanism

Frost damage is one of the fundamental durability problems of concrete structures, particularly for dams, bridges, concrete roads and pavements in cold-climate countries. Freeze-thaw cycles could adversely affect the performance of RC members internally by affecting the mechanical properties of concrete or externally by affecting the geometry of the member, such as scaling and spalling of the surface, which requires expenditures for repairs or rehabilitation (Hanjari et al. 2013). Powers (1945) postulated two theories to describe the mechanism of frost damage on cement paste: hydraulic pressure and osmotic pressure. Freezing water in cement paste pores followed by 9% dilation results in excess water moving to escape boundaries. During this process, the hydraulic pressure generated within the saturated cement paste was observed to be dependent on the ice formation rate, distance to the escape boundaries, and permeability of the cement paste. In this case, the presence of air-entraining agents tends to provide sufficient escape boundary to reduce the disruptive hydraulic pressure (Mehta and Monteiro 2001). Powers (1945) also proposed another cause of frost-induced cement expansion: osmotic pressure. Cement paste capillaries contain ionic solutions rather than pure water. The solutions' freezing temperature is lower than pure water. Due to the local salt concentration gradient, osmotic pressure appears. The entropy gradient between ice and super-cooled water is another reason for frost-attacked cement paste expansion (Mehta and Monteiro 2001). Water in the gel pores is estimated to freeze at a lower temperature compared to the water in larger cavities, which causes thermodynamic disequilibrium between the super cooled water with higher energy and the ice with lower energy. Hydraulic pressure due to ice formation, the crystallization and cryo-suction pressures due to thermodynamic equilibrium between the solid and liquid phase of water were also investigated by Gong and Maekawa (2018) through a multi-scale numerical study. In this study, the ice formation within the pores was studied, and the micro-scale pore pressure was calculated as Eq. 2.44 and Figure 2-18 (a).

$$p = p_{hydrau} + p_{cryst} + p_{cryo} \quad 2.44$$

where p_{hydrau}, p_{cryst}, and p_{cryo} are the hydraulic pressure, crystallization pressure, and cryo-suction pressure, respectively. The effective internal stress of the porous matrix induced by anisotropic solid pressure and isotropic accumulated water pressure within the pores were then calculated through a mesoscale poro-mechanical approach. It was assumed that the capillary pore liquid isotropy assumption is not valid anymore after cracking. The crack system internal stress was calculated as Eqs.2.45 and 2.46, considering the liquid water penetration into the cracks according to Darcy's law (liquid permeability) and increased ice volume in different directions (Figure 2-18, b).

$$\sigma_{ij,b-cr} = \sigma_{ij}^{*} + s_{ij} + \delta_{ij} p \quad 2.45$$

$$\sigma_{ij,a-cr} = \sigma_{ij}^{*} + s_{ij} + \delta_{ij} l_i p \quad 2.46$$

where $\sigma_{ij,b-cr}$ and $\sigma_{ij,a-cr}$ are the internal stresses of the porous matrix before and after cracking, respectively; σ_{ij}^{*} is the effective stress tensor; s_{ij} is the solid ice induced stress tensor; δ_{ij} is the Kronecker's delta; l_i is the unit directional vector normal to a crack plane; and p is the liquid induced stress tensor. Gong and Maekawa (2018) showed the efficiency of air-entraining agents in frost-attacked concrete as:

$$\Delta V'_{ICE} = \Delta V_{ICE} - Q = 0.09 S_{ICE} \cdot \phi \cdot \psi_{cp} - 0.1\phi_{air} \qquad 2.47$$

in which $\Delta V'_{ICE}$ is the ice-induced volume increase causing damage; ΔV_{ICE} is the original ice-induced volume increase; Q is the volume occupied by air bubbles; S_{ICE} is the ice saturation level; ϕ is the total volume ratio of paste ignoring the volume occupied by air bubbles; ψ_{cp} is the volume ratio of paste; and ϕ_{air} is the total air content.

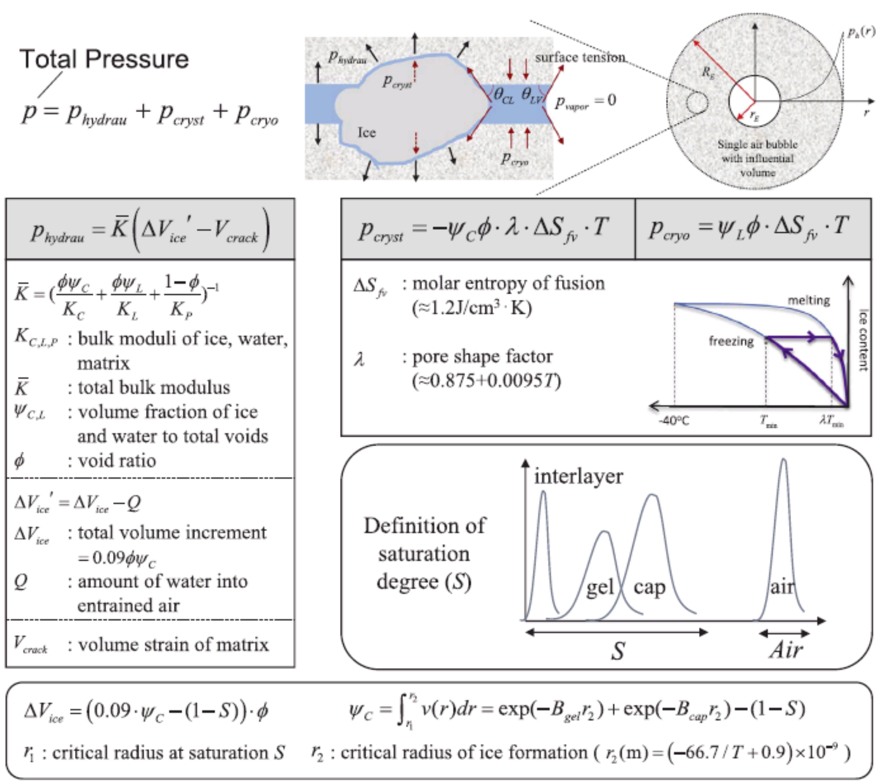

(a)

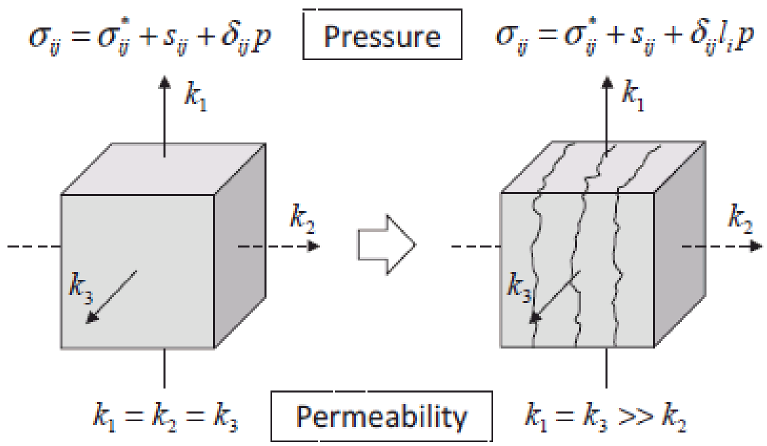

(b)

Figure 2-18- (a) Total pressure induced by frost action (reproduced from Gong et al. 2017), (b) anisotropy of stress and permeability caused by cracking (reproduced from Gong et al. 2017)

2.4.2 Effects of FTCs on the mechanical behaviour of concrete

Frost attacks the concrete, externally or internally; externally due to thermal expansion differential between ice and concrete, which appears as scaling or spalling of the surface concrete, or internally due to volume expansion inside the concrete pore structure, which appears as mechanical properties deterioration resulting in cracking and quality degradation of concrete. Currently, several standards are being used in different countries to test small-scale non-reinforced concrete members under FTCs, such as ASTM C666 (C666/C666M-15 2015), GB/T50082-2009, RILEM TC 117-CDF, CEN/TS 12390:9, 2006 and CEN/TS 15177. All these standards have specific test conditions, such as the number of freeze-thaw cycles, specimen size, cycle duration, specimen age, and temperature range. Researchers conducting studies on frost-damaged RC structural members need to use an equivalent number of cycles which are convertible to one of the abovementioned standards to be able to compare the results based on their studies to those based on others. Section 2.3.2.1 explains the equivalent number of FTCs (N_{eq}). Freeze-thaw cycles adversely affect the mechanical properties of concrete, i.e., compressive and tensile strength (constitutive law), modulus of elasticity and bond behaviour in RC members. The state-of-the-art on these effects is reviewed in Sections 2.3.2.2, 2.3.2.3, 2.3.2.4, and 2.3.2.5, respectively.

2.4.2.1Equivalent numbers of FTCs

Depending on the freezing-and-thawing rate, moisture content, temperature range during FTCs, and also the sample size (Berto et al. 2015), the number of FTCs in every test (*N*) needs to be converted into an equivalent number of FTCs as specified in one standard (N_{eq}) to obtain the identical amount of frost damage obtained based on that standard. Berto et al. (2015) proposed a non-linear function for N_{eq} which is the equivalent number of FTC according to ASTM C 666 ‘‘Procedure A” as Eq. 2.48.

$$N_{eq} = \chi N^{\gamma} \tag{2.48}$$

where *N* is the actual number of FTCs ; χ and γ are empirical parameters dependent on the cycles of temperature range and specimen size and are calibrated considering experimental data. Shang and Song (2006) conducted an experimental study on the behaviour of plain concrete under combined action of FTCs and biaxial compression. In this study, the freeze-thaw tests were performed according to GBJ82-85 requirements, which is very similar to the “ASTM C666 Procedure A” in terms of the temperature range. The only difference is the cube size, which does not conform to the “ASTM C666 Procedure A” requirements. Duan et al. (2011) also conducted an experimental study on frost-damaged plain concrete under uniaxial compression according to GBJ82-85. In these test sets, the temperature range and the specimen sizes were chosen within the recommended range by the “ASTM C666 Procedure A”. Hanjari et al. (2011) followed the “RILEM TC 117-IDC” specifications for freeze-thaw tests on concrete specimens, which is different than the “ASTM C666 Procedure A” recommendations. It is worth noting that in Petersen et al. (2007), the specimens were partially immersed in water with only one side underwater, whereas in Hanjari et al. (2011), the specimens were wholly immersed in water. The number of FTCs for the same amount of damage in Petersen et al. (2007)'s specimens was assumed to be 2.5-folds of that in Hanjari et al. (2011) tests, i.e., $N_{Petersen} = 2.5N_{Hanjari}$ (Qin et al. 2017). Table 2-1 compares the number of FTCs according to different procedures after Qin et al. (2017).

Table 2-2 summarizes the calibration results for χ and γ according to the aforementioned experimental studies conducted by Berto et al. (2015) and Qin et al. (2017). Qin et al. (2017) also proposed the N_{eq} following test data obtained in their study: $N_{eq} = 8.542\times10^{-2} N_{qin}{}^{1.384}$.

Table 2-1- Equivalent number of FTCs based on different experimental studies and ASTM C666 proc. A (Qin et al. 2017)

N_{qin}	N_{eq} (ASTM C666 proc. A)	$N_{Petersen}$ (RILEM TC176-IDC)
100	50.07	13.27
200	130.67	40.03
300	229.03	76.25

Table 2-2- Calibration of χ and γ conducted by Berto et al. (2015) and Qin et al. (2017)

Calibration of χ and γ	Experimental study	Standard	χ	γ	N_{eq} Berto et al. (2015)
Berto et al. (2015)	Shang and Song (2006)	GBJ82-85	1.36	1	$N_{eq} = 1.36N_{Shang\ and\ Song}$
Berto et al. (2015)	Duan et al. (2011)	ASTM C 666	1	1	$N_{eq} = N_{Duan}$
Qin et al. (2017)	Hanjari et al. (2011)	RILEM TC 117-IDC	11.71	0.87	$N_{eq} = 11.71\left(N_{Hanjari}\right)^{0.87}$
Qin et al. (2017)	Petersen et al. (2007)	RILEM TC 117-IDC	11.71	0.87	$N_{eq} = 11.71\left(2.5N_{Hanjari}\right)^{0.87}$

2.4.2.2Compressive constitutive models of frost-damaged concrete

Frozen water mainly causes internal frost damage within the pore system by expansion and micro-cracks development. It adversely affects concrete's mechanical properties, such as the constitutive model in compression. Many researchers have widely investigated the behaviour of frost-damaged concrete in tension and compression (Shang and Song 2006, Hasan et al. 2008, Hanjari et al. 2011, and Berto et al. 2015). Hasan et al. (2004) developed a constitutive model for concrete subjected to combined actions of FTCs and mechanical compressive loading based on the plasticity and fracture of concrete elements (adopted from Maekawa 1985). Maekawa's elastoplastic model assumed that concrete is made of a series of parallel constituent elements. Hasan et al. (2004) introduced a new fracture parameter due to FTCs action (β) by experimental data calibration in addition to the fracture parameter due to mechanical loading (K_0), introduced earlier by Maekawa (1985). The FTC fracture parameter is a function of the equivalent plastic strain (Eq. 2.49). It is representative of the initial stiffness degradation due to freeze-thaw action. The mechanical fracture parameter appears since the unloading-reloading stiffness is not constant because of the possible microcracking and collapse of mortar and aggregates. According to Maekawa's model, some unfractured elements with less plastic strain can regain their load-carrying capacity once the applied compression cancels out the plastic tensile strain. Accordingly, Hasan et al. (2004) introduced another parameter α in addition to the fracture parameters to account for the mentioned phenomenon. The modified compressive stress-strain relationship proposed by Hasan et al. (2004) is presented in Eq. 2.50 and Figure 2-19.

$$\beta = e^{-0.45E_{pf}\left(1-e^{-30E_{pf}}\right)} \qquad 2.49$$

$$S = \alpha\beta K_0 C_O\left(E - E_p\right) \qquad 2.50$$

$$E_p = E_{\max} - a\left(1-e^{-bE_{\max}}\right);\, a = \frac{20}{7} - 2.10E_{pf} + 0.34E_{pf}{}^2;\, b = 0.35 + 0.25E_{pf} + 0.18E_{pf}{}^2 \qquad 2.51$$

in which β is the FTC fracture parameter; E_{pf} is the FTC equivalent plastic strain; α is the effective parameter proposed by Hasan et al. (2004); K_0 is the mechanical fracture parameter as proposed by Maekawa (1985); $C_0 = 2.0$ as proposed by Maekawa (1985); E is the equivalent strain and; E_p is the equivalent plastic strain which was adopted from Maekawa (1985) and modified by Hasan et al. (2004) to account for the effect of FTCs as well as mechanical loading effects.

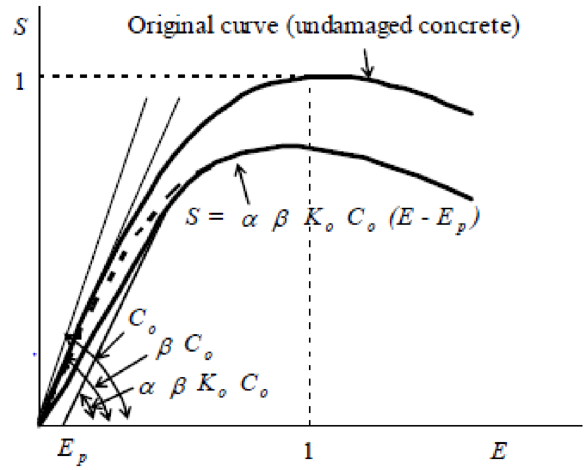

Figure 2-19- stress-strain relationship for the damaged concrete after Hasan et al. (2004)

Shang and Song (2006) investigated the effects of FTCs on the static compressive strength, stress-strain relationship and failure mode of plain concrete subjected to biaxial compression (different stress ratios, $\alpha = \sigma_2 / \sigma_3$, as shown in Figure 2-20) after FTCs according to the GBJ82-85 standard. In this study, the biaxial behaviour of plain concrete after FTCs exposure was observed to deteriorate significantly due to the presence and growth of micro-cracks within the interfacial transition zone. Freezing and expansion of water inside the interface zone and the thermal stress induced by FTCs were introduced as the main reasons for crack propagation inside the concrete subjected to repeated FCTs. The biaxial compressive strain at the peak stress was also observed to increase after repeated cycles of freezing and thawing due to a significant decrease in the compression-carrying capacity of the deteriorated concrete. The biaxial ultimate compressive strength of the plain concrete was reported to be higher than the uniaxial ultimate compressive strength of the same plain concrete under the same number of FTCs because of the presence of the transverse confinement stress for the specimens under biaxial stress (Shang and Song 2006). Lower initial stiffness and more post-peak ductile behaviour were also reported by Shang and Song (2006) for all the deteriorated specimens (Figure 2-21).

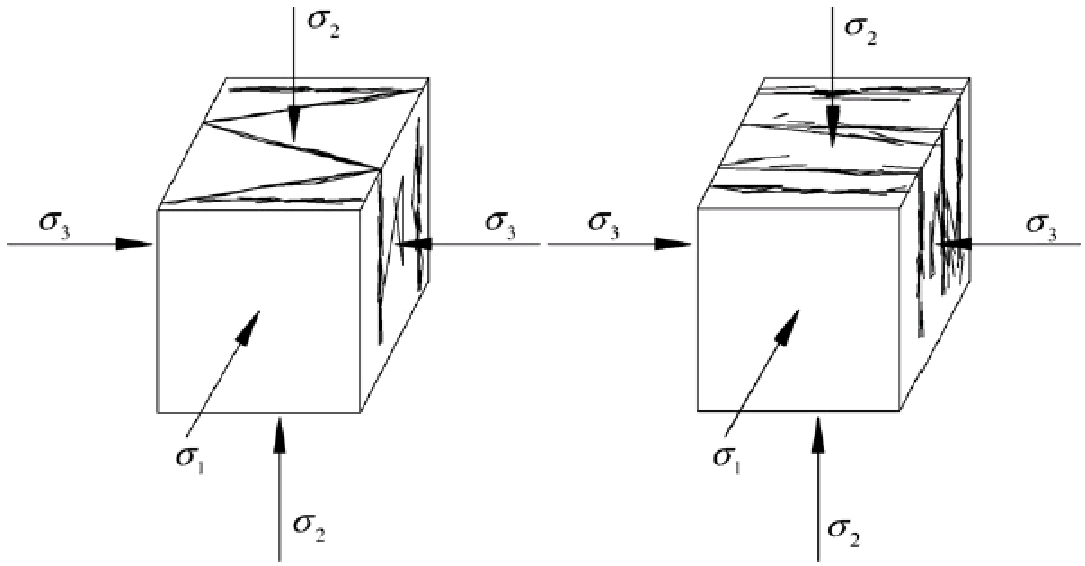

Figure 2-20 Stress directions in the study conducted by Shang and Song 2006- stress ratio $\alpha = \sigma_2/\sigma_3$

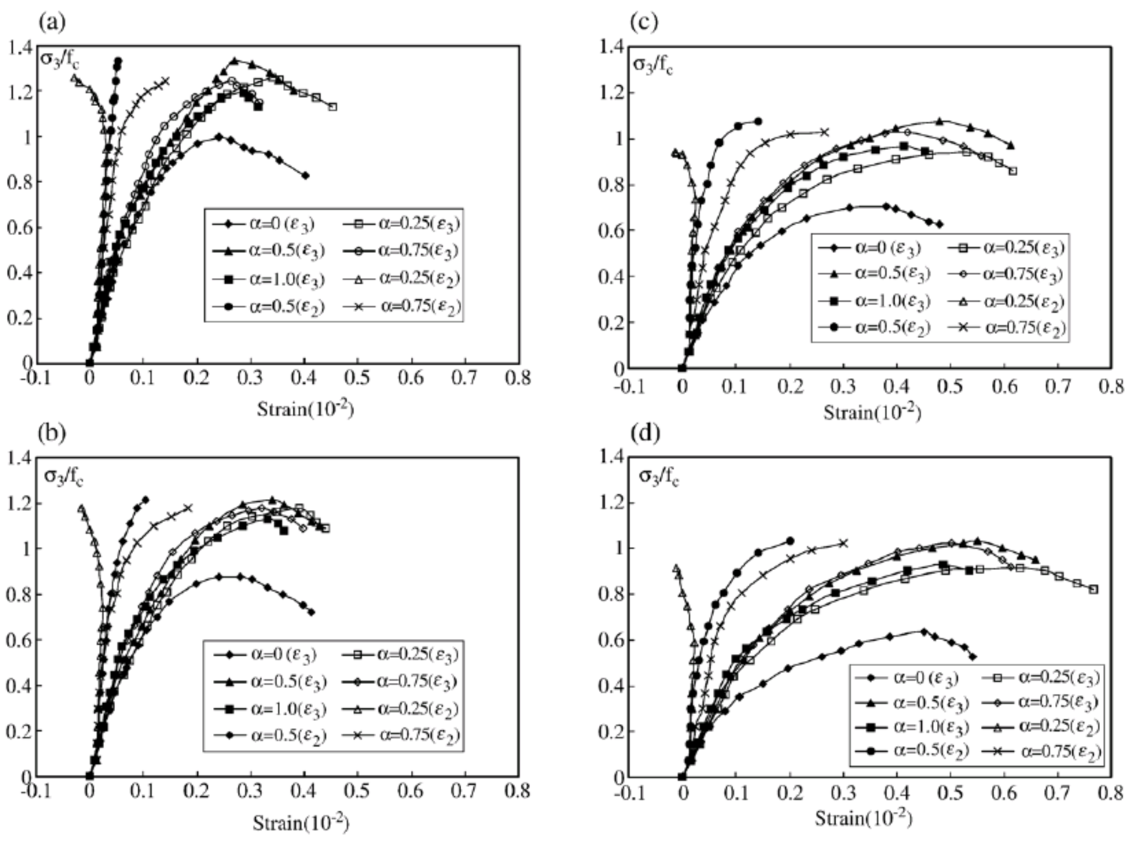

Figure 2-21 Effect of FTCs on the compressive stress-strain curves of plain concrete (under different stress ratios) tested by Shang and Song (2006) after (a) zero cycle of FT, (b) 25 cycles of FT, (c) 50 cycles of FT, and (d) 75 cycles of FT

Hanjari et al. (2013) adopted the compressive constitutive model by Thorenfeldt et al. (1987) and modified it for frost-damaged concrete considering the following factors (Eq. 2.52 and Figure 2-22):

i. A 50% reduction in compressive strength after frost attack (Zandi Hanjari et al. 2009a)

ii. Lower initial modulus of elasticity and larger peak strain for the damaged specimen (Shang and Song 2006 and Hasan et al. 2004),

iii. Variable stiffness for the ascending branch of the damaged concrete's stress-strain curve due to randomly oriented cracks and the possibility of regaining a portion of lost stiffness during loading (Ueda et al. 2009 and Zandi Hanjari et al. 2009b).

$$\sigma_{cc} = f_{cc}{}^{d}\left(\frac{\varepsilon}{\varepsilon_{cc}{}^{d}}\right).\left(\frac{n}{n-1+\left(\frac{\varepsilon}{\varepsilon_{cc}{}^{d}}\right)^{n.k}}\right) \qquad 2.52$$

in which σ_{cc} and ε are the stress and strain in the damaged concrete, respectively; f_{cc}^{d} and ε_{cc}^{d} are the compressive strength and compressive strain at the peak stress for damaged concrete, respectively; E_c^d and E_0^d are the secant and tangential modulus of elasticity of damaged concrete, respectively, and were determined as $E_c^d = f_{cc}^{d}/\varepsilon_{cc}^{d}$ and $E_0^d = 0.9E_D^d - 6$ (Petersen 2003) in which E_D^d is the dynamic modulus of elasticity of damaged concrete, and the correlation factors *n* and *k* are given by:

$$n = \frac{E_c^d}{E_c^d - E_0^d} \qquad 2.53$$

$$k = \begin{cases} 1 & for \quad 0 < \varepsilon < \varepsilon_{cc}^{d} \\ 0.67 + \dfrac{f_{cc}^{d}}{62} & for \quad \varepsilon > \varepsilon_{cc}^{d} \end{cases} \qquad 2.54$$

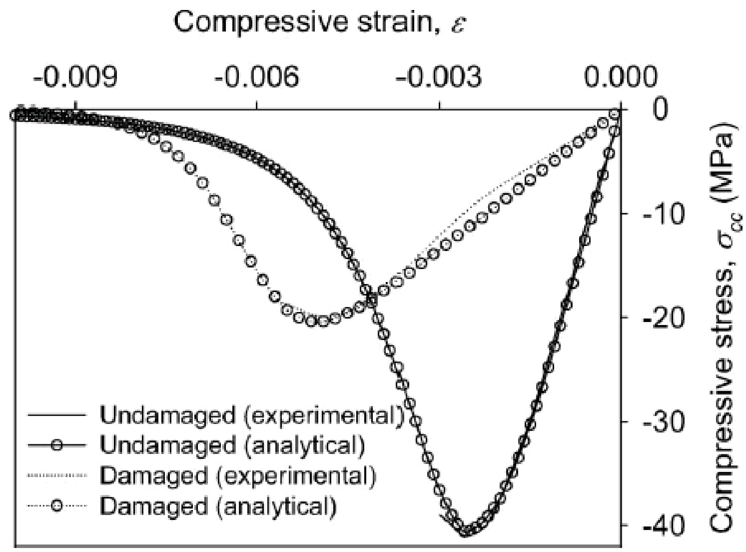

Figure 2-22 Comparison of analytical stress-strain relationship represented in Eq. 3.9 after Hanjari et al. (2013) and that based on experimental data after Zandi Hanjari et al. (2009b) for damaged and un-damaged concrete

Berto et al. (2015) conducted a numerical and experimental study to evaluate the coupled freeze-thaw-mechanical effects on the structural performance of RC beams. The coupled effects of freeze-thaw-induced degradation and mechanical behaviour were proposed by extending the previous work by Saetta et al. (1999), Saetta (2005), and Berto et al. (2014). Two different scalar environmental damage variables d_{env}^{+} and d_{env}^{-} were defined in addition to the earlier established mechanical variables d^{+} and d^{-}. The constitutive law for coupled environmental/mechanical effects was described in Eqs. 2.55, 2.56, 2.57 and Figure 2-23.

$$\begin{aligned} \sigma &= \left(1-d_{env}^{+}\right)\left(1-d^{+}\right)\bar{\sigma}^{+} + \left(1-d_{env}^{-}\right)\left(1-d^{-}\right)\bar{\sigma}^{-} \\ &= \left(1-d^{*+}\right)\bar{\sigma}^{+} + \left(1-d^{*-}\right)\bar{\sigma}^{-} \end{aligned} \qquad 2.55$$

where

$$d^{+} = 1 - \frac{r_0^{+}}{r^{+}} \exp\left[A^{+}\left(1 - \frac{r^{+}}{r_0^{+}} \right) \right]$$
$$d^{-} = 1 - \sqrt{\frac{r_0^{-}}{r^{-}}}\left(1 - A^{-}\right) - A^{-} \exp\left[B^{-}\left(1 - \sqrt{\frac{r^{-}}{r_0^{-}}} \right) \right] \qquad 2.56$$

and

$$d_{env}^{-} = a_d^{-} N_{eq} \le 1$$
$$d_{env}^{+} = a_{d,1}^{+} N_{eq} - \left\langle N_{eq} - N_c \right\rangle \left(a_{d,1}^{+} - a_{d,2}^{+} \right) \le 1$$

2.57

where σ is the Cauchy stress tensor; $\bar{\sigma}^{+}$ and $\bar{\sigma}^{-}$ are the positive and negative parts of the effective stress tensor; d^{*+} and d^{*-} are the positive and negative coupled damage variables respectively; r_0^{+} and r_0^{-} are the initial threshold variables; r^{+} and r^{-} are the current threshold variables; A^{+}, A^{-}, B^{-}, a_d^{-}, $a_{d,1}^{+}$, and $a_{d,2}^{+}$ are model parameters, which were calibrated according to different test parameters; N_{eq} is the equivalent number of FTCs as described in Eq. 2.48; and N_c was defined as the value of N_{eq} corresponding to the sudden change in the evolution of d_{env}^{+} as described in Shang and Song (2006). The compressive strength reduction due to FTCs was then proposed from Eq. 2.55 as:

$$\frac{f_c^{d}}{f_c} = 1 - d_{env}^{-} = 1 - a_d^{-} N_{eq} \qquad 2.58$$

in which f_c^{d} and f_c are the compressive strength after and before the frost-induced degradation.

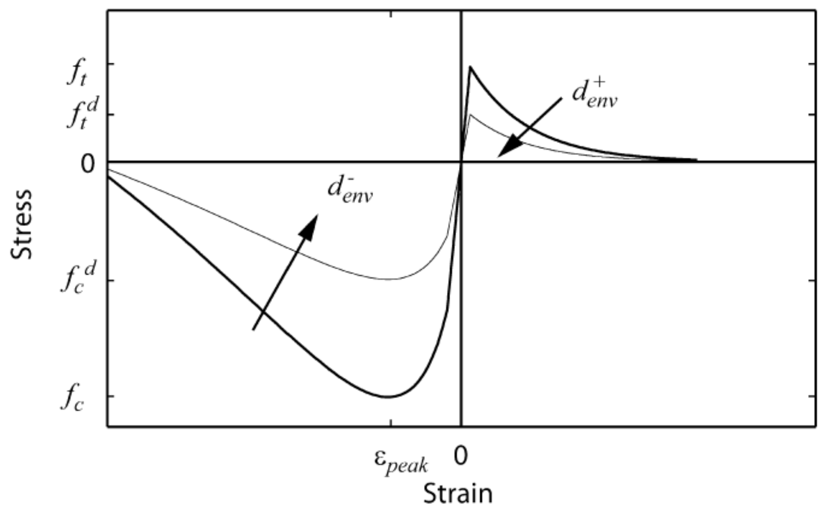

Figure 2-23 Constitutive law for frost-damaged concrete proposed by Berto et al. (2015)

Li et al. (2017) reported all the damaged mechanical properties of concrete, such as tensile strength and modulus of elasticity, as a function of the deteriorated concrete compressive strength. The authors believed that due to the variety of specimen sizes and methods of freezing and thawing in different experimental studies, conducting a regression analysis based on different experiments requires converting damaged compressive strength to a normalized index of damage degree for frost-damaged concrete. Li et al. (2017) introduced the relative compressive strength (RCS), the ratio between the damaged and un-damaged compressive strengths, as a normalized damage index. By introducing the dimensionless index (RCS), the frost-damaged modulus of elasticity and frost-damaged tensile strength were proposed through curve fitting.

2.4.2.3Tensile constitutive models of frost-damaged concrete

Many researchers have experimentally investigated the effects of FTCs on concrete tensile behaviour through tensile and wedge-splitting tests (Shang and Song 2006 and Zandi Hanjari et al. 2009b). Most of them reported slightly higher FT effects on tension behaviour compared to those effects on compression behaviour. Due to a lack of knowledge about the softening behaviour of frost-damaged concrete, which is essential for numerical modelling, a bilinear relation between tensile strength (σ_{ct}) and crack opening (w) was proposed by Zandi Hanjari et al. (2009b), as shown in Figure 2-24.

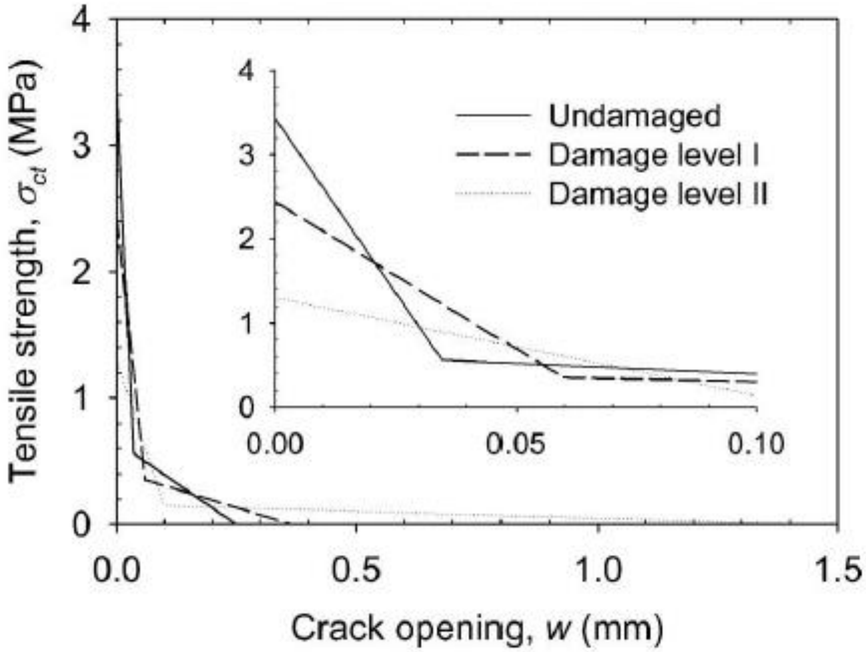

Figure 2-24 σ_{ct} -w relationship proposed by Zandi Hanjari et al. (2009b)

The relationship between the compressive and tensile strength of frost-damaged concrete was proposed by Hanjari et al. (2013) (Eq. 2.59 and Figure 2-25) using previously tested specimen data and the compressive-tensile relationship for the undamaged concrete as established in the Model Code 1990 (CEB. 1993).

$$f_{ct}^{d} = 0.027\left(f_{c}^{d}\right)^{1.2} \qquad 2.59$$

in which f_{ct}^{d} and f_{c}^{d} are the tensile and compressive strength of frost-damaged concrete, respectively.

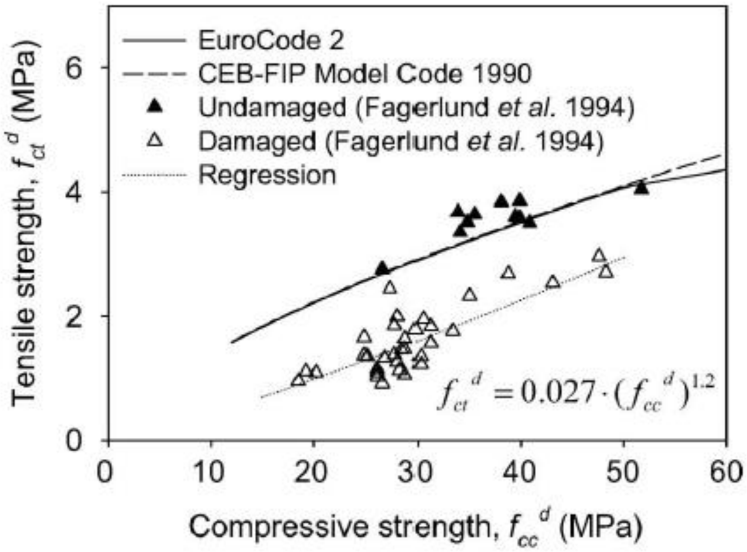

(a)

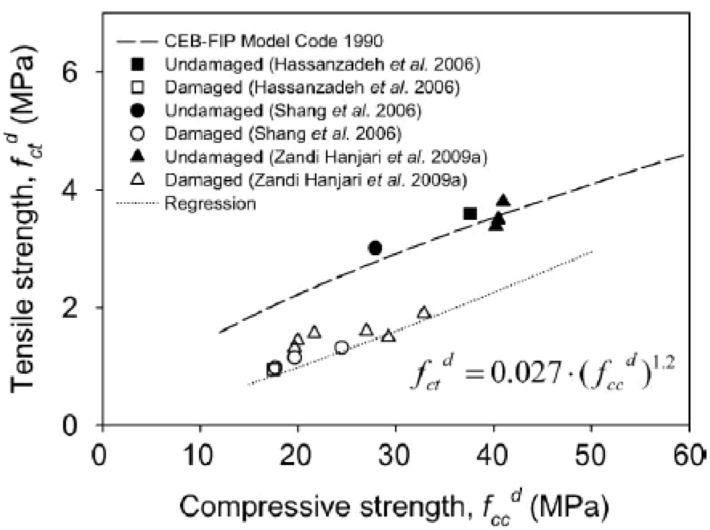

(b)

Figure 2-25 A comparison between the compressive-tensile relationship for damaged and un-damaged concrete established by different experimental tests and Hanjari et al. (2013)

Berto et al. (2015) proposed the ratio of tensile strength of damaged to un-damaged concrete using the coupled environmental/mechanical degradation parameters described in Eq. 2.55 (Figure 2-26).

According to the experimental data established by Shang and Song (2006), the value $a_{d,2}^{+}$ was calibrated as $a_{d,2}^{+} = 0.0017$. While there was not enough evidence for the values of $a_{d,1}^{+}$ and N_c, a linear relationship between the positive and negative environmental damage variables, d_{env}^{+} and d_{env}^{-}, was proposed by Berto et al. (2015) as $d_{env}^{+} = 1.29 d_{env}^{-} + 0.22 \le 1$, and the tensile strength degradation was suggested as:

$$\frac{f_t^d}{f_t} = 1 - d_{env}^{+} \tag{2.60}$$

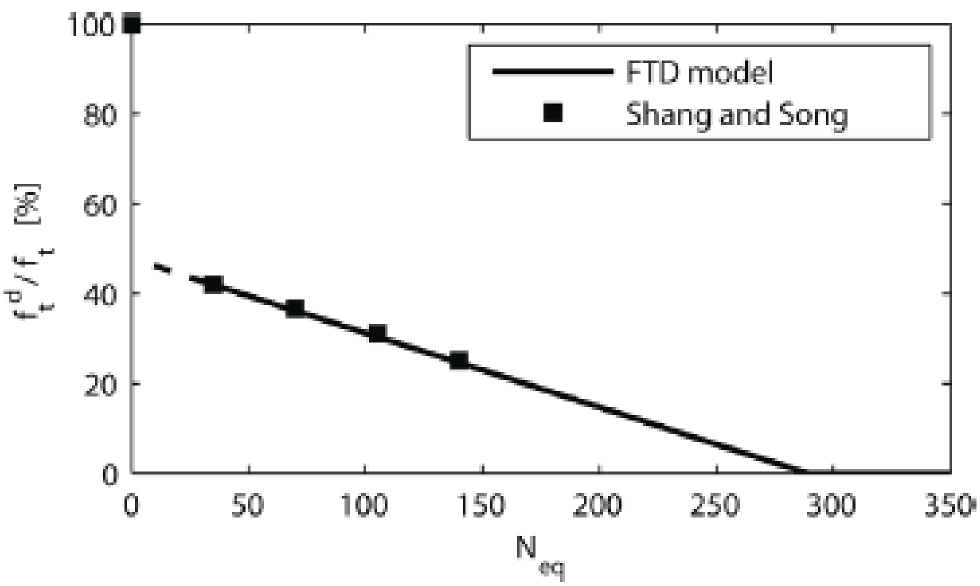

Figure 2-26 Tensile strength degradation proposed by Berto et al. (2015)

Li et al. (2017) proposed a relationship between the relative compressive strength (RCS) and frost-damaged tensile strength as Eq. 2.61 and Figure 2-32 (a) through a regression analysis based on the test results conducted by Lizhi (2010) and Hanjari et al. (2011). The tensile strength of frost-damaged concrete was measured through splitting tests by Shisheng (1997), Xiaodong (2007), and Hanjari et al. (2011), and it was measured through uniaxial tensile test in Lizhi (2010).

$$f_t^d = 0.302 f_c^{2/3} \left(1.04125 \frac{f_c^d}{f_c} - 0.04125 \right) \tag{2.61}$$

in which f_t^d is frost-damaged tensile strength of concrete; f_c is the compressive strength of un-damaged concrete; and f_c^d is the compressive strength of frost-damaged concrete.

2.4.2.4Modulus of elasticity

Shang and Song (2006) observed a significant reduction of the modulus of elasticity of concrete after different FTCs and under different stress ratios (as shown in Figure 2-27). In the experimental study conducted by Shang and Song (2006), a 62% reduction in elastic modulus after uniaxial compression and 50 cycles of FTCs was observed. It was also observed that under biaxial compression with a stress ratio $\alpha = 0.5$, a 59% reduction in elastic modulus under the same number of FTCs occurs. The authors also noted that confinement (increasing the stress ratio) increases the elastic modulus of concrete under the same number of FTCs (Figure 2-27).

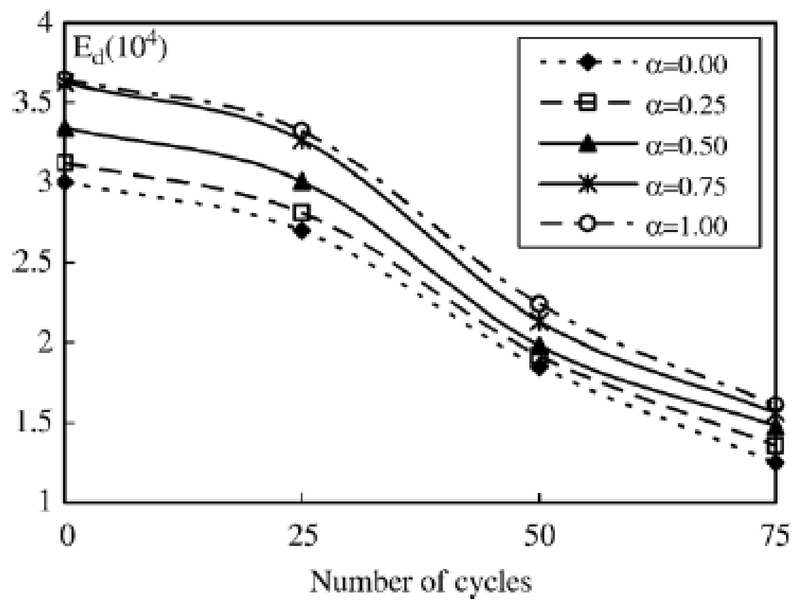

Figure 2-27 Effect of FTCs and confinement on dynamic modulus of elasticity of concrete after Shang and Song (2006)

Petersen et al. (2007) proposed a linear relationship for the freeze-thaw induced change in static modulus of elasticity (Figure 2-28). In the experimental part of this study, the uneven internal damage (dynamic modulus of elasticity) along three different distances from the exposed surface and along two different locations from the specimens (with two different compositions, A1 and B) were measured through ultrasonic measurement, and the mean value for all these six values was introduced as the equivalent internal damage. According to the test data and through regression analysis, a linear relationship for the decrease of static modulus of elasticity due to internal damage propagation was proposed (Figure 2-28).

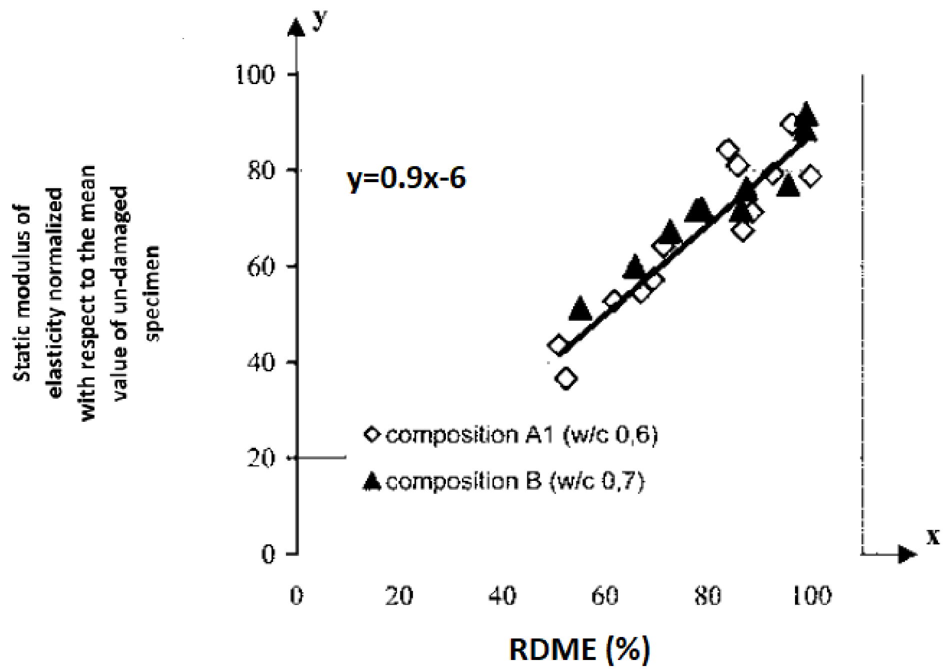

Figure 2-28 Static modulus of elasticity degradation due to FT action reproduced from Petersen et al. (2007)

Zandi Hanjari et al. (2009b) also proposed a significant reduction in the modulus of elasticity after FTCs exposure. In this study, thirty-two plain specimens were damaged under FTCs according to RILEM TC 176-IDC recommendations. In this standard, the specimen is called damaged only if the relative dynamic modulus of elasticity (RDME) reaches a ratio below 80%. Zandi Hanjari et al. (2009) observed that only after 20 FTCs, the RDME reaches 80%, followed by a lower rate of reduction for the higher number of FTCs (Figure 2-29). In a subsequent study, Hanjari et al. (2013) proposed a correlation between the dynamic modulus of elasticity and compressive strength of frost-damaged concrete according to the previously published test data (Shang and Song 2006 and Zandi Hanjari et al. 2009b).

$$E_D^d = \frac{a}{1+\left(\frac{f_{cc}^d}{b}\right)^c} \qquad 2.62$$

where $a = 52.8, b = 30.4, c = -3.3$

in which E_D^d, f_{cc}^d are the frost-damaged dynamic modulus of elasticity and compressive strength, respectively; and *a*, *b*, and *c* are the model parameters, which were defined through regression analysis on the test data by Shang and Song (2006) and Zandi Hanjari et al. (2009).

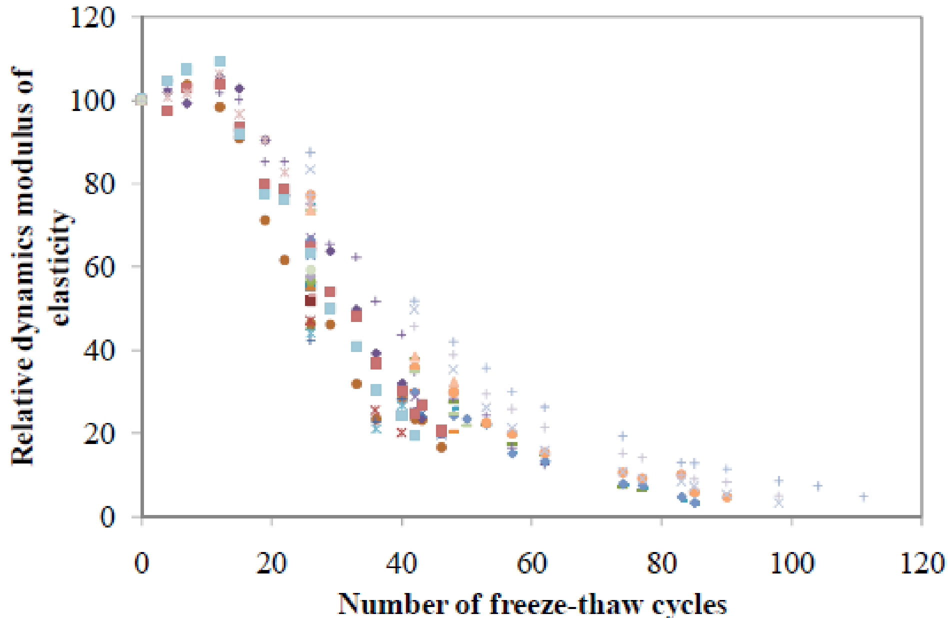

Figure 2-29 RDME-number of FTCs proposed by Zandi Hanjari et al. (2009)

Berto et al. (2015) proposed a model for the reduction in the static modulus of elasticity after frost action as a function of the equivalent number of FTCs (N_{eq}) and the model parameter (a_d^-) (Eq. 2.63). It was assumed that the effects of frost action are similar on the elastic modulus and strength (identical model for strength and modulus of elasticity as described in Eq. 2.58 and Eq. 2.63).

$$\frac{E_s^d}{E_s} = 1 - a_d^- N_{eq} \qquad 2.63$$

Berto et al. (2015) combined the relationship model between static and dynamic modulus of elasticity with Eq. 2.63 to propose a model for the relative dynamic modulus of elasticity (RDME) or reduction in dynamic modulus of elasticity after frost action as Eq. 2.64.

$$\frac{E_{dyn}^{d}}{E_{dyn}} = \frac{1}{0.9}\left(1.06 - a_{d}^{-} N_{eq}\right) \quad 2.64$$

in which E_s^d , E_s , E_{dyn}^d , E_{dyn} are the damaged and un-damaged static modulus of elasticity, and damaged and un-damaged dynamic modulus of elasticity, respectively. As shown in Figure 2-30, the damage model was then verified using previously published experimental data through regression analysis (Shang and Song 2006, Duan et al. 2011, and Hanjari et al. 2011).

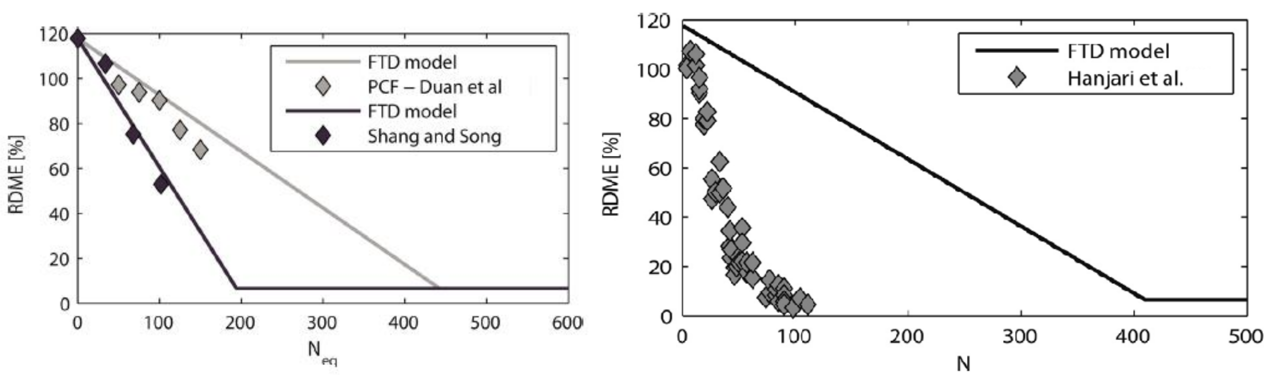

(a) (b)

Figure 2-30 Verification of Eq. 2.64 as proposed by Berto et al. (2015)

Considering the uneven frost damage distribution along the cross-section of the member, Qin et al. (2017) proposed a model for RDME as a function of the number of FTCs and the frost damage depth (Eq. 2.65 and Figure 2-31). Three main assumptions were made in this model: (1) the FT environment around the concrete member was constant, (2) the RDME was assumed to be constant before the number of FTCs reached its critical value, and (3) the RDME was assumed to decrease linearly after the critical number of FTCs.

$$RDME = \begin{cases} 1 & if \ N_{Qin} \le N_i^{'} \\ 1 - m_i \left(N_{Qin} - N_i^{'} \right) \ge 5\% & if \ N_{Qin} > N_i^{'} \end{cases}$$

$$N_i^{'} = 0.9 x_i + 3 \qquad 2.65$$

$$m_i = \frac{\left(1.3 - 0.008 x_i\right)}{100}$$

where N_{Qin} is the actual number of FTCs (Table 2-1); $N_i^{'}$ is the critical number of FTCs at which the RDME starts to decline at the frost depth x_i ; and m_i is the corresponding decline for the linear decrease.

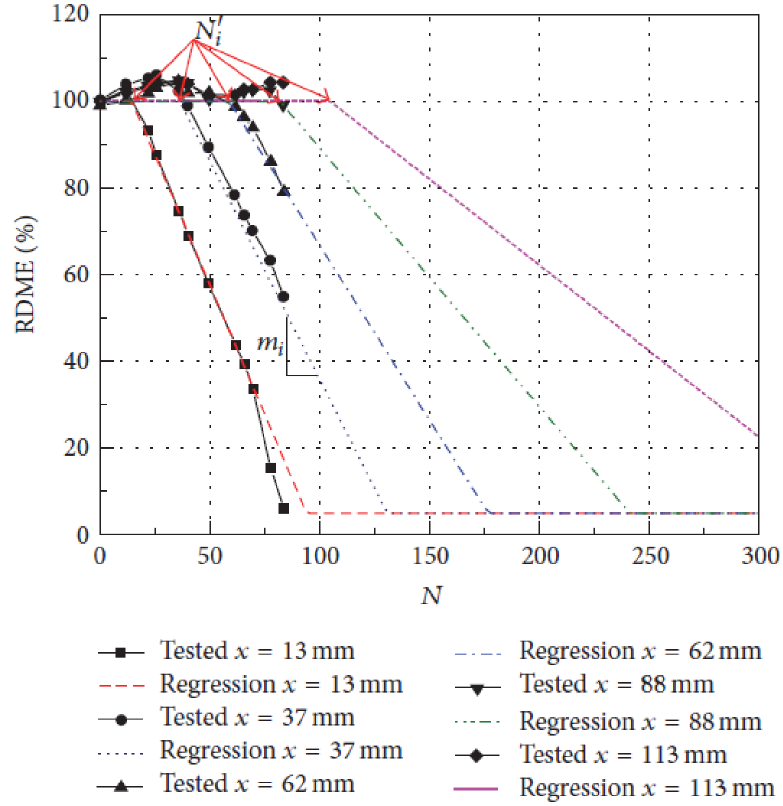

Figure 2-31 Proposed RDME model for the frost-damaged concrete member by Qin et al. (2017)

Qin et al. (2017) combined the relationship between the compressive strength and the dynamic modulus of elasticity from the British Code of Practice for Structural Use of Concrete CP110:

1972 ($E_{dyn} = 22 + 2.8\sqrt{f_c^{'}}$) with Eq. 2.65 to propose the dynamic modulus of elasticity of frozen-thawed damaged concrete with different damage depths (Eq. 2.66).

$$E^d{}_{dyn,i} = RDME.E_{dyn} \qquad 2.66$$

The elastic modulus of frost-damaged concrete (E_c^d) was proposed by Li et al. (2017) as a function of the relative compressive strength (RCS) through curve fitting based on earlier experimental data such as that by Hanjari et al. (2011) and Hasan et al. (2004) (Eq. 2.67 and Figure 2-32,b).

$$E_c^d = \frac{10^5}{2.2 + (26.4/f_c)}\left(1.4238\frac{f_c^d}{f_c} - 0.4238\right) \qquad 2.67$$

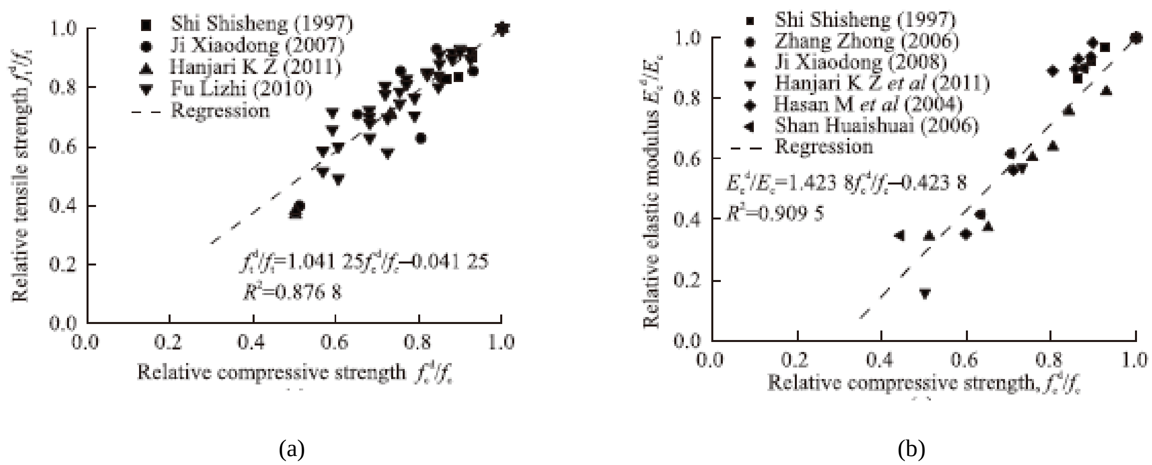

Figure 2-32 Correlation between the relative compressive strength (RCS) and (a) frost-damaged tensile strength, (b) frost-damaged modulus of elasticity (reproduced from Li et al. 2017)

2.4.2.5Bond behaviour

The deteriorating effects of FTCs on the bond-slip response of RC members have been investigated by many researchers (Fagerlund et al. 1994, Zandi Hanjari et al. 2009b, and Petersen et al. 2007). Fagerlund et al. (1994) reported a 30% to 70% reduction in bond strength. Zandi Hanjari et al. (2009b) reported 14%-50% bond deterioration for the cases of a damage level of 25% and 50% reduction in compressive strength of frost-damaged concrete, respectively (Figure 2-33).

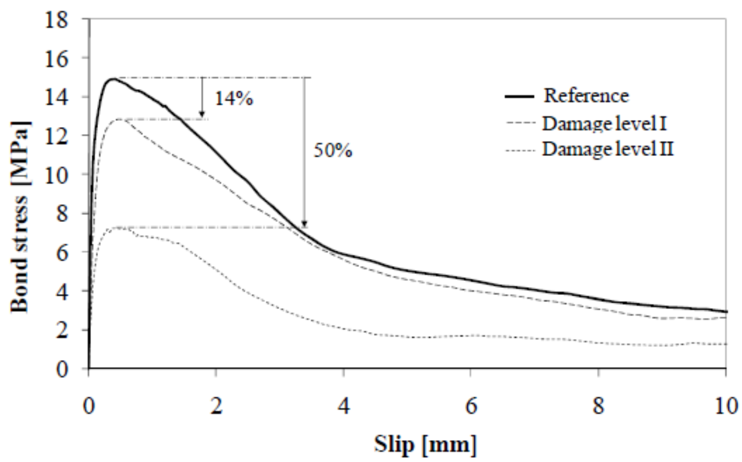

Figure 2-33 Deteriorated bond-slip model proposed by Zandi Hanjari et al. (2009b) for frost-damaged concrete

Petersen et al. (2007) studied the effects of FTCs and the absorption of capillary water on concrete's mechanical behaviour, including the bond behaviour, through experimental tests and numerical analysis. A pull-out test was conducted to evaluate the bond deterioration of specimens exposed to the FTCs from the smaller cover side. The bond between concrete and reinforcement triggers a ring tension stress around the rebar. The tension stress exceeding the concrete tensile strength initiates damage (Petersen et al. 2007). The variation of bond-slip behaviour as a function of the RDME during frost action was proposed by Petersen et al. (2007) (Figure 2-34, a). This study investigated different levels of frost damage (case A, case B, and case C). In case A, the internal frost damage propagated only in the concrete cover and the interaction between steel and concrete was not affected. The ascending branch of the bond tension-slip curve was observed to follow the un-damaged curve; however, the maximum bond stress was reduced due to the concrete cover damage, and the slip at the maximum bond decreased slightly (Figure 2-34, b). By propagating the frost damage to the interface between concrete and reinforcement, the maximum bond strength and the slip at the maximum bond stress were observed to decrease and increase, respectively. The deteriorating effects were also investigated analytically, adopting the bond-slip model presented by Kreller et al. (1990) as the un-damaged case. Kreller et al.'s model was adopted from the Model Code 1990 (CEB 1993) and defined the bond behaviour at different distances from the crack (Figure

2-35). The frost action effects on all the parameters of the bond-slip response of the Model Code 1990 (CEB 1993) were evaluated and then compared to the original curve.

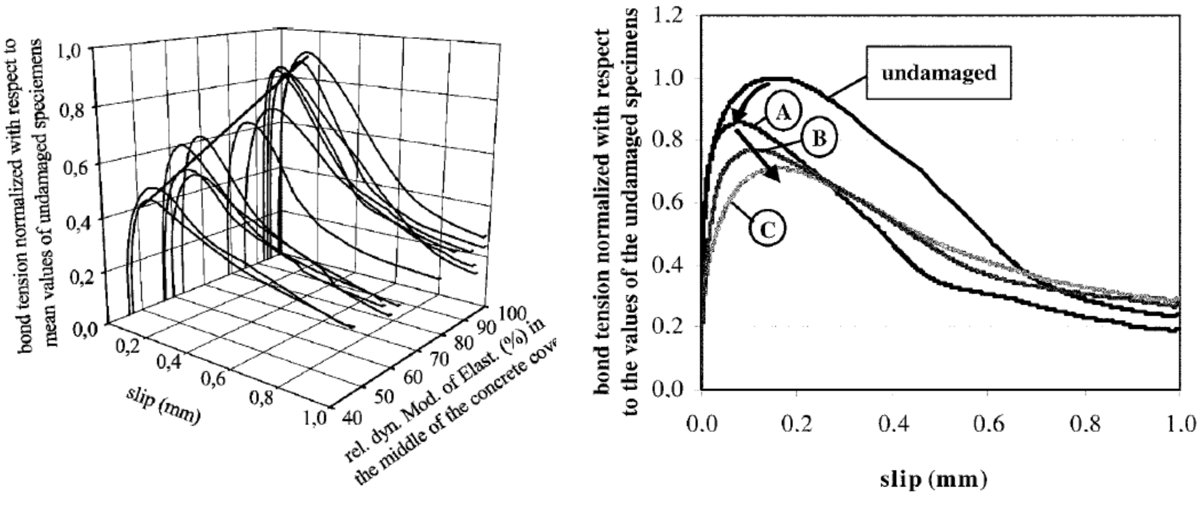

(a) (b)

Figure 2-34 (a) The variation of bond-slip behaviour as a function of RDME during frost action proposed by Petersen et al. (2007), (b) The deteriorated bond tension-slip relationship for three cases of frost damage proposed by Petersen et al. (2007)

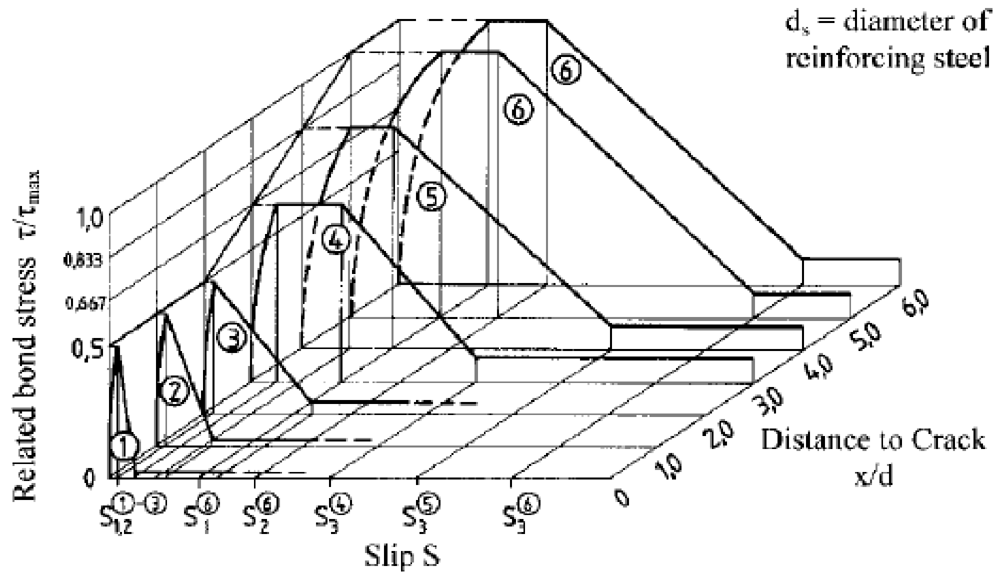

Figure 2-35 bond-slip response as a function of distance to crack proposed by Kreller et al. (1990)

The ratio between the damaged to un-damaged bond tension ($\frac{\tau_{\max}^{d}}{\tau_{\max}}$) was proposed by Petersen et al. (2007) as:

$$\frac{\tau_{\max}^{d}}{\tau_{\max}} = 0.17 + 0.007 \times RDME \qquad 2.68$$

The quantitative values for the slip reduction at maximum stress in case of low-level frost damage (90%<RDME<100%), when damage only occurs at the cover, and increase in the slip for a higher level of damage (RDME<90%), when damage propagates toward the interaction zone between rebar and concrete, were defined as:

$$s_{1,2}^{d} = \begin{cases} \sqrt[\alpha]{\left(\frac{\tau_{\max}^{d}}{\tau_{\max}}\right)} \times s_{1,2} & for \quad 90\% < RDME < 100\% \\ \left(335 - 0.03 \times RDME\right) \times s_{1,2} & for \quad RDME < 90\% \end{cases} \qquad 2.69$$

The bond-slip relationship for each level of frost damage before the maximum bond stress was defined as Eq. 2.70 and Figure 2-36.

$$\tau_{d} = \left(\frac{s}{s_{1}^{d}}\right)^{\alpha} \times \tau_{\max}^{d} \qquad 2.70$$

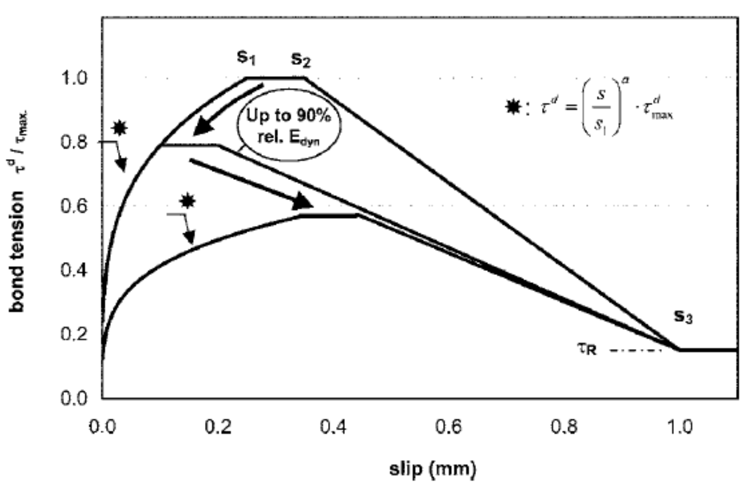

Figure 2-36 frost-damaged bond-slip model after Petersen et al. (2007)

Hanjari et al. (2013) assumed zero bond strength for the areas where the concrete cover spalled off entirely due to frost attack. The bond behaviour for the areas where the cover is still in place (albeit cracked) was adopted from Lundgren et al. (2009), which accounts for the intermediate case between confined and un-confined (Eq. 2.9). The ratio of maximum bond stress of frost-damaged to un-damaged concrete was adopted from Petersen et al. (2007) (Eq. 2.68).

The proportional relationship between the residual bond strength reduction and the bond capacity reduction was adopted from Zandi Hanjari et al. (2009 b) (Eq.2.71).

$$\tau_f^d = \left(\frac{\tau_{\max}^d}{\tau_{\max}} \right) \tau_f \tag{2.71}$$

where τ_f^d, τ_f, $\tau_{\max}^d$, $\tau_{\max}$ are the residual bond strength for frost-damaged and un-damaged concrete, and bond capacity for frost-damaged and un-damaged concrete, respectively.

2.4.2.6Surface scaling

Freeze-thaw cycles could adversely affect the performance of RC members internally by affecting the mechanical properties of concrete and cracking (as discussed in Sections 2.4.2.2, 2.4.2.3, 2.4.2.4, and 2.4.2.5) or externally by affecting the member geometry, such as scaling and spalling of the surface (Hanjari et al. 2013). The external surface of concrete members subjected to FTCs, in the presence of moisture and/or de-icing salts, can be easily damaged and scaled; this phenomenon is called surface scaling or frost scaling. Salt-frost scaling, called unsealed freeze-thaw, occurs when the concrete surface is in contact with a solution while it is freezing. In addition to the salt concentration, salt-frost scaling is highly dependent on the nature of FTCs, i.e., the minimum temperature during freezing, rate of FTCs, and duration of FTCs, which affect the moisture content of the surface concrete (Fagerlund 2004). It is worth noting that surfaces damaged by FTCs in the presence of salt and without salts are treated differently. The dry-weight loss in frost-damaged concrete, $\Delta Q(kg/m^2)$, was measured in many experimental studies. Fagerlund (2004) proposed a linear relationship between the number of FTCs (N) and the weight loss, which can be easily converted to the scaling depth in the cover, s, by dividing the mass loss by the dry-bulk density, γ. According to the test data conducted by Lindmark (1998) and assuming uniform mass loss, for the case of concrete with water to cement ratio of $W/C = 0.4$, a salt concentration of 3% NaCl solution and a minimum temperature of $-22^{\circ}C$, a linear relationship of $\Delta Q = 0.043N$ can be proposed.

2.4.3 Structural performance of frost-damaged RC members

A reliable assessment method to predict the load-carrying capacity and remaining service life of deteriorating structures is crucial for a repair strategy and optimized maintenance plans. As briefly reviewed, numerous studies have been conducted on the deteriorating effects of FTCs on the concrete and bond-slip response properties. To the best of the author's knowledge, there is still a scarcity of numerical investigations on the structural performance of real-scale frost-damaged RC members, especially RC columns. Only a few studies have been conducted on the load-carrying capacity and remaining service life of small-scale frost-damaged structural members.

Petersen et al. (2007) conducted an experimental/numerical study to investigate the effect of FTCs on the bending behaviour of damaged RC beams considering the effect of degraded bond behaviour and RDME. In this study, the formulation developed by Polak and Blackwell (1998) for beam flexural behaviour prediction was modified to account for the effect of FTCs by implementing the deteriorated bond and RDME into it.

The non-linear compressive constitutive law from the Model Code 1990 (CEB 1993) was implemented into the code. Polak and Blackwell's model was developed based on an iterative cross-sectional analysis and accounted for tension stiffening (additional force from the bond). The beam's cross-section was divided into finite numbers of horizontal strips, and the iterative analysis was conducted until a linear strain distribution was reached.

A linear elastic behaviour was performed for the uncracked portion of the section, and the effect of tension stiffening was added to the calculation after cracking. The generated moment-curvature curve for the frost-damaged and un-damaged beams with two different combinations (combination A, w/c=0.6 and combination B, w/c=0.7) was then compared to that based on experimental results conducted by the authors. A good agreement between the results showed the accuracy of the proposed deterioration model (Figure 2-37).

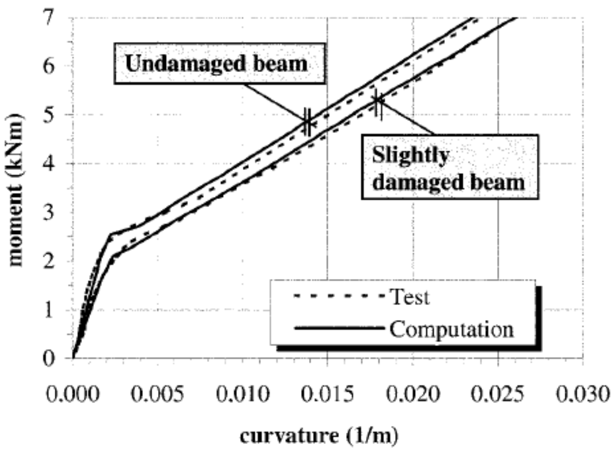

(a)

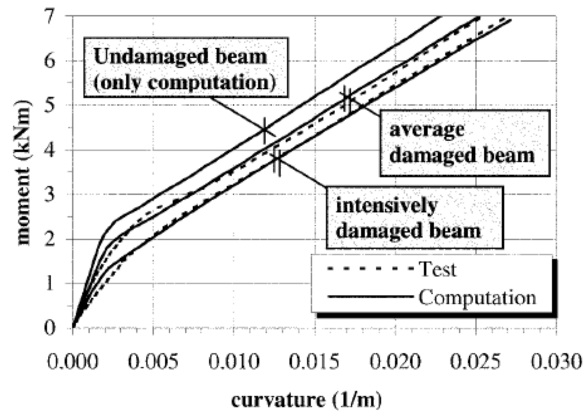

(b)

Figure 2-37- Flexural behaviour of frost damaged and un-damaged beams according to the experimental and numerical study conducted by Petersen et al. (2007) (a) Composition A (w/c=0.6), (b) composition B (w/c=0.7)

Hanjari et al. (2013) conducted a numerical methodology to predict the structural behaviour and mechanical properties of reinforced concrete structures attacked by frost damage in the ultimate limit state. In this study, two types of frost damage were considered, internal frost damage and surface scaling, which affect the mechanical/bond properties and geometry, respectively.

In the first part of the study, an analytical approach was conducted to investigate the effects of frost damage on the compression-tension strength relationship, compression and tension behaviour, and bond properties of the reinforced concrete member (as reviewed in the previous sections in detail). In this study, the compressive strength and dynamic modulus of elasticity were introduced as the indicators of frost damage.

According to Fagerlund et al. (1994), the compressive-tensile relationship of frost-damaged members was adopted by curve fitting. The authors also adopted the compressive constitutive model by Thorenfeldt et al. (1987) and modified it for frost-damaged concrete members. Such modifications were made by considering a 50% reduction in compressive strength after a frost attack, lower initial modulus of elasticity and larger peak strain for the damaged specimen (Shang and Song 2006, Hasan et al. 2008), and variable stiffness for the ascending branch of the stress-strain curve of damaged reinforced concrete members (Ueda et al. 2009). Hanjari et al. (2013) proposed the bilinear tensile strength-crack opening relation developed by Zandi Hanjari et al. (2009b) as the best option for the tensile behaviour of frost-damaged concrete, since it considers softening effects which play an essential role in the analysis of frost-damaged concrete.

Based on the Model Code 1990 (CEB. 1993), the bond stress-slip relationship was proposed for frost-damaged concrete. For both regions with a complete spalled cover or partial cover, the interpolation proposed by Lundgren et al. (2009) was adopted for the bond strength. In the second part of the study, considering the assumptions made in the analytical part, a numerical 2D finite element analysis was conducted using DIANA software and then verified by comparing the results to those based on an experimental study conducted by Hassanzadeh and Fagerlund (2006). The concrete was modelled using four-node quadrilateral plane-stress solid elements and a smeared-rotating crack constitutive model.

The longitudinal bars were modelled using two-node truss elements, and the bond-slip relation was adopted to model the interaction between steel and concrete. It was observed that frost damage affects the material properties resulting in a change of failure mode from ductile to a more brittle one. The test and numerical results were slightly different for the beams with larger cross sections due to the lack of information about frost damage distribution. Hassanzadeh and Fagerlund (2006) observed that in the beams with larger cross-section, the FTCs affect the surface more than the inner concrete.

A two-dimensional non-linear finite element analysis using a program called WCOMD was performed by Hayashida et al. (2014) to investigate the effect of FTCs on the structural behaviour of RC beams. A total of six specimens (without transverse reinforcement), including samples which are attacked by frost damage from the compression side, samples attacked from the tension side, and the reference sample without any frost attack, were analyzed in this study. The results were then compared to those based on experimental data conducted by Hayashida et al. (2012). An eight-node isoparametric plane-stress element was used in the finite element analysis. Smeared cracking and distributed reinforcement models were adopted for concrete and steel rebars. For implementing the tension stiffening effect, a default bonding parameter was adopted within the tension zone, and the fracture energy was computed to be used within the compression zone of RC beams.

The correlation between ultrasonic propagation velocity and compressive strength of the identical cylindrical specimen made from the same RC beam concrete was used to find the compressive strength of each element at different locations. The second approach calculated the average compressive strength of elements along the longitudinal direction. It was observed that the finite element analysis results did not match the experimental results where the RC beams lost the shear rigidity due to the damage in the compressive zone or the bond strength deterioration due to the attack in the tensile region.

Berto et al. (2015) conducted a numerical and experimental study to evaluate the coupled freeze-thaw-mechanical effects on the structural performance of RC beams. The FT degradation model was developed as explained in the previous sections, and deteriorated mechanical properties were calibrated according to the test data conducted by Duan et al. (2011) and Shang and Song (2006). The deteriorated mechanical properties were input into the finite element code OpenSees, and eight beams (with transverse reinforcement) were simulated using four-node plane-stress elements for concrete. The embedded longitudinal reinforcement and stirrups were modelled, assuming a perfect bond. The beams' structural performance and failure mode were analyzed, and the results were compared to those based on experimental data (Hassanzadeh and Fagerlund 2006) to evaluate the accuracy of the proposed degradation model.

The load-deflection curve of the damaged beams based on the numerical and experimental study was similar. However, the initial stiffness based on the numerical study was overestimated (Figure 2-38). Two possible reasons for that were reported: (1) the model assumed that the compressive degradation model is similar to the modulus of elasticity degradation model (as explained in the previous sections), and (2) the perfect bond assumption. A change of failure mode from ductile (for undamaged beam) to brittle (for frost-damaged beam) was observed. The load-deflection capacity of the degraded beams was reported to decrease significantly compared to the reference beams.

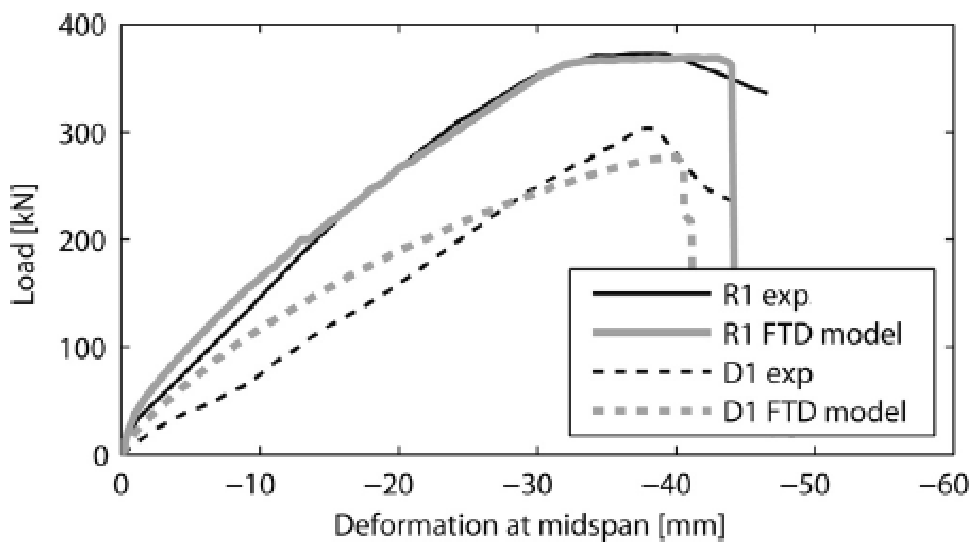

Figure 2-38 A comparison between the load-deflection based on the numerical study by Berto et al. (2015) and experimental data (Hassanzadeh and Fagerlund 2006)

Qin et al. (2017) studied the seismic behaviour of RC columns subjected to freeze-thaw cycles. In this study, four identical columns were tested experimentally. Four RC columns underwent 0, 100, 200, and 300 freeze-thaw cycles according to the Chinese code GB/T50082-2009. The specimens were then re-cast on a foundation, and low cyclic loading was applied at the top of the columns. According to Berto et al. (2015) and Petersen et al. (2007), N_{eq} and RDME were calculated (as explained in the previous sections).

The compressive strength of damaged concrete was then calculated according to the regression analysis by Hanjari et al. (2013) (Eq. 2.62). The peak strain, ultimate strain and ultimate stress were then calculated for the confined and un-confined damaged specimens and were implemented into the OpenSees software. All columns were simulated in the software using the displacement-based beam-column element, ignoring the bond-slip phenomenon. It was observed that the results based on the proposed FE simulation and the experimental tests are in good agreement before the peak point. It is slightly apart after the peak due to ignoring the bond-slip behaviour in the implemented freeze-thaw damage model. It was also observed that FTC does not tend to change the failure mode of the columns, and all the columns experienced flexural failure.

Liu et al. (2019) conducted a seismic fragility analysis on recycled aggregate concrete (RAC) bridge columns damaged by FTC. The authors adopted experimental data from the literature and developed a new freeze-thaw damage model. The damage model was then integrated into the finite element software OpenSees. Nine RAC columns tested by Liu et al. (2018) were simulated in this study. All the specimen parameters were the same, and the only variables in this study were the number of FTCs (0, 40, and 80) and the RCA replacement ratio [0% (represented as conventional concrete, NAC), 50% (represented as RAC50) and 100% (represented as RAC100)] to investigate the effect of these two parameters on the seismic behaviour of frost-damaged columns. Liu et al. (2019) adopted the cyclic stress-strain model for the frost-damaged RCA columns developed by Liu et al. (2018), as shown in Figure 2-39 and described in Eq. 2.72

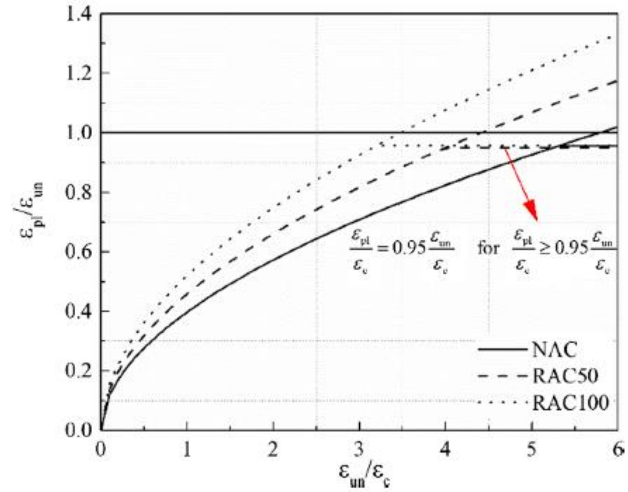

(a)

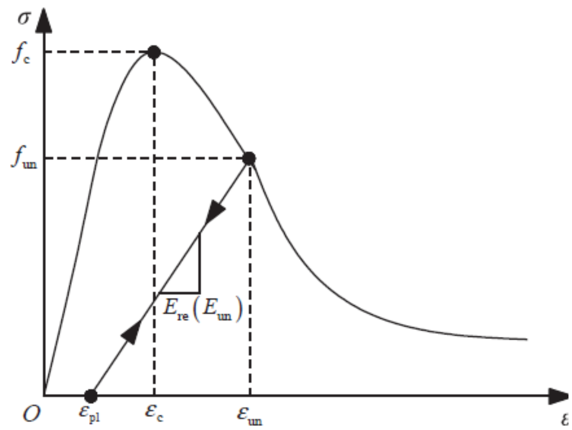

(b)

Figure 2-39 (a) Residual strain ε_{pl} versus unloading strain ε_{un} (Liu et al. 2018b), (b) General constitutive model for unconfined frost-damaged RAC column (Liu et al. 2019)

$$\frac{\varepsilon_{pl}}{\varepsilon_c}=\frac{\varepsilon_{un}}{\varepsilon_c}=\sqrt[0.525]{1/(0.398+0.122\omega)}=\begin{cases}5.783 & \omega=0\% \\ 4.407 & \omega=50\% \\ 3.475 & \omega=100\%\end{cases} \tag{2.72}$$

where ε_{pl}, ε_{un} , ε_c , and ω are the residual strain, unloading strain, peak strain, and RAC replacement ratio, respectively. To ensure ε_{pl} is always less than ε_{un}, Liu et al. (2019) set a limitation as follows:

$$\frac{\varepsilon_{pl}}{\varepsilon_c}=0.95\frac{\varepsilon_{un}}{\varepsilon_c} \quad for \quad \frac{\varepsilon_{pl}}{\varepsilon_c}\geq 0.95\frac{\varepsilon_{un}}{\varepsilon_c} \tag{2.73}$$

For confined frost-damaged RAC columns, Liu et al. (2019) adopted the model proposed by Guo (1999):

$$\begin{cases} y=A_{cg}x+\left(3-2A_{cg}\right)x^2+\left(A_{cg}-2\right)x^3 & 0\leq x\leq 1.0 \\ y=x\Big/\left[B_{cg}\left(x-1\right)^2+x\right] & x\geq 1.0\end{cases} \tag{2.74}$$

where y and x are the normalized stress and strain with respect to the peak stress and peak strain, respectively. Factors A_{cg} and B_{cg} were defined as $A_{cg}=\left(1+1.8\lambda_t\right)A$ and $B_{cg}=\left(1-1.75\lambda_t^{0.55}\right)B$, at which A and B are model parameters and λ_t was defined by Guo (1999) as confinement, i.e., $\lambda_t = \rho_{sv}\ f_{yt} / f_c$ (f_{yt} =yield strength of transverse reinforcement). According to the abovementioned equations, Liu et al. (2019) determined the peak stress and strain for the confined frost-damaged RAC. The rebar stress-strain response was adopted from the isotropic strain-hardening model proposed by Menegotto et al. (1973). The isotropic hardening parameters were defined as the pre-defined values of OpenSees. The Bond_SP01 model of OpenSees was used for the bond-slip model considering the end of the columns are not damaged during FTCs, and the un-damaged concrete strength was used in the software for determining the slip amount. The authors then conducted a sectional analysis to investigate the effects of frost damage at different section levels. Liu et al. (2019) investigated the maximum depth of frost damage, the standard and non-standard FTCs relationship, and the distribution of frost damage (RDME), considering an uneven damage distribution. The proposed model was then verified by comparing the results of the OpenSees simulation and the experiments.

2.5 Structural performance of RC members under combined actions of FT, corrosion, and mechanical loading

In many cold regions, such as Canada, using de-icing salt during the winter increases the potential risk of chloride-induced corrosion, which could be combined with carbonation-induced corrosion and accelerate the corrosion process. Global warming is an accelerating factor in corrosion initiation and propagation. Furthermore, global warming could lead to higher FTC frequency in cold regions, affecting the structural performance and service life of ageing (corroding) infrastructures. To the best of the author’s knowledge, few studies have been conducted on the combined/coupled effects of FT action and corrosion on the structural performance and remaining service life of ageing structures. Diao et al. (2011) conducted an experimental study to investigate the effect of coupled environmental-mechanical action on the structural performance of RC columns. In this test, the specimens underwent corrosion and freeze-thaw deterioration followed by sustained load application. Four groups of $100\times100\times100$ mm plain concrete specimens were tested under 0, 102, 201, and 300 FTCs, and the compressive strength of each group was determined upon completion of the test. It was observed that by increasing the number of FTCs, the compressive strength of the specimens decreased. The structural performance tests were carried out on five RC columns with 100×200 mm cross section and 700-mm long span attached to two brackets at the ends. The FTCs were applied according to the "Standard for test methods of long-term performance and durability of ordinary concrete" (GB/T 50082-2009) in China; each freeze-thaw cycle lasts for four hours, and the temperature varies between 8±20°C to −17±20°C. After every three cycles, the specimens were immersed in a solution of 3% sodium chloride (NaCl) and 0.34% magnesium sulphate ($MgSO_4$), for twelve hours. The sustained loading was simulated by tightening the bolts attached to the spiral rebars at the end bracket. A typical tension-controlled flexural tensile failure was observed for the specimens without any FTCs, seawater corrosion, and sustained loading (COL-0). For the specimens under coupled environmental actions and zero sustained loadings (COL-1), a 25.8%, 4.6%, and 11.5% reduction in cracking, yielding, and ultimate load were observed, respectively. It was also observed that all the stirrups were corroded for these types of specimens, and 70% of the longitudinal rebar was covered with a thin layer of rust. By increasing the sustained loading ratio to 0.2 in the specimen under environmental conditions and sustained loading (COL-2), it was noticed that the longitudinal rebar rust cover increased from 70% to 90% at the location of stirrup-rebar connections. By increasing the sustained load ratio to 0.3 and 0.5, all the stirrups and longitudinal rebars were corroded completely. It was identified that the ultimate capacity of the corroded and frost-damaged RC columns under sustained loading ranging from 0% to 0.5% decreases rapidly by 11.5% to 26.9%, respectively.

Wu et al. (2018) conducted an experimental study to investigate the coupled effect of corrosion, freeze-thaw cycles, and sustained monotonic eccentric loading on the ductility and hysteretic behaviour of air-entrained RC columns. In this study, five similar columns were cast and cured, similar to the study conducted by Diao et al. (2011). The control column was tested after 28 days without any freeze-thaw and corrosion exposure to obtain the ultimate capacity of the undamaged columns. One of the specimens was tested under the effect of 300 FTCs, 100 times of seawater immersion and low cyclic load after 128 days. Two of them were tested under the effect of freeze-thaw, corrosion, sustained monotonic eccentric load and low cyclic load after 128 days. Ductility and hysteretic behaviour analyses were conducted to investigate the effects of different environmental and loading parameters on the initiation and development of cracks and failure behaviour. It was noticed that by increasing the sustained compression loading, the adverse effect of environmental damage on the ductility and ultimate load capacity of the specimens increases in case of forwarding horizontal loading. It was also observed that in case of opposite direction horizontal loading, an increment of sustained compression load enhances the ductility and load capacity of the deteriorated RC columns.

2.6 Gap in the state-of-the-art

Numerous studies have been conducted on the deteriorating environmental effects on the material properties of RC members (Lundgren 2007, Vu et al. 2017). There are also numerous studies on the structural performance of corroded RC beams (Hussain and Miteva 2018, Sæther and Sand 2016) and few on small-scale corroded RC columns (for a specific degree of mass loss at a specific time) under concentric and eccentric compressive loading, both numerically and experimentally (Saito et al. 2007; Xia et al. 2016; Vu et al. 2017). Mohammed (2014) recently developed simplified 1D analysis tools to assess the ultimate capacity, serviceability, and seismic capacity of beam-columns. There is still a scarcity of 3D-NLFEA to investigate the structural performance of real-scale RC pier/columns subjected to environmental effects, traffic load or combination. Only a few studies have experimentally investigated the synergetic effects of frost damage and corrosion on the structural performance of small-scale RC members. The present study aims to propose a quantitative stage-based damage model and develop a comprehensive 3D-NLFEA to study the deteriorating effects of corrosion, FTCs, and a combination of corrosion and FTCs on the structural performance of existing RC bridge pier. The use of 3D-NLFEA allows to study not only strength capacity but also deformation capacity and post-peak response, and it helps to identify failure modes associated to different damage patterns. Although most of the existing bridges are designed conservatively (low service load over capacity ratio, i.e., SLOCR), newly constructed bridges are designed for higher SLOCR for cost and aesthetics (Mohammed 2014). This aspect that needs further investigation in a context where climate change might increase the rate of deterioration of RC infrastructure. The effect of environmental damages on the reduction of load capacity of damaged RC columns, which could lead to exceeding the acceptable limit state in the bridge design codes, needs further scrutiny.

2.7 References

Almusallam, A. A. (2001). “Effect of degree of corrosion on the properties of reinforcing steel bars.” Construction and Building Materials, 15(8), 361–368.

Almusallam A, A., Al-Gahtani A, S., Aziz, A., and Rasheeduzzafar. (1996). “Effect of reinforcement corrosion on bond strength.” Construction and Building Materials, 10(2), 123–129.

Andrade, C., and Alonso, C. (2001). “On-site measurements of corrosion rate of reinforcements.” Construction and Building Materials, 15(2–3), 141–145.

Andrade, C., Alonso, C., and Molina, F. J. (1993). “Cover cracking as a function of bar corrosion: Part I-Experimental test.” Materials and Structures, 26(8), 453–464.

ASTM C666/C666M-15, A. (2015). “Standard test method for resistance of concrete to rapid freezing and thawing.” ASTM International.

Berra, M., Castellani, A., and Coronelli, D. (1997). “Bond in reinforced concrete and corrosion of bars.” Proceedings of the International Conference Structural Faults and Repair, Edinburgh, vol. 2, Eng. Technics Press, pp. 349–357.

Berra, M., Castellani, A., Coronelli, D., Zanni, S., and Zhang, G. (2003). “Steel-concrete bond deterioration due to corrosion: finite-element analysis for different confinement levels.” Magazine of Concrete Research, 55(3), 237–247.

Berto, L., Saetta, A., Scotta, R., and Talledo, D. (2014). “A coupled damage model for RC structures: Proposal for a frost deterioration model and enhancement of mixed tension domain.” Construction and Building Materials, Elsevier Ltd, 65, 310–320.

Berto, L., Saetta, A., and Talledo, D. (2015). “Constitutive model of concrete damaged by freeze-thaw action for evaluation of structural performance of RC elements.” Construction and Building Materials, Elsevier Ltd, 98, 559–569.

Blomfors, M., Zandi, K., Lundgren, K., and Coronelli, D. (2018). “Engineering bond model for corroded reinforcement.” Engineering Structures, 156, 394–410.

Cairns, J., Plizzari, G., Du, Y., Law, D., and Franzoni, C. (2005). “Mechanical properties of corrosion-damaged reinforcement.” ACI Materials journal , 102(4), 256–264.

Di Carlo, F., Meda, A., and Rinaldi, Z. (2017). “Numerical evaluation of the corrosion influence on the cyclic behaviour of RC columns.” Engineering Structures, Elsevier, 153, 264–278.

Castellani, A., and Coronelli, D. (1999). “‘Section 13.7: Beams with corroded reinforcement: Evaluation of the effects of cross section losses and bond deterioration by finite element analysis.” Proc., 8th Int. Conf. on Structure Faults and Repair ‘99, ’ M. Forde, ed., Engineering Technics Press, Edinburgh, U.K. (CD-ROM).

CEB. (1993). CEB-FIP Model Code 1990. fib Model Code Concrete Structures 1990, Lausanne, Switzerland;

Coronelli, D., and Gambarova, P. (2004). “Structural assessment of corroded reinforced concrete beams: Modeling guidelines.” Journal of Structural Engineering, 130(8), 1214–1224.

Deng, P., Zhang, C., Pei, S., and Jin, Z. (2018). “Modeling the impact of corrosion on seismic performance of multi-span simply-supported bridges.” Construction and Building Materials, Elsevier Ltd, 185, 193–205.

Dhakal, R. P., and Maekawa, K. (2002). “Modeling for postyield buckling of reinforcement.” Journal of Structural Engineering, 128(9), 1139–1147.

DHAKAL, R. P., and MAEKAWA, K. (2001). "Geometrical Nonlinearity on Collapse of Reinforced Concrete Piers." J Mater Concr Struct Pavements, JSCE, 51(676), 135–147.

Diao, B., Sun, Y., Cheng, S., and Ye, Y. (2011). "Effects of Mixed Corrosion, Freeze-Thaw Cycles, and Persistent Loads on Behavior of Reinforced Concrete Beams." Journal of Cold Regions Engineering, 25(1), 37–52.

Duan, A., Jin, W., and Qian, J. (2011). "Effect of freeze-thaw cycles on the stress-strain curves of unconfined and confined concrete." Materials and Structures/Materiaux et Constructions, 44(7), 1309–1324.

Fagerlund, G. (2004). "'A Service Life Model for Internal Frost Damage in Concrete.'" Report TVBM-3119,Lund Institute of Technology, Lund, Sweden, Lund Institute of Technology, Lund, Sweden.

Fib. (2013). fib Model Code for concrete structures 2010. Lausanne, Switzerland.

GB/T50082-2009. (2009). "Standard for test method of long term performance and durability of ordinary concrete." China Architecture and Building Press, Beijing.

Giamundo, V., Lignola, G. P., Prota, A., and Manfredi, G. (2014). "Analytical Evaluation of FRP Wrapping Effectiveness in Restraining Reinforcement Bar Buckling." Journal of Structural Engineering, 140(7), 04014043.

Gilbert, R., and Warner, R. (1978). "Tension stiffening in reinforced concrete slabs. Journal of Structural Division ASCE." .104(ST12);1885-1900.

Gong, F., and Maekawa, K. (2018). "Multi-scale simulation of freeze-thaw damage to RC column and its restoring force characteristics." Engineering Structures, Elsevier, 156(December 2017), 522–536.

Hanja, Utgenannt, P., and Lundgren, K. (2011). "Experimental study of the material and bond properties of frost-damaged concrete." Cement and Concrete Research, Elsevier Ltd, 41(3), 244–254.

Hanjari, K. Z., Utgenannt, P., and Lundgren, K. (2011). "Experimental study of the material and bond properties of frost-damaged concrete." Cement and Concrete Research, 41(3), 244–254.

Hasan, M., Okuyama, H., Sato, Y., and Ueda, T. (2004). "Stress-strain model of concrete damaged by freezing and thawing cycles." Journal of Advanced Concrete Technology, 2(1), 89–99.

Hasan, M., Ueda, T., and Sato, Y. (2008). "Stress–strain relationship of frost-damaged concrete subjected to fatigue loading." Journal of Materials in Civil Engineering, 20 (1), 37–45., 20(January), 37–45.

Hassanzadeh, M., and Fagerlund, G. (2006). “Residual strength of the frost-damaged reinforced concrete beamsed.” 3rd European Conference on Computational Mechanics Solids, Structures and Coupled Problems in Engineering, Lisbon, 5–8.

Hayashida, H., Sato, Y., and Ueda, T. (2014). “Evaluation of Structural Properties of the Freeze–Thaw-Damaged RC Beam Members by Nonlinear Finite-Element Analysis.” Proceedings of the 4th International Conference on the Durability of Concrete Structures (ICDCS ’14), Purdue University, West Lafayette, Ind, USA, 45–51,.

Hognestad, E. (1951). "A Study of Combined Bending and Axial Load in Reinforced Concrete Members." Bulletin Series No. 399, 128.

Hussain, H., and Miteva, D. (2018). “Structural behavior of corroded reinforced concrete structures A study based on detailed 3D FE analyses,.” Master’s thesis, Department of Architecture and Civil Engineering CHALMERS UNIVERSITY OF TECHNOLOGY, Gothenburg, Sweden 2018.

Joshi, J., Arora, H. C., and Sharma, U. K. (2015). “Structural performance of differently confined and strengthened corroding reinforced concrete columns.” Construction and Building Materials, 82, 287–295.

Kashani, M. M., Crewe, A. J., and Alexander, N. A. (2013). “Nonlinear stress-strain behaviour of corrosion-damaged reinforcing bars including inelastic buckling.” Engineering Structures, 48, 417–429.

Kashani, M. M., Crewe, A. J., and Alexander, N. A. (2017). “Structural capacity assessment of corroded RC bridge piers.” Proceedings of the Institution of Civil Engineers: Bridge Engineering, 170(1), 28–41.

Kashani, M. M., Maddocks, J., and Dizaj, E. A. (2019). “Residual Capacity of Corroded Reinforced Concrete Bridge Components: State-of-the-Art Review.” Journal of Bridge Engineering, 24(7).

Li, A., Xu, S., and Wang, Y. (2017). “Effects of frost-damage on mechanical performance of concrete.” Journal Wuhan University of Technology, Materials Science Edition, 32(1), 129–135.

Lin, H., and Zhao, Y. (2016). “Effects of confinements on the bond strength between concrete and corroded steel bars.” Construction and Building Materials, Elsevier Ltd, 118, 127–138.

Lindmark, S. (1998). Division of Building Materials Mechanisms of Salt Frost Scaling of Portland Cement-bound Materials : Studies and Hypothesis. Building.

Liu, K., Yan, J., Alam, M. S., and Zou, C. (2019). “Seismic fragility analysis of deteriorating recycled aggregate concrete bridge columns subjected to freeze-thaw cycles.” Engineering Structures, Elsevier, 187(February), 1–15.

Liu, K., Yan, J., Zou, C., and Wu, H. (2018). “Cyclic stress-strain model for air-entrained recycled aggregate concrete after freezing-and-thawing cycles.” ACI Structural Journal, 115(3), 711–722.

Lizhi, F. (2010). “Experimental Study on the Strength of Concrete under Uniaxial Tensile Load after Freeze-thaw Cycles.” Yangzhou: Yangzhou University.

Lundgren, K. (1999). “Three-dimensional modelling of bond in reinforced concrete theoretical model, experiments and applications.” PhD thesis, Div. of Concrete Struct., Chalmers University of Technology, Göteborg, Sweden.

Lundgren, K. (2002). “Modelling the effect of corrosion on bond in reinforced concrete.” Magazine of Concrete Research, 54(3), 165–173.

Lundgren, K. (2005a). “Bond between ribbed bars and concrete. Part 1: Modified model.” Magazine of Concrete Research, 57(7), 371–382.

Lundgren, K. (2005b). “Bond between ribbed bars and concrete. Part 2: The effect of corrosion.” Magazine of Concrete Research, 57(7), 383–395.

Lundgren, K. (2007). “Effect of corrosion on the bond between steel and concrete: an overview.” Magazine of Concrete Research, 59(6), 447–461.

Lundgren, K., Kettil, P., Hanjari, K. Z., Schlune, H., and Roman, A. S. S. (2012). “Analytical model for the bond-slip behaviour of corroded ribbed reinforcement.” Structure and Infrastructure Engineering, 8(2), 157–169.

Maaddawy, N. E., Soudki, K., and Topper, T. (2005). “Analytical model to predict nonlinear flexural behavior of corroded reinforced concrete beams.” , ACI Struct. J., 102(4), 550–559.

Maekawa, K. (1985). “The Deformational Behavior and Constitutive Equation of concrete Based on the Elasto-Plastic and Fracture Model,.” Doctoral Dissertation, Field of Civil Engineering, Technological University of Nagaoka, Nagaoka, Niigata Pref, Japan.

Mander, J. B., Priestley, M. J., and Park, R. (1988). “Theoretical stress-strain model for confined concrete.” Journal of Structural Engineering (United States), 114(8), 1804–1826.

Meda, A., Mostosi, S., Rinaldi, Z., and Riva, P. (2014). “Experimental evaluation of the corrosion influence on the cyclic behaviour of RC columns.” Engineering Structures, Elsevier Ltd, 76, 112–123.

Mehta, P. K., and Monteiro, P. J. M. (2001). “Concrete: Microstructure, Properties, and Materials 4th edn, 704 (McGraw-Hill Professional, New York, NY, USA, 2014).”

Mohammed, A. M. (2014). “Semi-Quantitative Assessment Framework for Corrosion Damaged Slab-on-Girder Bridge Columns Using Simplified Nonlinear Finite Element Analysis, Ph.D. Thesis.” University of Ottawa,.

Molina, F. J., Alonso, C., and Andrade, C. (1993). “Cover cracking as a function of rebar corrosion : Part 2—Numerical model.” Materials and Structures, 26, 532–548.

Nguyen-Xuan, H., Thai, C. H., and Nguyen-Thoi, T. (2013). “Isogeometric finite element analysis of composite sandwich plates using a higher order shear deformation theory.” Composites Part B: Engineering, Elsevier Ltd, 55, 558–574.

Petersen, L., Lohaus, L., and Polak, M. A. (2007). “Influence of freezing-and-thawing damage on behavior of reinforced concrete elements.” ACI Materials Journal, 104(4), 369–378.

Polak, M. A., and Blackwell, K. G. (1998). “Modelling Tension in Reinforced Concrete Members Subjected to Bending and Axial Load.” Journal of Structural Engineering, American Society of Civil Engineers, 124(9), 1018-1024.

Powers, T. C. (1945). “A Working Hypothesis for Further Studies of Frost Resistance of Concrete.” ACI Journal Proceedings, 41(1).

Qin, Q., Zheng, S., Li, L., Dong, L., Zhang, Y., and Ding, S. (2017). “Experimental Study and Numerical Simulation of Seismic Behavior for RC Columns Subjected to Freeze-Thaw Cycles.” Advances in Materials Science and Engineering, 2017(2011).

Rodriguez, J., Ortega, L., and Garcia, A. M. (1994). “Corrosion of reinforcing bars and service life of reinforced concrete structures: corrosion and bond deterioration.” Proceedings of the International Conference on Concrete Across Borders, Odense, Denmark,.

Rodriguez, J., Ortega, L. M., and Casal, J. (1995). “Load carrying capacity of concrete structures with corroded reinforcement.” Proceedings of the International Conference on Structural Faults and Repair, 2. London, 189-198.

Rodriguez, J., Ortega, L. M., Casal, J., and Diez, J. M. (1996). “Assessing structural conditions of concrete structures with corroded reinforcement.” Proc., Int. Conf. on Concrete in the Service of Mankind, Sess. 5, Dundee, Scotland, R. K. Dhir and N. A. Henderson, eds., E-&-FN Spon, London, 141–150.

Saatcioglu, M., and Razvi, S. R. (1992). “Strength and ductility of confined concrete.” Journal of Structural Engineering (ASCE), 118(6), 1590–1607.

Saetta, A., Scotta, R., and Vitaliani, R. (1999). “Coupled environmental-mechanical damage model of RC structures.” Journal of Engineering Mechanics (ASCE), 125(8), 930–940.

Saetta, A. V. (2005). “Deterioration of Reinforced Concrete Structures due to Chemical–Physical Phenomena: Model-Based Simulation.” Journal of Materials in Civil Engineering, 17(3), 313–319.

Saito, Y., Oyado, M., Yasojima, A., Kanakubo, T., and Yamamoto, Y. (2007). “Structural Performance of Corroded RC Column under Uniaxial Compression Load,.” First International Workshop on Performance, Protection & Strengthening of Structures under Extreme Loading, Whistler, Canada.

Schlune, H. (2006). “Bond of corroded reinforcement - Analytical description of the bond-slip response.” Master’s Thesis, Chalmers University of Technology, Sweden.

Shang, H. S., and Song, Y. P. (2006). “Experimental study of strength and deformation of plain concrete under biaxial compression after freezing and thawing cycles.” Cement and Concrete Research, 36(10), 1857–1864.

Shisheng, S. (1997). “Effect of Freezing-thawing Cycles on Mechanical Properties of Concrete.” China Civil Engineering Journal, 30(4): 35-.

Tahershamsi, M. (2016). “Structural Effects of Reinforcement Corrosion in Concrete Structures,.” Doctoral Dissertation, Chalmers University of Technology, Sweden.

Thorenfeldt, E., Tomaszewicz, A., and Jensen, J. J. (1987). “Mechanical properties of high-strength concrete and applications in designed.” Conference on Utilization of High-Strength Concrete, Stavanger, Norway, 149–159.

Tørlen, A., and Horrigmoe, G. (1998). Modelling of bond between reinforcement and concrete for deteriorated and repaired beams”, Report No. NTAS A98034, NORUT Technology. Narvik, Norway. (in Norwegian).

Tuutti, K. (1982). “Corrosion of Steel in Concrete Structures.” Swedish Cement and Concrete ResearchInstitute.

Val, D. V. (2007). “Deterioration of Strength of RC Beams due to Corrosion and Its Influence on Beam Reliability.” Journal of Structural Engineering, 133(9), 1297–1306.

Val, D. V., and Melchers, R. E. (1997). “Reliability of deteriorating RC slab bridges.” J. Struct. Eng., 123 (12), 1638–1644.

Vecchio, F., and Collins, M. P. (1986). “The modified compression field theory for reinforced concrete elements subjected to shear.” Proc. ACI, 83(2), 219–231.

Vu, N. S., Yu, B., and Li, B. (2016). “Prediction of strength and drift capacity of corroded reinforced concrete columns.” Construction and Building Materials, 115, 304–318.

Vu, N. S., Yu, B., and Li, B. (2017). “Stress-strain model for confined concrete with corroded transverse reinforcement.” Engineering Structures, 151, 472–487.

Wu, J., Zhang, J., Diao, B., Cheng, S., and Ye, Y. (2018). "Hysteretic Behavior of Eccentrically Loaded Reinforced Air-Entrained Concrete Columns under Combined Effects of Freeze-Thaw Cycles and Seawater Corrosion." Advances in Civil Engineering, 2018.

Xia, J., Jin, W. L., and Li, L. Y. (2016). "Performance of corroded reinforced concrete columns under the action of eccentric loads." Journal of Materials in Civil Engineering, 28(1).

Xiaodong, J. (2007). "The Experimental Study and Theoretical Analysis on the Mechanical Performance of Concrete and Bond Behaviour between Concrete and Steel Bar after Freezing and Thawing." Thesis, Dalian: Dalian University of Technology.

Xin, J., Zhou, J., Zhou, F., Yang, S. X., and Zhou, Y. (2018). "Bearing capacity model of corroded RC eccentric compression columns based on hermite interpolation and fourier fitting." Applied Sciences (Switzerland), 9(1).

Zandi Hanjari, K., Kettil, P., and Lundgren, K. (2013). "Modelling the structural behaviour of frost-damaged reinforced concrete structures." Structure and Infrastructure Engineering, 9(5), 416–431.

Zandi Hanjari, K., Utgenannt, P., and Lundgren, K. (2009a). "Frost-damaged concrete: Part 2. Bond properties." 4th International Conference on Construction Materials: Performance, Innovations and Structural Implications. Nagoya, Japan, 761–766.

Zandi Hanjari, K., Utgenannt, P., and Lundgren, K. (2009b). "Frost-damaged concrete: Part 1." Material properties. 4th International Conference on Construction Materials: Performance, Innovations and Structural Implications, Nagoya, Japan, 753–760.

Zandi, K. (2015). "Corrosion-induced cover spalling and anchorage capacity." Structure and Infrastructure Engineering, 11(12), 1547–1564.

Chapter 3: Nonlinear Finite Element Modeling of the Impact of Reinforcement Corrosion on Bridge Piers under Concentric Loads[1]

Abstract

Corrosion of reinforcing steel in reinforced concrete (RC) infrastructure is one of the most detrimental deterioration mechanisms, affecting both safety and serviceability. In the present study, a comprehensive analysis methodology of corrosion damage is adopted. The detrimental effects of corrosion-induced degradation of material properties on the ultimate capacity of an existing ageing RC bridge pier under concentric loading are investigated. A three-dimensional nonlinear finite element analysis using the commercially available finite element program DIANA is used. The main corrosion-induced deteriorating factors considered in the present study are: concrete strength degradation within the cover and part of the confined concrete core due to corrosion-induced cracking, degradation of confinement effects, steel area reduction due to uniform corrosion (in both longitudinal and tie reinforcement), steel ductility degradation due to pitting corrosion, buckling of compressive steel bars due to cross-section reduction and confinement degradation, and bond strength degradation between steel and concrete induced by concrete cracking/spalling. The methodology is evaluated by comparing the numerical results to those of corroded column tests reported in the literature.

3.1 Introduction

Corrosion of reinforcing steel is one of the most widespread deterioration mechanisms in reinforced concrete (RC) infrastructure, affecting its serviceability and ultimate capacity. Many studies focus on the deteriorating effects of corrosion on the mechanical properties of steel and concrete in RC

[1]This chapter has been published in *Structural Concrete* (Zaghian, S., Martín-Pérez, B., and Almansour, H. (2022). "Nonlinear finite element modeling of the impact of reinforcement corrosion on bridge piers under concentric loads." Structural Concrete, 23(1), 138-153. https://doi.org/10.1002/suco.202100254)

structures (Cairns et al. 2005, Kashani et al. 2015, Blomfors et al. 2018) . The main deteriorating factors that have been considered in those studies are: concrete strength degradation within the cover zone and confined concrete, steel area reduction due to uniform and pitting corrosion (longitudinal and stirrups), pit-induced ductility degradation of the steel, buckling of compressive steel bars due to steel cross-section reduction and confinement degradation, and bond strength degradation between steel and concrete.

While many studies are conducted on corroded RC beams' structural performance, there is still a lack of studies on the effect of corrosion on the structural performance of RC columns. Corrosion-induced cracking weakens the concrete cover and core concrete, resulting in loss of confinement and potential risk of buckling in the compressive longitudinal rebars, which is a critical issue to be studied in corroded RC columns.

The steel rebar cross-section is usually reduced according to Faraday's law (Lu et al. 2011, Mohammed 2014). There have been some experimental studies on the deteriorating effects of corrosion on the strength and ductility of reinforcing bars (Almusallam 2001, Du et al. 2005) . The rebar strength and ductility as a function of the mass loss due to corrosion were expressed (Cairns et al. 2005). Corrosion of transverse reinforcement followed by loss of confinement and longitudinal reinforcement cross-section loss, increases the potential risk of buckling in the longitudinal reinforcing steel. Inelastic buckling of corroded longitudinal reinforcement under compression is another important limit state, especially in the seismic design of structures in earthquake zones.

A compression stress-strain response for corroded steel based on the Dhakal–Maekawa buckling model (Dhakal and Maekawa 2002) was developed and the effect of different corrosion levels on the inelastic buckling behaviour of steel reinforcement was evaluated (Kashani et al. 2013). Rodriguez et al. (1996a) recommended increasing the possibility of elastic buckling of corroded rebars by increasing the effective length in the Euler's elastic critical strength formula to 75% of the tie spacing, since there is a possibility of rotation between the ties and the longitudinal reinforcement due to corrosion, and the full fixity condition is not satisfied completely.

Coronelli and Gambarova (2004) proposed an expression to reduce the compressive strength of the concrete in the presence of corrosion-induced cracking, adopting the model developed by Vecchio and Collins (1986). Corrosion products exert an expanding pressure against the surrounding concrete due to their lower density compared to the original steel. As a result, splitting stresses within the concrete are induced, causing cover cracking, spalling and/or delamination over time. The corrosion products expansion also adversely affect the interaction between steel and concrete (Lundgren 2002).

Over the past few decades, many studies have been conducted on the effects of corrosion on the bond-slip behaviour of RC structural members (Lundgren 2002, Lundgren et al. 2012, Zandi 2015, Blomfors et al. 2018). On the other hand, there are several experimental studies on the structural performance of small-scale corroded RC columns (Saito et al. 2007, Xia et al. 2016a, Vu et al. 2017). There are also some numerical investigations that mostly focus on the seismic performance of corroded RC columns (Mohammed 2014, Di Carlo et al. 2017, Kashani et al. 2017). All of these studies revealed that the corrosion phenomenon significantly affects the ultimate strength and drift capacity of such columns.

Recently, Xin et al. (2018) conducted sectional analysis to predict the bearing capacity of corroded RC columns under eccentric loading. Xin et al. (2018) proposed a feasible method to construct the interaction diagram of corroded RC columns at a specific damage level which was successfully verified through some verification case studies. However, there is still a scarcity of research on modelling the structural performance of real-scale bridge piers under the combination of corrosion at different stages of damage and traffic loads, wherein all the deteriorating aspects of corrosion on reinforcing steel and concrete are considered. The present study aims to address this gap; the structural performance of an ageing designed large-scale RC bridge pier under concentric compression load is investigated by conducting a stage-based three-dimensional nonlinear finite element analysis (3D-NLFEA). The corrosion process is defined as a staged phenomenon with different percentages of steel reinforcement mass loss, and at each stage, it is simulated by incorporating all the deteriorating effects.

3.2 Proposed 3D nonlinear finite element model

3.2.1 General

In the present study, the structural performance of corroded RC bridge piers under concentric loading is evaluated. To this aim, a 3D-NLFEA is carried out using DIANA- a commercial nonlinear finite element software package (Diana 2019). In the present staged-base analysis, different corrosion stages are defined to incorporate the effects of variable deteriorating factors over the bridge's service life, which are explained in detail in the following sections. The validity of the proposed NLFEA is verified by stimulating previously tested corroded RC columns by Rodriguez et al. (1996a). In the proposed 3D-NLFEA, concrete is modelled by adopting solid brick and wedge elements. Pre-defined tension softening "Hordjik" is adopted as the concrete tensile response, and compression curves "fib 2010" and "Thorenfeldt" with a more brittle post-peak, according to the recommendation by Coronelli and Gambarova (2004), are adopted as the compressive response of undamaged and damaged concrete, respectively. The confinement effect is incorporated by adopting the confinement model by Saatcioglu and Razvi (1992) as in Eq.3.1:

$$f'_{CC} = f'_{C0} + k_1 f_{le} \qquad 3.1$$

Where f'_{cc} and f'_{c0} are the confined strength of concrete and unconfined in-place strength of concrete in structural members, respectively. Parameter f_{le} is the equivalent lateral confinement pressure and is introduced as $f_{le} = k_2 f_l$ at which f_l is the lateral confinement pressure, $k_2 = 0.15\sqrt{\frac{b_c}{s}\frac{b_c}{s_l}} \le 1.0$ for rectilinear reinforcement (b_c, s, and s_l are the section width, transverse reinforcement spacing, and spacing of laterally supported longitudinal reinforcement respectively) and $k_2 = 1$ for spiral reinforcement. Coefficient k_1 is an empirical parameter, and according to the test data regression analysis, Saatcioglu and Razvi (1992) proposed the variation of coefficient k_1 as given by Eq. 3.2. The variables f_l, , $\varepsilon_1$and ε_{85} were calibrated as Eqs. 3.3 , 3.4, and 3.5, respectively.

$$k_1 = 6.7\left(f_{le}\right)^{-0.17} \tag{3.2}$$

$$f_l = \frac{\sum_{i=1}^{q}\left(A_s f_{yt} \sin\alpha\right)_i}{s b_c} \tag{3.3}$$

$$\varepsilon_1 = \varepsilon_{01}\left(1+5K\right) \quad ; \quad K = \frac{k_1 f_{le}}{f'_{co}} \tag{3.4}$$

$$\varepsilon_{85} = 260\rho\varepsilon_1 + \varepsilon_{085} \quad ; \quad \varepsilon_1 = \varepsilon_{01}\left(1+5K\right) \tag{3.5}$$

in which A_s is the tie leg cross sectional area; f_{yt} is the yield strength of the tie; q is the number of tie legs that cross the side of core concrete for which the average lateral pressure, f_l, is computed; ε_{01}, ε_1, ε_{085}, ε_{85} are the strain at the peak and strain corresponding to 85% of peak stress for the unconfined and confined concrete, respectively.

In the verification case studies, the reinforcement is modelled by DIANA pre-defined two-node one-dimensional "embedded" reinforcement. In the RC bridge pier simulation, the reinforcement is modelled by the "bond-slip" reinforcement. The bond-slip interface elements are treated as beam elements to incorporate the effect of axial load-induced lateral pressure on the core. The pre-defined local bond-slip model by the fib Model Code 2010 (fib 2013) is adopted as the un-corroded bond-slip response and is modified to incorporate the effect of corrosion. The concentric load is applied as a uniform stress on a steel plate of 40-mm thickness located on the columns' top to avoid any local damage. Linear three-dimensional surface interface elements were applied at the connection between the column and the loading plate to assure a smooth load transfer. A regular Newton-Raphson iterative method is used along with the "Total Lagrange" as the geometrical nonlinear analysis.

3.2.2 Corrosion-damage model at the material level

In an earlier study (Zaghian et al. 2020), the adopted corrosion damage model was explained in detail. The main corrosion-induced deteriorating factors considered in the present study are described as follows:

1) In case of lack of gravimetric data, it is possible to estimate the corrosion level (X_{corr} (%)) as given in Eq. 3.6:

$$X_{corr} = \frac{d_b{}^2 - d_{b,corr}{}^2}{d_b{}^2} \times 100 \qquad 3.6$$

where d_b and $d_{b,corr}$ are the un-corroded and corroded rebar diameters, respectively.

2) Ductility degradation of the corroded ties and tensile flexural longitudinal reinforcing bars is estimated as in Eq. 3.7(Cairns et al. 2005):

$$\varepsilon_{ut,cor} = \left[1.0 - 100 \times \alpha_1 . X_{corr}\right] \varepsilon_{ut} \qquad 3.7$$

where ε_{ut} and $\varepsilon_{ut,corr}$ are the ultimate tensile strain of uncorroded and corroded rebar, respectively. The empirical coefficient α_1 has been calibrated by many researchers considering different types of rebars (plain and ribbed rebars) and exposure conditions (Du et al. 2005, Cairns et al. 2005). Herein, for chloride exposure and embedded rebar in concrete, the value $\alpha_1 = 0.035$ is adopted (Castel et al. 2000).

Figure 3-1 shows the tensile stress-strain response of uncorroded and corroded longitudinal reinforcing bars after 5% cross-section loss due to pitting corrosion.

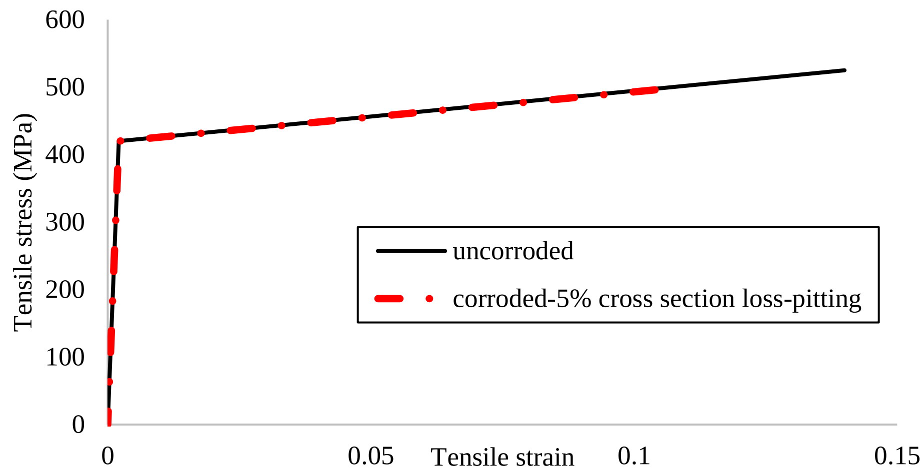

Figure 3-1 Tensile stress-strain response of uncorroded and corroded longitudinal rebars after 5% cross-section loss due to pitting corrosion

3) Possibility of elastic buckling (suggestion by Rodriguez et al. 1996a) and inelastic buckling (Kashani et al. 2013) in the corroded longitudinal rebars are investigated as in Eqs.3.8 and 3.9, respectively:

$$\sigma_{cr,corr} = \pi^2 E\left(0.25 d_{b,corr}\right)^2 / (0.75 s_{corr})^2 \tag{3.8}$$

$$\eta = \sigma / f_{yc,corr} = \begin{cases} \xi = \varepsilon / \varepsilon_{yc,corr} & \xi \le 1 \\ \dfrac{\eta_2 - 1}{\xi_2 - 1}\left(\xi - 1\right) + 1 & 1 < \xi \le 2 \\ \eta_2 - 0.02\left(\xi - \xi_2\right) & \xi_2 \le \xi \,\&\, \eta \ge 0.2 \\ 0.2 & otherwise \end{cases} \tag{3.9}$$

in which

$$\xi_2 = \max\left\{55 - 2.3\lambda_{p,corr};7\right\}$$
$$\eta_2 = \max\left\{\alpha\left(1.1 - 0.016\lambda_{p,corr}\right)\eta^*{}_2;0.2\right\}$$
$$\lambda_p = \sqrt{\frac{f_{yc,corr}}{100}}\frac{s}{d_b - 2x_{cp}}$$

$$f_{yc,corr} = f_{yc}\left[1 - 100 \times \beta.X_{corr}\right] \quad ; \quad \beta = \begin{cases} 0.005 & s/d_b \le 5 \\ 0.0065 & 5 < s/d_b \le 10 \\ 0.0125 & s/d_b > 10 \end{cases}$$

where s_{corr} is the tie spacing considering the possible loss of one or more ties; η and ξ are the non-dimensional stress and strain, respectively; α is the softening coefficient; s is the tie spacing; $\eta^*{}_2$ is the non-dimensional stress corresponding to ξ_2 (in case of no buckling); $f_{yc,corr}$ is the compressive strength of the corroded rebar; and, λ_p and $\lambda_{p,corr}$ are the non-dimensional buckling parameters of the un-corroded and corroded rebars, respectively.

4) Cover concrete cracking and even spalling within the affected regions are simulated by reducing the concrete compressive strength as in Eq. 3.10 (Coronelli and Gambarova 2004) . The tensile strength of the damaged cover concrete is reduced proportionally to the reduction ratio of the concrete compressive strength (recommendation by Hanjari et al. (Hanjari et al. 2011a)).

$$f'_{C0,corr} = \frac{f'_{C0}}{1 + K\varepsilon_1/\varepsilon_{c0}}, \varepsilon_1 = 2\pi n_{bars}\left(\nu_{rs} - 1\right)x_{cp}/b_0 \qquad 3.10$$

where f'_{C0} and $f'_{C0,corr}$ are the compressive strength of undamaged and damaged concrete; $K = 0.1$ is adopted by assuming ribbed bars with medium diameter; ε_{c0} is the concrete strain at the peak compressive strength (taken as 0.002); ε_1 is the average tensile strain perpendicular to compression; n_{bars} is the number of corroding rebars; $\nu_{rs} = 2$ is the volume expansion ratio (Molina et al. 1993); x_{cp} is the corrosion penetration depth and is calculated as

$x_{cp} = \frac{d_b}{2}\left[1-\sqrt{1-X_{corr}}\right]$ (as mentioned in Deng et al. 2018), and b_0 is the width of the un-corroded section.

5) The corrosion-induced degradation of confinement is estimated by substituting the degraded properties values, such as the reduced mechanical and geometrical properties of corroded ties and a possible increase in tie spacing due to pit-induced tie rupture into Eqs.3.1-3.5.

6) The engineering bond-slip model (Blomfors et al. 2018) is adopted in the present study. The reduced bond strength $\tau_{bu,spilit,red}$ and reduced residual bond capacity $\tau_{res,\mathrm{mod}}\left(k_{tr}\right)$ of corroded specimens are estimated as in Eqs. 3.11 and 3.12, respectively. Bond deterioration was modeled along the entire length of corroded rebars.

$$\tau_{bu,spilit,red} = \eta_2.6.5.\left(\frac{f_{C0}}{25}\right)^{0.25}\left(\frac{25}{d_b}\right)^{0.2}\left(1+k_m.k_{tr}\right) \quad 3.11$$

$$\tau_{res,\mathrm{mod}}\left(k_{tr}\right) = \begin{cases}\left(0.16+12k_{tr}\right).\tau_{bu,spilit,red} & for \quad 0 \le k_{tr} \le 0.02 \\ 0.4\tau_{bu,spilit,red} & for \quad 0.02 < k_{tr}\end{cases} \quad 3.12$$

in which variables η_2, k_m, and k_{tr} have been adopted from the Model Code 2010 (Fib 2013).

3.3 Validation of 3D nonlinear finite element analysis

In this section, two types of columns tested by Rodriguez et al. (1996a) under concentric loads are selected to evaluate the integrity of the proposed 3D-NLFEA. Among all the columns tested by Rodriguez et al. (1996a), columns type 1 and 2 with different tie spacing were selected for the simulation. Columns C11and C21 are selected as the control columns, and columns C18 and C27 are selected as the corroded columns (Figure 3-2). According to Rodriguez et al. (1996a), columns C11 and C21 were respectively fabricated with concrete with compressive strengths of 30 MPa and 34 MPa, 4-8 mm and 4-16mm longitudinal rebars, and 6-mm ties spaced at 100 mm and 150 mm. The reinforcement had a yield stress of 590 MPa and ultimate strength of 670 MPa. It was reported that the average corrosion attack penetration depth in the ties and longitudinal rebars of column C18 was 0.56 mm and 0.6 mm, respectively. Those values were reported as 0.47 mm and 0.62 mm for column C27. In the numerical simulation of the columns, the compressive strength of the concrete core is estimated according to Eqs.3.1-3.5. The corrosion of longitudinal reinforcement is assumed uniform considering the average attack penetration depths that were reported. In columns C18 and C27, it was reported that the non-symmetric damage of the concrete cover led to eccentricities of $e_{x,C18} = 7.8$ mm and $e_{y,C18} = 10.6$ mm for column C18, and $e_{x,C27} = 3.2$ mm and $e_{y,C27} = 4.6$ mm for column C27. These eccentricities were input in the analysis. Since no information about pit locations was reported, tie pitting corrosion was simulated using two methods; method (1) consisted of removing two and four ties within zone 3 of columns C18 and C27, respectively, as observed by Rodriguez et al. (1996a) after structural testing (Figure 3-2), and method (2) consisted of reducing the corroded tie's ductility in addition to the uniform cross-sectional area reduction. All the aforementioned mechanical properties are summarized in Table 3-1. A bi-linear behaviour with an initial stiffness of 200 GPa was adopted for the rebars. Figure 3-3 shows the proposed models for both uncorroded and corroded compressive longitudinal reinforcement in the present study. Based on the estimated calculations, elastic buckling is not critical for the uncorroded rebar and corroded rebars within zone 2 due to sufficient confinement. The possible failure was therefore assumed to be inelastic buckling rather than elastic buckling (yielding followed by a post-yield softening response). On the other hand, the allowable critical stress in the corroded compressive longitudinal rebars within zone 3 was estimated according Eq.3.8. The meshes based on 50-mm CTE30 elements were investigated. The column base was restrained from all translational movements at the base.

Table 3-1 Details of RC columns tested by Rodriguez et al. (1996)

Specimens	b×h (mm×mm)	L(mm)	Cover and core compressive strength (control and corroded) (MPa)						Broken ties
			Zone 1		Zone 2		Zone 3		
			f_c	f'_{CC}	$f_{c,cor}$	$f'_{CC,cor}$	$f_{c,cor}$	$f'_{CC,cor}$	
C11	200×200	1,200	30	33.5	NA	NA	NA	NA	0
C18	200×200	1,200	30	33.5	7.5	37.6 [1]	negligible	36.3	2
C21	200×200	1,200	34	36.2	NA	NA	NA	NA	0
C27	200×200	1,200	34	36.2	7.5	36.7 [1]	negligible	35.7	4

(1) The compressive strength of chloride contaminated concrete was reported as 35.8 MPa and 35.6 MPa in columns C18 and C27, respectively (Rodriguez et al. 1996)

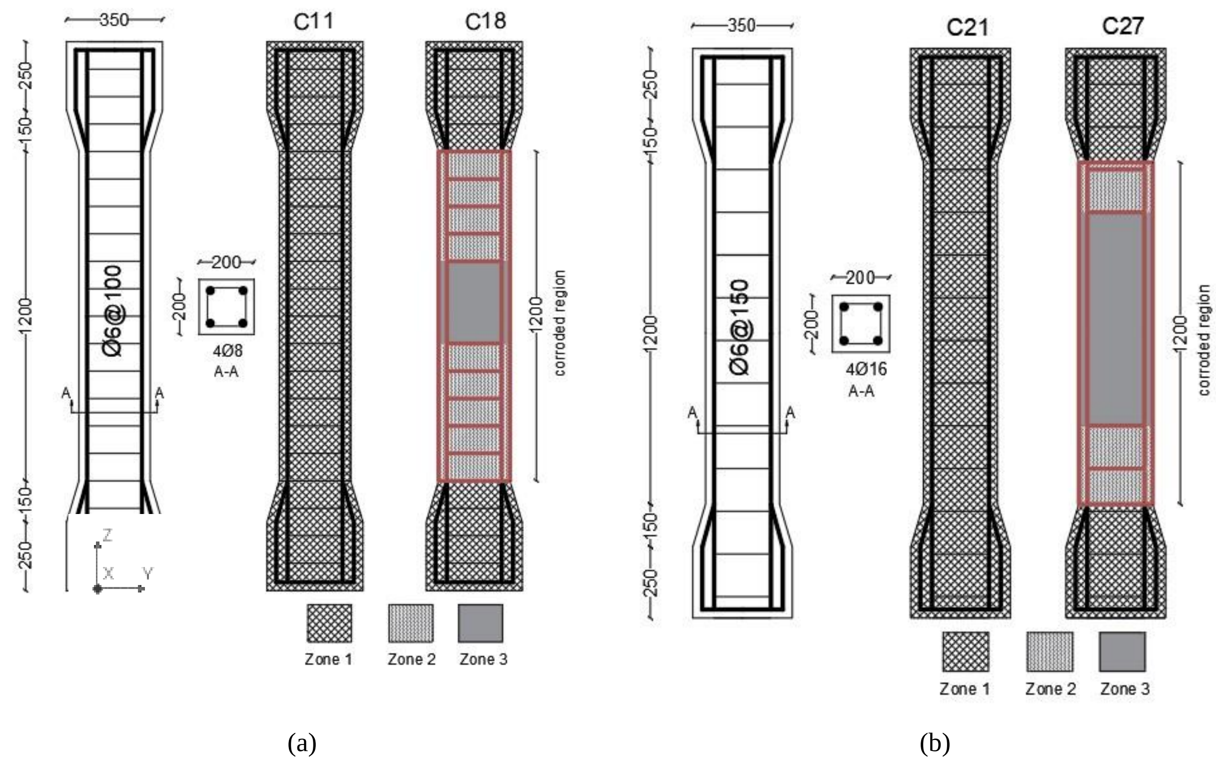

Figure 3-2 Details of RC columns tested by Rodriguez et al. (1996): (a) column type 1, (b) column type 2

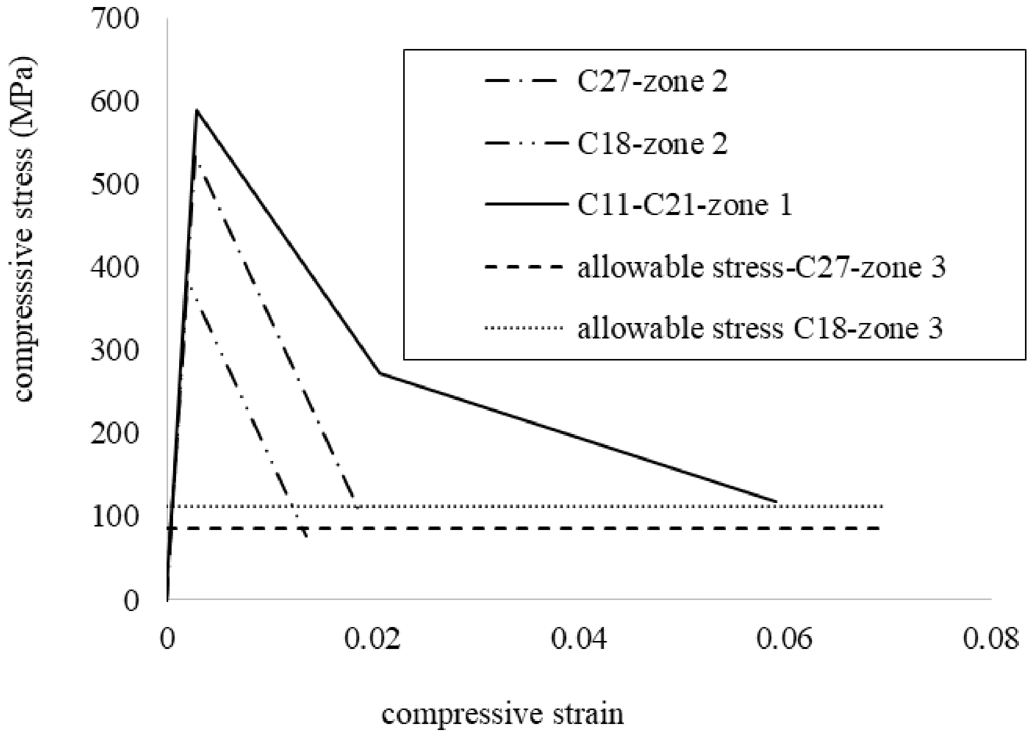

Figure 3-3 Estimated compressive stress-strain response for the rebars in different zones of columns tested by Rodriguez et al. (1996) according to the model adopted from Kashani et al. (2013)

The axial load versus the concrete mean strain at the mid-height section of the four sides of the control and corroded columns (C11, C18, C21, C27) based on the present study and Rodriguez et al. (1996a) is shown in Figure 3-4. Based on the experimental and numerical results, the ultimate capacity of the corroded columns, C18 and C27, drops by approximately 34% and 42%, respectively. As shown in Figure 3-4, methods 1 and 2 used to simulate tie pitting corrosion result in almost similar responses. For the corroded column C18, based on method 1, there is a possibility of premature elastic buckling in the compressive longitudinal reinforcing bars due to the absence of the two middle ties. According to the simulation's results shown in Figure 3-5 (a), the maximum stress in the reinforcement at failure surpassed the corroded rebar critical stress of 113 MPa provided by Eq.3.8. By inspecting the minimum principal stresses and strains, it is observed that the corroded column experiences crushing within the corroded cover region (Figure 3-5, b) and the core concrete in the middle region where ties are removed (Figure 3-5, c). According to the test results, the corroded column's failure was reported as crushing of the concrete and buckling of the longitudinal rebars under the quasi-static loading, which is in a good agreement with the failure characteristics of the column simulated in the present study. Comparing the rebar stress at the failure point of column C27 based on method 1 (Figure 3-5, d) with the corroded rebar critical stress of 86 MPa confirms that the compressive longitudinal reinforcement indeed undergoes elastic buckling. It is also observed that the minimum principal stress and strain within the cover concrete and core concrete (zones 2 and 3) surpass the compressive strength values assigned to these zones. This shows the possibility of concrete crushing within zone 3 where four ties were removed (Figure 3-5, e-f). For the two sets of columns, both the axial capacity-mean strain response and the failure pattern from the experimental tests and the 3D-NLFEA were found to agree within an acceptable range.

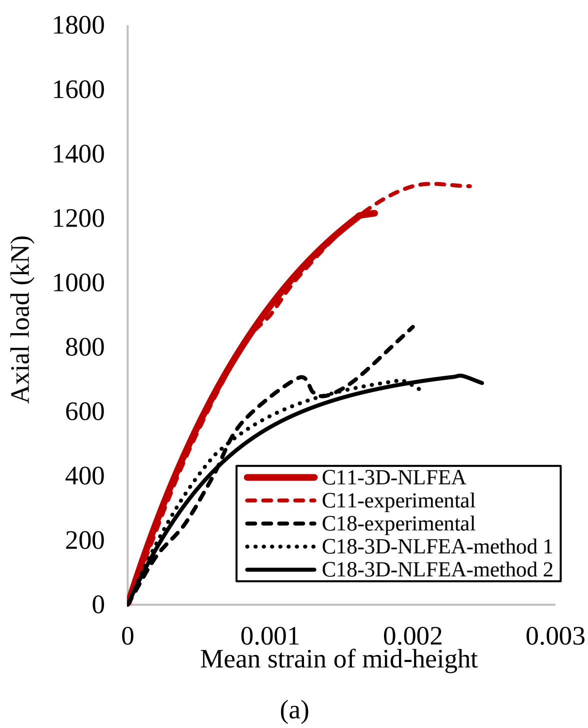

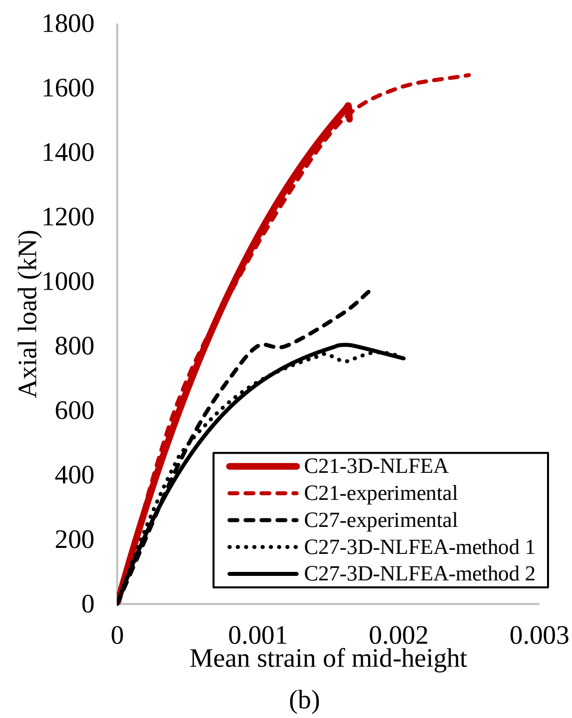

Figure 3-4 (a) Comparison between the results based on experimental test conducted by Rodriguez et al. (1996) and the present 3D-NLFEA for (a) columns C18, C11, and (b) columns C27, C21

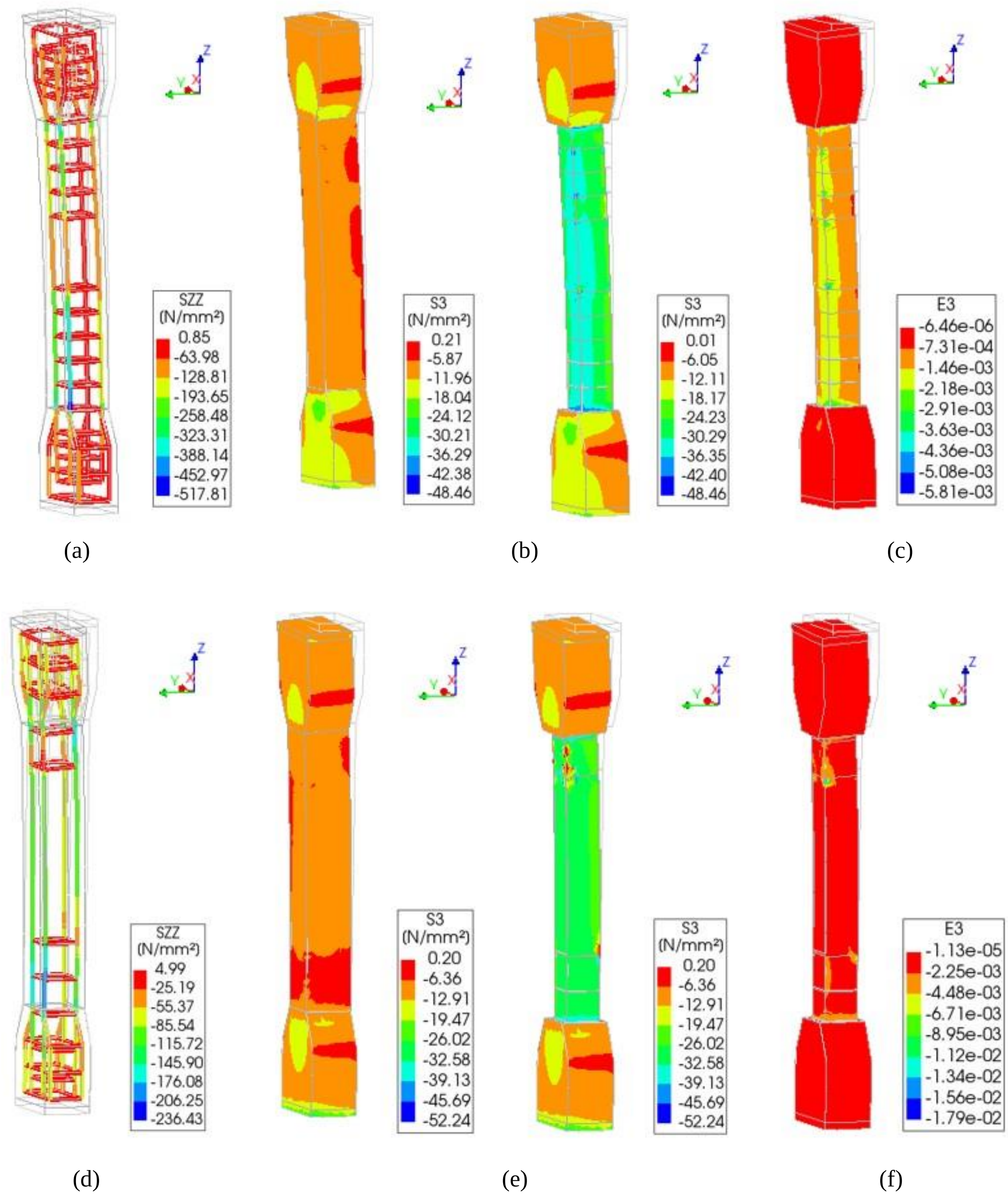

Figure 3-5 Graphical results based on 3D-NLFEA at the failure point of corroded columns tested by Rodriguez et al. (1996) (method 1): (a) stress in reinforcement (C18), (b) minimum principal stress showing the possibility of crushing of concrete cover and core concrete (C18), (c) minimum principal strain showing the possibility of crushing of concrete cover and core concrete (C18), (d) stress in reinforcement (C27), (e) minimum principal stress showing the possibility of crushing of concrete cover and core concrete (C27), (f) minimum principal strain showing the possibility of crushing of concrete cover and core concrete (C27)

3.4 Structural performance of an existing corroded RC bridge pier

3.4.1 Design considerations

The adopted 3D-NLFEA methodology is applied to an RC pier of a two-span slab on a pre-stressed girder bridge with a center-to-center span of 30.81 m. The geometry of the superstructure of the one-span bridge was adopted from the Virginia State Bridge Inventory (Hevener 2003, Nutt et al. 1988). The design follows the CSA-S6-19 (CSA 2019). The main goal was designing the critical RC column of the bents to have the 0.4<LOCR<0.6 under different eccentricities ($0 < e < e_p = 0.15h$), in which e_p is the allowable practical eccentricity and h is defined as a square column cross-section dimension in mm. In design practice, usual LOCR of the piers is as low as 0.3 (CSA 2019), but for architectural reasons it is common to use slender piers with higher LOCR in bridge design. A seven-column bent was selected as the multi-column bent of the aforementioned bridge, as shown in Figure 3-6. The designed pier has a cross-section of 500×500 mm^2, with twenty 20M longitudinal rebars and 10M ties spaced at 50 mm. The cover depth is 40 mm, which is representative of older structures. Further geometric and material details of the designed bridge are provided in Table 3-2.

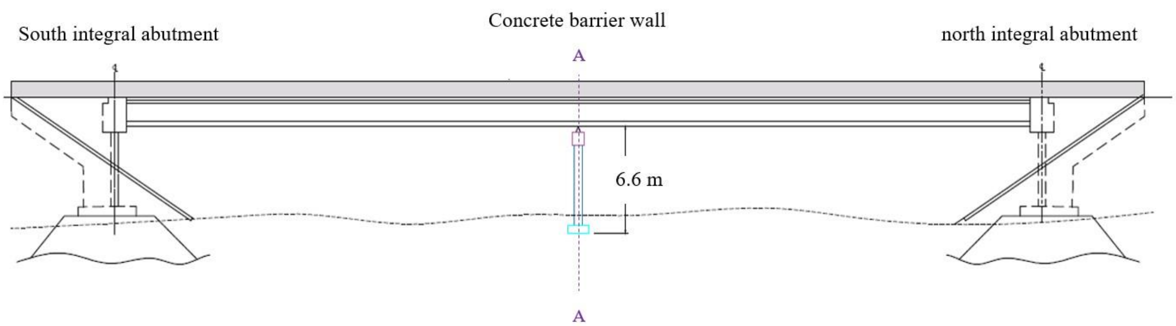

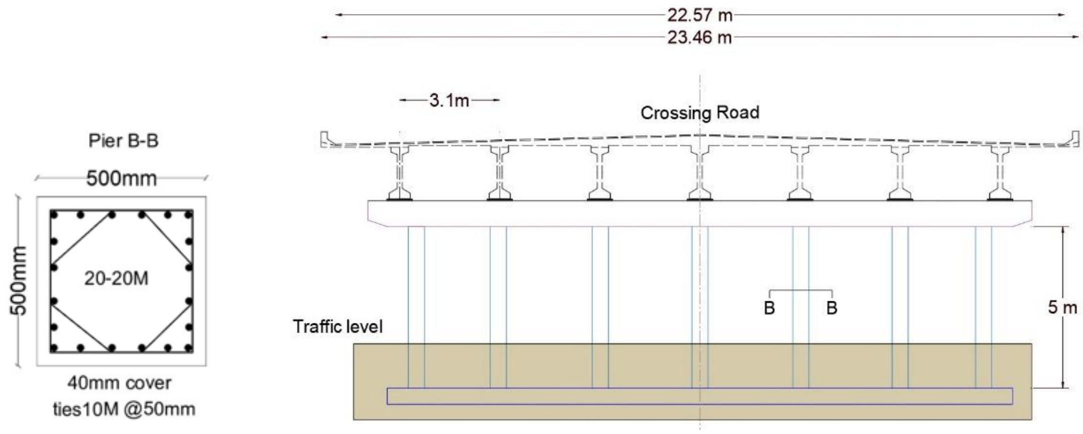

Figure 3-6 Configuration of the designed pier

Table 3-2 General information of designed bridge

Bridge substructure geometry	
Intermediate pier:	Multi-column bent (7-columns spacing at 3.1 m) with speared footings on bedrock
Pier cap size:	1.5 m by 0.8 m cross section
End abutment:	Integral abutment
Bridge substructure material	
Pier cap and pier in-place concrete strength:	$f_c = 35\,MPa$
Concrete elastic modulus:	$E_c = 35000 MPa$ [1]
Concrete cracking strength (normal-density concrete):	$f_{cr} = 0.4\sqrt{f_c^{'}} = 2.37 MPa$ [2]
Yield strength, ultimate strength and strain of rebars[3]	$f_y = 420 MPa,\ f_u = 525\ MPa, \varepsilon_u = 0.14$

[1] Model code 2010, CEB 2013
[2] CSA-S6-19
[3] CSA G30.18 Gr. 40

3.4.2 Proposed corrosion damage scenarios

The deteriorating effects of stage-based corrosion-induced damage on the structural performance of the RC bridge pier under pure compression were investigated using the 3D-NLFEA. To this aim, it was assumed that reinforcement corrosion occurs at the zone of the pier subjected to splashing of de-icing salt contaminated water by moving traffic, as observed in field investigations (Andersen 1997) and on-site observations by the authors, as shown in Figure 3-7. Foundation footings in cold climates are required to be placed below the depth of frost penetration, with a minimum of 1.2 m below ground level (CSA 2019). Considering the traffic level with respect to the foundation of the column, it was assumed the splash zone corresponded to approximately the middle third of the column. Following the adopted methodology, corrosion was assumed to degrade the material properties. It should be pointed out that the corrosion-induced mass loss percentage of the ties at each stage of damage was assumed to be twice the one associated with the longitudinal reinforcing bars in the present study. Such assumption was made based on the fact that: (i) the ties are closer to the cover concrete and ambient environment, with aggressive agents such as chlorides, CO_2 and water reaching the ties faster; and (ii) the tie diameter is smaller compared to the longitudinal reinforcement diameter.

(a) Toronto Gardiner Expressway

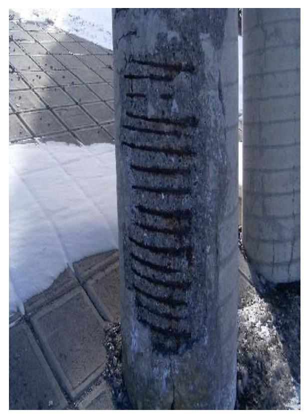

(b) Underpass in Bells Corners, Ottawa

Figure 3-7 Corroded bridge piers (on-site observations by the Authors)

Three different stages of corrosion were defined: longitudinal rebar mass loss of 5% and tie mass loss of 10% (Stage 1), longitudinal rebar mass loss of 20% and tie mass loss of 40% (Stage 2), and longitudinal rebar mass loss of 30% and tie mass loss of 60% (Stage 3). It should be noted that at each stage, different assumptions were made, summarized in Table 3-4.

At Stage 2, in addition to corrosion-induced material properties degradation, it was assumed that the fully-rigid connection between the ties and the two middle longitudinal rebars at each side of the column in the corroded region (mid-third of column) was lost. At Stages 1 and 2, the degraded confinement effect was incorporated into the model by reducing the yield strength and diameter of the ties at each stage of corrosion. At Stage 3, it was assumed that the material properties degrade due to corrosion and all the ties and longitudinal rebars at the corroded region lose their connection. Due to major damage in the concrete cover at this stage, it was assumed that the cover all around the column along the corroded region had spalled off. As a result, the concrete core region and ties were supposed to be more exposed to the ambient environment and more susceptible to damage.

An analytical investigation was conducted to determine the tie strain considering the bridge pier for design LOCR. As a result of corrosion, the tie leg segment between two adjacent longitudinal rebars was assumed as a pin-pin beam (loss of connection rigidity). The axial tie strain due to axial load-induced lateral pressure in the RC bridge pier was estimated as the bending-induced change in the projected length of the assumed beam. For both cases, the axial strain ε_t was estimated according to Eq.3.13 (Young and Budynas 1980) .

$$\varepsilon_t = \frac{\Delta l}{l} = \frac{1}{2l}\int_0^l \left(\frac{dy}{dx}\right)^2 dx \qquad 3.13$$

where l is the length of the tie leg between two adjacent longitudinal rebars (i.e., l = 75.6 mm), and y is the bending-induced deflection.

By substituting the deflection functions $y(x)$ into Eq.3.13, the tie strain was estimated and compared to the corroded tie strain corresponding to Stage 2 and Stage 3, as tabulated in Table 3-3. It is observed that at Stage 3, the strain along the entire length of the tie beam exceeds the yield limit, so tie rupture is a reasonable assumption at this stage.

Moreover, there is a high likelihood of pitting corrosion at this stage, leading to more severe damage, and it can thus be assumed that three adjacent ties have broken. As depicted in Figure 3-8, all the regions are shown as zone 1 in the case of the uncorroded column. At Stages 1 and 2, the uncorroded and corroded regions are shown as zone 1 and zone 2, respectively. At Stage 3, three damage zones are defined: zone 1 as the uncorroded region, zone 2 as the corroded region where there are not any broken ties, and a 200-mm zone 3 where three ties are ruptured. At "Stage 3", the degraded confinement effect was incorporated into the model by reducing the yield strength and diameter of the ties, increasing the tie spacing within zone 3, and reduction in compressive strength due to corrosion-induced cracking. To study the effect of the latter factor, the in-place compressive strength of concrete used in the confinement model was reduced from 35 MPa to 33MPa, 30 MPa, 28 MPa, 25 MPa, and 20 MPa and substituted in the confinement model, corresponding to damage scenarios in the present study called "Stage 3,a", "Stage 3,b", "Stage 3,c", "Stage 3,d", and "Stage 3,e", respectively. The compressive strength of the cover and core concrete at each stage and each zone are tabulated in Table 3-5. The compressive stress-strain response of confined concrete at different stages of corrosion is estimated according to the confinement model by Saatcioglu and Razvi (1992) and shown in Figure 3-10.

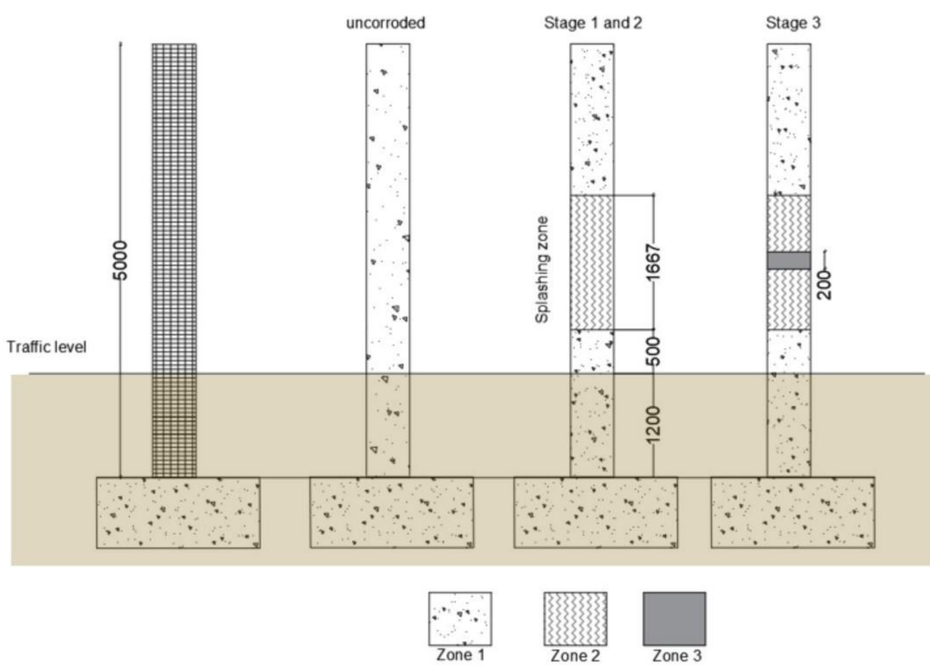

Figure 3-8 Configuration of designed RC pier at each damage state (all the dimensions are in mm)

The un-corroded reinforcing steel compressive behaviour was modelled using the average monotonic stress-strain model proposed by Dhakal and Maekawa (2002), as illustrated in Figure 3-9. For all the damage stages considered, from an uncorroded column to a corroded column at Stage 3, the estimated Euler critical strength is higher than the yield strength of the reinforcement due to sufficient lateral confinement and a small effective length (i.e., the tie spacing-to- rebar diameter ratio s/d_b), with no possibility of elastic buckling in any of the cases considered. Failure of the reinforcement was therefore assumed to be governed by yielding the reinforcing steel, followed by a softening response in the corroded columns. As shown in Figure 3-9, a steep softening post-yield response was estimated for the corroded rebars located in zone 3 at Stage 3. Note that for this analysis, uniform corrosion was assumed. Finally, the bond model developed by Blomfors et al. (2018) was adopted for the corroded RC columns.

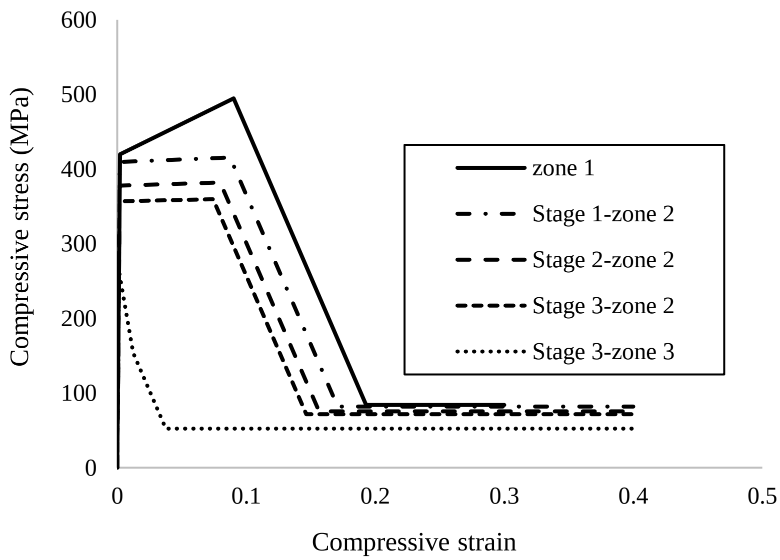

Figure 3-9 Compressive stress-strain response of longitudinal rebars in different stages of corrosion

Table 3-3 Analytical axial tie strain due to axial-load induced lateral pressure in the RC bridge pier

Stage	Initial tie diameter (mm)	Area loss rebar	Area loss tie	Corroded tie diameter (mm)	Corroded tie yield strain	Corroded tie yield stress (MPa)	ε_t
Stage 3	11.3	0.3	0.6	7.14	0.00084	168	0.012

Table 3-4 Summary of assumptions made in different stages of corrosion in the present study

<table>
<tr><td>Stage 1</td><td colspan="3">• Longitudinal rebar mass loss of 5%
• Tie mass loss of 10%
• Material properties degradation as described in corrosion damage model section
• In-place compressive strength of 35 MPa in the confinement model (=35MPa)</td></tr>
<tr><td>Stage 2</td><td colspan="3">• Longitudinal rebar mass loss of 20%
• Tie mass loss of 40%
• Material properties degradation as described in corrosion damage model section
• Loss of fully-rigid connection between the ties and two middle longitudinal rebars at each side of column within the corroded zone
• In-place compressive strength of 35 MPa in the confinement model (f_c =35MPa)</td></tr>
<tr><td rowspan="6">Stage 3</td><td rowspan="6">• Longitudinal rebar mass loss of 30%
• Tie mass loss of 60%
• Material properties degradation as described in corrosion damage model section
• Loss of fully-rigid connection between all the ties and longitudinal rebars at each side of the column within the corroded zone
• Rupture of three adjacent ties at the middle height of the RC column</td><td colspan="2">f_c
used in the confinement model</td></tr>
<tr><td>Stage 3,a</td><td>33(MPa)</td></tr>
<tr><td>Stage 3,b</td><td>30(MPa)</td></tr>
<tr><td>Stage 3,c</td><td>28(MPa)</td></tr>
<tr><td>Stage 3,d</td><td>25(MPa)</td></tr>
<tr><td>Stage 3,e</td><td>20(MPa)</td></tr>
</table>

Table 3-5 Properties of concrete at each stage of corrosion

Corrosion stages	Longitudinal rebar X_{corr}	Tie X_{corr}	Concrete compressive strength (MPa)					
			Zone 1		Zone 2		Zone 3	
			cover	core	cover	core	cover	core
uncorroded	NA	NA	35	56.2	NA	NA	NA	NA
Stage 1	5%	10%	35	56.2	9	52.8	NA	NA
Stage 2	20%	40%	35	56.2	negligible	44.0	negligible	NA
Stage 3,a	30%	60%	35	56.2	negligible	37.6	negligible	33.8
Stage 3,b	30%	60%	35	56.2	negligible	34.6	negligible	30.8
Stage 3,c	30%	60%	35	56.2	negligible	32.6	negligible	28.8
Stage 3,d	30%	60%	35	56.2	negligible	29.6	negligible	25.8
Stage 3,e	30%	60%	35	56.2	negligible	24.6	negligible	20.8

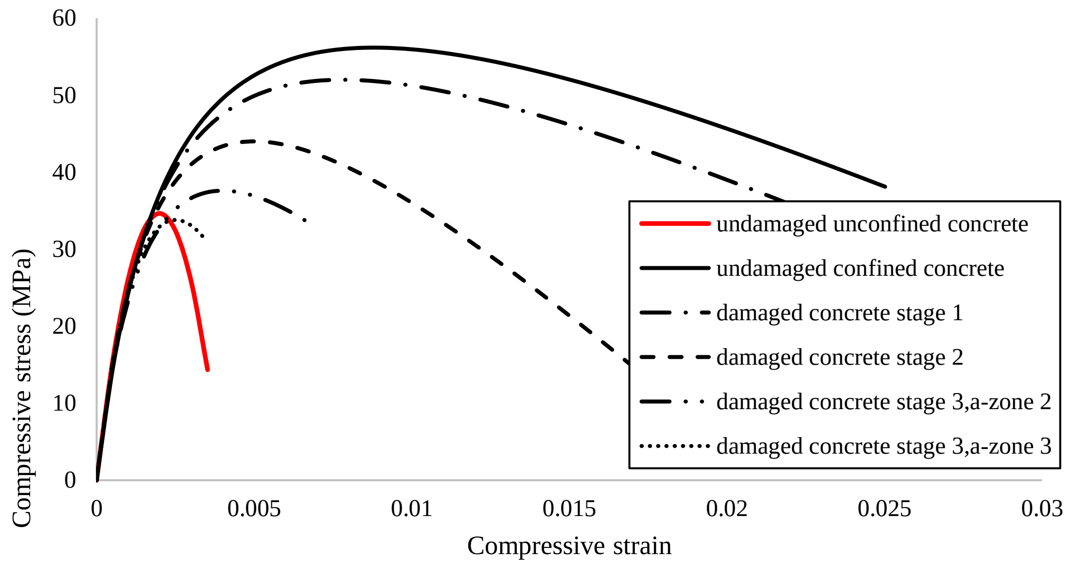

3-10 Compression stress-strain model for confined concrete at different stages of corrosion (confinement model by Saatcioglu and Razvi 1992)

3.4.3 Numerical procedure and discussion of results

In the present simulation of the corroded RC bridge pier, the pre-defined tension softening "Hordjik" is adopted as the concrete tensile response, and the compression curves "fib 2010" and "Thorenfeldt" with a more brittle post-peak, according to the recommendation by Coronelli and Gambarova (2004) are adopted as the compressive response of undamaged and damaged concrete, respectively (Figure 3-11).

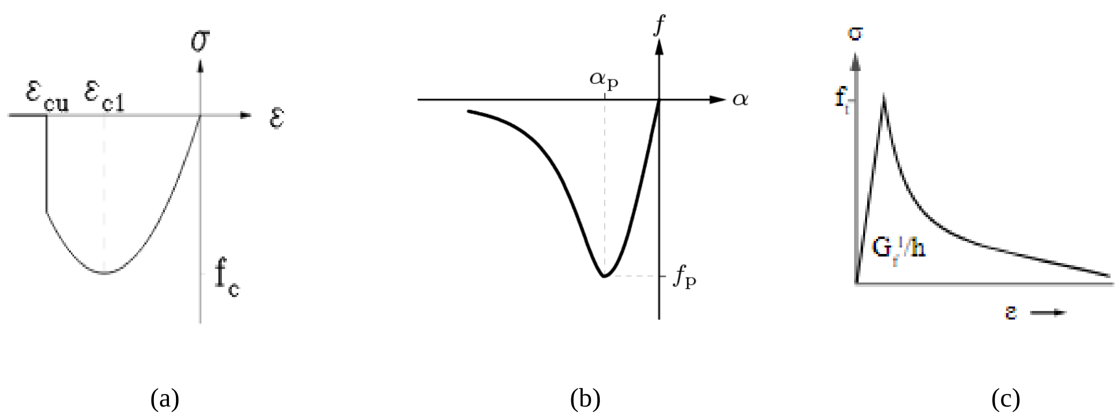

Figure 3-11 Concrete constitutive models: (a) compression-undamaged "fib 2010", (b) compression-damaged "Thorenfeldt" , (c) tension "Hordjik"

Meshes based on 20×20 mm, 40×40 mm, 50×50 mm, and 60×60 mm elements were investigated. The solution based on a 50×50–mm mesh was selected. The solution based on smaller mesh size was very time and memory consuming, and the solution based on the larger mesh size was not able to show the failure and cracking pattern at the specific locations.

All the nodes of the base were restrained from all the translational movement to simulate the full fixity condition of the foundation. The column was also restrained at the top against translational movements in the bent direction due to the bent-induced stiffness. To avoid any local stress concentration, the two faces of the column in the "xz" plane (with total depth of 250 mm from the top) were restrained against the translational movement in the y-direction. The translational movement in the traffic direction was free (Figure 3-12, a). A quasi-static concentric loading was applied as uniform stress (Figure 3-12, c).

A structural nonlinear analysis assuming both physical and geometrical nonlinearity was performed in the present modelling. A regular Newton-Raphson iterative method was used along with the "Total Lagrange" as the geometrical nonlinear analysis. A force-control together with the arc-length control option was used to control the post-peak behaviour in the column. In addition to the arc-length control method, the line search control method was activated in order to improve the solution convergence.

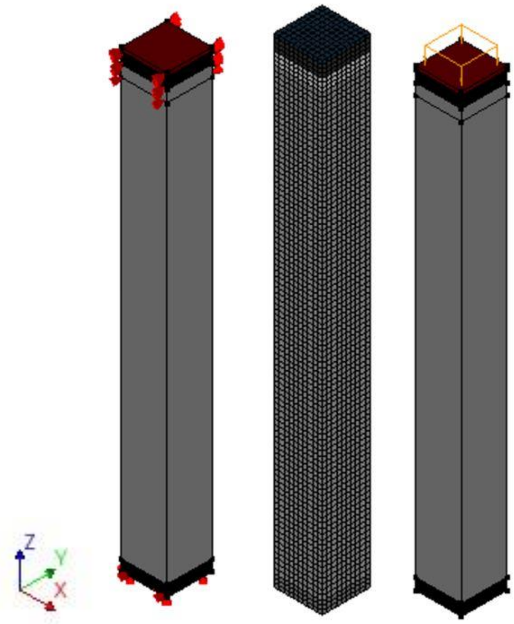

Figure 3-12 Designed bridge pier (a) boundary conditions, (b) concrete section mesh, (c) uniform stress as concentric loading

The load-maximum vertical displacement curves of the uncorroded and corroded columns at different stages of damage are shown in Figure 3-13. It is observed that by increasing the level of corrosion (going from Stage 1 to Stage 3,e), the ultimate capacity of the RC bridge column decreases by 9%, 33%, 36%, 40%, 43%, 47%, and 56%, respectively.

At the early stages of corrosion (Stage 1), it is observed that the ultimate capacity of the column decreases by 9% without a significant drop in the axial displacement. As corrosion propagates to significant levels in Stage 2, deterioration of the rebars and the cover and core concrete occur, with consequent loss of fully-rigid connection between the ties and two middle longitudinal rebars at each side of the column. All these effects lead to a more significant reduction in the ultimate capacity (33% as shown in Figure 3-13). For a LOCR=0.6, the RC column at Stage 3, b is observed to lose almost 40% of the initial ultimate capacity, and it fails under the applied load of 6,200 kN (60% of ultimate capacity). Stage 3 (b) can be suggested as a warning threshold and should be seriously avoided by periodic inspection and non-destructive testing to measure the degree of cracking and concrete compressive strength. As shown in Figure 3-14(a) and (b) for the uncorroded column under pure concentric axial load, comparing the minimum principal cover concrete stress S_3 and minimum principal strain with the concrete compressive strength f'_c = 35 MPa and strain at maximum stress reveals that crushing of concrete starts at the ultimate load. As shown in Figure 3-14 (c), the longitudinal rebars reach almost 81% of the proportional limit at the ultimate capacity, and no yielding nor buckling is observed, showing compression failure in the column.

Corrosion-induced damage increases drastically for longer periods of exposure of the middle-third zone of the column to deteriorating environmental factors, and assuming no periodic inspection, effective maintenance and repair interventions (Stage 3). As shown in Figure 3-13, by decreasing the in-place concrete compressive strength from 33 MPa to 20 MPa, the ultimate capacity is observed to drop from 36% to 56%. The graphical failure patterns based on the 3D-NLFEA at "Stage 3,b" and Stage 3,e (worst-case scenario) are presented in Figure 3-15 and Figure 3-16, respectively. For the corroded column at "Stage 3, b", it is observed that at the onset of ultimate capacity and failure point, the damage is more localized at the mid-region (corroded zone). It should be pointed out that even after losing three ties at 'Stage 3" and increasing the slenderness ratio of the longitudinal reinforcing bars in this region, there is no possibility of elastic buckling of corroded rebars according to the modified critical strength of corroded rebars formula proposed by Rodriguez et al. (1996a); however, inelastic buckling of the longitudinal reinforcing bars results in a post-peak softening behaviour in the stress-strain response of the corroded rebars due to the increase in the slenderness ratio in zone 3 (Kashani et al. 2015) . At "Stage 3, b", it is observed that at the onset of ultimate capacity, the minimum principal stress and strain of the core concrete reach almost ultimate capacity, which corresponds to the uniaxial compressive strength that is softened due to corrosion effects, and they exceed the threshold at the failure point (Figure 3-15, a-d), indicating crushing of the core concrete. Comparing the compressive Cauchy stress in the rebars at the onset of ultimate and failure point with the compressive stress-strain response of the corroded rebars defined at different zones, it is observed that the reinforcing steel in zones 2 and 3 reach the yielding point followed by inelastic buckling of the longitudinal reinforcing bars in zone 3 (Figure 3-15, e and f). This phenomenon can be explained by the fact that confinement effects are reduced at the middle-height of the corroded column, and there is a high chance of buckling of the longitudinal reinforcing bars and crushing of the concrete. As shown in (Figure 3-16, a-f), a similar failure mode is observed at "Stage 3,e" with a more severe pattern. The failure of the corroded column is governed by the crushing of the concrete core at the middle region and the inelastic buckling of the corroded rebar in zone 3.

Based on a regression analysis, two prediction equations of the ultimate axial displacement and ultimate capacity of the corroded column at different scenarios of Stage 3 as a function of the reduced in-place concrete compressive strength which is used in the confinement model, are proposed in Eqs.3.14 and 3.15 (Figure 3-17). It is worth noting that the proposed equations are specifically for the geometry and properties of the designed pier. The methodology can be used for any other geometry to propose a specific prediction equation.

$$D_{zu} = 0.0973 f_c + 2.3453 \tag{3.14}$$

$$P_u = 153.82 f_c + 1575.5 \tag{3.15}$$

in which D_{zu} is the ultimate axial displacement of the corroded column at Stage 3, P_u is the ultimate axial capacity of the corroded column at Stage 3.

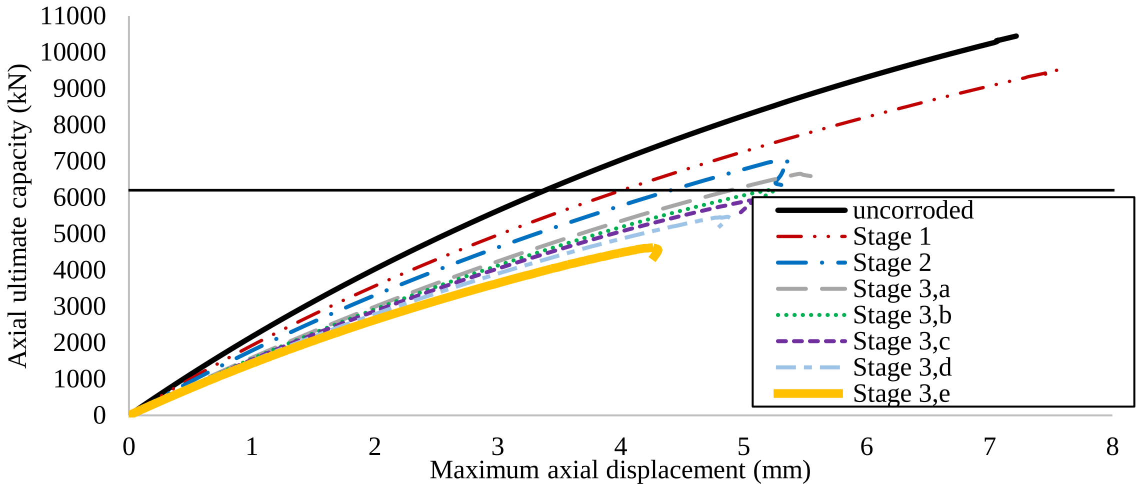

Figure 3-13 Load-maximum axial displacement of control and corroded RC bridge pier

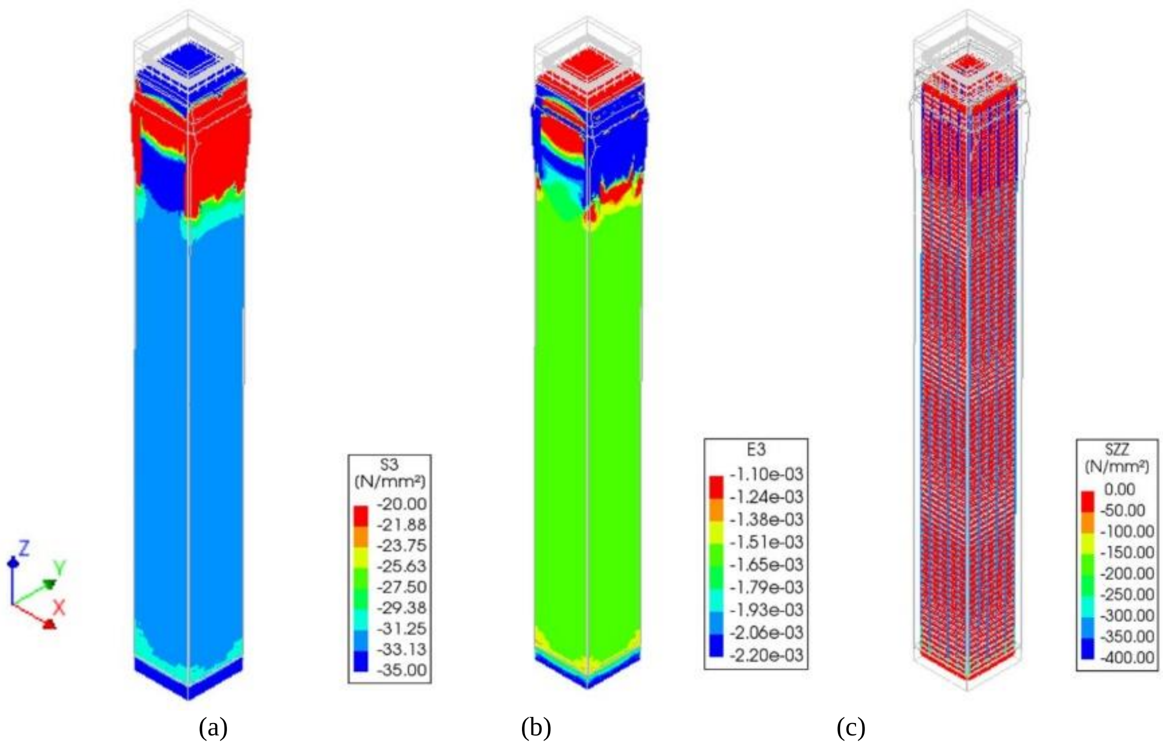

Figure 3-14Failure patterns of control pier: (a) minimum principal stress distribution at ultimate capacity of uncorroded column, (b) minimum principal strain distribution at ultimate capacity of uncorroded column (c) reinforcement Cauchy total stress distribution in z direction at ultimate capacity of uncorroded column

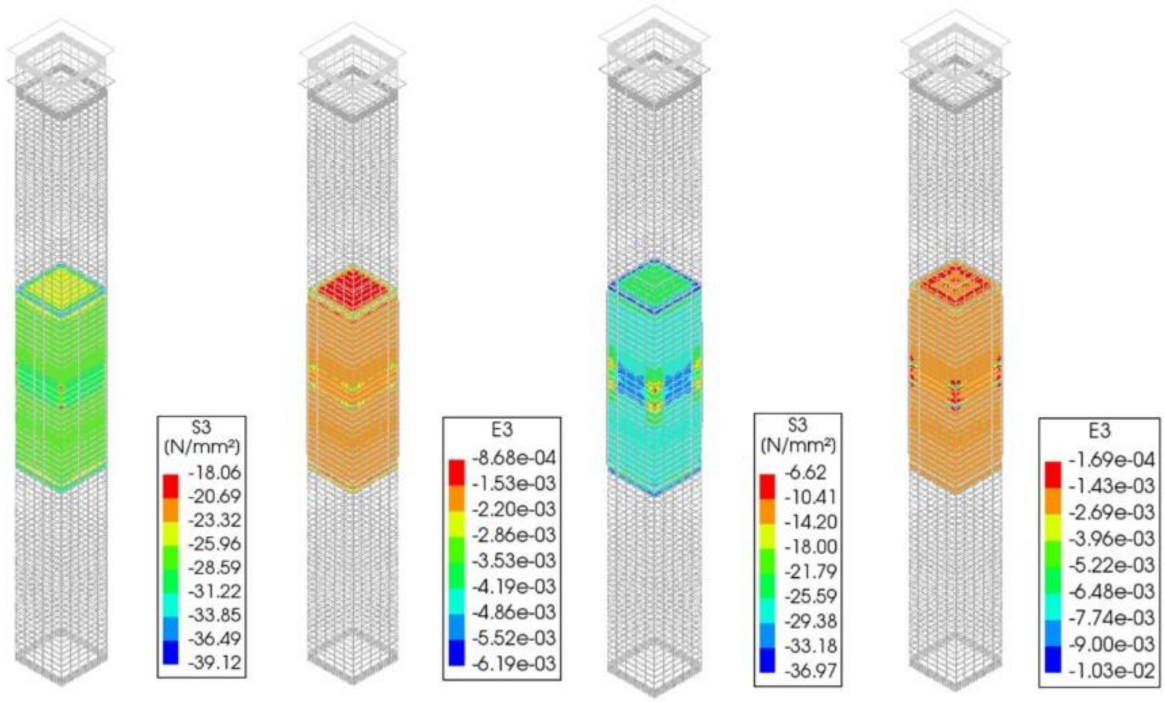

(a) (b) (c) (d)

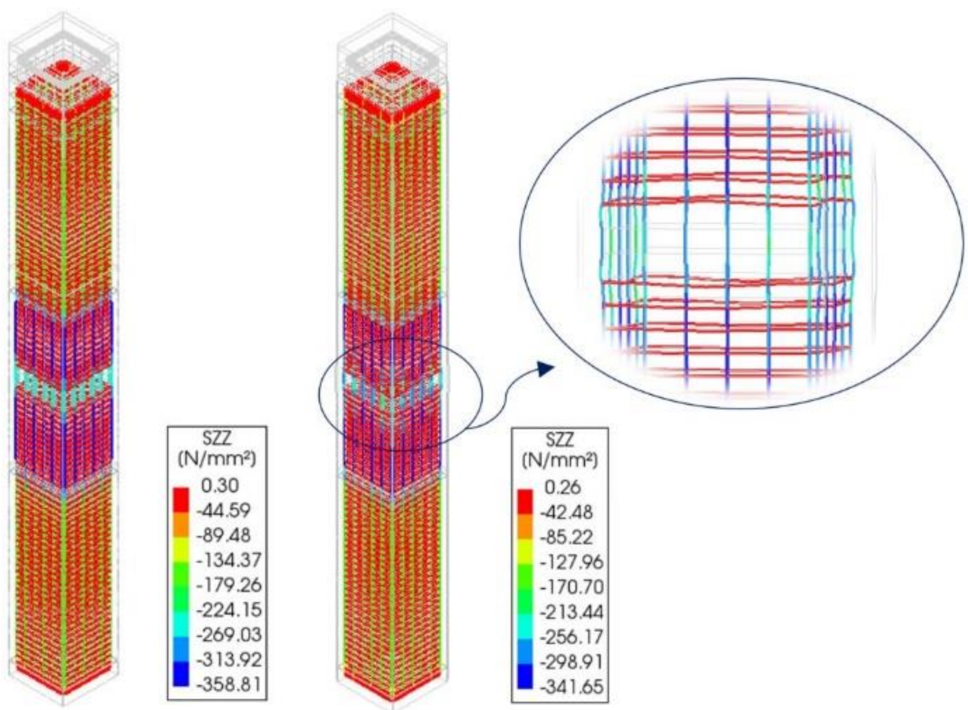

(e) (f)

Figure 3-15 "Stage 3,b", (a) minimum principal stress distribution at onset of ultimate capacity of RC pier (b) minimum principal strain distribution at the onset of ultimate capacity of RC pier (c) minimum principal stress distribution at failure point of RC pier (d) minimum principal strain distribution at failure point of RC pier, (e) reinforcement Cauchy total stress distribution in the z-direction at the onset of ultimate capacity of RC pier, (f) reinforcement Cauchy total stress distribution in the z-direction at failure point of RC pier

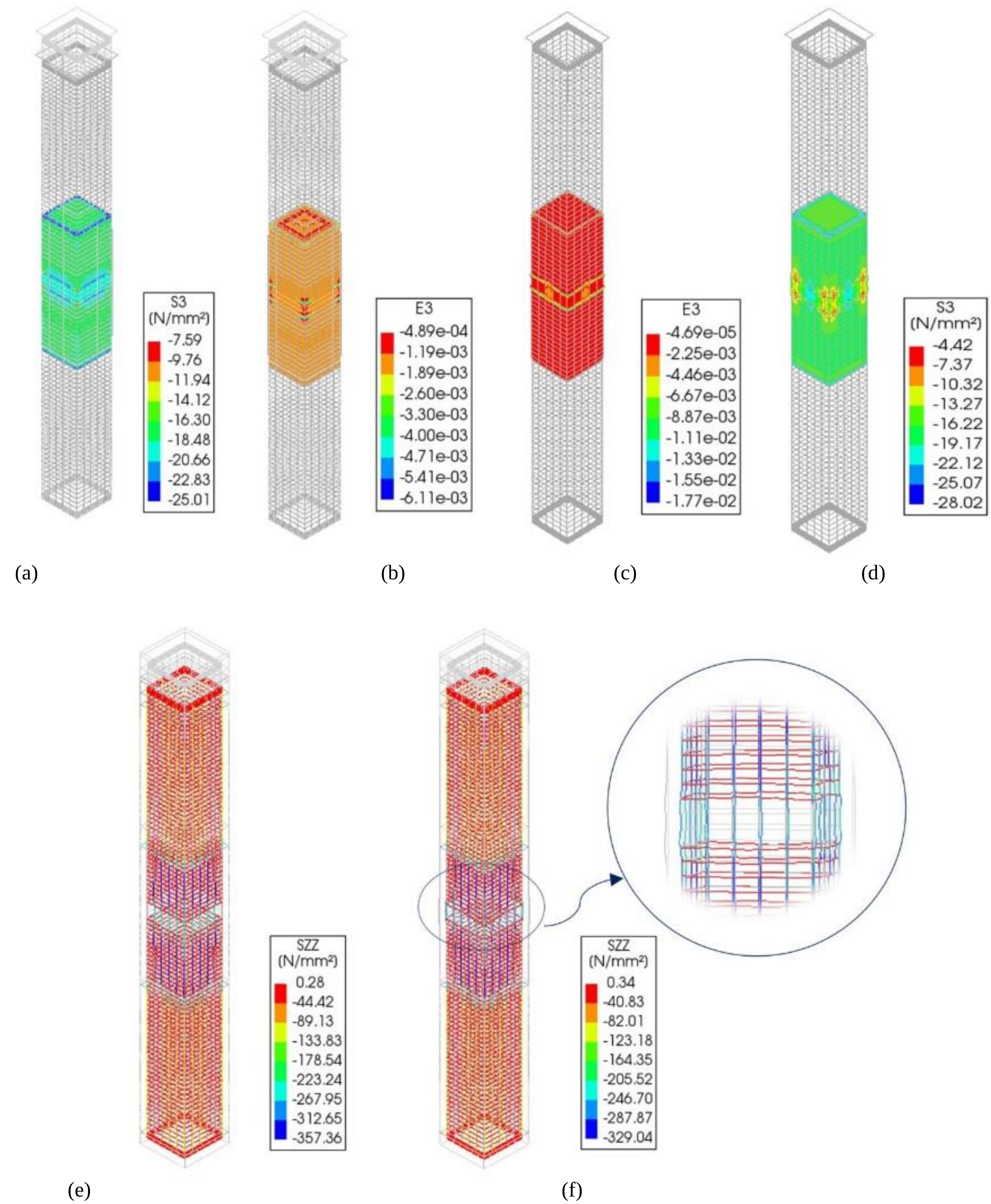

Figure 3-16 "Stage 3,e" (a) minimum principal stress distribution at the onset of ultimate capacity of RC pier (b) minimum principal strain distribution at the onset of ultimate capacity of the pier (c) minimum principal stress distribution at failure point of RC pier (d) minimum principal strain distribution at failure point of the pier, (e) reinforcement Cauchy total stress distribution in the z-direction at the onset of ultimate capacity of RC pier, (f) reinforcement Cauchy total stress distribution in the z-direction at failure point of RC pier

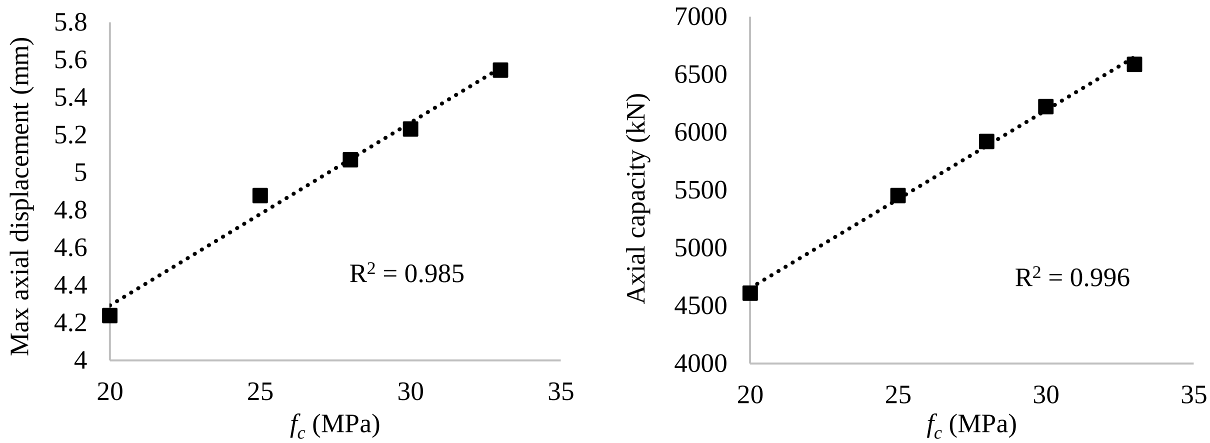

(a) (b)

Figure 3-17 Analytical relationships between in-place concrete strength and (a) maximum axial displacement, and (b) axial capacity of the corroded RC pier at Stage 3

3.5 Summary and conclusions

In the present study, a 3D-NLFEA was conducted to evaluate the structural performance of corroded RC columns subjected to different corrosion patterns and concentric axial loading up to failure. The efficiency of the conducted 3D-NLFEA was verified by simulating previously tested corroded columns reported in the literature. The present numerical model is also capable of successfully capturing the failure modes of the corroded columns, yielding/buckling of the reinforcement or crushing of concrete cover/core for different considered damage cases. The proposed 3D-NLFEA was then adopted to study the structural performance of a real-scale ageing bridge pier at various stages of corrosion localized at the middle third (splash zone) of the column under concentric axial load. The proposed stage-based quantitative approach was conducted based on various damage scenarios to evaluate the pier's performance at different service times. The proposed evaluation approach starts with low levels of corrosion damage (Stage 1), which propagates to higher levels as Stages 2 and, assuming no periodic inspection/maintenance and repair in between. The structural performance degradation was observed to be more pronounced under higher corrosion levels (Stages 2 and 3), with a loss of ultimate capacity of up to 60%, than at lower corrosion levels (Stage 1), with a reduction of 9% in ultimate capacity. At the stages with higher-level of corrosion, in addition to the deteriorating effects on the material properties, it was assumed that corrosion would result in the loss of fully-rigid connection between the ties and longitudinal rebars and would enable rotation at the connection locations. According to the proposed analytical approach, it was also suggested that at higher levels of corrosion, there would be a possibility of one or more tie ruptures in the corroded zones. At Stage 3, the core concrete is more exposed to the deteriorating agents and more susceptible to damage when it is assumed that the concrete cover has spalled off all around the column in the corroded regions. It was observed that by reducing the in-place compressive strength of concrete at Stage 3 to account for corrosion-induced cracking, the confinement effects decrease significantly, and the ultimate capacity was observed to be remarkably sensitive to such parameter. Considering a loss of three ties in zone 3 and increasing the effective length of the longitudinal reinforcing bars, it was estimated that the compressive stress-strain response of the rebars degrades (decreasing the compressive yield strength and softening the post-yield response). By going from low to higher levels of corrosion, the column fails in a more brittle pattern. The failure is observed to be more localized in the corroded zones and is governed by yielding of the longitudinal reinforcing bars in zone 2 and 3, and crushing of the core concrete in zone 3 followed by inelastic buckling of the longitudinal reinforcing bars in zone 3. According to the proposed evaluation approach, it is found that corrosion-induced cracking and spalling of the concrete cover and premature buckling of the longitudinal rebars due to tie rupture are the most relevant consequences of corrosion-induced damage with the most significant impact on the ultimate capacity of the corroded columns. The proposed performance-based quantitative approach shows the importance of periodic inspection and monitoring of changes in the characteristics of partially-damaged critical bridge piers.

3.6 References

Almusallam, A. A. 2001. "Effect of degree of corrosion on the properties of reinforcing steel bars." Construction and Building Materials., 15 (8): 361–368. https://doi.org/10.1016/S0950-0618(01)00009-5.

Andersen, A. 1997. HETEK, Investigation of chloride penetration into bridge columns exposed to de-icing salt-report No.82. Danish Road Directorate, Copenhagen,37pp.

Blomfors, M., K. Zandi, K. Lundgren, and D. Coronelli. 2018. "Engineering bond model for corroded reinforcement." Engineering Structures, 156: 394–410. https://doi.org/10.1016/j.engstruct.2017.11.030.

Cairns, J., G. Plizzari, Y. Du, D. Law, and C. Franzoni. 2005. "Mechanical properties of corrosion-damaged reinforcement." ACI Materials Journal, 102 (4): 256–264.

Di Carlo, F., A. Meda, and Z. Rinaldi. 2017. "Numerical evaluation of the corrosion influence on the cyclic behaviour of RC columns." Engineering Structures, 153: 264–278. Elsevier. https://doi.org/10.1016/j.engstruct.2017.10.020.

Castel, A., R. François, and G. Arliguie. 2000. "Mechanical behaviour of corroded reinforced concrete beams - Part 1: experimental study of corroded beams." Materials and Structures, 33: 539–544. https://doi.org/10.1007/bf02480533.

Coronelli, D., and P. Gambarova. 2004. "Structural assessment of corroded reinforced concrete beams: Modeling guidelines." Journal of Structural Engineering, 130 (8): 1214–1224. https://doi.org/10.1061/(ASCE)0733-9445(2004)130:8(1214).

CSA (2019) "CSA S6:19 Canadian Highway Bridge Design Code, CSA Group, Toronto." CSA Group, Toronto, Ontario.

Deng, P., C. Zhang, S. Pei, and Z. Jin. 2018. "Modeling the impact of corrosion on seismic performance of multi-span simply-supported bridges." Construction and Building Materials, 185: 193–205. Elsevier Ltd. https://doi.org/10.1016/j.conbuildmat.2018.07.015.

Dhakal, R. P., and K. Maekawa. 2002. "Modeling for postyield buckling of reinforcement.", Journal of Structural Engineering, 128 (9): 1139–1147. https://doi.org/10.1061/(ASCE)0733-9445(2002)128.

Diana. 2019. "DIANA Finite Element Analysis, User's Manual, Release 10." TNO Building and Construction Research, Delft, Netherlands.

Du, Y. G., L. A. Clark, and A. H. C. Chan. "Residual capacity of corroded reinforcing bars." Magazine of Concrete Research, 57 (3): 135–147. https://doi.org/10.1680/macr.2005.57.3.135.

Fib. 2013. fib Model Code for concrete structures 2010. Lausanne, Switzerland.

Hanjari, K. Z., P. Kettil, and K. Lundgren. 2011. "Analysis of mechanical behavior of corroded reinforced concrete structures." ACI Structural Journal, 108: 532–541. https://doi.org/10.14359/51683210.

Hevener, W. 2003. "Simplified live-load moment distribution factors for simple span slab on I-girder bridges. MSc. Thesis, Dept. Civil and Environmental Engineering, University of West

Virginia, Morgantown,West Virginia,USA.” MSc. Thesis, Dept. Civil and Environmental Engineering, University of West Virginia, Morgantown, West Virginia, USA.

Kashani, M. M., A. J. Crewe, and N. A. Alexander. 2013. “Nonlinear stress-strain behaviour of corrosion-damaged reinforcing bars including inelastic buckling.” Engineering Structures, 48: 417–429. https://doi.org/10.1016/j.engstruct.2012.09.034.

Kashani, M. M., A. J. Crewe, and N. A. Alexander. 2017. “Structural capacity assessment of corroded RC bridge piers.” Proceedings of the Institution of Civil Engineers -Bridge Engineering, 170 (1): 28–41. https://doi.org/10.1680/jbren.15.00023.

Kashani, M. M., L. N. Lowes, A. J. Crewe, and N. A. Alexander. 2015. “Phenomenological hysteretic model for corroded reinforcing bars including inelastic buckling and low-cycle fatigue degradation.” Computers and Structures, 156: 58–71. Elsevier Ltd. https://doi.org/10.1016/j.compstruc.2015.04.005.

Lu, C., W. Jin, and R. Liu. 2011. “Reinforcement corrosion-induced cover cracking and its time prediction for reinforced concrete structures.”, Corrosion Science, 53: 1337–1347. Elsevier Ltd. https://doi.org/10.1016/j.corsci.2010.12.026.

Lundgren, K. 2002. “Modelling the effect of corrosion on bond in reinforced concrete.”, Magazine of Concrete Research, 54 (3): 165–173. https://doi.org/10.1680/macr.54.3.165.38798.

Lundgren, K., P. Kettil, K. Z. Hanjari, H. Schlune, and A. S. S. Roman. 2012. “Analytical model for the bond-slip behaviour of corroded ribbed reinforcement.” Structure and Infrastructure Engineering, 8 (2): 157–169. https://doi.org/10.1080/15732470903446993.

Mohammed, A. M. 2014. “Semi-Quantitative Assessment Framework for Corrosion Damaged Slab-on-Girder Bridge Columns Using Simplified Nonlinear Finite Element Analysis, Ph.D. Thesis.” University of Ottawa,.

Molina, F. J., C. Alonso, and C. Andrade. 1993. “Cover cracking as a function of rebar corrosion : Part 2—Numerical model.” Materials and Structures, 26, 532–548.

Nutt, R. V., Schamber, R.A, and T. Zokaie. 1988. “Distribution of Wheel Loads on Highway Bridges.” Final Report. National Cooperative Highway Research Program Report.

Rodriguez, J., L. M. Ortega, and J. Casal. 1996. “Load bearing capacity of concrete columns with corroded reinforcement.” Corrosion Of Reinforcement In Concrete Construction. Proceedings of Fourth International Symposium, Cambridge, 1-4 July 1996. Special publication no 183, 220–230.

Saatcioglu, M., and S. R. Razvi. 1992. “Strength and ductility of confined concrete.” Journal of Structural Engineering, 118 (6): 1590–1607. https://doi.org/10.1061/(ASCE)0733-9445(1993)119:10(3109).

Saito, Y., M. Oyado, A. Yasojima, T. Kanakubo, and Y. Yamamoto. 2007. “Structural Performance of Corroded RC Column under Uniaxial Compression Load.” First International Workshop on Performance, Protection & Strengthening of Structures under Extreme Loading, Whistler, Canada.

Vecchio, F., and M. P. Collins. 1986. “The modified compression field theory for reinforced concrete elements subjected to shear.” Journal of the American Concrete Institute, 83(2), 219–231.

Vu, N. S., B. Yu, and B. Li. 2017. “Stress-strain model for confined concrete with corroded transverse reinforcement.” Engineering Structures, 151: 472–487. https://doi.org/10.1016/j.engstruct.2017.08.049.

Xia, J., Jin, W., and L. Li. 2016. “Performance of Corroded Reinforced Concrete Columns under the Action of Eccentric Loads.” Journal of Materials in Civil Engineering, 28 (1): 04015087. https://doi.org/10.1061/(ASCE)MT.1943-5533.0001352.

Xin, J., J. Zhou, F. Zhou, S. X. Yang, and Y. Zhou. 2018. “Bearing capacity model of corroded RC eccentric compression columns based on hermite interpolation and fourier fitting.” Applied Sciences, 9 (1). https://doi.org/10.3390/app9010024.

Young, W. C., and R. G. Budynas. 1980. Roark’s formulas for stress and strain. McGraw-Hill Companies

Zaghian, S., B. Martín-Pérez, and H. and Almansour. 2020. “The effect of corrosion and traffic loads on bridge columns using three-dimensional non-linear finite element analysis.” Proc., CACRCS DAYS 2020 Capacity Assessment of Corroded Reinforced Concrete Structures, Fédération Internationale du Béton – International Federation for Structural Concrete, 349-356.

Zandi, K. 2015. “Corrosion-induced cover spalling and anchorage capacity.” Structure and Infrastructure Engineering, 11 (12): 1547–1564. https://doi.org/10.1080/15732479.2014.979836.

Chapter 4: Finite Element Modelling of Bridge Piers Subjected to Eccentric Load Combined with Reinforcement Corrosion[2]

Abstract

Corrosion of reinforcing steel in reinforced concrete infrastructure has been identified as the leading cause of concrete deterioration in North America. As the most critical bridge element, piers are more susceptible to reinforcement corrosion, especially in coastal areas and cold regions due to the application of de-icing salts. The combination of second-order effects and local nonlinearity dictates the failure mode of slender and eccentrically loaded columns. Degradation effects would be more critical in the presence of corrosion, at which the nonlinearity effects become more dominant. A comprehensive corrosion damage model is adopted from the literature in the present study. A stage-based corrosion scenario is then proposed to study the detrimental corrosion effects on the ultimate capacity, rigidity, and ductility of bridge piers subjected to eccentric load through finite element analysis. The interaction diagram of the corroded pier is then generated at different corrosion stages to introduce new safety margins. The accuracy of the proposed model is investigated by comparisons with available test data from the literature.

4.1 Introduction

Recent investigations have evaluated the effect of climate change on the service life and ultimate capacity of reinforced concrete (RC) infrastructures, especially in cold-climate regions such as Canada (Mohammed 2014, Deng et al. 2018). Global warming is a critical parameter known as an accelerating factor in reinforcement corrosion initiation and propagation (Bastidas-Arteaga et al.

---

[2]This chapter has been published in *Engineering Structures* (Zaghian, S., Martín-Pérez, B., and Almansour, H. (2023). "Finite element modelling of bridge piers subjected to eccentric load combined with reinforcement corrosion." *Engineering Structures*, 283, 115822.
https://doi.org/10.1016/j.engstruct.2023.115822)

2010). An increase in traffic intensity has been reported as an additional accelerating factor in the deterioration mechanism of aging bridges (Lounis et al. 2010). A literature survey has revealed that a considerable number of studies have been conducted on the deteriorating effects of corrosion at the material level (Cairns et al. 2005, Du et al. 2005, Kashani et al. 2013). It has been reported that the primary contribution to corrosion-induced damage are: cross-section loss of corroded rebars (Cairns et al. 2005, Val 2007), uniform corrosion-induced degradation of nominal steel strength and pitting corrosion-induced ductility degradation of corroded rebars (Almusallam 2001, Du et al. 2005, and Cairns et al. 2005), development of tensile stress due to expansion of corrosion products surrounding the rebars followed by concrete cover cracking and gradual spalling (Coronelli and Gambarova 2004, Chernin and Val 2011), degradation of compressive stress-strain response of corroded longitudinal rebars (Kashani et al. 2013), and reduction of bond strength (Lundgren 2002, Lundgren 2005, Schlune 2006, Lundgren et al. 2009, Zandi 2015, and Blomfors et al. 2018). There are numerous studies on the effect of corrosion on RC beams' flexural and shear behaviour (Maaddawy et al. 2005, Cairns et al. 2008, Sæther and Sand 2016). However, there are limited experimental and numerical investigations on small-scale RC columns' concentric and eccentric axial behaviour (Saito et al. 2007, Xia et al. 2016b, Vu et al. 2017). Limited numerical investigations also focus on the seismic performance of corroded RC columns (Mohammed 2014, Di Carlo et al. 2017, Kashani et al. 2017, Deng et al. 2018). In all of the studies above, it has been observed that the ultimate strength, ductility, and drift capacity of corroded RC members are significantly affected.

Bridge piers are often subjected to eccentric compressive loads. The axial load eccentricity with respect to the pier centerline is caused by the amplification of out-of-straightness of the pier and non-tangential load-induced deformation (AASHTO 2014). In some cases, the girders are not placed at the centerline of the piers, which causes additional eccentricity. Therefore, CSA S6:19 (Canadian Highway and Bridge Design-CHBDC) recommends considering a minimum eccentricity of

15+0.03h (mm) (in which h is the square column cross-section depth in mm) about the principal axis (CSA 2019). There is still a scarcity of research on 3D modelling of the eccentric axial performance of real-scale bridge piers under the combined effects of all the deteriorating aspects coming from reinforcement corrosion. The geometrical and material nonlinearity affect the failure mode and post-peak response of flexural columns significantly (Dhakal and Maekawa 2002). One of RC bridge piers' most common failure modes, especially under seismic loading, has been reported as the crushing of the core concrete and buckling of the longitudinal reinforcement (Kashani et al. 2019). For corroded RC columns, the failure mechanism is expected to follow a more severe pattern due to deterioration of concrete and rebars, consequent nonlinearity increase, and flexural and axial rigidity reduction. The adverse effect of reinforcement corrosion on the strength and ductility of RC columns depends on the initial degree of confinement. It is expected to be more pronounced in case of inadequate confinement (Joshi et al. 2015). Gradual degradation of confinement effects due to transverse rebars corrosion, loss of one or more ties, and possible buckling of longitudinal reinforcing bars are observed to govern the structural performance deterioration of RC members when an axial load is dominant (Mohammed 2014). If, in addition, the members are subjected to significant bending moments (high eccentricity), the generation of flexural cracks along with longitudinal corrosion-induced cracks accelerates cover spalling (Mohammed 2014).

According to current standards, the bridge condition is first assessed from visual inspections (Federal Highway Administration 2001 and Ontario Ministry of Transportation 2008). The inspection frequency is justified depending on the type of structure, existing problems, and performance history. In case of any damage detection, a more detailed investigation and non-destructive testing techniques are required to mitigate the deficiency (Federal Highway Administration 2001 and Ontario Ministry of Transportation 2008). There are still a considerable number of bridges identified as deficient in North America (Federal Highway Administration 2001), since the integrity and accuracy of visual inspections strongly depend on the inspection quality. It is, therefore, crucial to develop a quantitative assessment approach to evaluate the structural performance of bridge piers subjected to the combination of reinforcement corrosion and service load during their service life. The present study comprehensively investigates the eccentric behaviour of corroded large-scale RC bridge piers by conducting a three-dimensional nonlinear finite element analysis (3D-NLFEA). Reinforcement corrosion is defined as a staged phenomenon and is simulated by reducing the cross-section of ties and longitudinal rebars, reducing the ductility of reinforcing steel due to pitting corrosion, modifying the compressive response of longitudinal rebars (with the possibility of inelastic buckling), reducing the cover concrete compressive strength (to account for possible cracking and spalling of the cover), degrading confinement effects, and finally degrading bond-slip behavior at each stage accordingly.

4.2 Proposed stage-based analysis

4.2.1 General

In the present study, the eccentric compressive behaviour of a corroded RC pier located in the intermediate bent of an existing bridge is evaluated by developing a quantitative stage-based analysis. A 3D-NLFEA is carried out using the commercial nonlinear finite element software package DIANA (DIANA 2019) to propose a staged failure mechanism for aging bridges under the combined effects of external axial load, moment, and reinforcement corrosion. In the present model, the reinforcement is modelled by the "bond-slip reinforcement". The bond-slip interface elements are treated as beam elements to incorporate the effect of axial load-induced lateral pressure on the core. Concrete is modelled by adopting solid brick and wedge elements. Pre-defined tension softening "Hordjik" and compression "fib 2010" curves are adopted as concrete tensile and compressive responses. The confinement effect is incorporated by adopting the confinement model by Saatcioglu and Razvi (1992), i.e.,

$$f'_{CC} = f_c + k_1 f_{le} \qquad 4.1$$

in which

$$k_1 = 6.7\left(k_2 f_l\right)^{-0.17} \qquad 4.2$$

$$f_l = \frac{\sum_{i=1}^{q}\left(A_s f_{yt} \sin\alpha\right)_i}{sb_c} \qquad 4.3$$

$$\varepsilon_1 = \varepsilon_{01}\left(1+5K\right) \qquad 4.4$$

$$K = \frac{k_1 f_{le}}{f'_{co}} \qquad 4.5$$

$$\varepsilon_{85} = 260\rho\varepsilon_1 + \varepsilon_{085} \qquad 4.6$$

Where f'_{CC} is the core compressive strength; f_c is the concrete in-place compressive strength; $f_{le} = k_2 f_l$ is the equivalent lateral confinement pressure; f_l is the lateral confinement pressure, and $k_2 = 0.15\sqrt{\frac{b_c}{s}\frac{b_c}{s_l}} \leq 1.0$ for rectilinear transverse reinforcement (with b_c, s and s_l being the section width, transverse reinforcement spacing, and spacing of laterally supported longitudinal reinforcement, respectively); k_1 is an empirical parameter; A_s is the transverse cross-sectional area; f_{yt} is the yield strength of the tie; q is the number of tie legs; and ε_{01}, ε_1, ε_{085}, and ε_{85} are the strains at the peak and corresponding to 85% of peak stress for unconfined and confined concrete, respectively.

A nonlinear structural analysis assuming both material and geometrical nonlinearities was performed. A regular Newton-Raphson iterative method and the "Total Lagrange" option were used to perform geometrical-nonlinear analysis. The force-control, arc-length, and line search control options were used to control the post-peak behaviour and improve the solution convergence.

4.2.2 Corrosion-damage model

Assuming a constant corrosion rate, the main corrosion-induced deteriorating effects on RC piers that are adopted in the present study are summarized in Table 4-1. In an earlier study by the author, the adopted damage model is described in detail (Zaghian et al. 2020).

Table 4-1 Summary of the adopted corrosion damage model (Zaghian et al. 2020)

References	Deteriorating effects	Equation	Equation No.
NA	Rebar cross-section loss	$X_{corr} = \frac{{d_b}^2 - {d_{b,corr}}^2}{{d_b}^2} \times 100$	4.7
Cairns et al. (2005)	Rebar's ductility degradation	$\varepsilon_{ut,cor} = \left[1.0 - 100 \times \alpha_1 . X_{corr}\right] \varepsilon_{ut}$	4.8
suggestion by Rodriguez et al. (1996)	Possibility of elastic buckling	$\sigma_{cr,corr} = \pi^2 E \left(0.25 d_{b,corr}\right)^2 / (0.75 s_{corr})^2$	
Kashani et al. (2013)	Possibility of inelastic buckling	$\eta = \sigma / f_{yc,corr} = \begin{cases} \xi = \varepsilon / \varepsilon_{yc,corr} & \xi \le 1 \\ \frac{\eta_2 - 1}{\xi_2 - 1}\left(\xi - 1\right) + 1 & 1 < \xi \le 2 \\ \eta_2 - 0.02\left(\xi - \xi_2\right) & \xi_2 \le \xi \,\&\, \eta \ge 0.2 \\ 0.2 & otherwise \end{cases}$ $\xi_2 = \max\left\{55 - 2.3\lambda_{p,corr} ; 7\right\}$ $\eta_2 = \max\left\{\alpha\left(1.1 - 0.016\lambda_{p,corr}\right){\eta^*}_2 ; 0.2\right\}$ $\lambda_p = \sqrt{\frac{f_{yc,corr}}{100}} \frac{s}{d_b - 2x_{cp}}$ $f_{yc,corr} = f_{yc}\left[1 - 100 \times \beta . X_{corr}\right] \quad ; \quad \beta = \begin{cases} 0.005 & s/d_b \le 5 \\ 0.0065 & 5 < s/d_b \le 10 \\ 0.0125 & s/d_b > 10 \end{cases}$	4.9
Coronelli and Gambarova (2004)	Cover concrete cracking	$f_{c,cor} = \frac{f_c}{1 + K \varepsilon_1 / \varepsilon_{c0}}$, $\varepsilon_1 = 2\pi n_{bars}\left(\nu_{rs} - 1\right) x_{cp} / b_0$	4.10
Saatcioglu and Razvi (1992)	Confinement degradation	substituting degraded values into Eqs. 4.1-4.6	NA

Blomfors et al. (2018)	Degraded bond-slip response	$\tau_{bu,spilit,red} = \eta_2 .6.5.\left(\frac{f_c}{25}\right)^{0.25}\left(\frac{25}{d_b}\right)^{0.2}\left(1+k_m.k_{tr}\right)$	4.11
		$\tau_{res,\mathrm{mod}}\left(k_{tr}\right)=\begin{cases}\left(0.16+12k_{tr}\right).\tau_{bu,spilit,red} & for \quad 0\le k_{tr}\le 0.02\\ 0.4\tau_{bu,spilit,red} & for \quad 0.02<k_{tr}\end{cases}$	4.12

where d_b and $d_{b,corr}$ are the un-corroded and corroded rebar diameter, respectively; ε_{ut} and $\varepsilon_{ut,corr}$ are the ultimate tensile strain of uncorroded and corroded rebar, respectively; s_{corr} is tie spacing considering the possible loss of one or more ties; η and ξ are the non-dimensional stress and strain respectively; α is the softening coefficient; s is the tie spacing; η^*_2 is the non-dimensional stress corresponding to ξ_2 (in case of no buckling); $f_{yc,corr}$ is the compressive strength of corroded rebar; and, λ_p and $\lambda_{p,corr}$ are the non-dimensional buckling parameters of the un-corroded and corroded rebar, respectively; where f_c and $f_{c,cor}$ are the compressive strength of undamaged and damaged concrete; $K = 0.1$ is adopted by assuming ribbed bars with medium diameter; ε_{c0} is the concrete strain at the peak compressive strength (taken as 0.002); ε_1 is the average tensile strain perpendicular to compression; n_{bars} is the number of corroding rebars; $v_{rs} = 2$ is the volume expansion ratio and is adopted from Molina et al. (1993); x_{cp} is the corrosion penetration depth and is calculated as $x_{cp} = \frac{d_b}{2}\left[1-\sqrt{1-X_{corr}}\right]$ (as mentioned in Deng et al. (2018)), and b_0 is the width of the un-corroded section; $\tau_{bu,spilit,red}$ is the reduced bond strength and $\tau_{res,\mathrm{mod}}\left(k_{tr}\right)$ is the reduced residual bond capacity; variables η_2 , k_m , and k_{tr} have been adopted from the Model Code 2010 (CEB. 2013).

4.2.3 Stage-based corrosion damage scenario

The current quantitative evaluation approach aims at proposing a stage-based analysis to study the structural performance of RC bridge piers under different levels of corrosion. According to field investigations (Andersen 1997) and on-site observations (Figure 4-1 (a) and (b)), the damage is assumed to be localized in the splashing zone (middle third) of the pier. Foundation footings in cold climates are required to be placed below the depth of frost penetration, with a minimum of 1.2 m below ground level (CSA 2019). Considering the traffic level with respect to the foundation of the column, it was assumed the splash zone corresponded to approximately the middle third of the column. The proposed stage-based damage scenario starts with the undamaged stage, followed by three stages each representing different levels of damage accumulation over the bridge pier's service life, assuming no repair/rehabilitation intervention had occurred during that period. Since there is a lack of field/laboratory time-dependent data reporting bridge piers damage induced by reinforcement corrosion, the staged corrosion-induced deteriorating effects are assumed for low, medium and high levels of damage accumulation at a specific elapsed times and are estimated according to the adopted corrosion damage model. In the proposed stage-based scenario, the cross-section reduction in the ties is assumed to be twice that of the longitudinal rebars at each stage. Two reasons explain this assumption are: (a) the tie diameter is smaller than that of the longitudinal rebar diameter, and (b) the ties are closer to the ambient environment and aggressive agents and are likely to start corroding earlier. Stage 1 is defined as the early stages of corrosion in which the mass loss percentage in the longitudinal rebars and ties are assumed to be 5% and 10%, respectively. The material properties of both steel and concrete degrade accordingly using the models tabulated in Table 4-1.

Stage 2 is assumed to represent a medium level of damage accumulation, with the mass loss in the longitudinal rebars and ties increasing to 20% and 40%, respectively. At this stage, it is further assumed that increasing the corrosion-induced deterioration effects leads to connection loss between two middle longitudinal rebars and ties at the corroded zone. The worst-case scenario assumes that corrosion propagates to stage 3, in which the mass loss percentage in the longitudinal rebars and ties increases to 30% and 60%, respectively. At this stage, it is assumed that there is a possibility of losing the fully rigid connection between all the longitudinal rebars and ties at the corroded zone and of rupturing three adjacent middle ties, in addition to material deterioration.

In order to corroborate the above assumptions of loss of connection between longitudinal reinforcing bars and ties, an analytical approach was used to estimate the axial tie strain ε_t due to the axial load-induced lateral pressure in the RC bridge pier (Zaghian et al., 2022). As a result of corrosion, the tie segment between two adjacent longitudinal rebars was assumed as a pin-pin beam (corrosion-induced loss of rigidity). The bending-induced change in the projected length of the beam tie segments between the longitudinal rebars was estimated using Eq. 4.13.

$$\varepsilon_t = \frac{\Delta l}{l} = \frac{1}{2l}\int_0^l \left(\frac{dy}{dx}\right)^2 dx \qquad 4.13$$

in which l is the length of the ties leg between two adjacent longitudinal rebars, and y is the bending-induced deflection function. The possibility of tie rupture was then investigated by comparing the bending-induced strain in Eq. 4.13 with the yield strain of the corroded tie at each stage (Cairns et al. 2005). More detailed explanations are provided in Zaghian et al. (2022).

(a) Toronto Gardiner Expressway

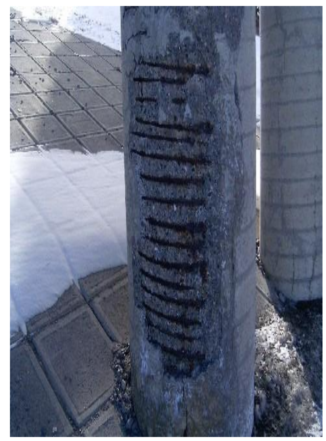

(b) Underpass in Bells Corners, Ottawa

Figure 4-1 (a) and (b) Corroded bridge piers (on-site observations by the Authors)

4.3 Validation of the proposed 3D nonlinear finite element analysis

Two different corroded RC columns tested by Wang and Liang (2008), ZDY350-2 and ZXY350-2, were simulated to assess the proposed 3DNLFEA (Figure 4-2, a). Columns ZDY350-2 and ZXY350-2, with partial corroded length at the compressive side (350 mm long), were eccentrically loaded with 152 mm and 54 mm eccentricities, respectively. The yield and ultimate strength of 18-mm longitudinal rebars were reported as 397.5 and 602.5 MPa, and those of 8-mm ties were reported as 402.5 MPa and 475 MPa, respectively. The average weight loss of the corroded longitudinal top tensile bars (side of casting), longitudinal bottom tensile bars (opposite side of casting), longitudinal top compressive bars (side of casting), longitudinal bottom compressive bars (opposite side of casting), tensile side ties, and compressive side ties in ZDY350-2 were reported as 0.88%, 1%, 3.94%, 3.94%, 5.95%, and 6.21%, respectively, and those in column ZXY350-2 were reported as 1.62%, 1.48%, 5.59%, 5.43%, 6.5%, and 5.24%, respectively. An average mass loss of 6% was used for the ties in the corroded zones in both columns. As shown in Figure 4-2 (a), four zones are defined: Zone 1 as undamaged corbels, Zone 2 as a damaged compressive zone, Zone 3 as an undamaged zone of the column, and Zone 4 as a damaged tensile zone. Tie spacing within zones 1 and 3 are 50 mm, and within zones 2 and 4 are 100 mm. Following the adopted corrosion-damage model, the mechanical properties of the rebars and concrete were degraded and then implemented into the model. The compressive stress-strain response of the uncorroded and corroded rebars for both columns is presented in Figure 4-2 (b). As shown in Figure 4-2 (b), the uncorroded compressive rebar follows a hardening post-yield response. After corrosion, there is a softening post-yield behaviour that results from decreasing the rebar diameter and increasing the tie spacing-to-rebar diameter ratio ($\frac{s}{d}$) (Kashani et al. 2013). In these columns, there is no possibility for the compressive longitudinal reinforcement (both uncorroded and corroded) to experience buckling within the material proportional limit (Euler's formula and Rodriguez et al. 1996). The possible failure mechanism is therefore expected to be steel yielding. The columns were meshed using 60-mm solid CTE30 elements. The tensile longitudinal reinforcement and the column ties were modelled by two-node one-dimensional "bond-slip" reinforcement. The compressive longitudinal reinforcement was modelled using two-node one-dimensional embedded elements. The middle line of the steel plate support, located at the column base, was restrained from any translational movement to simulate a simple support. The middle line of the steel loading plate at the column's top surface was restrained against in-plane translational movement (Figure 4-2, c). Further details of the columns are provided in Table 4-2.

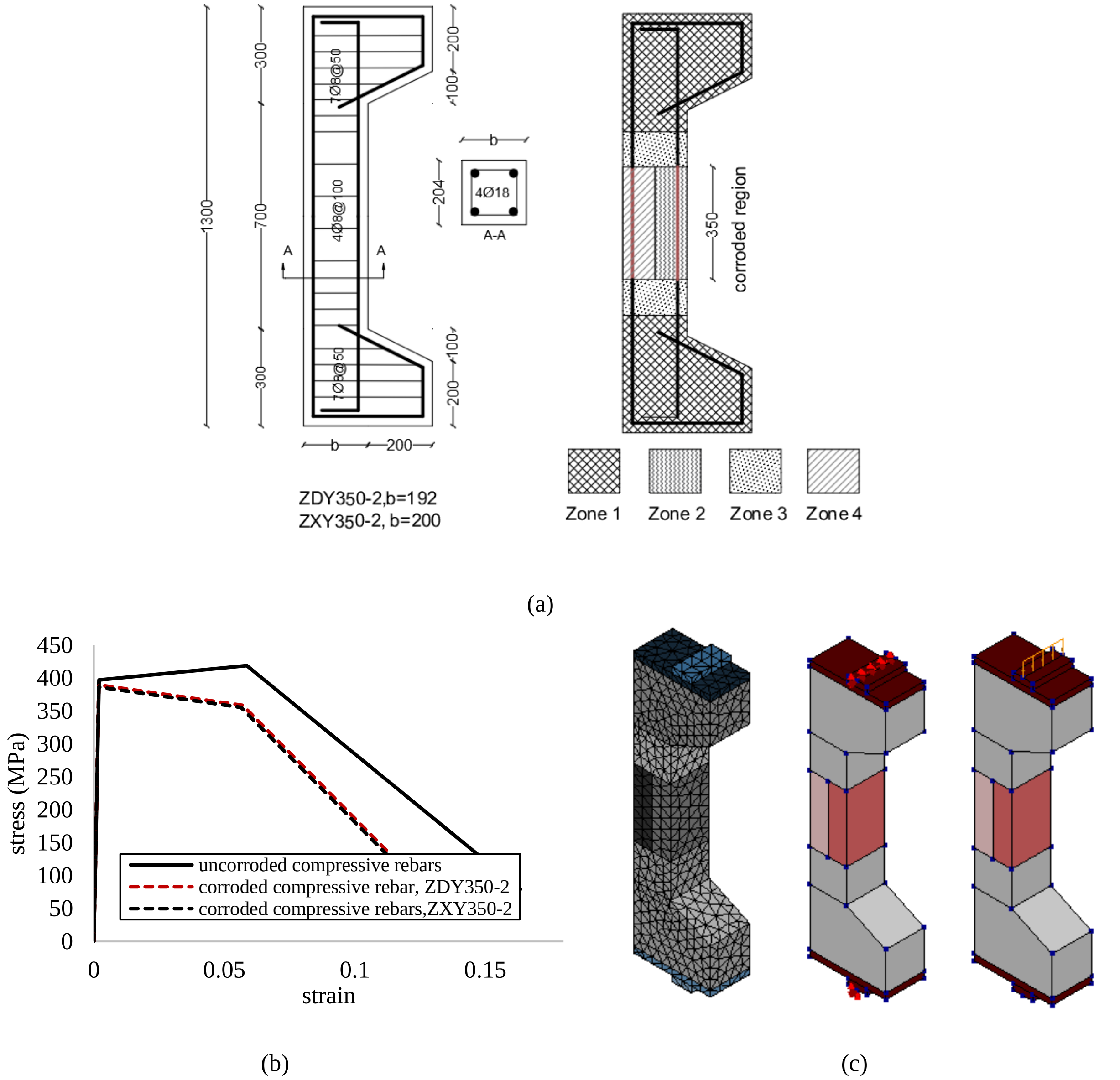

Figure 4-2 (a) Details of columns (casting side) tested by Wang and Liang (2008), all dimensions in mm; (b) compressive stress-strain response of the rebars; (c) modelling details: meshing, supports, loading

Table 4-2 Details of RC columns tested by Wang and Liang (2008)

Specimens	b×h (mm×mm)	L(mm)	Cover and core compressive strength (control and corroded) (MPa) Zone 1		Zone 2		Zone 3		Zone 4	
			f_c	f'_{CC}	$f_{c,cor}$	$f'_{CC,corr}$ (*)	f_c	f'_{CC}	$f_{c,cor}$	$f'_{CC,corr}$
ZDY350-2	192×204	1300	45.3	55.5	25.6	43.6	45.3	55.5	35.0	43.6
ZXY350-2	200×204	1300	45.3	55.5	22.36	43.6	45.3	55.5	32.8	43.6

(*) $f'_{CC,corr}$ is the concrete compressive strength of the core (confinement model by Saatcioglu and Razvi, 1992)

The axial load-lateral deflection at the mid-height of corroded columns ZDY350-2 and ZXY350-2 based on the present model and the experimental test is presented in Figure 4-3. The figure shows the numerical results are in good agreement in terms of ultimate capacity and rigidity. It is also observed that the failure characteristics of the simulated columns match the experimental observations with an acceptable agreement. The compressive bearing capacity of the corroded column under larger eccentricity (ZDY350-2) is expected to reduce significantly due to the appearance of tensile stresses on one side of the column in addition to the second-order effects of the compressive force. For column ZDY350-2, by comparing the longitudinal stress of the main longitudinal reinforcing bars (in the z-direction) and the yield stress of corroded reinforcement (393.5 MPa), the tensile corroded longitudinal reinforcing bars are observed to undergo yielding under ultimate load (Figure 4-4, a). By looking at the maximum principal stresses in the concrete within the tensile side of the column, where the tensile strength of concrete is reduced by 3.3 MPa, it is observed that flexural cracks with a maximum width of almost 0.75 mm spread into the casting side and opposite of casting side (Figure 4-4, b and c). Likewise, by comparing the minimum principal stresses in the concrete within the compressive side with the reduced compressive strength of the damaged concrete (25.6 MPa), it is observed that the possibility of crushing within this zone exists (Figure 4-4, d). The failure characteristics of the simulated column represented well the observations in the experimental test by Wang and Liang (2008), during which it was observed that the failure mode of olumn ZDY350-2 (under larger eccentricity) was characterized by yielding of the tensile steel bars followed by failure of the column along two longitudinal corrosion-induced cracks. The failure in the compressive side of the concrete was categorized as splitting or crushing of concrete along the longitudinal corrosion-induced cracks.

By comparing the maximum axial stress in the longitudinal direction of the main reinforcement (Figure 4-4 (e)) with the steel yield stress of corroded compressive longitudinal reinforcing bars

(396.7 MPa as shown in Figure 4-4 (b)), and by comparing the concrete minimum principal stresses and strains (Figure 4-4 (g) and (h)) with the compressive strength (22.4 MPa according to Table 4-2) and corresponding strain of cracked concrete, it is observed that the final failure of column ZXY350-2 is attributed to yielding of the corroded compressive longitudinal reinforcing bars and crushing of the concrete in the compressive corroded side. There is no yielding in the tensile longitudinal reinforcing bars (Figure 4-4 (e)). Figure 4-4 (f), shows the crack pattern in the column's tensile side. The same failure characteristics were reported by Wang and Liang (2008).

The experimental cracking load in columns ZDY350-2 and ZXY350-2 was reported as 60 kN and in the range of 200-400 kN, respectively. By inspecting the cracking patterns in the present 3DNLFEA, cracking for columns ZDY350-2 and ZXY350-2 starts at a load of 54 kN and 220 kN, respectively, which is in good agreement with the test observations.

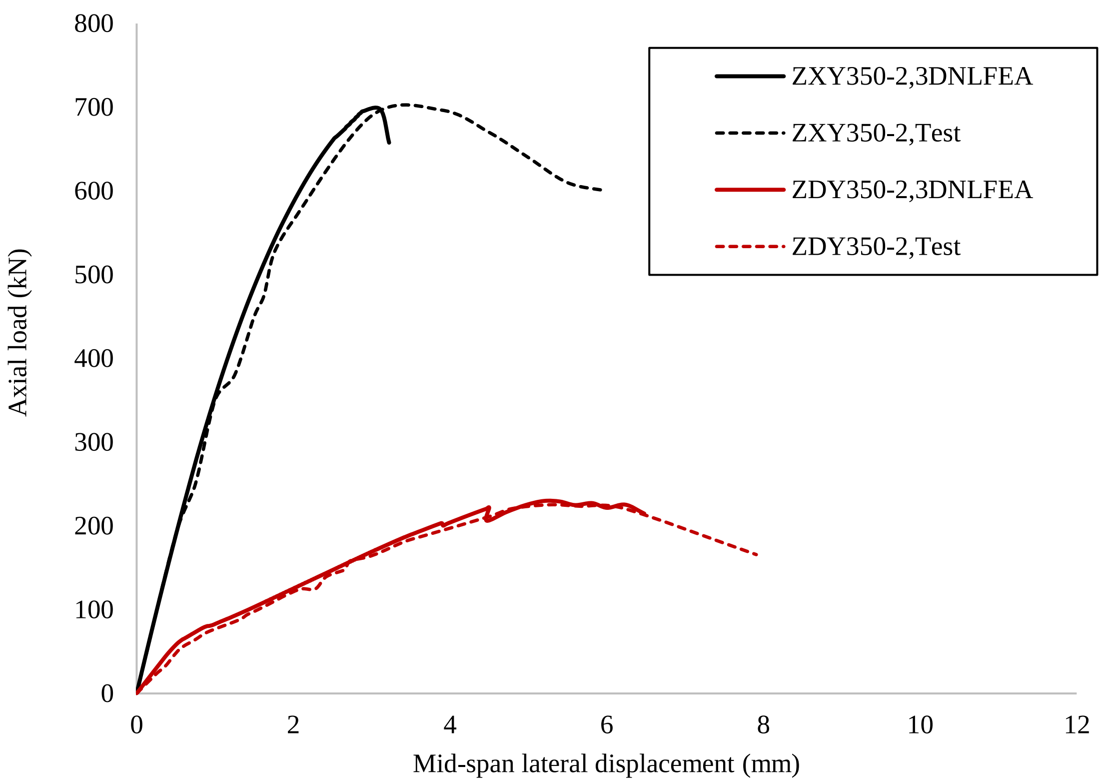

Figure 4-3 Axial load-mid-span lateral deformation of columns ZDY350-2 and ZXY350-2 based on the present 3DNLFEA and test by Wang and Liang (2008)

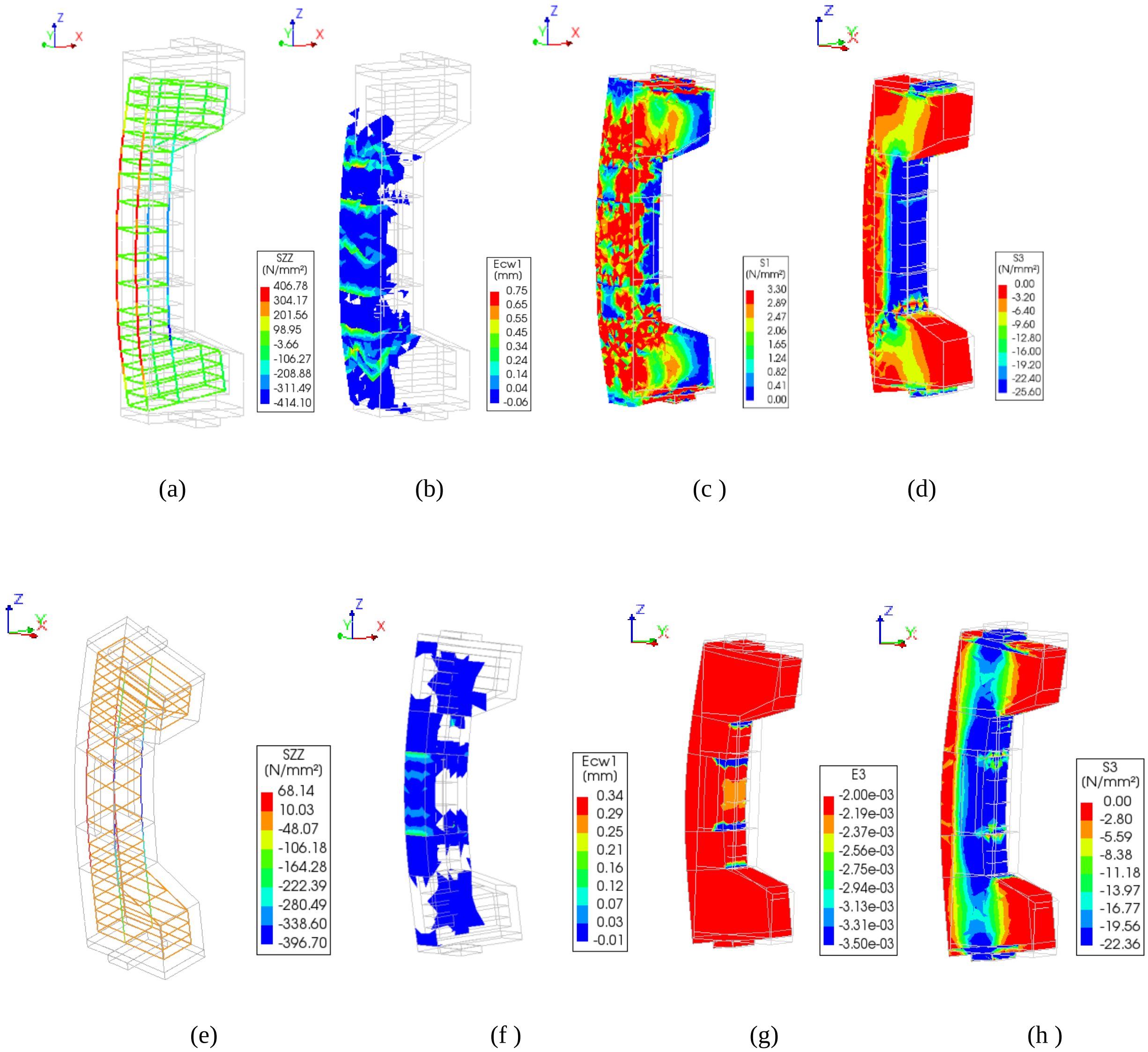

Figure 4-4 Results based on 3D-NLFEA at the failure point of column ZDY350-2: (a) stress in reinforcement, (b) crack width, (c) maximum principal stress, (d) minimum principal stress; and column ZXY350-2: (e) stress in reinforcement, (f) crack width, (g) minimum principal strain, (h) minimum principal stress

4.4 Case study, results, and discussion

4.4.1 General

An intermediate 7-column bent of a two-span slab on a pre-stressed girder bridge with a center-to-center span of 30.81 m from the Virginia State Bridge Inventory (Hevener 2003, based on Nutt et al. 1998, NCHRP Report 12-26) was selected as the case study. The critical column of the bent was designed for a range of load over capacity ratio (LOCR) of 0.4<LOCR<0.6 under different eccentricities ($0< e <e_p=0.15h$). Eccentricity e_p is the allowable practical eccentricity, and h is defined as a square column cross-section depth. The reason behind such a high LOCR selection is the possible increase in traffic intensity on aging bridges. The bent design follows CSA S6:19 (CSA 2019). Figure 4-5 and Table 4-3 show more details of the selected RC bent and pier.

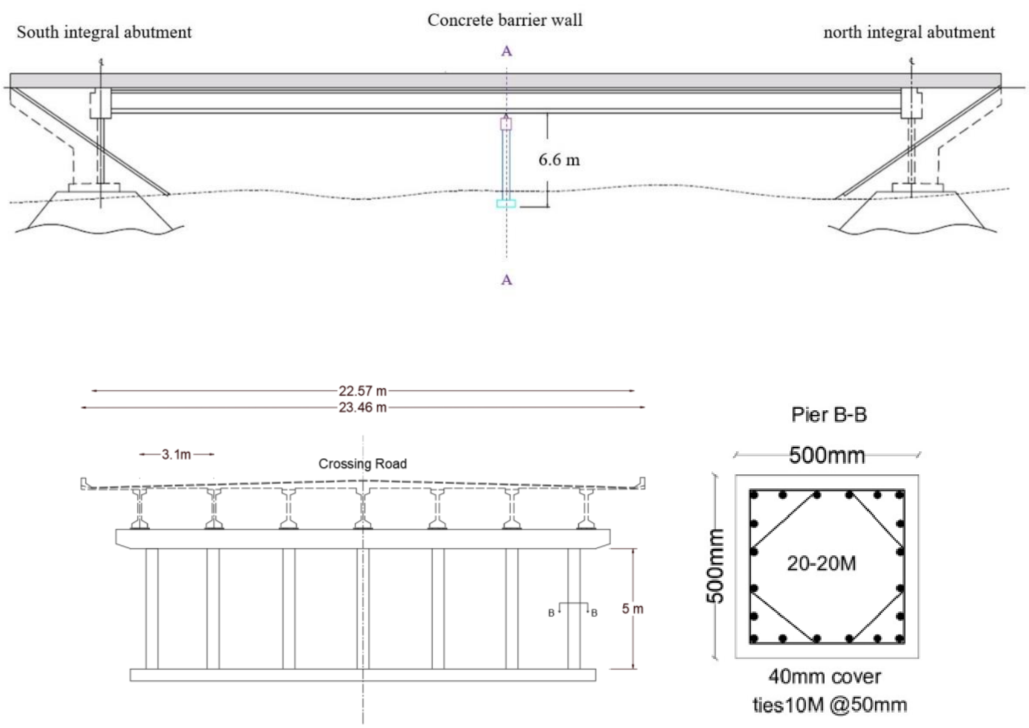

Figure 4-5 Configuration of bridge bent and pier

Table 4-3 General information of designed bridge

Bridge substructure geometry	
Intermediate pier:	Multi-column bent (7-columns spacing at 3.1 m) with spread footings on bedrock
Pier cap size:	1.5 m by 0.8 m cross-section
End abutment:	Integral abutment
Bridge substructure material	
Pier cap and pier in-place concrete strength:	$f_c = 35 MPa$
Concrete elastic modulus:	$E_c = 35000 MPa$ [1]
Concrete cracking strength (normal-density concrete):	$f_{cr} = 0.4\sqrt{f_c^{'}} = 2.37 MPa$ [2]
Yield strength, ultimate strength and strain of rebars[3]	$f_y = 420 MPa,\ f_u = 525\ MPa, \varepsilon_u = 0.14$

[1] Model code 2010, CEB 2013
[2] CSA S6:19
[3] CSA G30.18 Gr. 40

4.4.2 Finite element model

A 3DNLFEA was conducted using DIANA to study the structural performance of the RC pier under the combination of the proposed corrosion scenario and eccentric load during its service life. The load was applied in the traffic direction with a minimum allowable eccentricity $e_{\min} = 15 + 0.03h = 30$ mm (CSA S6:19) and an allowable practical eccentricity, e_p=0.15h. The column was restrained against all translational and rotational movements at the base to simulate the foundation's full rigidity. The column top was restrained against the translational movement in the bending direction to simulate the bent-induced partial stiffness, but it was unrestrained in the traffic direction. The eccentric load was applied as non-uniform stress on a steel plate of 40-mm thickness to ensure the smooth transfer of the load and to avoid any possible local concrete damage below the load (Figure 4-6, a and b). Concrete was modelled using twenty-node isoparametric solid brick elements "CHX60", based on quadratic interpolation and Gauss integration, and fifteen-node isoparametric solid wedge elements "CTP45", based on quadratic interpolation and numerical integration (Figure 4-6, c). Meshes with 50×50 mm elements were used in the 3DNLFEA. The reinforcement was modelled using two-node one-dimensional "bond-slip" reinforcement. The bond-slip interface elements were treated as beam elements.

It was assumed that corrosion-induced deterioration effects are generated in three stages, as discussed earlier and summarized in Table 4-4. At stage 3, the in-place compressive strength of concrete in the confinement model by Saatcioglu and Razvi (1992) was assumed to reduce from the initial value of 35 MPa due to corrosion-induced cracking and possible damage propagation towards the core. A parametric study was conducted to investigate the effect of the in-place compressive strength of concrete on the proposed evaluation approach. The in-place compressive strength of concrete was reduced from 35 MPa to 33 MPa, 30 MPa, 28 MPa, 25 MPa, and 20 MPa, corresponding to stage 3a, stage 3b, stage 3c, stage 3d, and stage 3e, respectively. At Stage 3, the degraded confinement effect is assumed to be attributed to the reduced concrete in-place compressive strength and the tie properties degradation.

By comparing the ties' bending-induced strain (Eq. 4.13) and the corroded ties yield strain at each corrosion stage, it is observed that there is a possibility of tie failure at the corroded zone at stage 3 (Table 4-5). Three adjacent middle ties of a highly corroded pier (stage 3) were assumed to rupture since the ties are spaced tightly. In the FE model, three different zones were defined in the RC pier: zone 1 as uncorroded, zone 2 as the mid-third zone of the RC pier (corroded zone), and zone 3 as the zone where three ties are ruptured (Figure 4-6,d). The compressive stress-strain response of the uncorroded rebars was modelled using the model proposed by Dhakal and Maekawa (2002) (Figure 4-6, e). There is no possibility of elastic buckling of the compressive longitudinal rebars, even if affected by corrosion, due to sufficient lateral confinement provided by the tightly spaced ties (estimated according to Euler's formula and recommendations by Rodriguez et al., 1996). Figure 4-6 (e) shows the deteriorated compressive stress-strain response of the corroded rebars at each corrosion stage in different zones (Kashani et al., 2013). The constitutive model of the uncorroded and corroded rebars at stages 1, stage 2, and stage 3 (zone 2) is observed to follow a hardening post-yield response. The constitutive model of the compressive rebars in zone 3 at stage 3 follows a softening post-yield response, which shows that failure is governed by yielding, followed by inelastic buckling. The properties of the damaged concrete cover and core at different stages are summarized in Table 4-6. The compressive strength of the damaged cover and core were estimated according to Coronelli and Gambarova (2004) and by modifying the confinement model by Saatcioglu and Razvi (1992), respectively.

Table 4-4 Summary of assumptions made for different corrosion stages (Zaghian et al., 2022)

Stage	Assumptions
Stage 1	• Longitudinal rebar mass loss of 5% • Tie mass loss of 10% • Material properties degradation (Table 4-1) • Initial in-place compressive strength in the confinement model
Stage 2	• Longitudinal rebar mass loss of 20% • Tie mass loss of 40% • Material properties degradation (Table 4-1) • Loss of fully-rigid connection between the ties and two middle longitudinal rebars • Initial in-place compressive strength in the confinement model
Stage 3	• Longitudinal rebar mass loss of 30% • Tie mass loss of 60% • Material properties (Table 4-1) • Loss of fully-rigid connection between all the ties and longitudinal rebars • Rupture of three adjacent ties at the middle height of the RC column • Variable In-place compressive strength (a,b,c,d,e)

Table 4-5- Analytical axial tie strain due to axial-load induced lateral pressure in the RC bridge pier

Stage	Initial tie diameter (mm)	Area loss rebar	Area loss tie	Corroded tie diameter (mm)	Corroded tie yield strain	Corroded tie yield stress (MPa)	ε_t
Stage 3	11.3	0.3	0.6	7.14	0.00084	168	0.012

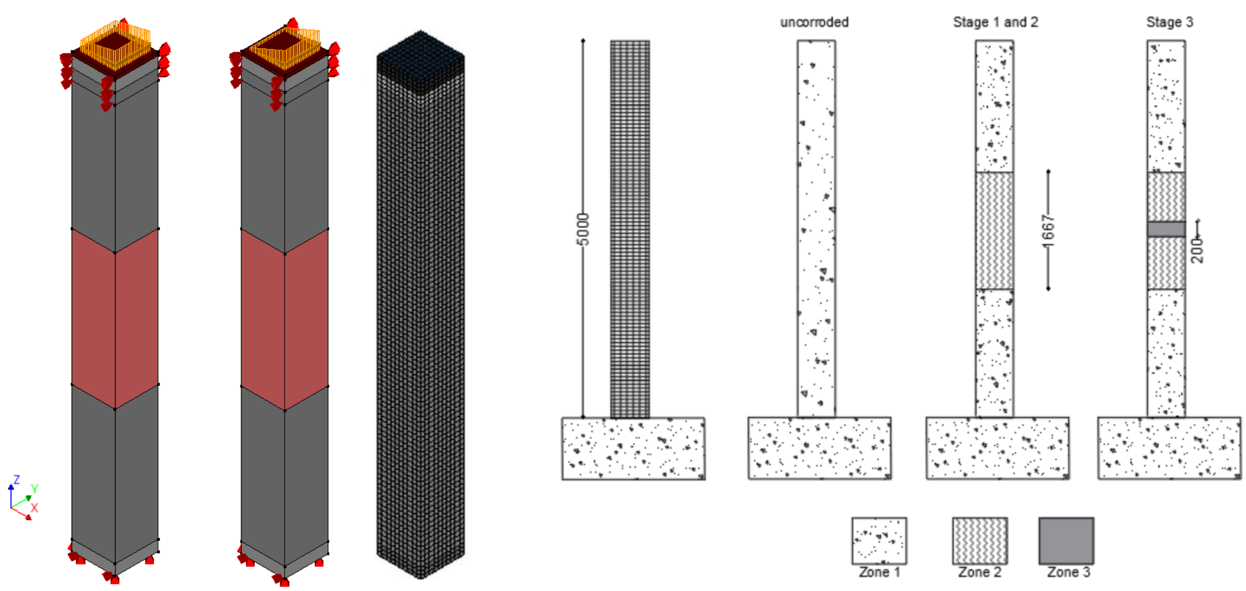

(a) (b) (c) (d)

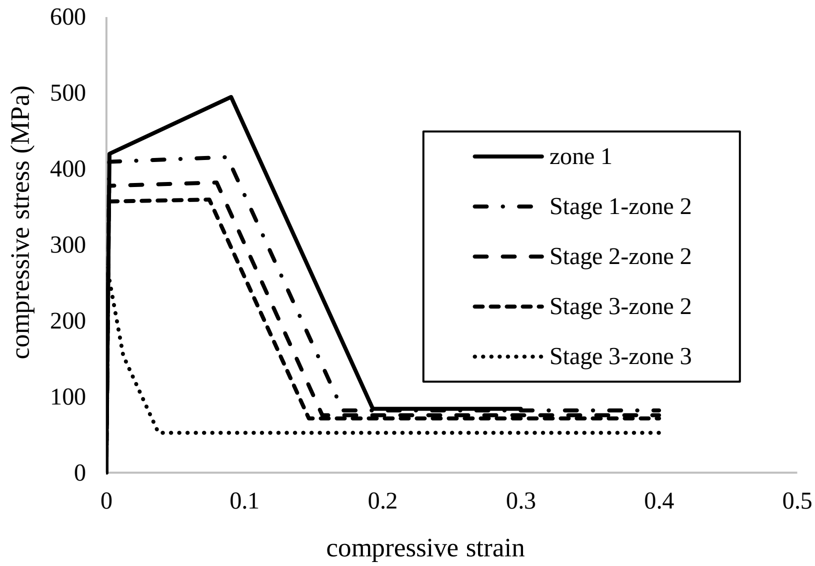

(e)

Figure 4-6 (a) Configuration of RC bridge column in DIANA (e=30mm), (b) Configuration of RC bridge column in DIANA (e=75mm), (c) Concrete section mesh, (d) Configuration of designed RC column (uncorroded and corroded), all dimensions are in mm, (e) Compressive stress-strain response of longitudinal rebars at different stages of corrosion

Table 4-6 Properties of concrete at each stage of corrosion

Corrosion stages	**Longitudinal rebar** X_{corr}	**Tie** X_{corr}	**Concrete compressive strength (MPa)**					
			Zone 1		**Zone 2**		**Zone 3**	
			cover	**core**	**cover**	**core**	**cover**	**core**
uncorroded	NA	NA	35	56.17	NA	NA	NA	NA
Stage 1	5%	10%	35	56.17	9	52.82	NA	NA
Stage 2	20%	40%	35	56.17	negligible	44	negligible	NA
Stage 3,a	30%	60%	35	56.17	negligible	37.58	negligible	33.82
Stage 3,b	30%	60%	35	56.17	negligible	34.58	negligible	30.82
Stage 3,c	30%	60%	35	56.17	negligible	32.58	negligible	28.82
Stage 3,d	30%	60%	35	56.17	negligible	29.58	negligible	25.82
Stage 3,e	30%	60%	35	56.17	negligible	24.58	negligible	20.82

4.4.3 Discussion of results

4.4.3.1 Load-deflection response and failure pattern

The load-maximum lateral displacement and the load-maximum vertical displacement of the uncorroded and corroded RC pier under load with eccentricities of $e_{\min} = 30$ mm and $e_p = 75$ mm are shown in Figure 4-7 through 4-10. A staged drop in ultimate capacity, ductility, and rigidity is observed in the corroded RC pier by increasing corrosion levels. In Figure 4-7, up to 54% reduction in ultimate capacity and up to 52% reduction in lateral deformation are observed for the heavily corroded RC pier (stage 3,e) subjected to the axial load applied at an eccentricity of $e_{\min} = 30$ mm. As shown in Figure 4-11 (a), a staged drop in ultimate capacity of 14%, 37%, 39%, 41%, 44%, and 47% is observed for the corroded RC pier subjected to the combination of eccentric load ($e_{\min} = 30$ mm) and corrosion (stage 1 through stage 3, d, respectively). A sudden drop in the ultimate capacity of the RC pier from stage 1 to stage 2 is attributed to both cover and core concrete deterioration, with consequent loss of the connection between the affected ties and the two middle longitudinal rebars. The staged reduction of the maximum lateral deformation of the corroded RC column is evident in Figure 4-7. Comparing the results shown in Figure 4-7 and Figure 4-8, it is observed that the present 3DNLFEA is efficiently capable of capturing the decrease in load capacity and increase in lateral deformation of the corroded RC pier with larger eccentricity. For the heavily corroded RC pier (stage 3,e) with larger eccentricity ($e_p = 75$ mm), up to 51% reduction in ultimate capacity is observed (Figure 4-11, b). Up to 55% reduction in lateral deformation compared to the uncorroded pier is observed (Figure 4-8). Figures 4-9 and 4-10 show the effect of different stages of corrosion on the reduction of ultimate axial capacity, axial deformation, and axial rigidity of eccentric corroded RC piers.

Figure 4-12 illustrates the failure pattern of the uncorroded RC pier with minimum eccentricity ($e_p = 30$ mm). The figure shows that the compression side within the lower half of the column undergoes crushing by comparing the minimum principal stresses and the compressive strength of the concrete cover (Figure 4-12, a). No flexural cracks on the tensile side are observed. The tensile longitudinal rebar close to the fixed support reaches $S_{zz} = 8$ MPa without yielding, and the compressive rebars close to the fixed support reach almost 93% of the proportional limit (Figure 4-12, b). Crushing of concrete on the compressive side is the primary failure mechanism of the RC column with smaller eccentricity.

The failure pattern of the uncorroded RC pier with an allowable practical eccentricity of 75 mm is shown in Figure 4-14. By increasing the eccentricity to 75 mm, the presence of flexural tensile cracking (Figure 4-14, a) results in a more ductile failure pattern compared to the case of the pier with minimum eccentricity. By comparing the minimum principal stresses and the compressive strength of the concrete cover, concrete crushing in the lower half of the RC pier is detected (Figure 4-14, b). The tensile longitudinal rebar's Cauchy stresses close to the fixed support increase to $S_{zz} = 96$ MPa without yielding. The compressive longitudinal reinforcing bars close to the fixed support reach almost 81% of the proportional limit (Figure 4-14, c). It is observed that even under an eccentricity of 75 mm, final failure is characterized by concrete crushing without any tensile rebar yielding, as it was expected from the design interaction diagram.

Figures 4-13 and 4-15 show the corroded RC pier's local and global failure mechanisms at stage 3,e, with eccentricities of 30 mm and 75 mm, respectively. For both piers, the damage is localized in the mid-region (corroded zone) at ultimate capacity and failure. As mentioned earlier, it is assumed that cover concrete spalls off at stage 3. Furthermore, even after the loss of three ties at “Stage 3" and the consequent increase in slenderness ratio in zone 3, there is no possibility of elastic buckling of the compressive longitudinal reinforcement in the corrosion zone according to the modified critical strength of corroded rebar proposed by Rodriguez et al. (1996). Inelastic buckling of the longitudinal reinforcing bars results in a possible post-peak softening behaviour in the stress-strain response of the corroded rebars due to the increase in the slenderness ratio up to $\frac{s}{d} = 13 > 8$ (Kashani et al., 2015).

By comparing the minimum principal strains of concrete at the onset of ultimate capacity and failure to the ultimate strain of concrete in Figures 4-13 (a) and (b), it can be observed that core crushing occurs within the mid-height compressive side (zone 3). The same conclusion can be drawn from Figures 4-13 (c) and (d), by comparing the minimum principal stresses in the core concrete with its reduced compressive strength from Table 4-6. The corroded rebars at the middle height of the column are observed to yield (zone 2) and buckle (zone 3) at the onset of ultimate capacity and failure (Figure 4-13, e,f). Figure 4-15 (a-f) shows a similar failure mechanism for the highly corroded RC pier with an eccentricity of 75 mm. Pier failure is governed by crushing the core concrete and yielding the corroded compressive longitudinal reinforcing bars, followed by inelastic buckling at the mid-height of the column (zone 3). By increasing the eccentricity to 75 mm, the maximum tensile rebar stress increases to 50 MPa and 170 MPa at the onset of ultimate capacity and failure, respectively (Figure 4-15, e,f). These stresses are still under the proportional limit of corroded rebars. Both Figures 4-13 and 4-15 illustrate a brittle global failure pattern for heavily corroded piers (stage 3,e) under axial load eccentricity of 30 mm and 75 mm, attributed to the localized damage in zone 3 at the mid-height of the in-service piers (assumed to be the region observed with the most damage in in-service bridge piers).

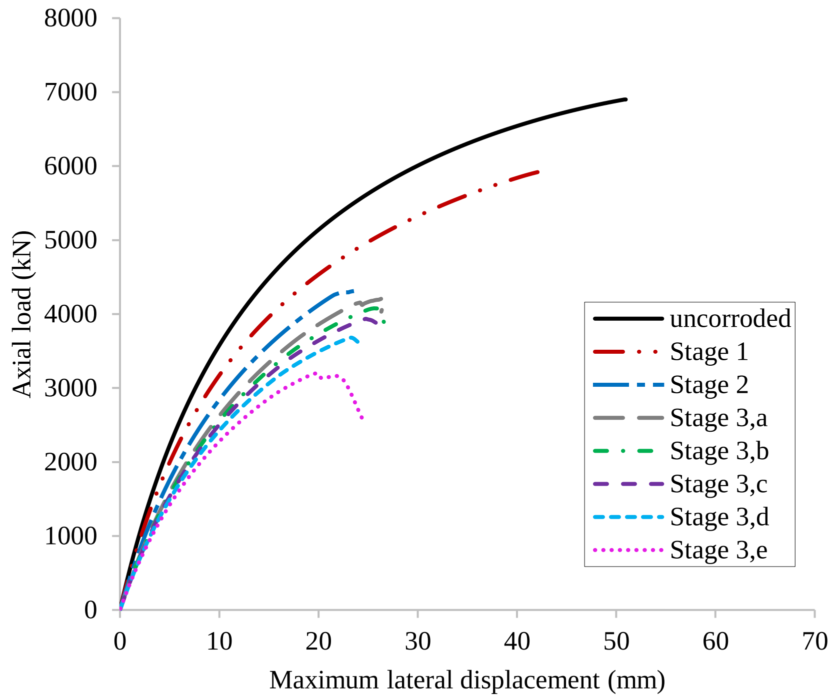

Figure 4-7 Load-top lateral displacement of RC column at different stages of corrosion with an eccentricity of $e_{\min} = 30$ mm

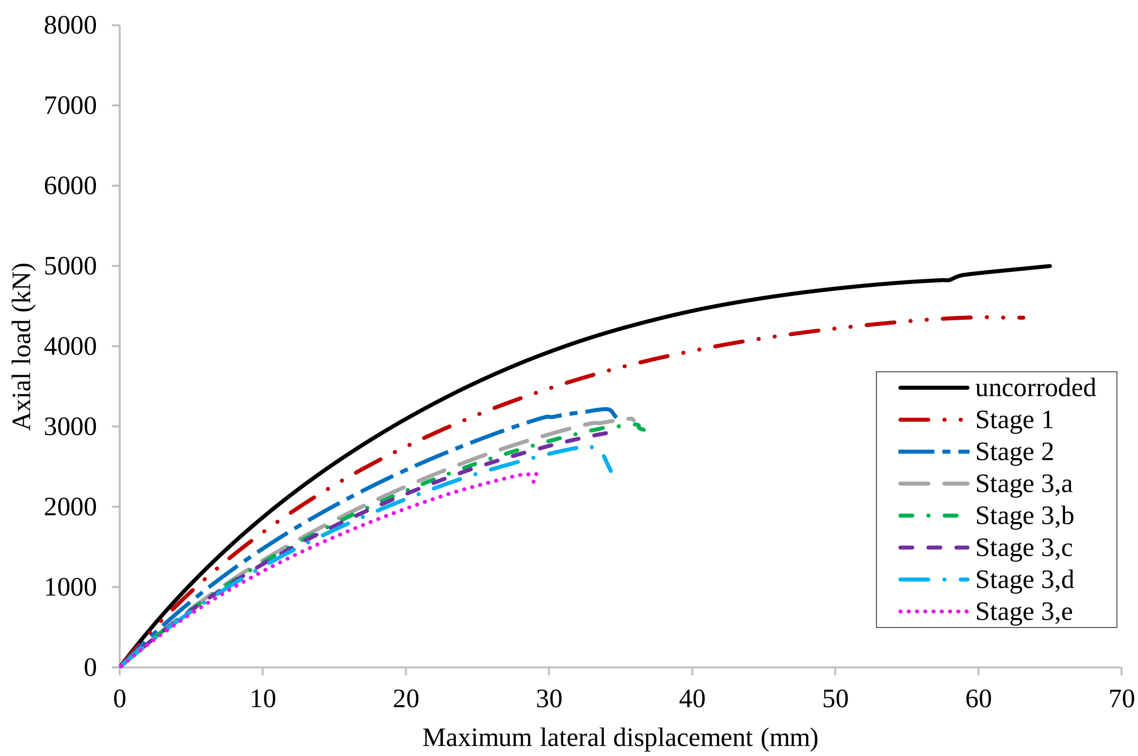

Figure 4-8 Load-top lateral displacement of RC column at different stages of corrosion with an eccentricity of $e_p = 75$ mm

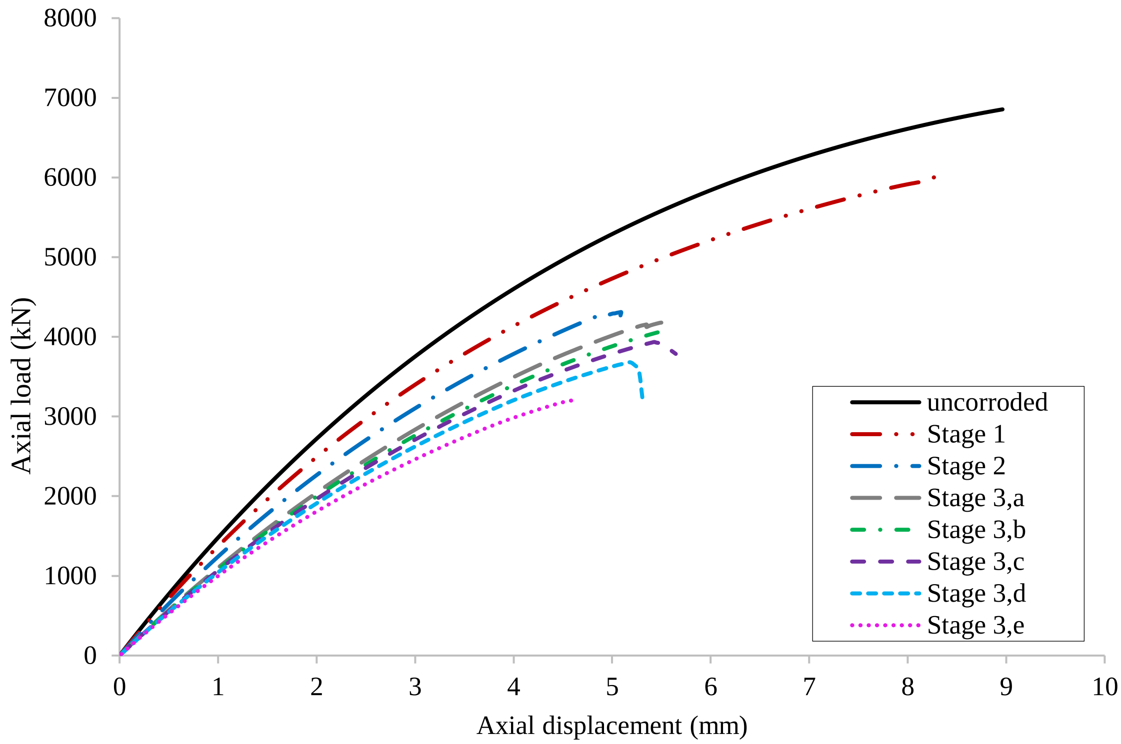

Figure 4-9 Load-axial displacement of RC column at different stages of corrosion with an eccentricity of $e_p = 30$ mm

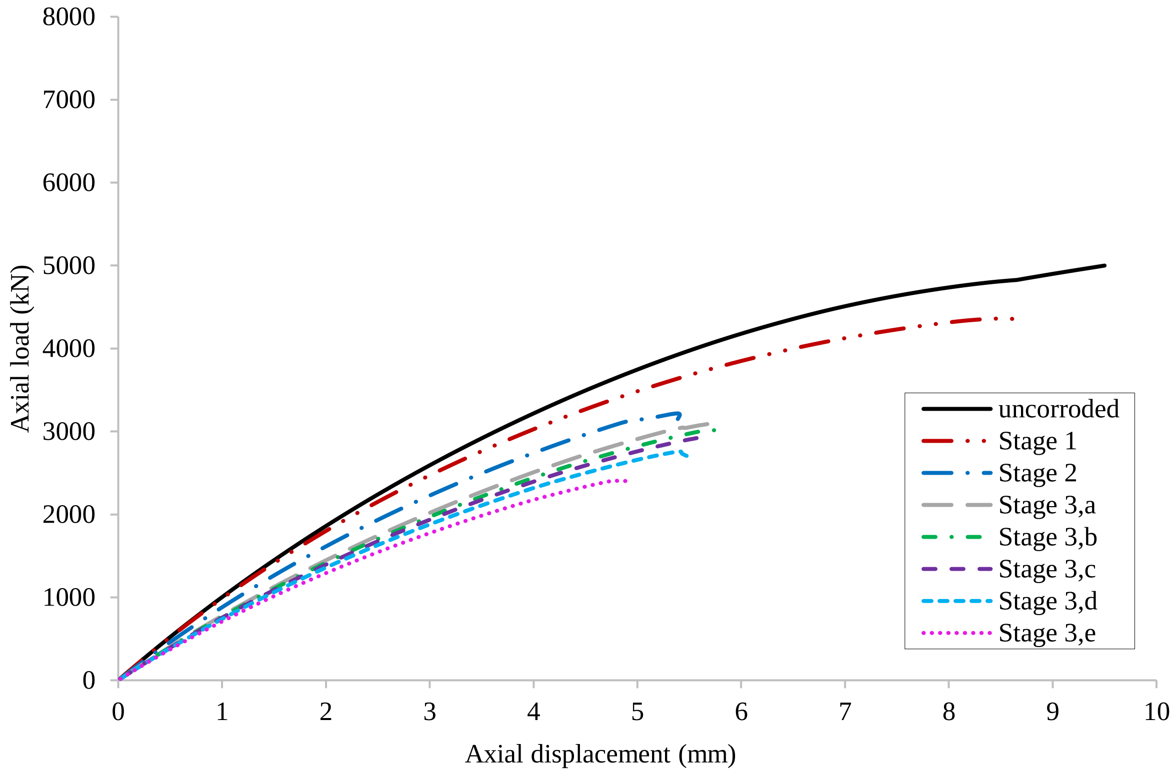

Figure 4-10 Load-axial displacement of RC column at different stages of corrosion with an eccentricity of $e_p = 75$ mm

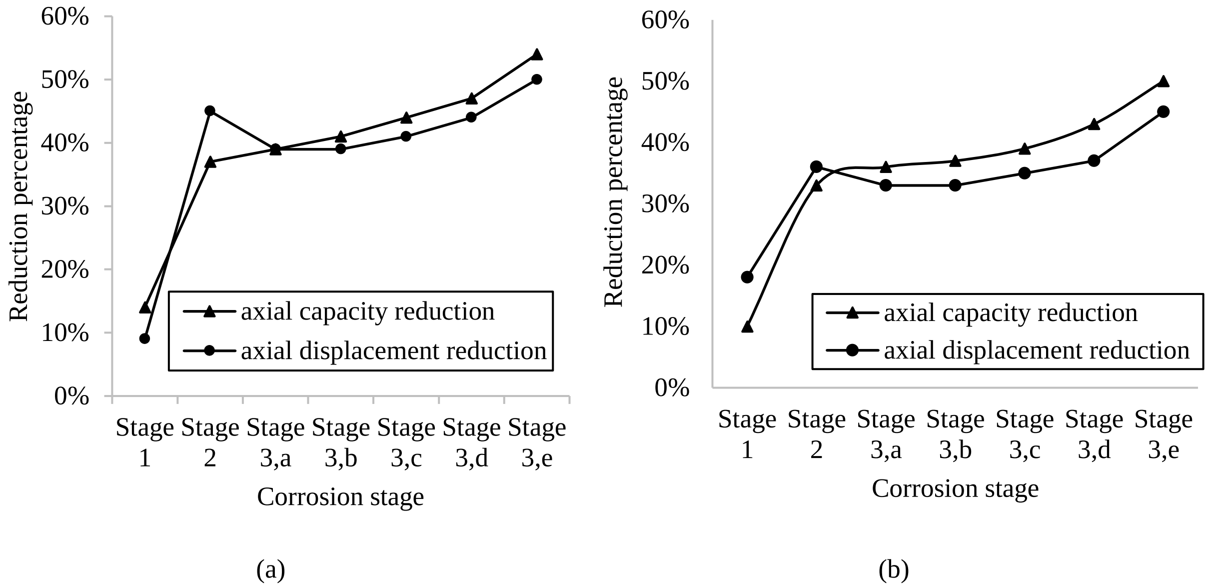

Figure 4-11 Reduction of axial capacity and displacement with respect to the uncorroded column under eccentricity of (a) 30 mm, (b) 75 mm

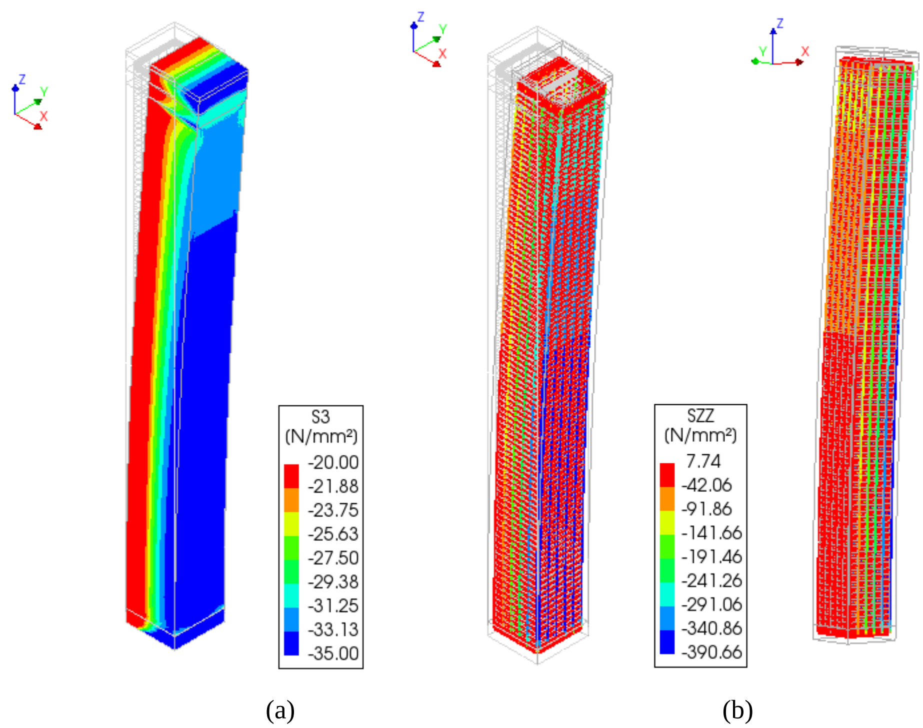

Figure 4-12 Failure pattern of the uncorroded pier with minimum eccentricity ($e_{\min} = 30$ mm): (a) minimum principal stresses at ultimate capacity, (b) reinforcement Cauchy total stresses in the z-direction at ultimate capacity

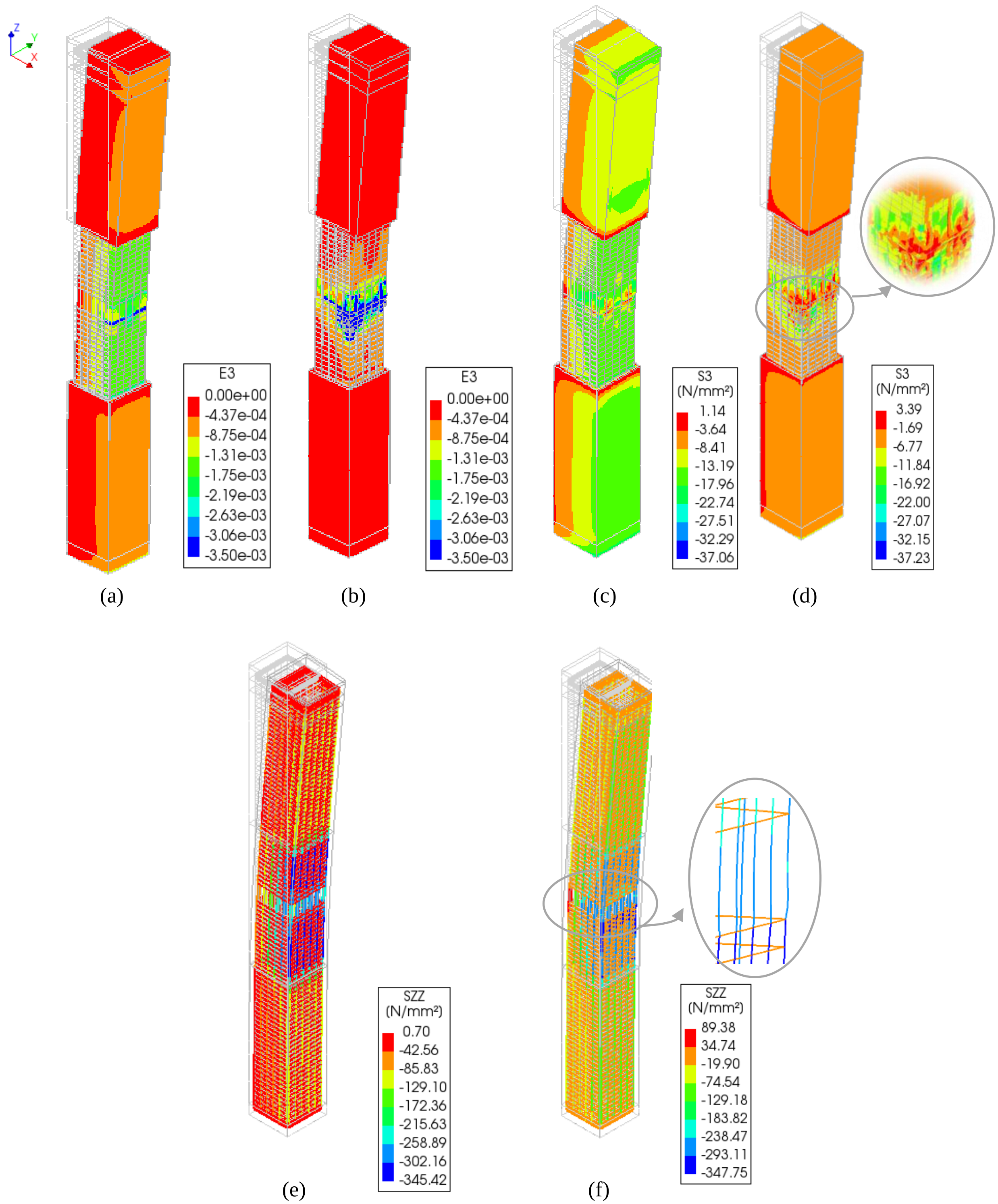

Figure 4-13 Failure pattern of the pier at "Stage 3,e" under minimum eccentric load ($e_{\min} = 30$ mm): (a) minimum principal strains at the onset of ultimate capacity, (b) minimum principal strains at the failure point, (c) minimum principal stresses at the onset of ultimate capacity, (d) minimum principal stresses at failure point, (e) reinforcement Cauchy total stresses in the z-direction at the onset of ultimate capacity, (f) reinforcement Cauchy total stresses in the z-direction at the failure point

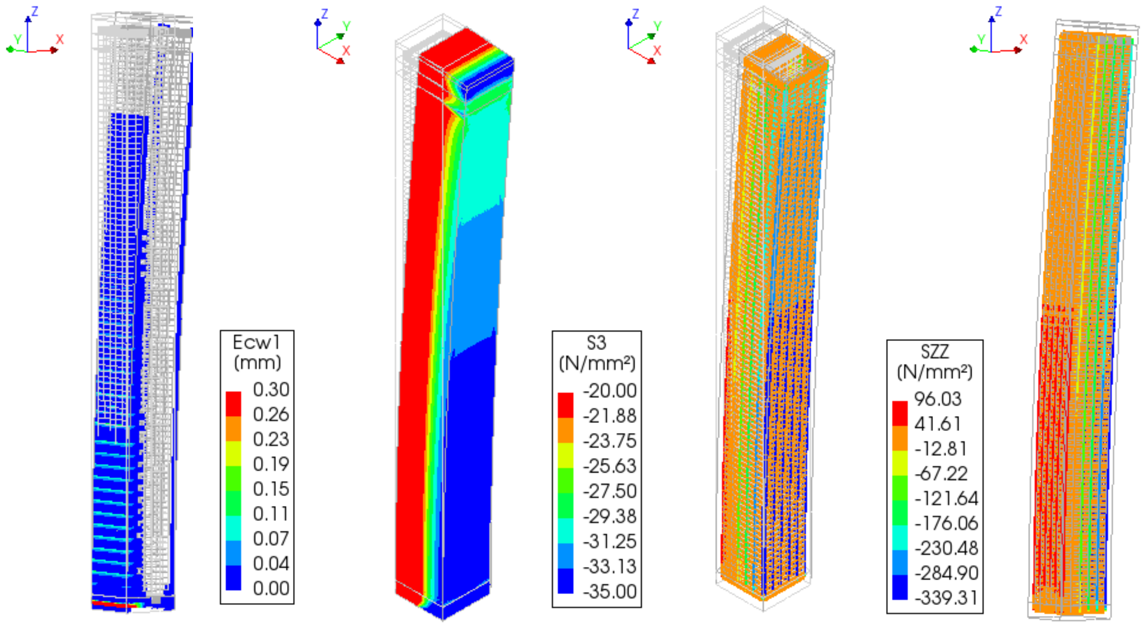

(a) (b) (c)

Figure 4-14 Failure pattern of the uncorroded pier with allowable practical eccentricity ($e_p = 75$ mm): (a) crack pattern on the tensile side, (b) minimum principal stresses at ultimate capacity, (c) reinforcement Cauchy total stresses in the z-direction at ultimate capacity

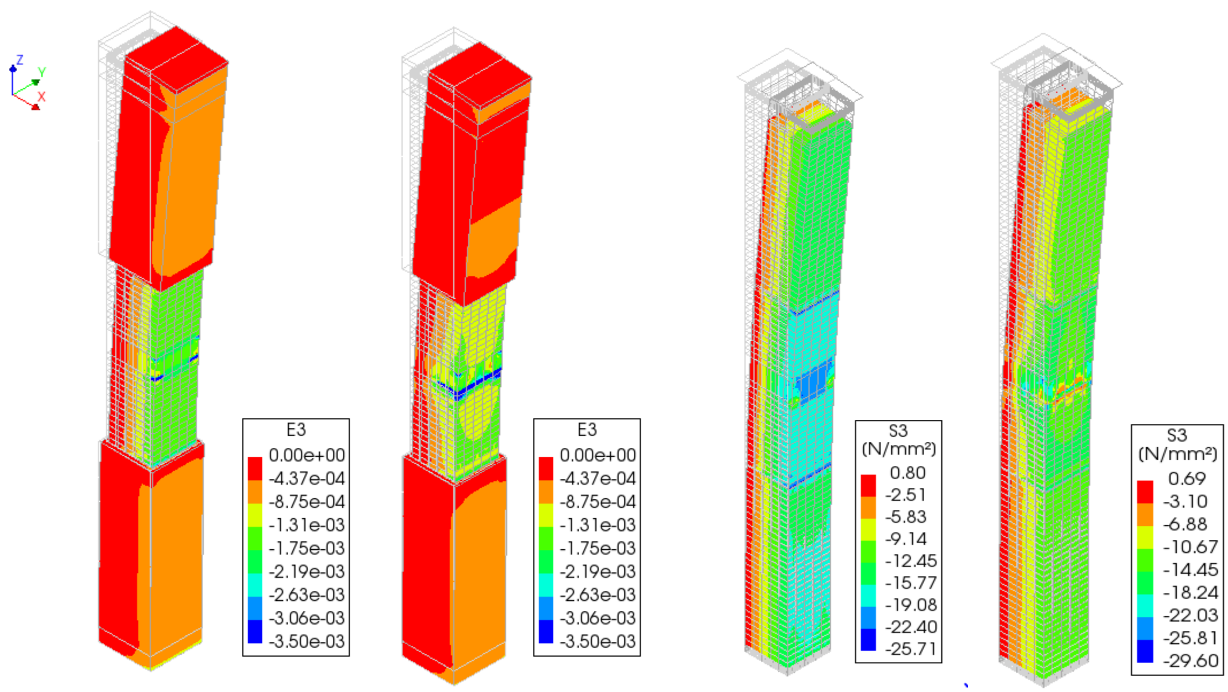

(a) (b) (c) (d)

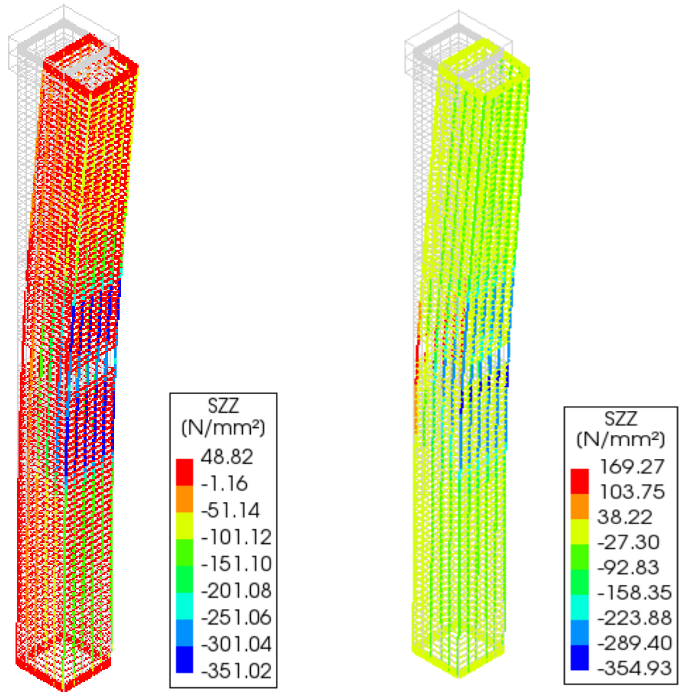

(e) (f)

Figure 4-15 Failure pattern of the pier at "Stage 3,e" under maximum practical eccentricity ($e_{min} = 75$ mm): (a) minimum principal strains at the onset of ultimate capacity, (b) minimum principal strains at failure, (c) minimum principal stresses at the onset of ultimate capacity, (d) minimum principal stresses at failure, (e) reinforcement Cauchy total stresses in the z-direction at the onset of ultimate capacity, (f) reinforcement Cauchy total stresses in the z-direction at failure

4.4.3.2 M_u–N_u interaction diagram

Generally, the actual axial and moment resistance of RC columns subjected to combined axial loads and moments are related through the M_u–N_u interaction diagram. The interaction diagrams of the RC pier at different stages of its service life (uncorroded and corroded at stages 1, 2, and 3b) were generated based on the proposed 3D NLFEA, illustrated in Figure 4-16. The interaction diagram shows the nominal axial load resistance $N_u = 0.75N_{r0}$ as given in CSA S6:19, in which N_{r0} is the nominal pure axial capacity based on the present FE model. The M_u shows the nominal moment resistance of the pier. The contraction of the interaction diagram and LOCR increase for a specific applied service load as corrosion-induced damage in the RC pier accumulates, going from the uncorroded stage to stage 3, is evident in Figure 4-16. In Figure 4-16, the range of allowed and practical eccentricities as dictated by the code for bridge piers (CSA S6:19) are shown as Line 1 and Line 2. The area of the interaction diagram at each stage of corrosion, bounded by Line 1 and Line 2, is an indicator of the safe zone. Going from stage 1 to stage 2, it is assumed that the cover spalls off and the middle longitudinal rebars and ties lose connection, which causes a loss in stiffness and an increasing in eccentricity. This is the main reason that leads to the bilinear pattern of lines 1 and 2 in Figure 4-16.

For a load combination leading to steel-controlled failure, the present 3D NLFEA results in the failure mechanism that would be expected. As an example, the 3D NLFEA framework was conducted on the RC pier subjected to an axial load with an eccentricity $e = 220\ \text{mm}$ and assumed to have corrosion-induced deterioration corresponding to stage 2. The failure characteristics of the corroded pier are shown in Figure 4-17. Global failure starts with flexural cracks development on the tensile side of the pier (Figure 4-17, b), followed first by yielding of corroded tensile reinforcement and then by yielding of corroded compressive reinforcement in zone 2 (Figure 4-17, c). According to the stress-strain response of corroded compressive longitudinal reinforcing bars at stage 2 (Figure 4-6, e), the rebars follow a hardening post-peak response without buckling due to the small slenderness ratio. Concrete on the compressive side of the pier is observed to reach the onset of crushing by comparing the minimum principal strain with the ultimate concrete strain (Figure 4-17, a).

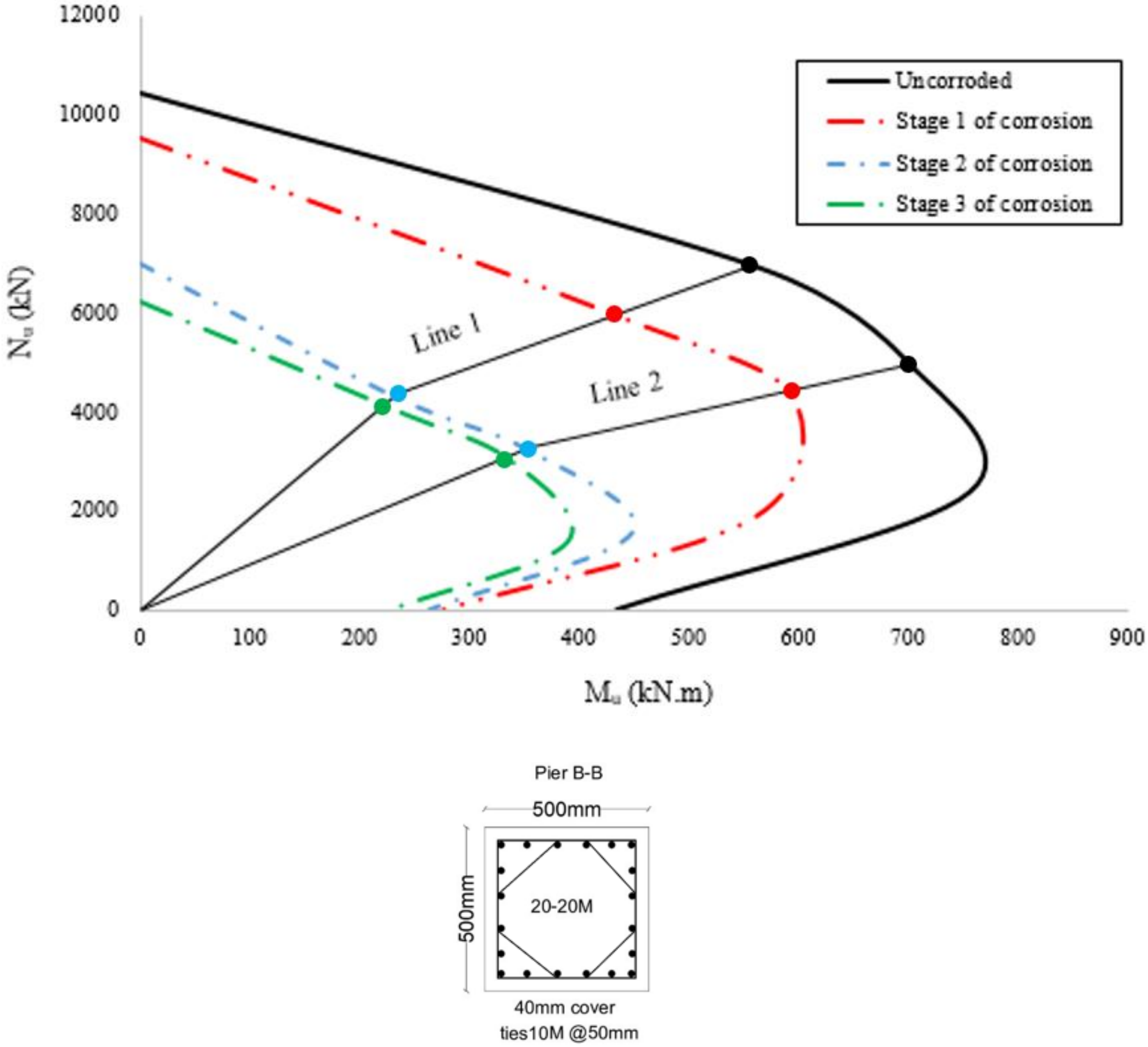

Figure 4-16 Interaction diagram of the RC pier at different corrosion stages

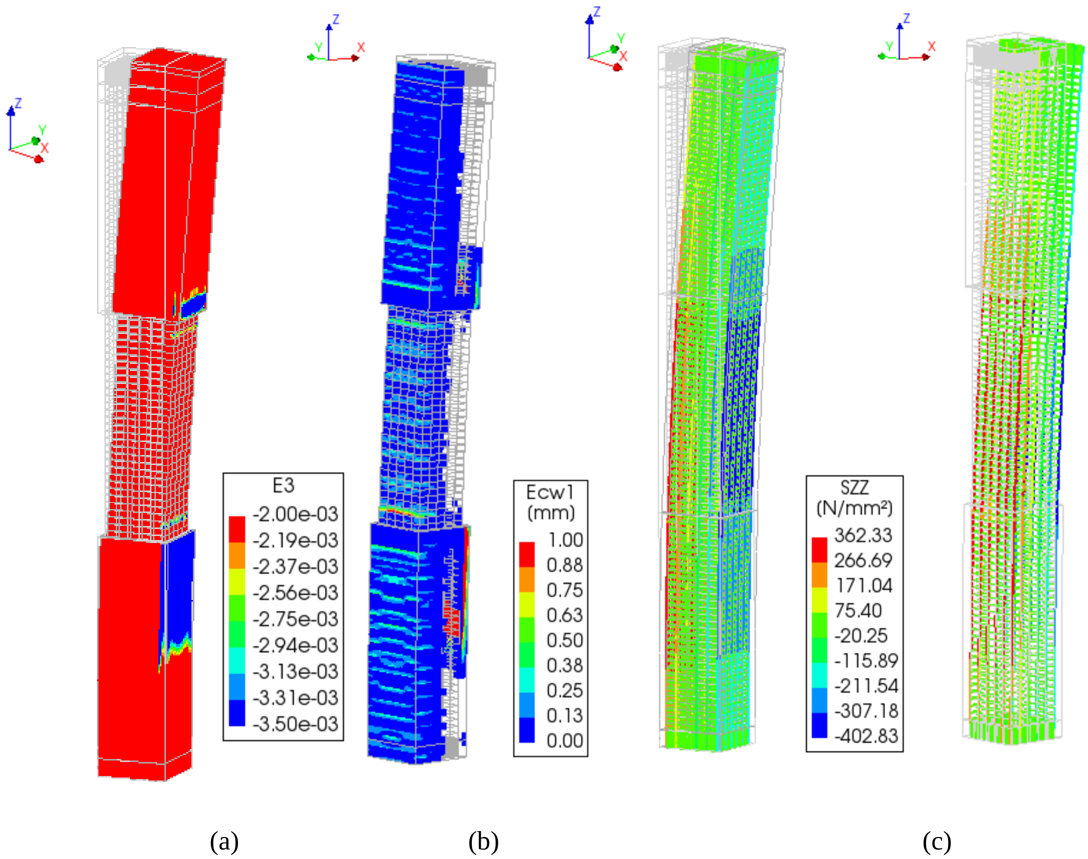

Figure 4-17 Failure pattern of the pier at "Stage 2" with an eccentricity of $e = 220$ mm: (a) minimum principal strains at the onset of ultimate capacity, (b) cracking pattern, (c) reinforcement Cauchy total stresses in the z-direction at the onset of ultimate capacity (tensile and compressive side)

4.5 Summary and conclusions

In the present study, a comprehensive NLFEA was proposed to investigate the structural performance of RC bridge piers subjected to the combination of staged corrosion-induced damage and axial load at different eccentricities. A comprehensive corrosion damage model was adopted from the literature. The corrosion was simulated by incorporating the reinforcement mechanical and geometrical degradation, concrete core and cover deterioration, and bond-slip response degradation. In the present model, the mid-third of the bridge pier was assumed to be subjected to possible corrosion-induced damage. A stage-based corrosion scenario was then assumed and introduced during different stages of the bridge's service life. Three comprehensive corrosion stages were studied in the proposed scenario: stage 1, stage 2, and stage 3. The results show a gradual reduction in the ultimate capacity, ductility, and rigidity of the pier by increasing the corrosion level to stage

3. The present model is efficiently and quantitatively capable of capturing the failure mechanism of the corroded bridge pier under eccentric load. The corroded pier (at all stages of damage) subjected to smaller eccentricities was observed to follow a compression-controlled failure mechanism by concrete core crushing, compressive corroded rebar yielding and post-yield buckling at the middle height of the pier (corroded zone). The present model can also capture the tension-controlled failure mechanism in RC pier with larger eccentricities. The ultimate capacity occurs due to increased tensile stresses, consequent formation and growth of cracks and yielding of tensile corroded rebars, followed by yielding of compressive longitudinal reinforcing bars and crushing of the concrete core in the corroded region at the middle height of the pier.

A gradual reduction of corroded piers' capacity to unsafe levels and the possibility of an increase in traffic intensity should be considered as leading contributions to a significant increase in the load-over-capacity ratio of the bridge piers. The present methodology proposes a quantitative tool to evaluate the corrosion-induced capacity reduction in the bridge piers during their service life.

4.6 References

AASHTO. (2020). AASHTO LRFD Bridge Design Specifications — U.S. Units, 6th Edition, American Association of State High way and Transportation Officials.

Almusallam, A. A. (2001). "Effect of degree of corrosion on the properties of reinforcing steel bars." Construction and Building Materials, 15(8), 361–368.

Andersen, A. (1997). HETEK, Investigation of chloride penetration into bridge columns exposed to de-icing salt-report No.82. Danish Road Directorate, Copenhagen, 37pp.

Bastidas-Arteaga, E., Chateauneuf, A., Sánchez-Silva, M., Bressolette, P., and Schoefs, F. (2010). "Influence of weather and global warming in chloride ingress into concrete: A stochastic approach." Structural Safety, Elsevier Ltd, 32(4), 238–249.

Blomfors, M., Zandi, K., Lundgren, K., and Coronelli, D. (2018). "Engineering bond model for corroded reinforcement." Engineering Structures, 156, 394–410.

Cairns, J., Plizzari, G., Du, Y., Law, D., and Franzoni, C. (2005). “Mechanical properties of corrosion-damaged reinforcement.” ACI Materials Journal, 102(4), 256–264.

Di Carlo, F., Meda, A., and Rinaldi, Z. (2017). “Numerical evaluation of the corrosion influence on the cyclic behaviour of RC columns.” Engineering Structures, Elsevier, 153, 264–278.

Chernin, L., and Val, D. V. (2011). “Prediction of corrosion-induced cover cracking in reinforced concrete structures.” Construction and Building Materials, Elsevier Ltd, 25(4), 1854–1869.

Coronelli, D., and Gambarova, P. (2004). “Structural assessment of corroded reinforced concrete beams: Modeling guidelines.” Journal of Structural Engineering, 130(8), 1214–1224.

CSA. (2019). “CSA S6:19 Canadian Highway Bridge Design Code, CSA Group, Toronto.” CSA Group, Toronto, Ontario.

Deng, P., Zhang, C., Pei, S., and Jin, Z. (2018). “Modeling the impact of corrosion on seismic performance of multi-span simply-supported bridges.” Construction and Building Materials, Elsevier Ltd, 185, 193–205.

Dhakal, R. P., and Maekawa, K. (2002). “Modeling for postyield buckling of reinforcement.” Journal of Structural Engineering, 128(9), 1139–1147.

Diana. (2019). “DIANA Finite Element Analysis, User’s Manual, Release 10.” TNO Building and Construction Research, Delft, Netherlands.

Du, Y. G., Clark, L. A., and Chan, A. H. C. (2005). “Effect of corrosion on ductility of reinforcing bars.” Magazine of Concrete Research, 57(7), 407–419.

Federal Highway Administration. (2001). Reliability of Visual Inspection for Highway Bridges Volume I: Final Report.

Joshi, J., Arora, H. C., and Sharma, U. K. (2015). “Structural performance of differently confined and strengthened corroding reinforced concrete columns.” Construction and Building Materials, 82, 287–295.

Kashani, M. M., Crewe, A. J., and Alexander, N. A. (2013). “Nonlinear stress-strain behaviour of corrosion-damaged reinforcing bars including inelastic buckling.” Engineering Structures, 48, 417–429.

Kashani, M. M., Crewe, A. J., and Alexander, N. A. (2017). “Structural capacity assessment of corroded RC bridge piers.” Proceedings of the Institution of Civil Engineers: Bridge Engineering, 170(1), 28–41.

Kashani, M. M., Lowes, L. N., Crewe, A. J., and Alexander, N. A. (2015). "Phenomenological hysteretic model for corroded reinforcing bars including inelastic buckling and low-cycle fatigue degradation." Computers and Structures, Elsevier Ltd, 156, 58–71.

Kashani, M. M., Maddocks, J., and Dizaj, E. A. (2019). "Residual Capacity of Corroded Reinforced Concrete Bridge Components: State-of-the-Art Review." Journal of Bridge Engineering, 24(7).

Lounis, Z., Vanier, D. J., Daigle, L., Sadiq, R., and Almansour, H. (2010). Framework for Assessment of State, Performance and Management of Core Public Infrastructure, NRC Canada, Project 5332- Final Report.

Lundgren, K. (2002). "Modelling the effect of corrosion on bond in reinforced concrete." Magazine of Concrete Research, 54(3), 165–173.

Lundgren, K. (2005). "Bond between ribbed bars and concrete. Part 1: Modified model." Magazine of Concrete Research, 57(7), 371–382.

Lundgren, K., Kettil, P., Hanjari, K. Z., Schlune, H., and Roman, A. S. S. (2012). "Analytical model for the bond-slip behaviour of corroded ribbed reinforcement." Structure and Infrastructure Engineering, 8(2), 157–169.

Maaddawy, N. E., Soudki, K., and Topper, T. (2005). "Analytical model to predict nonlinear flexural behavior of corroded reinforced concrete beams." ACI Structural Journal, 102(4), 550–559.

Mohammed, A. M. (2014). "Semi-Quantitative Assessment Framework for Corrosion Damaged Slab-on-Girder Bridge Columns Using Simplified Nonlinear Finite Element Analysis, Ph.D. Thesis." University of Ottawa.

Molina, F. J., Alonso, C., and Andrade, C. (1993). "Cover cracking as a function of rebar corrosion : Part 2—Numerical model." Materials and Structures, 26, 532–548.

Ontario Ministry of Transportation. (2008). Ontario Structure Inspection Manual (OSIM), Policy, planning & Standards division engineering standards branch bridge office;

Rodriguez, J., Ortega, L. M., and Casal, J. (1996). "Load bearing capacity of concrete columns with corroded reinforcement." 4th Int. Symp. on Corrosion of Reinforcement in Concrete Construction, 220–30.

Saatcioglu, M., and Razvi, S. R. (1992). "Strength and ductility of confined concrete." Journal of Structural Engineering (ASCE), 118(6), 1590–1607.

Saito, Y., Oyado, M., Yasojima, A., Kanakubo, T., and Yamamoto, Y. (2007). "Structural Performance of Corroded RC Column under Uniaxial Compression Load,." First International Workshop on Performance, Protection & Strengthening of Structures under Extreme Loading, Whistler, Canada.

Vu, N. S., Yu, B., and Li, B. (2017). “Stress-strain model for confined concrete with corroded transverse reinforcement.” Engineering Structures, 151, 472–487.

Wang, X. H., and Liang, F. Y. (2008). “Performance of RC columns with partial length corrosion.” Nuclear Engineering and Design, 238(12), 3194–3202.

Xia, J., Jin, W. L., and Li, L. Y. (2016). “Performance of corroded reinforced concrete columns under the action of eccentric loads.” Journal of Materials in Civil Engineering, 28(1).

Zaghian, S., Martín-Pérez, B., and Almansour, H. (2022). “Nonlinear Finite Element Modeling of the Impact of Reinforcement Corrosion on Bridge Piers under Concentric Loads.” Structural Concrete, 23(1), 138-153, https://doi.org/10.1002/suco.202100254.

Zaghian, S., Martín-Pérez, B., and and Almansour, H. (2020). “The effect of corrosion and traffic loads on bridge columns using three-dimensional non-linear finite element analysis.” CACRCS 2020 Capacity Assessment of Corroded Concrete Structures.

Zandi, K. (2015). “Corrosion-induced cover spalling and anchorage capacity.” Structure and Infrastructure Engineering, 11(12), 1547–1564.

Chapter 5: Nonlinear Finite Element Modelling of Bridge Piers under the Combined Effect of Corrosion, Freeze-Thaw Cycles, and Service Load[3]

Abstract

Corrosion of reinforcing steel in reinforced concrete (RC) infrastructure is one of the most concerning durability problems affecting its serviceability and ultimate capacity in North America. The rise of greenhouse emissions in recent decades and the use of de-icing salts during the winter increase the potential risk of corrosion. Furthermore, global warming could lead to higher freeze-thaw cycles (FTC) frequency in cold regions. The combined effects of corrosion and frost damage tend to affect ageing RC infrastructure's structural performance and service life. The present study adopts comprehensive reinforcement corrosion and frost damage models from the literature and proposes a stage-based damage analysis scenario. Three-dimensional nonlinear finite element analyses using the commercially available finite element program DIANA are conducted to evaluate the structural performance of RC bridge piers under the synergetic effects of FTCs, corrosion, and service load during their service life. The proposed methodology for each damage mechanism is assessed by comparison with available experimental data from the literature. The synergetic effects cannot be validated because there is no data, but the methodology highlights the deterioration rate at which several mechanisms acting at the same time can affect the structural performance of these members.

[3]This chapter is published in *Structural Concrete* (Zaghian, S., Martín-Pérez, B., Almansour, H., and Shirkhani, H. (2023). "Nonlinear finite element modelling of bridge piers under the combined effect of corrosion, freeze-thaw cycles, and service load." Structural Concrete, Published online ahead of print February 28th, 2023. https://doi.org/10.1002/suco.202200370). The paper is the own work of the candidate; author H. Shirkhani has contributed to the climate data analysis obtained from Environment and Climate Change Canada.

5.1 Introduction

Chloride-induced corrosion of reinforcing steel due to the use of de-icing salts in winter and frost damage due to freeze and thaw cycles (FTCs) are known as the prevalent deteriorating mechanisms of reinforced concrete (RC) infrastructure in Canada. While there has been a growing number of studies on the effects of corrosion on the mechanical properties of reinforcing bars, concrete, bond properties between rebars and concrete (Berra et al. 1997, Coronelli and Gambarova 2004, Kashani et al. 2013) and structural performance of RC members (Xia et al. 2016a, Deng et al. 2018, Mohammed 2014) in the last two decades, the structural performance of RC members, especially RC columns damaged by FTCs or synergetic effects of corrosion and FTCs, has been studied scarcely.

The degrading effects of pitting and uniform corrosion on the material properties of steel and concrete have been observed as rebar cross-sectional loss (Faraday's law), rebar's pit-induced ductility degradation (Cairns et al. 2005), the possibility of elastic and inelastic buckling of corroded rebars due to the rebar's cross-sectional reduction and confinement degradation (Rodriguez et al. 1996b, Kashani et al. 2015), reduction in compressive strength of the concrete cover due to possible cracking and spalling (Coronelli and Gambarova 2004), loss of partial confinement, and bond behaviour degradation (Berra et al. 1997, Lundgren 2001). Some studies have expressed the effect of corrosion on the strength and ductility of steel rebars as a function of corrosion-induced steel mass loss (Almusallam 2001, Du et al. 2005). Longitudinal rebar's cross-sectional loss and transverse reinforcement corrosion followed by loss of partial confinement increase the possibility of longitudinal rebar buckling, which is considered a critical corrosion outcome in RC columns. Corrosion increases the possibility of rotation between ties and longitudinal reinforcement, leading to loss of the full-fixity condition. Based on Rodriguez et al.'s recommendation, increasing the effective length in Euler's elastic critical strength formula to 75% of the tie spacing allows the incorporation of the possibility of corroded rebars' elastic buckling (Rodriguez et al. 1996b). It is also crucial to consider the possibility of inelastic buckling of corroded rebars in earthquake zones. To this end, a compressive stress-strain response for corroded rebar based on the Dhakal–Maekawa buckling model (Dhakal and Maekawa 2002) was developed (Kashani et al. 2013), and the effect of different corrosion levels on the inelastic buckling behaviour of steel reinforcement was evaluated (Kashani et al. 2013). Coronelli and Gambarova (2004) proposed an expression to reduce the compressive strength of the concrete in the presence of corrosion-induced cracking, adopting the model developed by Vecchio and Collins (1986). Over the past few decades, many studies have also been conducted on the adverse effects of corrosion-induced product expansion on RC members' bond-slip behaviour (Lundgren 2005a, Blomfors et al. 2018). The structural performance of small-scale corroded RC columns has been studied experimentally (Saito et al. 2014, Xia et al. 2016a), with few numerical studies also investigating the seismic performance of corroded RC columns (Mohammed 2014, Kashani et al. 2017). In a recent study, the authors investigated the structural performance of real-scale corroded RC bridge piers under the combination of different levels of corrosion and concentric traffic load (Zaghian et al. 2022).

There are also numerous studies on the primary mechanism of frost damage and concrete mechanical properties degradation induced by FTCs (Petersen et al. 2007, Li et al. 2017). Frost attacks the concrete externally due to thermal expansion differential between ice and concrete, which appears as scaling or spalling of the surface concrete, or internally due to volume expansion inside the concrete pore structure, which appears as mechanical properties deterioration resulting in cracking and quality degradation of the concrete (Zandi Hanjari et al. 2013). Currently, several standards are used in different countries to test small-scale non-reinforced concrete members under FTCs, such as ASTM C666 (C666/C666M-15 2015), GB/T 50082-2009 (GB/T50082-2009 2009), and RILEM TC 117-CDF (RILEM TC-117 FDC - 1993). These standards have specific test conditions, such as the number of FTCs, specimens' size, cycle duration, specimen age, and temperature range. Researchers conducting studies on frost-damaged RC structural members need to use an equivalent number of cycles convertible to one of the abovementioned standards to compare the results based on their studies to those based on others (Berto et al. 2015). Many researchers have widely investigated the behaviour of frost-damaged concrete in tension and compression (Li et al. 2017, Hanjari et al. 2011b, Hasan et al. 2008). A significant reduction of frost-damaged concrete modulus of elasticity has been reported extensively (Shang and Song 2006, Petersen et al. 2007, Li et al. 2017). Many researchers have also studied the deteriorating effect of frost damage on the bond behaviour (Petersen et al. 2007, Zandi Hanjari et al. 2009a). While the frost damage mechanisms and effects of FTCs on the mechanical behaviour of concrete have been evolving research topics during the last decades, a reliable assessment method to predict the load-carrying capacity and remaining service life of frost-damaged RC structures is crucial for repair strategy and optimized maintenance plans. To the best of the authors' knowledge, not enough attention has been given to the real-scale structural behaviour of frost-damaged RC members, especially RC columns. Only a few studies have investigated the destructive effects of frost damage on the load-deflection capacity of RC beams (Hassanzadeh and Fagerlund 2006, Petersen et al. 2007, Zandi Hanjari et al. 2013). Qin et al. (2017) studied the seismic behaviour of RC columns subjected to FTCs. In this study, four identical columns were tested experimentally, undergoing 0, 100, 200, and 300 FTCs according to the Chinese code GB/T50082-2009 (GB/T50082-2009 2009). The specimens were then assembled onto a foundation, and low cyclic loading was applied at the top of the columns. The results were then verified by comparing to those based on simulations for hysteretic response. It was observed that the strength degradation results based on the proposed finite element (FE) simulation and the experimental tests were in good agreement before the peak point, and they were slightly different after the peak due to ignoring the bond-slip behaviour in the implemented freeze-thaw damage model. It was also observed that FTC deterioration did not tend to change the column's failure mode, and all the columns experienced flexural failure. Liu et al. (2019) conducted a seismic fragility analysis on recycled aggregate concrete (RAC) bridge columns damaged by FTCs. In this study, the authors adopted the earlier published experimental data (Liu et al. 2018a) and developed a new freeze-thaw damage model. The damage model was then integrated into the FE software OpenSees. It was observed that by increasing the number of FTCs and recycled coarse aggregate, the fragility increases significantly.

There is still a scarcity of numerical studies on the effects of frost damage or synergetic effects of corrosion and frost damage on real-scale RC bridge piers under service load. Only a few studies have investigated the synergetic effects of frost damage and corrosion on the structural performance of small-scale RC members experimentally (Diao et al. 2011, Diao et al. 2012, Dabas et al. 2019). The present study aims to address this gap; the structural performance of an ageing large-scale RC bridge pier under the synergetic effect of corrosion, FTCs, and concentric/eccentric load is investigated by conducting a stage-based three-dimensional nonlinear finite element analysis (3D-NLFEA). Comprehensive reinforcement corrosion and frost damage models are adopted from the literature. Previously tested damaged RC beams and columns are modelled, and the results are then compared to those based on available test data to assess the accuracy of the adopted damage models and proposed methodology. The synergistic effect of corrosion and frost damage on the designed RC bridge pier is defined as a staged phenomenon during the bridge service life, and at each stage, it is simulated by incorporating all the deteriorating effects adopted from the literature. The combined damage model is then incorporated into the finite element model to investigate the structural performance of the ageing bridge pier over time.

5.2 Proposed 3D nonlinear finite element model

5.2.1 General

A 3D-NLFEA is carried out in the present study using DIANA (a commercial finite element software package (Diana 2019). In the proposed stage-based analysis, different corrosion and frost-damage stages are defined to incorporate the effects of variable deteriorating factors over the bridge's service life, explained in detail in the following sections. The adopted corrosion damage model was explained in detail in an earlier study by the authors (Zaghian et al. 2022). The corrosion-induced deteriorating effects include rebar’s cross-sectional loss, rebar’s ductility degradation (Cairns et al. 2005), rebar’s compressive stress-strain response degradation (possibility of elastic and inelastic buckling) (Rodriguez et al. 1996b, Kashani et al. 2013), confinement degradation, and bond-slip response degradation (Blomfors et al. 2018). A summary of the adopted corrosion damage model is tabulated in Table 5-1. The adopted frost damage model is explained in the following section. In the proposed 3D-NLFEA, concrete is modelled by adopting solid brick and wedge elements, and the confinement effect is incorporated by adopting the confinement model by Saatcioglu and Razvi (1992). A regular Newton-Raphson iterative method is used along with the "Total Lagrange" as the geometrically nonlinear analysis.

Table 5-1 Summary of the adopted corrosion damage model

Reference	Deteriorating effects	Equation
NA	Rebar cross-section loss	$X_{corr} = \frac{d_b{}^2 - d_{b,corr}{}^2}{d_b{}^2} \times 100$
Cairns et al. (2005)	Rebar's ductility degradation	$\varepsilon_{ut,cor} = [1.0 - 100 \times \alpha_1 . X_{corr}]\varepsilon_{ut}$
Rodriguez et al. (1996a)	Possibility of elastic buckling	$\sigma_{cr,corr} = \pi^2 E\left(0.25 d_{b,corr}\right)^2 / (0.75 s_{corr})^2$

Kashani et al. (2013)	Possibility of inelastic buckling	$\eta=\sigma/f_{yc,corr}=\begin{cases}\xi=\varepsilon/\varepsilon_{yc,corr} & \xi\le 1\\ \frac{\eta_2-1}{\xi_2-1}(\xi-1)+1 & 1<\xi\le 2\\ \eta_2-0.02(\xi-\xi_2) & \xi_2\le\xi \,\&\, \eta\ge 0.2\\ 0.2 & otherwise\end{cases}$ $\xi_2=\max\{55-2.3\lambda_{p,corr};7\}$ $\eta_2=\max\{\alpha(1.1-0.016\lambda_{p,corr})\eta^{*}{}_2;0.2\}$ $\lambda_p=\sqrt{\frac{f_{yc,corr}}{100}}\frac{s}{d_b-2x_{cp}}$ $f_{yc,corr}=f_{yc}\left[1-100\times\beta.X_{corr}\right]$; $\beta=\begin{cases}0.005 & s/d_b\le 5\\ 0.0065 & 5<s/d_b\le 10\\ 0.0125 & s/d_b>10\end{cases}$
Coronelli and Gambarova (2004)	Cover concrete cracking	$f_{c,cor}=\frac{f_c}{1+K\varepsilon_1/\varepsilon_{c0}}$, $\varepsilon_1=2\pi n_{bars}(\nu_{rs}-1)x_{cp}/b_0$
Saatcioglu and Razvi (1992)	Confinement degradation	By substituting degraded values into the confinement model by Saatcioglu and Razvi(Saatcioglu and Razvi 1992)
Blomfors et al. (2018)	Degraded bond-slip response	$\tau_{bu,spilit,red}=\eta_2.6.5.\left(\frac{f_c}{25}\right)^{0.25}\left(\frac{25}{d_b}\right)^{0.2}(1+k_m.k_{tr})$ $\tau_{res,\mathrm{mod}}(k_{tr})=\begin{cases}(0.16+12k_{tr}).\tau_{bu,spilit,red} & for\quad 0\le k_{tr}\le 0.02\\ 0.4\tau_{bu,spilit,red} & for\quad 0.02<k_{tr}\end{cases}$

where d_b and $d_{b,corr}$ are the un-corroded and corroded rebar diameter, respectively; ε_{ut} and $\varepsilon_{ut,corr}$ are the ultimate tensile strain of uncorroded and corroded rebar, respectively; s_{corr} is tie spacing considering the possible loss of one or more ties; η and ξ are non-dimensional compressive stress and strain, respectively; α is a softening coefficient; s is the tie spacing; $\eta^{*}{}_2$ is the non-dimensional stress corresponding to ξ_2 (in case of no buckling); $f_{yc,corr}$ is the compressive strength of corroded rebar; and, λ_p and $\lambda_{p,corr}$ are the non-dimensional buckling parameters of the un-corroded and corroded rebar, respectively; f_c and $f_{c,cor}$ are the compressive strength of undamaged and damaged concrete, respectively; $K=0.1$ is adopted by assuming ribbed bars with medium diameter; ε_{c0} is the concrete strain at the peak compressive strength (taken as 0.002); ε_1 is the average tensile strain perpendicular to compression; n_{bars} is the number of corroding rebars; $\nu_{rs}=2$ is the volume expansion ratio and is adopted from Molina et al(Molina et al. 1993); x_{cp} is the corrosion penetration depth and is calculated as $x_{cp}=\frac{d_b}{2}\left[1-\sqrt{1-X_{corr}}\right]$(as mentioned in Deng et al.(Deng et al. 2018)); b_0 is the width of the un-corroded section; $\tau_{bu,spilit,red}$ is the reduced bond strength and $\tau_{res,\mathrm{mod}}(k_{tr})$ is the reduced residual bond capacity; variables η_2 , k_m , and k_{tr} have been adopted from the Model Code 2010(Fib 2013).

5.2.2 Modelling frost-damage

During the cold months of Canada, RC bridge piers are susceptible to frost damage, especially in the presence of splashed de-icing salts. The internal damages caused by FTCs are incorporated into the present 3D-NLFEA by changing the concrete mechanical properties. The critical degree of saturation S_{CR} is an essential parameter in defining the frost-induced damage level, which is unique for different concretes (Fagerlund 2004). Even under many FTCs, no damage has been reported in concretes with a saturation degree S below the critical saturation level S_{CR} (Fagerlund 2004). When the saturation degree S is higher than the critical saturation level S_{CR}, the effect of fatigue or repeated FTCs becomes more significant. Fagerlund proposed a linear relationship between the damage level D, defined as the relative reduction in modulus of elasticity ($D = \left(E_c - E_c^d\right)/E_c$), the degree of concrete saturation S and the critical value S_{CR}, as given by Eq. 5.1 (Fagerlund 2004). Variables E_c and E_c^d are respectively the sound and damaged modulus of elasticity of concrete. In the present study, a critical degree of saturation of S_{CR} = 0.77 corresponding to concrete with w/c of 0.4 was used (Romben 1973). Here it is assumed that concrete is fully saturated, i.e., S = 1, which corresponds to the worst case condition.

$$\begin{cases} S \le S_{CR} \quad , \quad D = 0 \\ S > S_{CR} \quad , \quad D = K_N\left(S - S_{CR}\right) \end{cases} \tag{5.1}$$

in which K_N is a coefficient of fatigue taken as $K_N = 1.2N/\left(N+4\right)$, and N is the number of FTCs.

In the present study, frost damage is simulated by incorporating models of frost-induced deteriorating effects proposed in the literature. The primary degradation effects include: degrading the concrete compressive and tensile stress-strain responses and reducing the concrete modulus of elasticity in the concrete cover and core. The frost-damage model proposed by Li et al. (2017) is adopted. In Li et al.'s model, the degraded mechanical performance indexes, modulus of elasticity and concrete tensile strength, were established as a function of the relative compressive strength (ratio of degraded to sound concrete compressive strength) by collecting and analyzing previously tested frost-damaged samples (Eqs.5.2 and 5.3, respectively). In the present study, the damage level D was estimated using Eq. 5.1 , considering the number of FTCs. The degraded modulus of elasticity E_c^d was then estimated using $E_c^d = E_c\left(1-D\right)$. The degraded compressive strength of the concrete f_c^d was estimated from Eq. 5.2 (Li et al. 2017), which was then substituted into Eq. 5.3 (Li et al. 2017) to estimate the frost-induced reduced tensile strength of concrete f_t^d.

$$\frac{E_c^d}{E_c} = 1.4238\frac{f_c^d}{f_c} - 0.4238 \qquad 5.2$$

in which f_c is the sound concrete compressive strength.

$$\frac{f_t^d}{f_t} = 1.04125\frac{f_c^d}{f_c} - 0.04125 \qquad 5.3$$

in which f_t is the sound concrete tensile strength. The compressive strain at the peak stress of frost-damaged concrete (ε_c^d) is estimated according to Zandi Hanjari et al. (2013):

$$\varepsilon_c^d = 0.0001e^{\left(\frac{548.3}{f_c^d+124.2}\right)} \qquad 5.4$$

The degraded fracture energy (G_F^d) is assumed to increase significantly as frost damage progresses, as expressed in Eq.5.5 (Zandi Hanjari et al. 2013).

$$G_F^d = G_{F0}\left(\frac{f_c^d}{f_c}\right)^{-4} \qquad 5.5$$

in which G_{F0} is the fracture energy before any damage.

5.2.3 Validation of 3D nonlinear finite element analysis

The adopted corrosion damage model was assessed by simulating corroded RC columns reported in the literature (Zaghian et al. 2020). The details of the verification study conducted on the corroded RC columns tested by Rodriguez et al. (1996b) and Wang and Liang (2008) are presented in an earlier study by the authors (Zaghian et al. 2020). There is a scarcity of research on the structural performance of RC columns subjected to frost damage. The accuracy and efficiency of the adopted frost-damage model are verified by simulating the frost-damaged flexural-governed beam (B_1) tested by Hassanzadeh and Fagerlund (2006). Beam 1 has a span of 4.4 m with a cross-section of 0.2 m by 0.5 m, and it is reinforced with four 20-mm longitudinal rebars at the tensile zone and 28 8-mm stirrups spaced at 130mm. The control beam was cast with concrete with a compressive strength of 37.6 MPa, and the compressive strength of frost-damaged concrete was reported as 17.5 MPa. The reinforcement yield strength was reported as 590 MPa. The beam was loaded with two-point loads at the middle thirds of the beam. The deteriorated properties of the frost-damaged beam were estimated according to Eqs. 5.1-5.5. The load-deflection response of the control and frost-damaged beam is shown in Figure 5-1 (a). A significant reduction in stiffness and capacity and deflection increase for the same load level is attributed to the deterioration of frost-induced mechanical properties. The numerical results compare well with the experimental ones, although the stiffness and capacity of the damaged beam are slightly overestimated and underestimated, respectively. Comparing the results of the present model and experimental test, the present model underestimates the ultimate capacity and deflection of the damaged beam (B_1) by 10% and 1.6%, respectively, which shows an acceptable agreement. Comparing the minimum principal stress (S_2) in the compressive zone of the damaged beam with the degraded compressive strength of the deteriorated concrete suggests a brittle failure in the frost-damaged beam (crushing of concrete as shown in Figure 5-1,b).

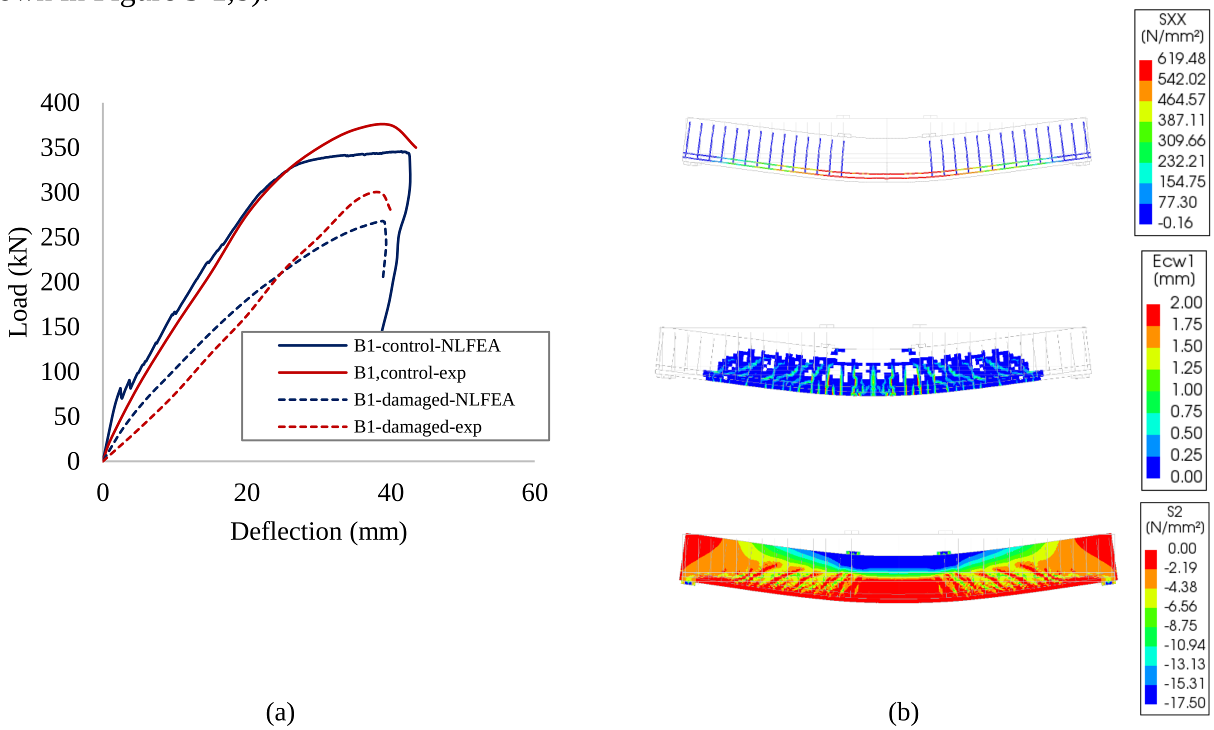

Figure 5-1 (a) Load-deflection of control and frost-damaged beam tested by Hassanzadeh and Fagerlund(Hassanzadeh and Fagerlund 2006), (b) rebars Cauchy total stress distribution (S_{XX}), crack width (E_{CW1}), and principal minimum stress (S_2)

The combined effects of corrosion and frost damage on the structural performance of real-scale RC members have not been studied widely to the best of the authors' knowledge. Diao et al. studied the coupled effects of corrosion and FTCs on the structural performance of small-scale RC columns (Diao et al. 2012). In this study, five RC columns were cast with a total length of 700 mm, and width and depth of the cross-section in the middle length of 100 mm and 200 mm, respectively. Four longitudinal rebars of 10 mm with a yield strength of 360 MPa and transverse reinforcement of 6 mm with a yield strength of 300 MPa were used. The axial load was applied with an eccentricity of 130 mm. The “Standard for test methods of long-term performance and durability of ordinary concrete” (GB/T 50082-2009) in China was used to perform the FTCs. The specimens were immersed in seawater after every three FTCs. The failure mode of all the five columns, including the control (undamaged) and damaged columns with different degrees of damage, was reported as flexural tensile. The interaction diagrams of the undamaged column (COL-0) and damaged column (COL-1), which were subjected to 300 FTCs and 100 seawater immersions, were generated in the present study, as illustrated in Figure 5-2, in which solid lines and dotted lines show the interaction curves and reported ultimate loads, respectively. In Diao et al. (2012), it was reported that the ties were all corroded and covered by rust thoroughly and the cross-secion loss rate of the longitudinal rebars was 70%. The load was applied with an eccentricity of 130 mm to the designed brackets at the end of the columns.

The compressive strength of concrete subjected to 300 FTCs was reported as 30.7 MPa. The degraded properties of the material were estimated according to the adopted corrosion and frost damage models to generate the confined interaction diagram of the COL-1. The ultimate capacity of COL-0 and COL-1 were reported as 260 kPa and 230 kPa in Diao et al. (2012). Considering the reported ultimate capacity and the applied load eccentricity, as shown in Figure 5-2 and as reported by Diao et al. (2012), both columns experience flexural-governed failure. These small-scale columns did not fail by global buckling, local buckling, or axial crushing but rather by bending.

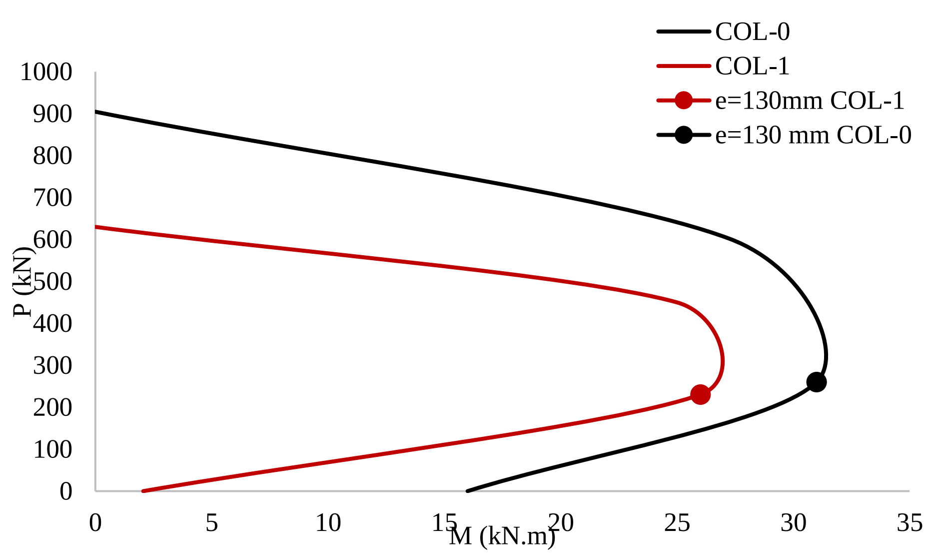

Figure 5-2 Generated confined interaction diagrams of columns COL-0 and COL-1 tested by Diao et al. (2012)

5.3 Structural performance of an existing ageing RC bridge pier

5.3.1 Case study

An intermediate 7-column bent of a two-span slab on a pre-stressed girder bridge, with a center-to-center span of 30.81 m from the Virginia State Bridge Inventory (Hevener 2003) based on Nutt et al. (1988), was selected as the case study. A 3DNLFEA was performed using software DIANA to evaluate the structural performance of the critical RC pier of the bent subjected to the synergetic effects of staged corrosion, frost damage, and service load. As explained in the following section, the progressive staged-damage model is simulated as level 1, level 2, and level 3. The pier design was performed according to the requirements of Canadian Highway Bridge Design Code CSA S6:19) for a range of load over capacity ratio (LOCR) of 0.4<LOCR<0.6 under different eccentricities ($0< e < e_p = 0.15h$), where e_p is defined as the maximum allowable practical eccentricity, and h is the square cross-sectional width. The designed pier has a cross-section of 500×500 mm^2, with twenty 20M longitudinal rebars and 10M ties spaced at 50 mm (Figure 5-3).

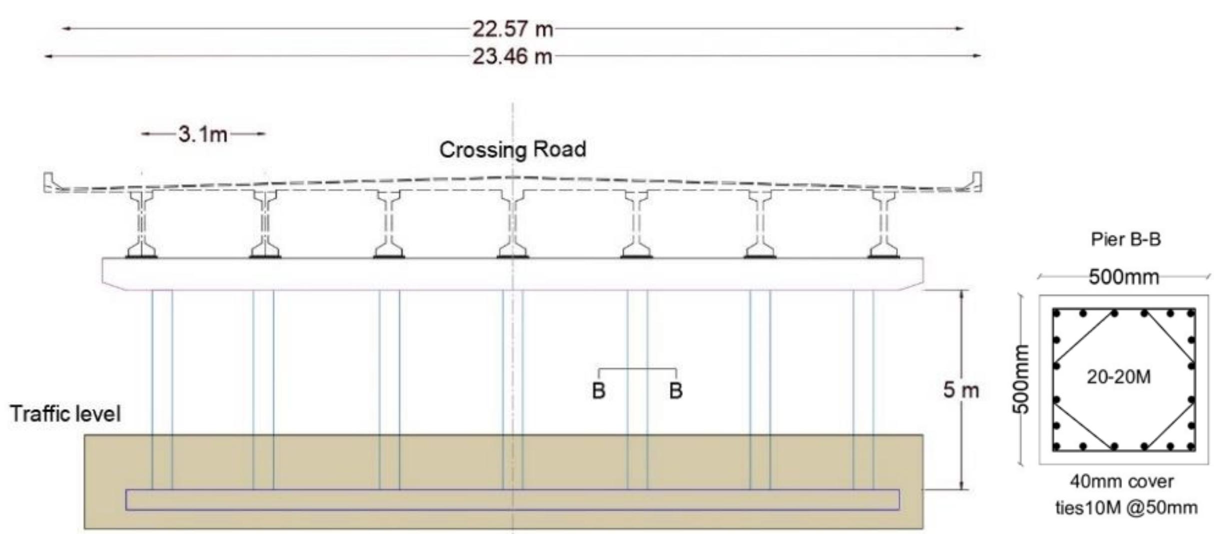

Figure 5-3 Configuration of bridge bent and pier

Table 5-2 summarizes the general design output of the bridge considered in this case study. Two load cases are studied: LC1 and LC2 corresponding to a pier under concentric and eccentric load with an eccentricity of e_p, respectively.

Table 5-2 General information of the bridge in the case study

Bridge substructure geometry	
Intermediate pier:	Multi-column bent (7-columns spacing at 3.1 m) with speared footings on bedrock
Pier cap size:	1.5 m by 0.8 m cross-section
End abutment:	Integral abutment
Bridge substructure material	
Pier cap and pier in-place concrete strength:	$f_c = 35\,MPa$
Concrete elastic modulus:	$E_c = 35000 MPa$ (1)
Concrete cracking strength (normal-density concrete):	$f_{cr} = 0.4\sqrt{f_c^{'}} = 2.37 MPa$ (2)
Yield strength, ultimate strength and strain of rebars(3)	$f_y = 420 MPa,\ f_u = 525\ MPa, \varepsilon_u = 0.14$

(1)Model Code 2010, CEB 2013
(2) CSA S6:19
(3)CSA G30.18 Gr. 40

5.3.2 Proposed combined stage-based damage scenario

The proposed corrosion damage scenario assumes that the progressive corrosion-induced deterioration effects are generated in three stages: stage 1, stage 2, and stage 3 (Zaghian et al. 2022). According to field investigations (Andersen 1997) and on-site observations (Figure 5-4, a (Whitmore 2022) and b), the damage is assumed to be localized in the splashing zone (middle third) of the pier (Zaghian et al. 2022). Foundation footings in cold climates are required to be placed below the depth of frost penetration, with a minimum of 1.2 m below ground level. Considering the traffic level with respect to the foundation of the column, it was assumed the splash zone corresponded to approximately the middle third of the column (Figure 5-4, c). Three different stages of corrosion were defined: longitudinal rebar mass loss of 5% and tie mass loss of 10% (Stage 1), longitudinal rebar mass loss of 20% and tie mass loss of 40% (Stage 2), and longitudinal rebar mass loss of 30% and tie mass loss of 60% (Stage 3). In the proposed model, it was assumed that the corrosion-induced mass loss associated with the ties is twice the one associated with the longitudinal rebars due to two possible reasons: (i) the tie diameter is smaller compared with the longitudinal reinforcement, and (ii) the ties are closer to the ambient environment which leads to faster penetration of aggressive agents such as chlorides, CO_2, and water. The deteriorated properties of corroded rebars, bond-slip response, and reduced compressive strength of the cover and core concrete were estimated according to the adopted corrosion damage model (Table 5-1). It was assumed that there is a strong possibility of corroded tie rupture at stage 3, according to an analytical approach proposed by the authors (Zaghian et al. 2022). A summary of assumptions made in the different stages of corrosion in the proposed model is presented in Table 5-3. The combined corrosion-frost damage analysis in the present study is simulated by incorporating the corrosion-induced deterioration effects for the reinforcement and bond-slip response and FTCs-induced deterioration effects for the cover and core concrete. This study proposes different frost damage scenarios based on the number of FTCs occurring during the last 60 years in Montreal, Canada. The maximum cumulative number of FTCs was estimated by analyzing the historical hourly ambient air temperature obtained from the Environment and Climate Change Canada's (ECCC) climate data ("Environment and Climate Change Canada, 2021), considering exposure duration and different ranges of minimum and maximum temperatures for each cycle. The analysis was performed from climatic data ranging from 1953 to 2013. According to Faraday's law, assuming a high corrosion level, a corrosion current density of 2.5 $\mu A/cm^2$ (François 2021) leads to stage 1 of corrosion-induced damage after ten years of service (longitudinal mass loss of 5%, tie mass loss of 10%, and subsequent deterioration effects on the concrete and bond-slip response (Zaghian et al. 2022)), leads to stage 2 after 40 years (longitudinal mass loss of 20%, tie mass loss of 40%, and subsequent deterioration effects on concrete and bond-slip response (Zaghian et al. 2022)), and leads to stage 3 after 60 years (longitudinal mass loss of 30%, tie mass loss of 60%, and subsequent deterioration effects on concrete and bond-slip response (Zaghian et al. 2022)) in Montreal. A cycle of -18°C to 4°C (C666/C666M-15 2015) over the last 10, 40, and 60 years in Montreal was observed to lead to 22, 113, and 165 FTCs, respectively (Figure 5-5). Three different frost damage scenarios were defined in the proposed model: (1) frost-induced damage in the cover is detected after ten years, (2) the presence of invisible core damage due to the high frequency of FTCs over 40 years, and (3) extensive damage in the cover, beyond repair, that leads to frost damage penetration towards the concrete core after 60 years. In the present study, three combined corrosion-frost damage levels are assumed: level 1, level 2, and level 3. At level 1, it is assumed that all the reinforcement, core concrete, and the bond-slip response in the splashing zone are affected by stage 1-corrosion, and the cover concrete is degraded under 22 FTCs after 10 years. At level 2, the steel rebars and the bond-slip response are affected by stage 2-corrosion, cover concrete and the corrosion-induced damaged core concrete are assumed to degrade under 113 FTCs after 40 years. Level 3, the worst-case scenario, corresponds to extensive corrosion of rebars (stage 3), spalling of the cover concrete, and frost-induced damage penetration towards the core concrete (splashing zone). In the proposed combined damage scenario, it is assumed that only the saturation level of the splash zone (middle third of pier) exceeds the critical saturation level which causes frost induced deterioration. The details of each level of the proposed combined damage scenario are presented in Table 5-4.

Table 5-3 Summary of assumptions made in different corrosion stages

Stage	Assumptions
Stage 1	• Longitudinal rebar mass loss of 5% • Tie mass loss of 10% • Material properties degradation (Table 5-1) • Initial in-place compressive strength in the confinement model
Stage 2	• Longitudinal rebar mass loss of 20% • Tie mass loss of 40% • Material properties degradation (Table 5-1) • Loss of fully-rigid connection between the ties and two middle longitudinal rebars • Initial in-place compressive strength in the confinement model
Stage 3	• Longitudinal rebar mass loss of 30% • Tie mass loss of 60% • Material properties (Table 5-1) • Loss of fully-rigid connection between all the ties and longitudinal rebars • Rupture of three adjacent ties at the middle height of the RC column • Variable in-place compressive strength (a,b,c,d,e)

(a) Toronto Gardiner Expressway

(b) Underpass in Bells Corners, Ottawa

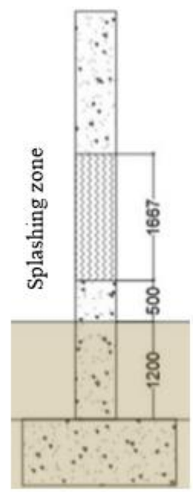

(c)

Figure 5-4 (a) and (b) Corroded bridge piers (on-site observations by the Authors), (c) Bridge pier configuration (case study), dimensions are in mm

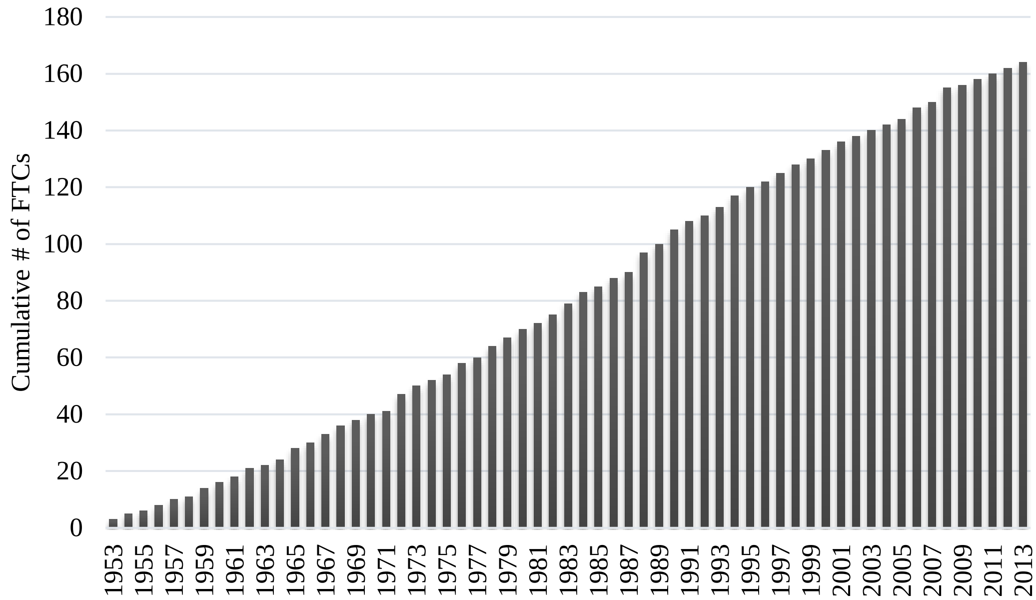

Figure 5-5 Cumulative number of FTCs (cycles of -18°C to 4°C) during 60-year service (1953-2013) of a bridge in Montreal

Table 5-4 Summary of assumptions made in different levels of combined corrosion-frost damage scenarios in the present study

Level 1 (after 10 years)	• Longitudinal rebar mass loss of 5% • Tie mass loss of 10% • Corrosion-induced bond-slip response degradation • Concrete core degradation induced by corrosion only • Concrete cover degradation under 22 FTCs
Level 2 (after 40 years)	• Longitudinal rebar mass loss of 20% • Tie mass loss of 40% • Corrosion-induced bond-slip response degradation • Loss of fully-rigid connection between the ties and two middle longitudinal rebars at each side of the pier within the corroded zone • Concrete cover degradation under 113 FTCs • Corrosion-induced damaged core concrete degradation under 113 FTCs (by substituting the in-place compressive strength of concrete used in the confinement model (corrosion-induced damaged model) with the frost-damaged concrete compressive strength)
Level 3 (after 60 years)	• Longitudinal rebar mass loss of 30% • Tie mass loss of 60% • Corrosion-induced bond-slip response degradation • Loss of fully-rigid connection between all the ties and longitudinal rebars at each side of the column within the corroded zone • Rupture of three adjacent ties at the middle height of the RC column • Spalling of the cover concrete • Corrosion-induced damaged core concrete degradation under 165 FTCs (by substituting the in-place compressive strength of concrete used in the confinement model (corrosion-induced damaged model) with the frost-damaged concrete compressive strength)

5.3.3 Finite element model, results, and discussion

The finite element model defines three zones in the pier (Figure 5-6, a): zone 1 as undamaged and zones 2 and 3 as damaged (splashing zone corresponds to approximately the pier's middle third (Zaghian et al. 2022). In zone 3, corrosion-induced tie rupture and loss of three adjacent ties, corresponding to stage 3 corrosion damage, are possible according to the proposed analytical approach (Zaghian et al. 2022). Concrete is modelled using twenty-node isoparametric solid brick elements and 15 nodes wedge elements, "CHX60" and "CTP45", respectively. Following a mesh sensitivity analysis, a mesh with 50×50 mm elements is used in the 3DNLFEA. The reinforcement is modelled using two-node one-dimensional "bond-slip" reinforcement. The top surface of the pier is assumed to be restrained in the bent direction (*y*-axis) and unrestrained in the traffic direction (*x*-axis). The pier base is assumed to be fully restrained to simulate the full rigidity condition of the foundation. Concentric and eccentric loads are applied as quasi-static uniform and non-uniform stress on the pier's top surface, respectively (Figure 5-6, b). At each level of combined damage, deteriorating effects are simulated according to Table 5-4, considering the frost-induced damage level (Eq. 5.1) and corrosion stage. At level 1, the cross-section of longitudinal rebars and the ties is reduced by 5% and 10% due to stage 1-corrosion, respectively. The corrosion-induced bond-slip response degradation is estimated according to the model (Blomfors et al. 2018) (Table 5-1). Concrete mechanical performance indexes are reduced according to Eqs. 5.2-5.5. At level 1, frost damage is assumed to deteriorate the cover concrete only. The core concrete is assumed to be intact and is degraded only due to corrosion. The mechanical properties are degraded at levels 2 and 3 according to the assumptions in Table 5-4. At level 2, it is assumed that there is non-visible frost-induced damage in the core. The core frost-induced damage is incorporated into the simulation by degrading the confinement effects of a corrosion-induced damaged core concrete due to 113 FTCs (degrading the confinement model by Saatcioglu and Razvi 1992). At level 3, the cover concrete is assumed to be spalled. The reinforcement properties and bond-slip response are degraded due to stage 3-corrosion. The confinement effects of the damaged core concrete (due to stage 3-corrosion) are degraded due to 165 FTCs (by degrading the confinement model by Saatcioglu and Razvi (1992).

The axial load-axial displacement responses of the RC pier subjected to combined damage level 1, level 2, and level 3 under concentric and eccentric loads with an eccentricity of $e_p=0.15h=75mm$ are shown in Figures 5-7 and 5-8, respectively. In the graphs, LC1 and LC2 refer to concentric load and eccentric load with an eccentricity of 75 mm, respectively. Cases L0, L1, L2, and L3 respectively correspond to no damage, level 1, level 2, and level 3 of combined damage (combination of corrosion and frost damage as expressed in Table 5-4). A staged drop in the ultimate capacity, axial displacement, and rigidity is attributed to the progressive deterioration effects assumed in each damage level. In Figure 5-7, a sudden increase of axial displacement in going from L0 to L1 can be attributed to the difference between the failure localization. By increasing the damage level to L1, the failure is localized on the splashing zone of the RC pier, while in the undamaged pier under the concentric load, failure is observed to start from the top due to localized damage (Figure 5-12). In LC1, the pier's ultimate capacity is reduced by 2%, 19%, and 42% after 10, 40, and 60 years, respectively (Figure 5-7). The ultimate capacity of the pier subjected to LC2 and level 1, level 2, and level 3 of combined damage is reduced by 5%, 14%, and 40%, respectively (Figure 5-8). By comparing Figure 5-7 and Figure 5-8, it is observed that the ultimate capacity of the pier subjected to all the damage levels decreases by increasing the eccentricity, while the deformability slightly increases. Figure 5-9 shows the pier's applied moment versus the maximum lateral deformation (pier's top deformation in the traffic direction) up to the ultimate capacity (LC2). A significant reduction in the ultimate moment capacity and deformability is observed by increasing the damage level. A sudden drop in ultimate capacity and deformation from L2 to L3 is attributed to cover spalling, penetration of frost damage towards the core, loss of partial confinement effects, tie rupture, and loss of full rigidity between the rebars and ties (Figures 5-7, 5-8, 5-9). Figure 5-10 shows the pier height versus the pier's top lateral deformability for combined damage level 1, level 2, and level 3 and for load case 2 (eccentric load). As seen in the figure, the deformability of the column is considerably reduced as damage accumulates. Figure 5-11 shows the generated interaction diagrams of the undamaged and damaged RC pier after 10, 40, and 60 years (level 1, level 2, and level 3). The N_u and M_u are defined as the RC pier's nominal axial and moment resistances, respectively. The coloured dotted horizontal lines show 0.75 of the nominal pure axial capacity of the pier at each level of combined damage (CSA S6:19). The interaction diagram is observed to contract by increasing the damage level. It is also observed that the LOCR for a specific applied load increases significantly when the damage level is increased. Note that the area bounded by lines 1 and 2 (minimum allowable eccentricity of $e_{\min} = 15 + 0.03h = 30$ mm and $e_p = 75$ mm (CSA S6:19) represents load eccentricity conditions allowed by the code.

The failure patterns of the undamaged and damaged pier at levels 2 and 3 subjected to load cases LC1 and LC2 are shown in Figures 5-12 to 5-15. Under concentric load and at level 2 of combined damage, the minimum principal stress of the cover concrete is observed to almost reach the compressive strength of frost-damaged concrete, indicating the concrete cover onset of crushing. The core concrete does not show crushing at ultimate capacity (Figure 5-13, a). Comparing the rebars' Cauchy stress with the corroded rebars' stress-strain response at zone 2 (Zaghian et al. 2022) shows that the longitudinal rebars reach yielding (Figure 5-13, b). After 60 years, the minimum principal stress of the core concrete in zones 2 and 3 is observed to exceed the threshold, suggesting core crushing (Figure 5-13, c). By comparing the rebars Cauchy stress with the corroded rebars stress-strain response at zones 2 and 3 (Zaghian et al. 2022) at level 3, the longitudinal rebars at zone 2 are observed to reach the yielding point followed by inelastic buckling of the rebars at zone

3 (Figure 5-13, d). This can be explained by cover concrete spalling, crushing core concrete, tie rupture, and confinement loss. In the case of the pier subjected to load case 2, the pier subjected to the synergetic effects of stage 2-corrosion and 113 FTCs after 40 years of service is observed to experience tensile side cracking starting from the base (Figure 5-14, a), yielding of compressive rebars at zone 2 (Figure 5-14, b) and the onset of crushing of cover concrete in the compressive side of zone 2 (Figure 5-14, c) at ultimate capacity. At level 3, crushing of compressive core concrete in zones 2 and 3 (Figure 5-15, a) and yielding of corroded compressive rebars in zone 2 followed by inelastic buckling of corroded compressive rebars in zone 3 (Figure 5-15, b) are observed to govern the failure of the pier subjected to load case LC2 with an eccentricity of 75 mm.

The structural performance of the RC pier subjected to frost damage only (after 60 years and 165 FTCs according to Figure 5-5) and concentric load (LC1) is also evaluated to study the differences between the two deterioration cases (frost damage only and combined effects of corrosion and frost damage). To this aim, the frost damage after 60 years is simulated without incorporating corrosion-induced damage. The reinforcement in the splashing zone is assumed to be intact, and the deteriorating effects of FTCs on the cover and core concrete, according to Table 5-4, are incorporated into the model. The frost damage stage after 60 years is defined as F3. The failure modes, ultimate capacity, ductility, and stiffness of the RC pier subjected to level 3 of combined damage are then compared to those with frost damage only (F3). A significant difference between the ultimate capacity, deformability, and rigidity of the 60-year old pier subjected to LC1, L3 and LC1,F3 suggests the intensifying effects of corrosion when combined with the deteriorating effects of frost damage (Figure 5-16). Comparing Figure 5-13 (c) and (d) with Figure 5-17 (a) and (b) indicates a quite different failure pattern for the 60-year old pier; the pier under LC1,F3 is observed to experience zone 1-cover concrete crushing (close to zone 2) at the failure point, and the rebars in zones 2 and 3 are observed to reach almost 75% of the proportional limit without yielding or buckling.

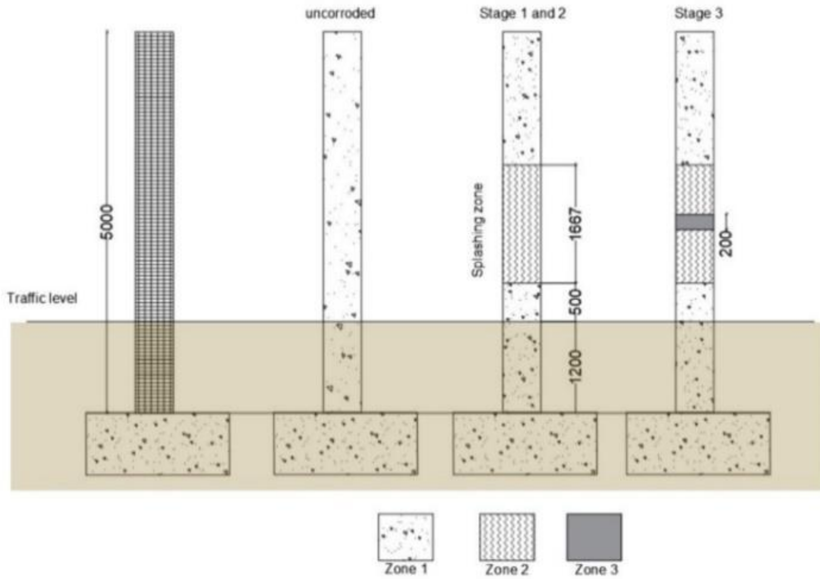

(a)

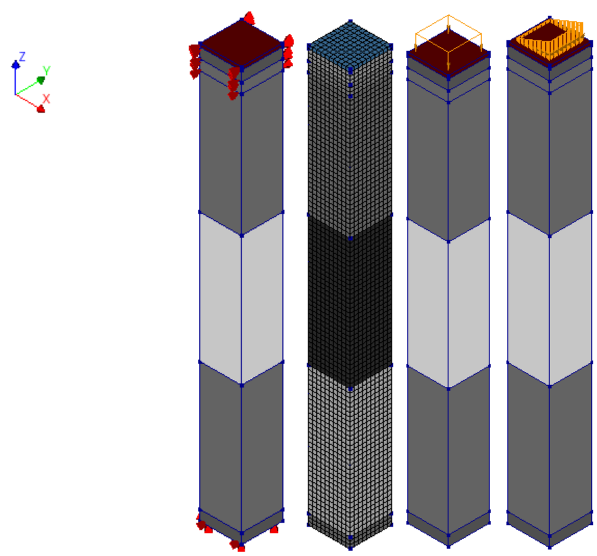

(b)

Figure 5-6 (a) Configuration of bridge pier and traffic level, (b) 3DNLFE model, boundary conditions, meshing, concentric and eccentric loading

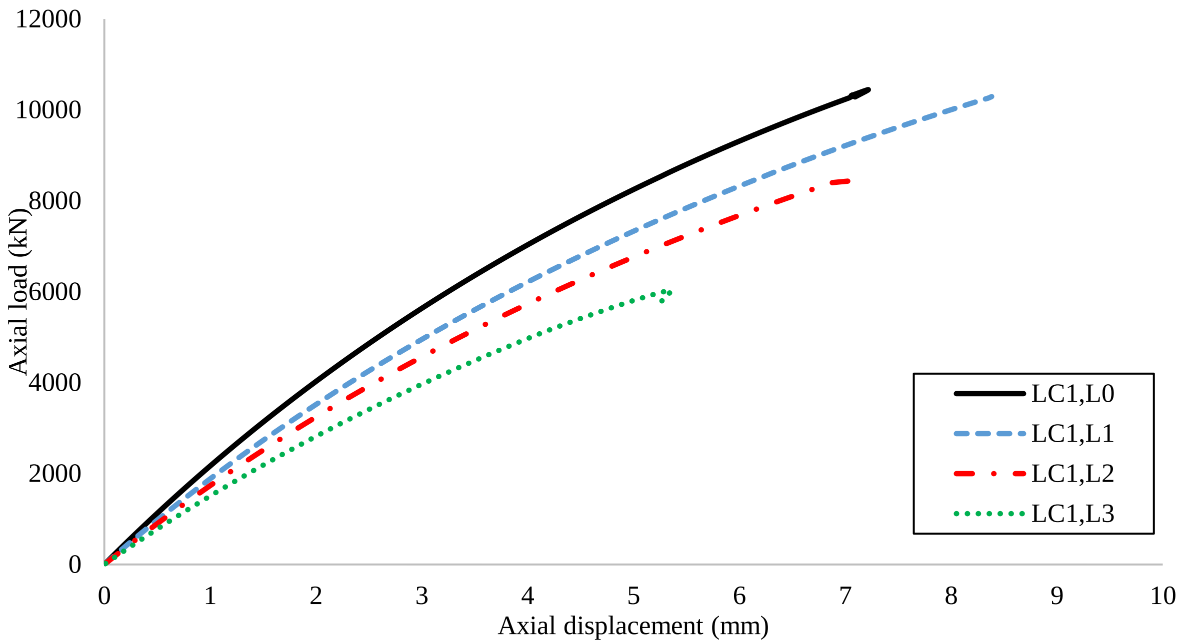

Figure 5-7 Axial load-axial displacement response of control and damaged RC pier (under combined effects of level 1, level 2, level 3 damage) subjected to concentric load

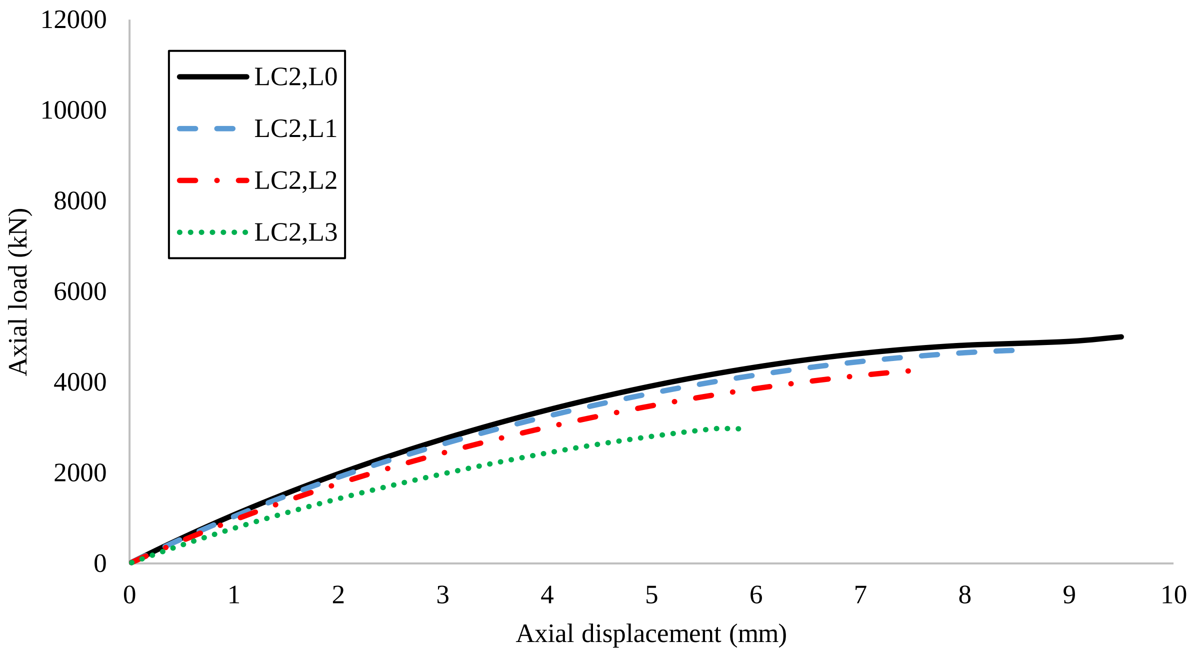

Figure 5-8 Axial load-axial displacement response of control and damaged RC pier (under combined effects of level 1, level 2, level 3 damage) subjected to eccentric load

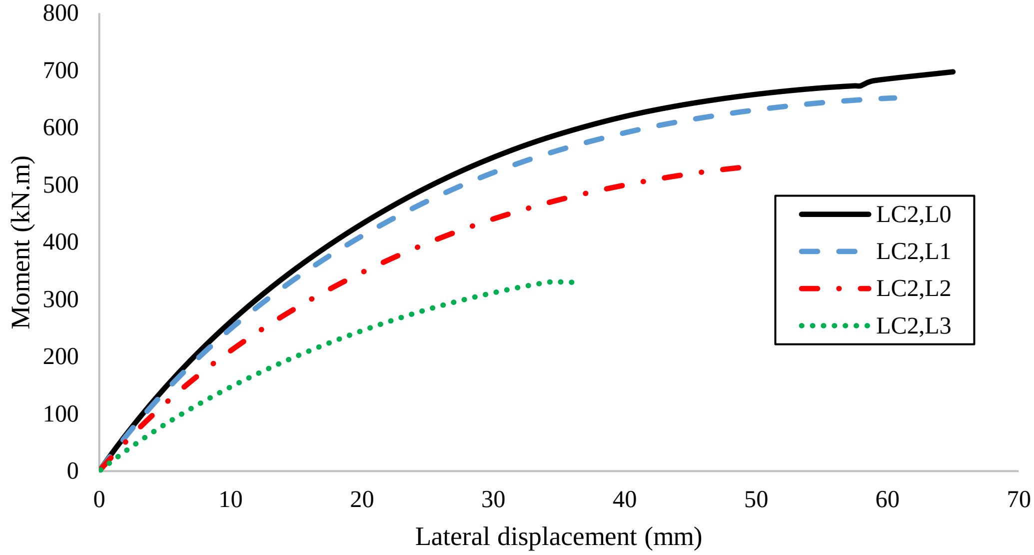

Figure 5-9 Moment-maximum lateral displacement in traffic direction of the control and damaged RC pier (under combined effects of level 1, level 2, level 3 damage) subjected to eccentric load

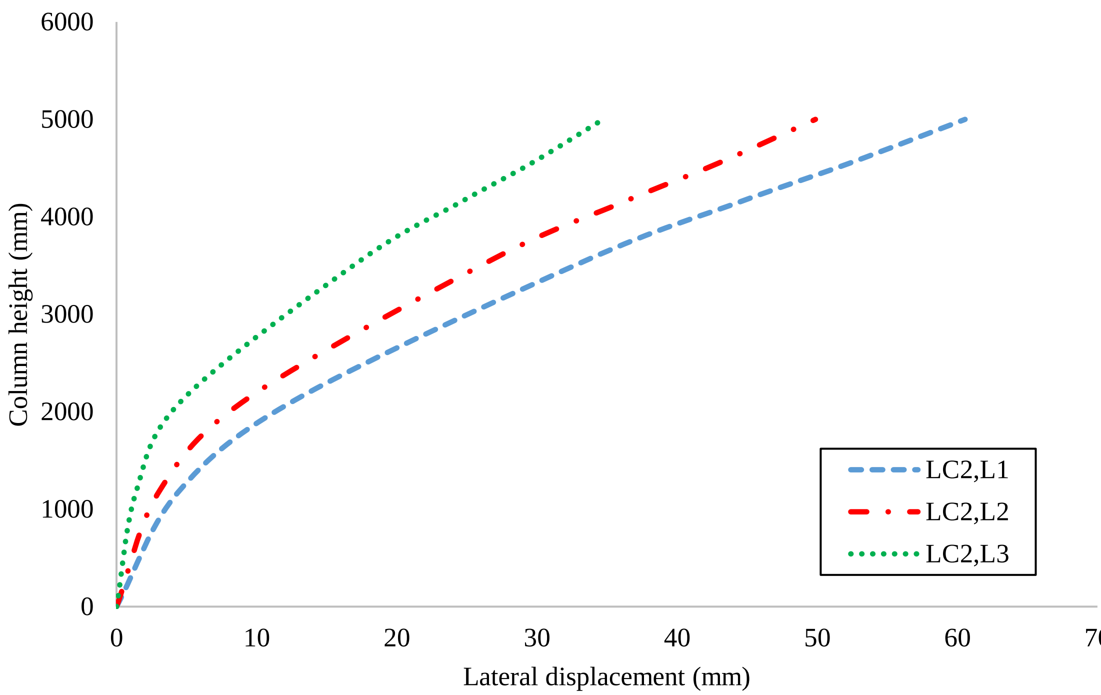

Figure 5-10 Column height-maximum lateral displacement in traffic direction of the damaged RC pier (under combined effects of level 1, level 2, level 3 damage) subjected to eccentric load

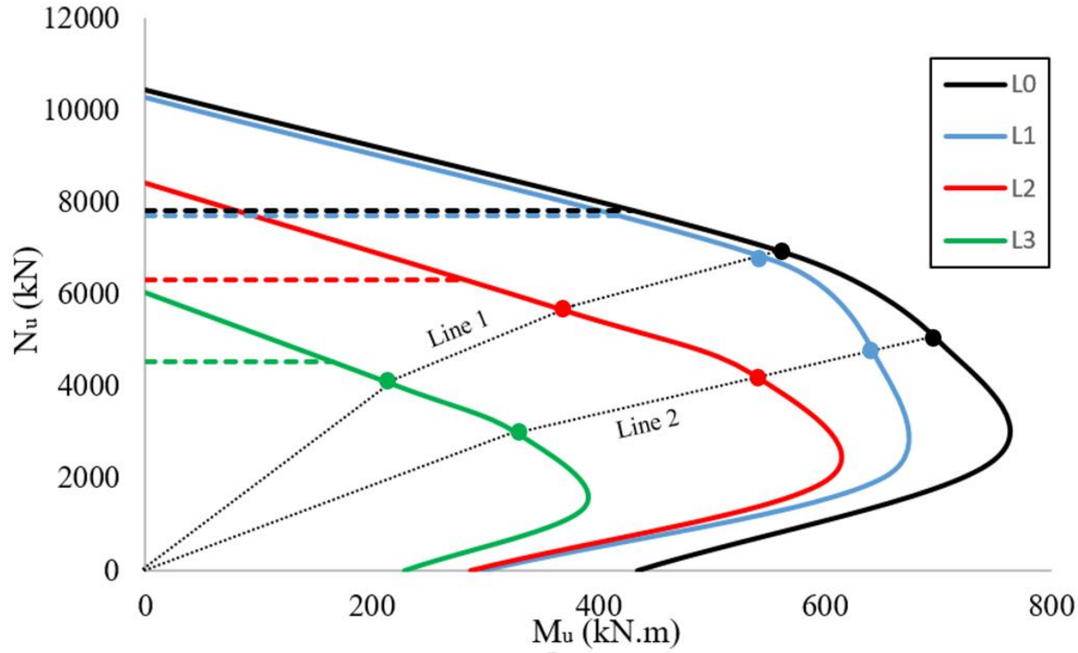

Figure 5-11 Interaction diagram of the undamaged and damaged RC pier (level 1, level 2, and level 3)

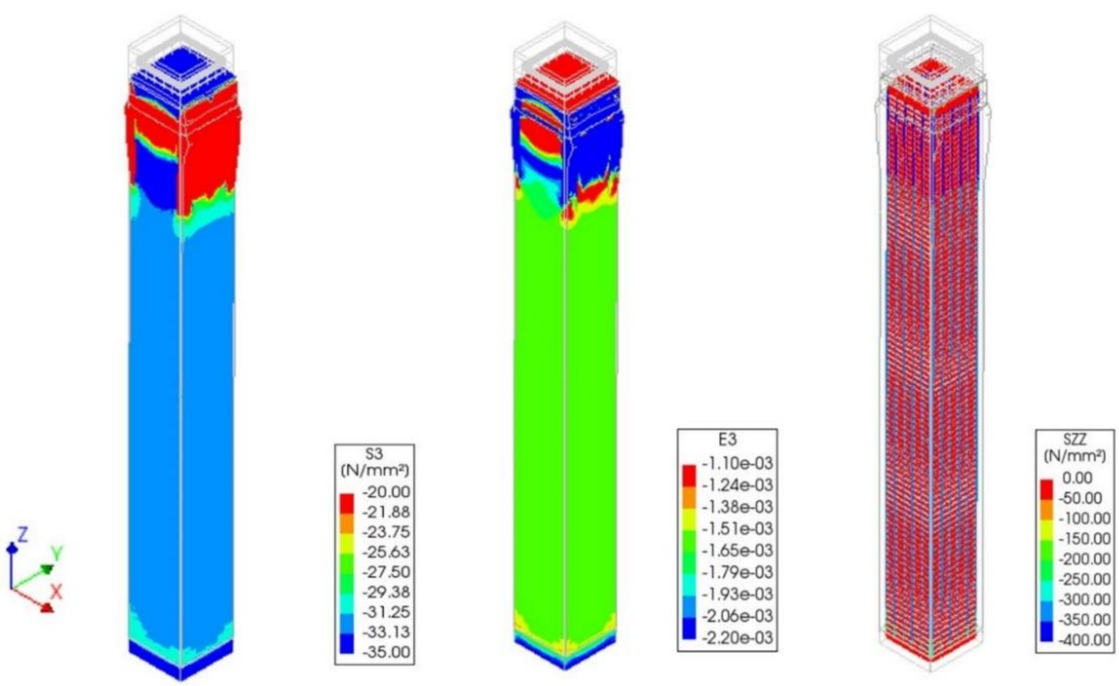

(a) (b) (c)

Figure 5-12 Failure patterns of control pier (LC1): (a) minimum principal stress distribution at ultimate capacity of undamaged pier, (b) minimum principal strain distribution at ultimate capacity of undamaged pier (c) reinforcement Cauchy total stress distribution in the z-direction at ultimate capacity of undamaged pier

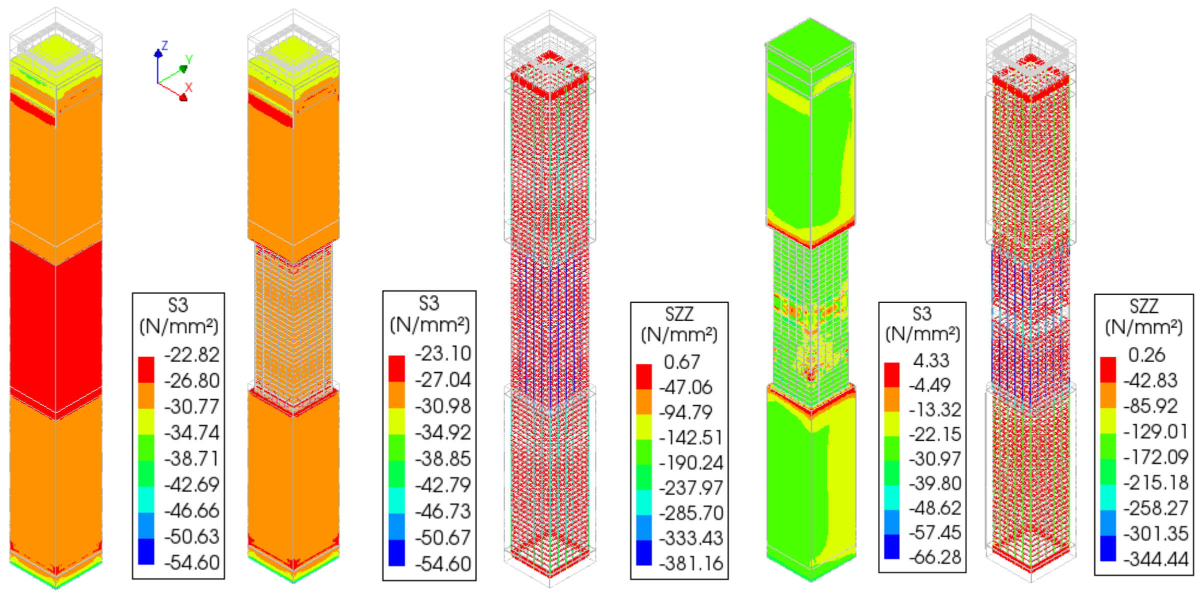

(a) (b) (c) (d)

Figure 5-13 Failure patterns of 40- and 60-year old pier under the combination of corrosion and FTC and LC1: (a) minimum principal stress distribution at ultimate capacity of damaged pier (L2), (b) reinforcement Cauchy total stress distribution in the z-direction at ultimate capacity of damaged pier (L2), (c) minimum principal stress distribution at ultimate capacity of damaged pier (L3), (d) reinforcement Cauchy total stress distribution in the z-direction at ultimate capacity of damaged pier (L3)

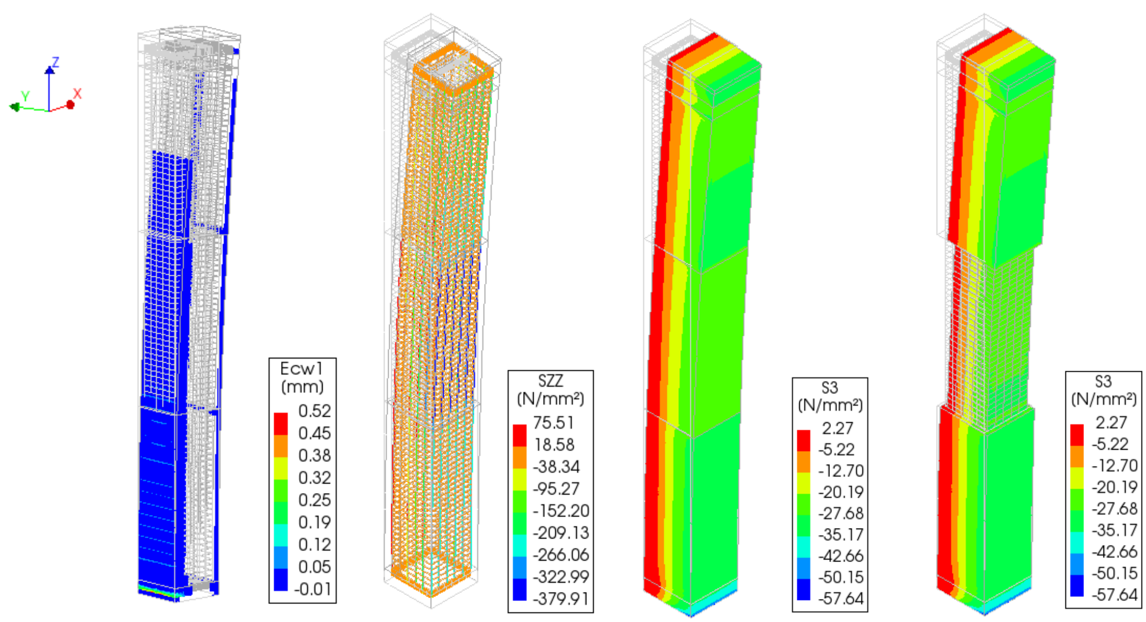

(a) (b) (c)

Figure 5-14 Failure patterns of 40-year old pier under the combination of corrosion and FTC (L2) and LC2: (a) crack pattern on the tensile side, (b) reinforcement Cauchy total stress distribution in the z-direction at ultimate capacity of damaged pier, (c) minimum principal stress distribution at ultimate capacity of damaged pier

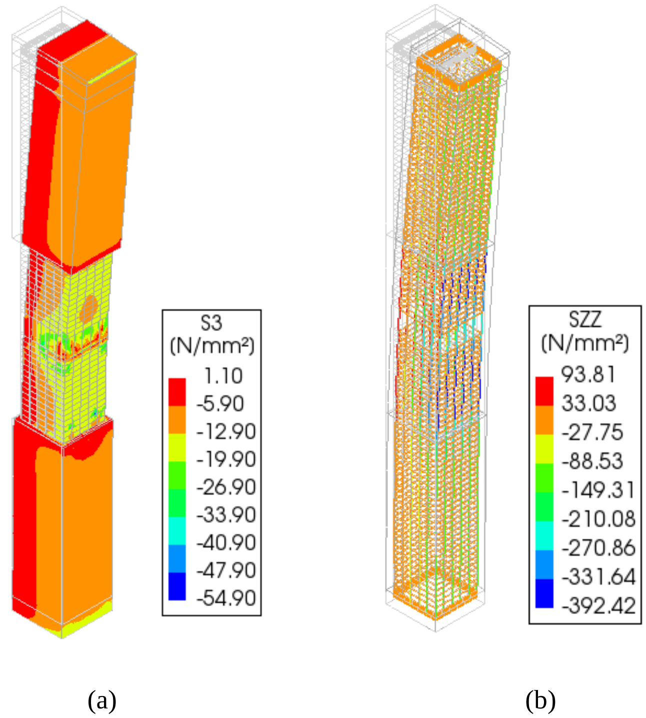

Figure 5-15 Failure patterns of the 60-year-old pier under the combination of corrosion and FTC (L3) and LC2: (a) minimum principal stress distribution at the ultimate capacity of the damaged pier, (b) reinforcement Cauchy total stress distribution in the z-direction at the ultimate capacity of the damaged pier

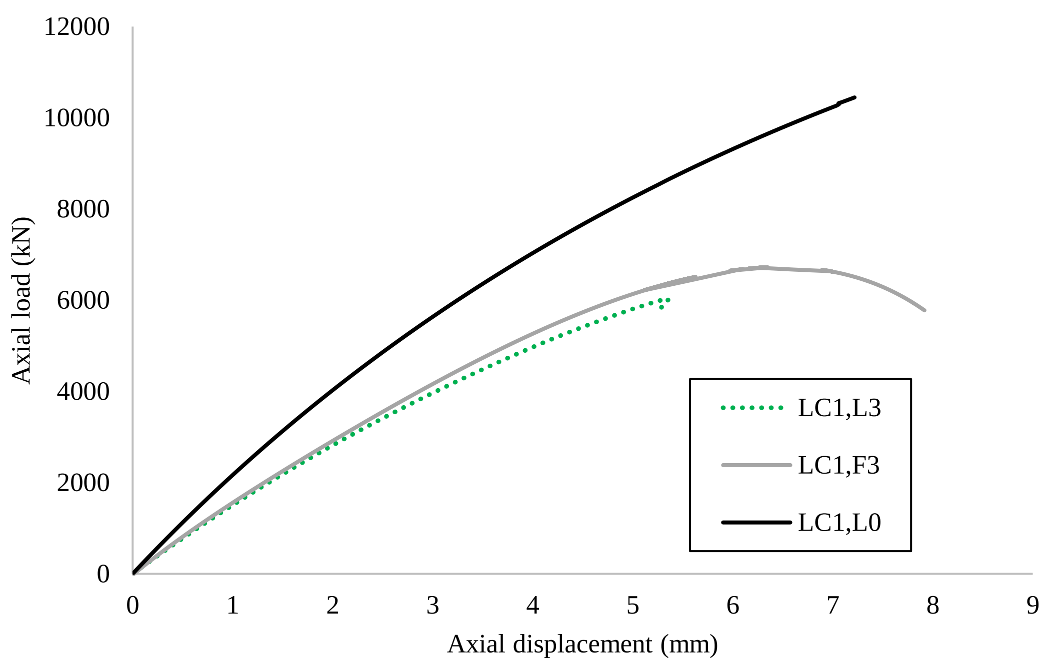

Figure 5-16 A comparison between the axial load-axial displacement response of the pier under the combined effects of corrosion and FTCs (LC1,L3) and FTCs only (LC1,F3)

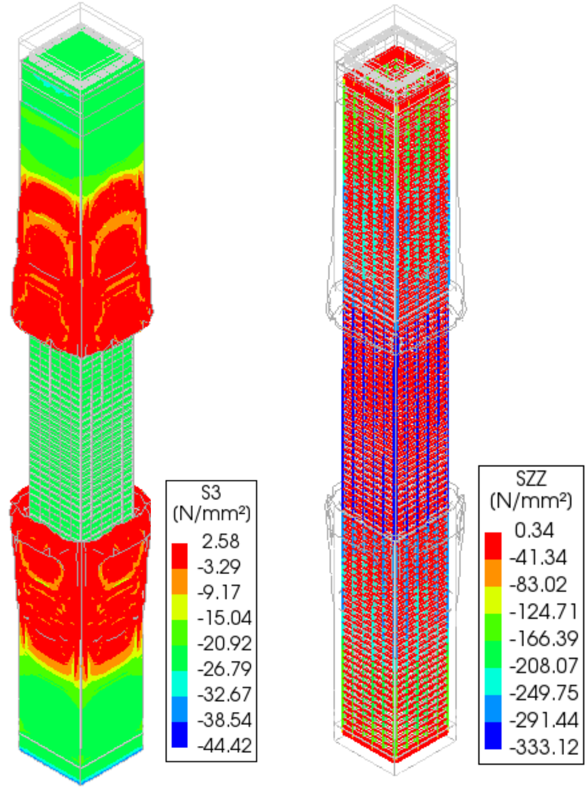

(a) (b)

Figure 5-17 Failure patterns of the 60-year-old pier under the effects of FTC only (F3) and LC_1: (a) minimum principal stress distribution at the failure point of damaged pier, (b) reinforcement Cauchy total stress distribution in the z-direction at failure point of the damaged pier

5.4 Summary and conclusions

In the present study, a 3D-NLFEA was conducted to evaluate the structural performance of real-scale ageing RC bridge piers subjected to different patterns of combined damage and concentric/eccentric loading up to failure over their service life. The synergetic effects of corrosion and frost damage induced by FTCs on the RC pier's structural performance after 10, 40, and 60 years of service were evaluated to characterize the pier’s service life performance. The efficiency of the conducted 3D-NLFEA was verified by simulating previously tested corroded columns and frost-damage beams reported in the literature. A real-scale bridge pier was then simulated as a case study, and the structural performance of the pier at various levels of combined damage (corrosion and frost damage) and concentric/eccentric loading was studied. Three combined damage levels were defined: level 1, which occurs after ten years of service and is a combination of a low corrosion stage (stage 1) and 22 FTCs; level 2, which occurs after 40 years of service and is a combination of stage 2-corrosion and 113 FTCs; and level 3, which occurs after 60 years and is a combination of the most severe corrosion stage (stage 3) and 165 FTCs. The combined damage at each level is defined as corrosion-induced degradation in steel rebars and bond-slip response, and frost-induced damage in the concrete. It is worth noting that the deterioration is assumed to be localized in the splashing zone of the pier (middle third). At level 3, the cover concrete in the splashing zone is assumed to spall thoroughly. The pier's ultimate axial capacity, moment capacity, rigidity, and deformability are observed to degrade as the damage level propagates over the years. After 60 years, the ultimate capacity of the pier subjected to level 3 of combined damage and concentric/eccentric load is observed to reduce by almost 40%. Based on these results, it is crucial to perform periodic inspections within the first 40 years of service, considering the design LOCR (0.4<LOCR<0.6). It is also observed that the LOCR for a specifically applied load increases significantly by increasing the damage level. The pier's failure shows a more brittle pattern by going from a lower level of damage to a higher one. At level 2, the pier failure is governed by the compressive rebars yielding in zone 2 and the onset of zone 2-compressive cover concrete crushing. At level 3, cover concrete spalling, tie rupture, and confinement loss lead to a more brittle failure pattern: compressive core concrete crushing, yielding of compressive rebars in zone 2, followed by compressive longitudinal reinforcing bars inelastic buckling in zone 3. The structural performance of the pier damaged by only 165 FTCs (no corrosion) was also studied. A more pronounced decrease in the ultimate capacity, deformability, and rigidity is noted for the pier subjected to combined damage compared to that subjected to frost damage only, suggesting the intensifying effects of corrosion-induced damage in the rebars and concrete confinement.

The proposed performance-based quantitative approach shows the importance of periodic inspection (every two years) in the first ten years of the bridge service life. A more refined inspection and rehabilitation planning is highly recommended in a more severe damage level during the first 40 years of service to prevent significant performance degradation and extensive damage beyond repair.

5.5 References

Almusallam, A. A. (2001). “Effect of degree of corrosion on the properties of reinforcing steel bars.” Construction and Building Materials, 15(8), 361–368.

Andersen, A. (1997). HETEK, Investigation of chloride penetration into bridge columns exposed to de-icing salt-report No.82. Danish Road Directorate, Copenhagen, 37pp.

Berra, M., Castellani, A., and Coronelli, D. (1997). “Bond in reinforced concrete and corrosion of bars.” Proceedings of the International Conference Structural Faults and Repair, Edinburgh, vol. 2, Engineering Technics Press, pp. 349–357.

Berto, L., Saetta, A., and Talledo, D. (2015). “Constitutive model of concrete damaged by freeze-thaw action for evaluation of structural performance of RC elements.” Construction and Building Materials, Elsevier Ltd, 98, 559–569.

Blomfors, M., Zandi, K., Lundgren, K., and Coronelli, D. (2018). “Engineering bond model for corroded reinforcement.” Engineering Structures, 156, 394–410.

C666/C666M-15, A. (2015). “Standard test method for resistance of concrete to rapid freezing and thawing.” ASTM International.

Cairns, J., Plizzari, G., Du, Y., Law, D., and Franzoni, C. (2005). “Mechanical properties of corrosion-damaged reinforcement.” ACI Materials Journal, 102(4), 256–264.

Coronelli, D., and Gambarova, P. (2004). “Structural assessment of corroded reinforced concrete beams: Modeling guidelines.” Journal of Structural Engineering, 130(8), 1214–1224.

CSA (2019). CSA S6:19 Canadian Highway Bridge Design Code, CSA Group, Toronto, Ontario.

Dabas, M., Martin-Perz, B., Almansour, H. (2019). “State of the Art on the combined effects of Freeze/Thaw exposure and reinforcement corrosion on the structural performance of RC structures.” CSCE Annual Conference, Laval.

Deng, P., Zhang, C., Pei, S., and Jin, Z. (2018). "Modeling the impact of corrosion on seismic performance of multi-span simply-supported bridges." Construction and Building Materials, Elsevier Ltd, 185, 193–205.

Dhakal, R. P., and Maekawa, K. (2002). "Modeling for postyield buckling of reinforcement." Journal of Structural Engineering, 128(9), 1139–1147.

Diana. (2019). "DIANA Finite Element Analysis, User's Manual, Release 10." TNO Building and Construction Research, Delft, Netherlands.

Diao, B., Sun, Y., Cheng, S., and Ye, Y. (2011). "Effects of Mixed Corrosion, Freeze-Thaw Cycles, and Persistent Loads on Behavior of Reinforced Concrete Beams." Journal of Cold Regions Engineering, 25(1), 37–52.

Diao, B., Sun, Y., Ye, Y., and Cheng, S. (2012). "Impact of seawater corrosion and freeze-thaw cycles on the behavior of eccentrically loaded reinforced concrete columns." Ocean Systems Engineering, 2(2), 159–171.

Du, Y. G., Clark, L. A., and Chan, A. H. C. "Residual capacity of corroded reinforcing bars." Magazine of Concrete Research, 57(3), 135–147.

"Environment and Climate Change Canada, Retrieved from https:https://www.canada.ca/en/services/environment/weather/climatechange.html." (2021).

Fagerlund, G. (2004). "'A Service Life Model for Internal Frost Damage in Concrete.'" Report TVBM-3119, Lund Institute of Technology, Lund, Sweden, Lund Institute of Technology, Lund, Sweden.

Fib. (2013). fib Model Code for concrete structures 2010. Lausanne, Switzerland.

François, R. (2021). "A discussion on the order of magnitude of corrosion current density in reinforcements of concrete structures and its link with cross-section loss of reinforcement." RILEM Technical Letters, 6(2021), 158–168.

GB/T50082-2009. (2009). "Standard for test method of long term performance and durability of ordinary concrete." China Architecture and Building Press, Beijing.

Hanjari, K. Z., Utgenannt, P., and Lundgren, K. (2011). "Experimental study of the material and bond properties of frost-damaged concrete." Cement and Concrete Research, 41(3), 244–254.

Hasan, M., Ueda, T., and Sato, Y. (2008). "Stress–strain relationship of frost-damaged concrete subjected to fatigue loading." Journal of Materials in Civil Engineering, 20 (1), 37–45., 20(January), 37–45.

Hassanzadeh, M., and Fagerlund, G. (2006). “Residual strength of the frost-damaged reinforced concrete beamsed.” 3rd European Conference on Computational Mechanics Solids, Structures and Coupled Problems in Engineering, Lisbon, 5–8.

Hevener, W. (2003). “Simplified live-load moment distribution factors for simple span slab on I-girder bridges. MSc. Thesis, Dept. Civil and Environmental Engineering, University of West Virginia, Morgantown,West Virginia,USA.” MSc. Thesis, Dept. Civil and Environmental Engineering, University of West Virginia, Morgantown, West Virginia, USA.

Kashani, M. M., Crewe, A. J., and Alexander, N. A. (2013). “Nonlinear stress-strain behaviour of corrosion-damaged reinforcing bars including inelastic buckling.” Engineering Structures, 48, 417–429.

Kashani, M. M., Crewe, A. J., and Alexander, N. A. (2017). “Structural capacity assessment of corroded RC bridge piers.” Proceedings of the Institution of Civil Engineers: Bridge Engineering, 170(1), 28–41.

Kashani, M. M., Lowes, L. N., Crewe, A. J., and Alexander, N. A. (2015). “Phenomenological hysteretic model for corroded reinforcing bars including inelastic buckling and low-cycle fatigue degradation.” Computers and Structures, Elsevier Ltd, 156, 58–71.

Li, A., Xu, S., and Wang, Y. (2017). “Effects of frost-damage on mechanical performance of concrete.” Journal Wuhan University of Technology, Materials Science Edition, 32(1), 129–135.

Liu, K., Yan, J., and Zou, C. (2018). “A pilot experimental study on seismic behavior of recycled aggregate concrete columns after freeze-thaw cycles.” Construction and Building Materials, Elsevier Ltd, 164(March), 497–507.

Lundgren, K. (2001). “Modelling bond between corroded reinforcement and concrete.” Fracture mechanics of concrete structures, 247–254.

Lundgren, K. (2005). “Bond between ribbed bars and concrete. Part 1: Modified model.” Magazine of Concrete Research, 57(7), 371–382.

Mohammed, A. M. (2014). “Semi-Quantitative Assessment Framework for Corrosion Damaged Slab-on-Girder Bridge Columns Using Simplified Nonlinear Finite Element Analysis, Ph.D. Thesis.” University of Ottawa,.

Molina, F. J., Alonso, C., and Andrade, C. (1993). “Cover cracking as a function of rebar corrosion : Part 2—Numerical model.” Materials and Structures, 26, 532–548.

Nutt, R. V., Schamber, R.A, and Zokaie, T. (1988). “Distribution of Wheel Loads on Highway Bridges.” Final report for national cooperative highway research program.

Petersen, L., Lohaus, L., and Polak, M. A. (2007). "Influence of freezing-and-thawing damage on behavior of reinforced concrete elements." ACI Materials Journal, 104(4), 369–378.

Qin, Q., Zheng, S., Li, L., Dong, L., Zhang, Y., and Ding, S. (2017). "Experimental Study and Numerical Simulation of Seismic Behavior for RC Columns Subjected to Freeze-Thaw Cycles." Advances in Materials Science and Engineering, 2017(2011).

RILEM TC-117 FDC -. (1993). Draft recommendation for test method for the freeze-thaw resistance of concrete. Tests with water (CF) or with sodium chloride solution (CDF)." Material and Structures

Rodriguez, J., Ortega, L. M., and Casal, J. (1996a). "Load bearing capacity of concrete columns with corroded reinforcement." Corrosion of reinforcement in concrete construction. Proceedings of fourth international symposium, Cambridge, 1-4 July 1996. specialpublication no 183, 220–230.

Rodriguez, J., Ortega, L. M., Casal, J., and Diez, J. M. (1996b). "Assessing structural conditions of concrete structures with corroded reinforcement." Proc., International Conference on Concrete in the Service of Mankind, Sess. 5, Dundee, Scotland, R. K. Dhir and N. A. Henderson, eds., E-&-FN Spon, London, 141–150.

Romben, L. (1973). Report of Activities 1972-73. The Swedish Cement and Concrete Research Institute, Stockholm.

Saatcioglu, M., and Razvi, S. R. (1992). "Strength and ductility of confined concrete." Journal of Structural Engineering (ASCE), 118(6), 1590–1607.

Saito, Y., Oyado, M., Yasojima, A., Kanakubo, T., and Yamamoto, Y. (2007). "Structural Performance of Corroded RC Column under Uniaxial Compression Load,." First International Workshop on Performance, Protection & Strengthening of Structures under Extreme Loading, Whistler, Canada.

Shang, H. S., and Song, Y. P. (2006). "Experimental study of strength and deformation of plain concrete under biaxial compression after freezing and thawing cycles." Cement and Concrete Research, 36(10), 1857–1864.

Vecchio, F., and Collins, M. P. (1986). "The modified compression field theory for reinforced concrete elements subjected to shear." Journal of the American Concrete Institute, 83(2), 219–231.

Wang, X. H., and Liang, F. Y. (2008). "Performance of RC columns with partial length corrosion." Nuclear Engineering and Design, 238(12), 3194–3202.

Whitmore D. Extending the Service Life of Existing Concrete Structures to Last Beyond 100 Years. MATEC Web Conf. 2022;364:04025. doi:10.1051/matecconf/202236404025

Xia, J., Jin, W., and Li, L. (2016). "Performance of Corroded Reinforced Concrete Columns under the Action of Eccentric Loads." Journal of Materials in Civil Engineering, 28(1), 04015087.

Zaghian, S., Martín-Pérez, B., and Almansour, H. (2020). "The effect of corrosion and traffic loads on bridge columns using three-dimensional non-linear finite element analysis." Proc., CACRCS DAYS 2020 Capacity Assessment of Corroded Reinforced Concrete Structures, Fédération Internationale du Béton – International Federation for Structural Concrete, 349-356.

Zaghian, S., Martín-Pérez, B., and Almansour, H. (2022). "Nonlinear finite element modeling of the impact of reinforcement corrosion on bridge piers under concentric loads." Structural Concrete, 23(1), 138-153. https://doi.org/10.1002/suco.202100254

Zandi Hanjari, K., Kettil, P., and Lundgren, K. (2013). "Modelling the structural behaviour of frost-damaged reinforced concrete structures." Structure and Infrastructure Engineering, 9(5), 416–431.

Zandi Hanjari, K., Utgenannt, P., and Lundgren, K. (2009). "Frost-damaged concrete: Part 2. Bond properties." 4th International Conference on Construction Materials: Performance, Innovations and Structural Implications, Nagoya, Japan, 761–766

Chapter 6: Concluding Remarks

6.1 Introduction

This chapter presents a comprehensive summary of all chapters. The effectiveness and trend of the proposed methodology are evaluated by generating the interaction diagrams of the RC pier at different levels of damage during its service life based on the present FEA and nonlinear sectional analysis. Possible future work is finally presented.

6.2 Conclusions

This section presents a summary of the conclusions of Chapters 3 through 5. Detailed conclusions are presented at the end of each chapter. The summaries of each chapter are as follows:

- Chapter 3 presents the proposed 3D-NLFEA to evaluate the structural performance of a corroded RC bridge pier subjected to concentric loading. This chapter proposes a comprehensive stage-based corrosion damage model which accounts for all the corrosion-induced deterioration effects during the bridge's service life. The deteriorating effects include concrete strength degradation within the cover zone and confined concrete, steel area reduction due to uniform corrosion (longitudinal and stirrups), pit-induced ductility degradation of the steel, buckling of compressive steel bars due to steel cross-section reduction and confinement degradation, and bond-slip response degradation. A stage-based damage scenario, assuming the damage localized at the middle third of the pier, is proposed as (1) stage 1, at which there is longitudinal rebar mass loss of 5% and tie mass loss of 10%, (2) stage 2, at which there is longitudinal rebar mass loss of 20% and tie mass loss of 40%, and (3) stage 3 at which there is longitudinal rebar mass loss of 30% and tie mass loss of 60%. Various assumptions were made for each stage. At the stages with higher-level corrosion, in addition to the deteriorating effects on the material properties, it was assumed that corrosion would result in the loss of a fully-rigid connection between the ties and longitudinal rebars and would enable rotation at the connection locations. According to the proposed analytical approach, it was also suggested that at higher levels of corrosion, there would be a possibility of one or more tie ruptures in the corroded zones. The proposed performance-based quantitative approach shows that increasing the corrosion level changes the pier failure mode to a more brittle pattern. At failure, the damage is observed to be more localized in the corroded regions, specifically in the regions where the ties ruptured. The failure mode of the severely damaged pier is observed to be governed by the yielding of the corroded rebars and core concrete crushing, followed by the inelastic buckling of the longitudinal reinforcing bars located in the middle zone with ruptured ties. The results show the importance of periodic inspection and monitoring of the properties' deterioration during the bridge service life to prevent severe damage, provide additional safety, and reduce rehabilitation costs.

- Chapter 4 presents the proposed finite element modelling of bridge piers subjected to eccentric load combined with reinforcement corrosion. The same three damage stages defined in Chapter 3 were adopted here, with assumptions similar to those of Chapter 3. The damaged pier was subjected to eccentric loading with eccentricities of 30 mm and 75 mm, which respectively correspond to the allowable minimum and allowable practical eccentricities by the bridge code. The corroded pier (at all stages of damage) subjected to smaller eccentricities is observed to follow a compression-controlled failure mechanism by concrete core crushing, compressive corroded rebar yielding and post-yield buckling at the middle height of the pier (corroded zone). The present model can also capture the tension-controlled failure mechanism in the RC pier with larger eccentricities. The model shows a significant decrease in capacity, stiffness, and deformability of the pier by increasing the damage level. The proposed quantitative approach helps estimate the capacity reduction, which, with the possibility of an increase in traffic intensity, leads to an increase in the load-over capacity ratio. By comparing the results of Chapters 3 and 4, it is observed that the present model is capable of successfully capturing a variety of failure patterns, i.e., compression-controlled failure of the pier under concentric load and smaller eccentricities and tension-controlled failure of pier subjected to larger eccentricities.

- Chapter 5 presents the nonlinear finite element modelling of bridge piers under the combined effect of corrosion, freeze-thaw cycles, and service load. The structural performance of an RC bridge pier located in Montréal, Canada, is evaluated after 10, 40, and 60 years of service. The proposed evaluation approach assumed that the deterioration is also localized in the middle third or the pier. Three combined deterioration damage levels were defined. At level 1, it is assumed that the rebars are deteriorated due to stage 1 corrosion (as described in Chapters 3 and 4), and the cover concrete is affected by 22 FTCs. Level 2 corresponds to a combination of stage 2-corrosion of the rebars and 113 FTCs. At level 3, it is assumed that the cover concrete spalls thoroughly, rebars are affected by stage 3-corrosion, and the core is deteriorated by a combination of stage 3-corrosion and 165 FTCs. In addition, the RC pier only subjected to 165 FTCs, without corrosion, was also studied. The results show a more pronounced structural performance degradation in the case of the pier subjected to the combined effect compared to the one subjected to FTCs only. A significant decrease in the ultimate capacity, rigidity, and deformability of the pier shows the importance of periodic investigation and inspection in the first ten years to monitor deterioration process and of rehabilitation planning in the first 40 years of bridge service life to prevent pier collapse.

6.3 Evaluation of damaged RC bridge piers

The present study has proposed a modelling framework to investigate the potential impact of different damage scenarios due to reinforcement corrosion and frost damage on the structural performance of ageing RC bridge piers during their service life. The capabilities of such an evaluation framework are illustrated by applying it to the assessment of an RC pier as part of a multi-column bent of an ageing bridge.

As stated in Chapter 1, the Ontario Structure Inspection Manual (OSIM) proposes regular detailed visual inspections of bridges to ensure public safety and convenience, to prolong the bridges' useful life, and to set out a structure management system for maintenance and rehabilitation (Ontario Ministry of Transportation 2008). The OSIM adopts a new "severity and extent" philosophy in order to estimate bridge rehabilitation requirements and costs. A thorough qualitative data is collected and recorded as the elements condition statement. As a general rule, this philosophy assesses the structural element condition according to the defect severity (Ontario Ministry of Transportation 2008):

- Excelent: It refers to an element which is in new condition without any visible defects
- Good: It refers to an element with initial signs of "light" defects. No specific remedies are recommended in this case.
- Fair: It refers to an element with the first signs of "medium" defects. A preventative maintenance remedy is recommended in this case.
- Poor: It refers to an element with "severe" and "very severe" defects. Any member with types of spalling and delaminations are usually categorized in "poor" condition, which triggers immediate rehabilitation and replacement.

Although these guiding principles provide a reasonable qualitative assessment approach, there is still lack of a quantitative numerical, experimental, and/or field studies to estimate the residual capacity of the ageing piers subjected to corrosion, FTCs, or combined effects that can be compared with the proposed methodology as an evaluation approach. To validate and evaluate the trend and reliability of the proposed modelling approach, the column load-moment interaction diagrams of the pier at different damage levels (corrosion and combined damage) were generated based on both the 3D-NLFEA results presented in Chapters 3-5 and nonlinear sectional analysis (NLSA). In the NLSA method, the confined capacity of the pier under pure concentric load (N_u) is estimated as:

$$N_u = \alpha_{cover} f_c \left(A_g - A_c\right) + \alpha_{core} f'_{cc} \left(A_{cc}\right) + A_s f_y \qquad 6.1$$

in which α_{cover} and α_{core} are the stress block parameters of cover and core concrete, respectively; f_c and f'_{cc} are the compressive strength of the undamaged cover and core concrete, respectively; A_g, A_c, A_{cc}, and A_s are the gross cross-section of the undamaged pier, gross area of the undamaged core, net area of the core, and undamaged rebar cross-section, respectively; f_y is the uncorroded rebar yield strength.

In the present NLSA, the flexural strength of the RC pier is evaluated assuming the material's nonlinear constitutive laws, perfect bond between reinforcing steel and concrete, negligible tensile strength in concrete, and plane sections remaining plane after bending. Figure 6-1 illustrates the bending moment M and axial load N in balance with the internal forces within the pier's critical cross-section. The flexural capacity of the pier is estimated from Eqs. 6.2 and 6.3. It is worth noting that the moment capacity of the pier is calculated about the mid-height of the cross section. The core concrete properties are calculated according to Saatcioglu and Razvi (1992).

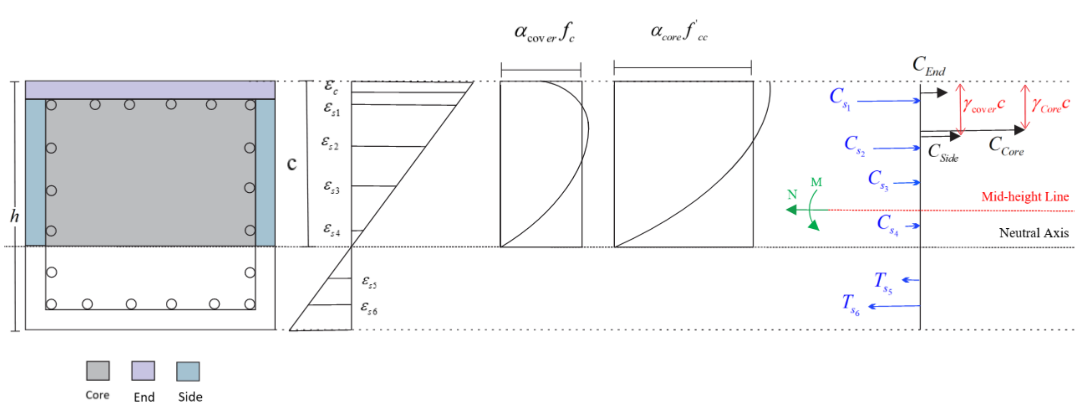

Figure 6-1 Confined section of the pier and corresponding stress/strain distribution and internal forces

$$N = C_{End} + C_{Core} + C_{Side} + \sum_{i=1}^{m} C_{s_i} + \sum_{j=m+1}^{n} T_{s_j} \qquad 6.2$$

$$M = C_{Core}\left[\left(c - d_{\text{cover}} - \frac{d_{bt}}{2}\right) - \gamma_{Core}\left(c - d_{\text{cover}} - \frac{d_{bt}}{2}\right)\right] +$$

$$C_{Side}\left[\left(c - d_{\text{cover}} - \frac{d_{bt}}{2}\right) - \gamma_{Cover}\left(c - d_{\text{cover}} - \frac{d_{bt}}{2}\right)\right] + \qquad 6.3$$

$$C_{End}\left[c - \left(\frac{d_{\text{cover}} + \frac{d_{bt}}{2}}{2}\right)\right] + \sum_{i=1}^{m} C_{s_i}\left(\frac{h}{2} - d_i\right) + \sum_{j=m+1}^{n} T_{s_j}\left(\frac{h}{2} - d_j\right)$$

in which *m* is the number of rebars layer in compression, *n* is the number of rebars layer in tension, d_{cover} is the cover depth, d_{bt} is the tie diameter, γ_{Cover} and γ_{Core} are the stress block parameters based on Hognestad's model, and d_i is the distance of each layer *i* of rebars to the section's top layer.

At each stage and level of damage, the properties of the concrete cover, core, and rebars are degraded according to the adopted damage models presented in Chapters 3 to 5 (Table 6-1) and substituted into Eq. 6.1 to obtain the concentric capacity (Eqs. 6.4 and 6.5). The M-N couple of the damaged pier is estimated by substituting the degradation factors described in Table 6-1 into Eqs. 6.2 and 6.3.

$$N_{u,cor} = \alpha_{\text{cover}} f_{c,cor}\left(A_g - A_c\right) + \alpha_{core} f'_{cc,cor}\left(A_{cc}\right) + A_{s,cor} f_{yc,cor} \qquad 6.4$$

$$N_{u,comb} = \alpha_{\text{cover}} f_c^d\left(A_g - A_c\right) + \alpha_{core} f'_{cc,comb}\left(A_{cc}\right) + A_{s,cor} f_{yc,cor} \qquad 6.5$$

Table 6-1 Degradation effects considered in the proposed NLSA

References	Degradation factors	Equation
Coronelli and Gambarova (2004)	Concrete cover compressive strength (corroded pier)	$f_{c,cor} = \frac{f_c}{1 + K\varepsilon_1 / \varepsilon_{C0}}$
Kashani et al. (2013)	Corroded rebar yield strength	$f_{yc,cor} = f_{yc}\left[1 - 100 \times \beta.\rho(t)\right]$; $\beta = \begin{cases} 0.005 & s/d_b \le 5 \\ 0.0065 & 5 < s/d_b \le 10 \\ 0.0125 & s/d_b > 10 \end{cases}$
	Corroded rebar yield strength	$A_{s,cor} = \frac{\pi {d^2}_{b,cor}}{4}$; $d_{b,cor} = d_b\sqrt{1 - X_{cor}}$
Li et al. (2017)	Concrete cover compressive strength (frost-damaged)	$f_c^d = \frac{f_c\left(0.4238 + \frac{E_c^d}{E_c}\right)}{1.4238}$

Figures 6-2 (a) through (g) show the interaction diagrams generated based on the proposed 3D-NLFEA (Chapters 3-5) and NLSA for the undamaged pier, pier subjected to stage 1 of corrosion, stage 2 of corrosion, stage 3 of corrosion, combined effects of 22 FTCs and stage 1 corrosion, 113 FTCs and stage 2 corrosion, and 165 FTCs and stage 3 corrosion, respectively. By comparing the generated interaction diagram based on the proposed 3D-NLFEA and NLSA, it is observed that both methods estimate the residual capacity of the pier with a reasonable agreement. Although the present NLSA proposes a more efficient approach to be used in daily engineering practice, it cannot predict the failure pattern and behaviour of the pier during its service life. The proposed 3D-NLFEA is deemed a reliable tool to estimate the residual capacity and capture the failure pattern of the damaged pier.

Based on a regression analysis of the FE results, prediction equations are proposed for the axial capacity of the pier under the combined effect of pure axial load and corrosion as a function of rebar cross-section loss (Figure 6-3(a)), the axial capacity of the pier under the combined effect of axial load with an eccentricity of 30 mm (LC1) and corrosion as a function of rebar cross-section loss (Figure 6-3(b)), the axial capacity of the pier under the combined effect of axial load with an eccentricity of 75 mm (LC2) and corrosion as a function of rebar cross-section loss (Figure 6-3(c)), the axial capacity of the pier under the combined effect of pure axial load, corrosion (different stages of corrosion associated with each FTC number) and FTCs as a function of the number of FTCs (Figure 6-3(d)), the axial capacity of the pier under the combined effect of axial load with an eccentricity of 30 mm (LC1), corrosion and FTCs as a function of the number of FTCs (Figure 6-3(e)), and the axial capacity of the pier under the combined effect of axial load with an eccentricity of 75 mm (LC2), corrosion and FTCs as a function of the number of FTCs (Figure 6-3(f). From Figure 6-3, it is observed that the reduction in axial capacity follows a cubic curve for all cases simulated. For longitudinal reinforcement cross-section loss greater than 20%, the reduction in axial capacity levels off to 60% of the undamaged value and seems to be independent of load eccentricity. A more pronounced capacity reduction up to this level damage is attributed to the deterioration of the cover and core concrete along with the loss of connection between the longitudinal reinforcing bars and ties (Figures 6-3 (a), (b), and (c)). When considering the damage caused by both reinforcement corrosion and FTCs, the reduction in the pier axial capacity follows a cubic concave down curve (Figures 6-3 (d), (e), and (f)), as opposed to a concave up curve when only corrosion is accounted for. The decrease in axial capacity for the case of combined damage is more dependent on the number of freeze-thaw cycles, with the ensuing deteriorating effects on the strength and stiffness of the concrete cover and core, than the applied load eccentricity, as illustrated in Figures 6-3 (d)-(f). This highlights the importance of properly quantifying the effect of induced damage on the material constitutive behaviour.

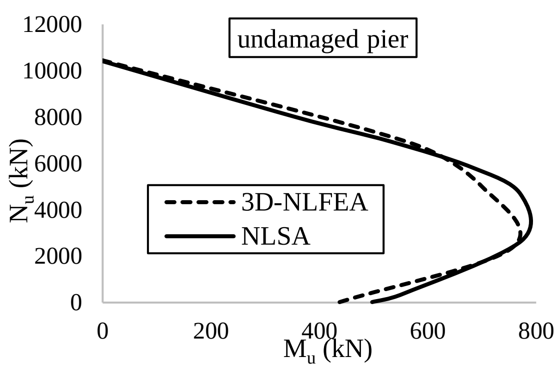

(a)

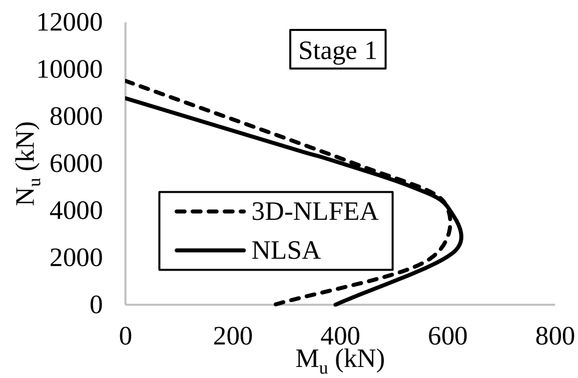

(b)

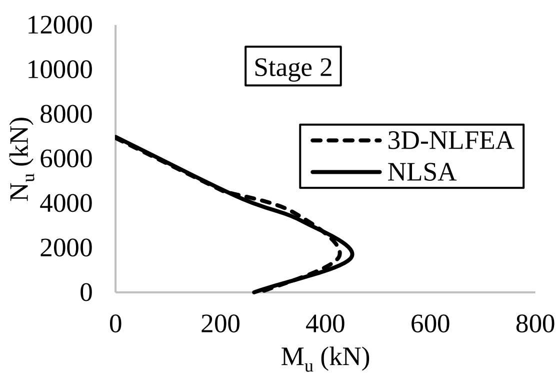

(c)

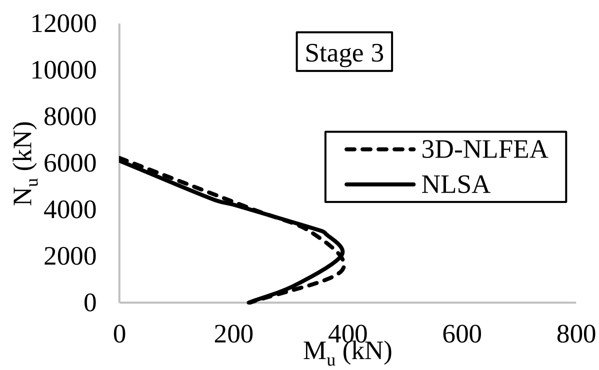

(d)

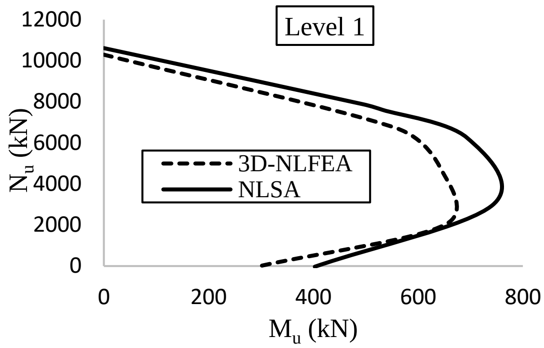

(e)

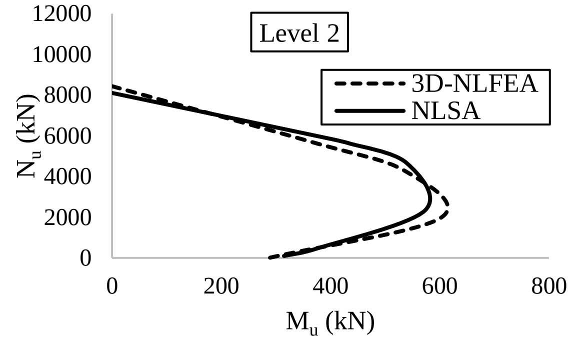

(f)

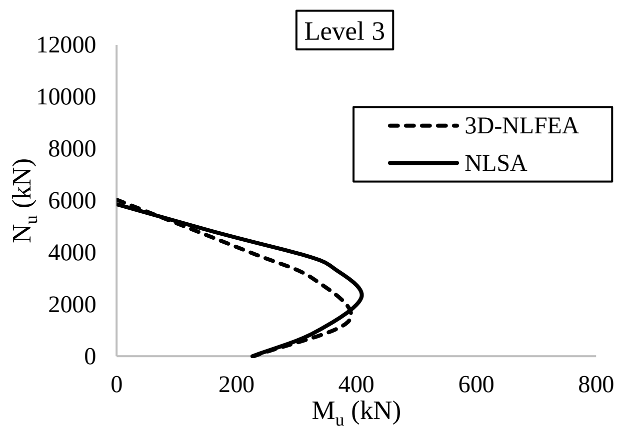

(g)

Figure 6-2- Interaction diagrams based on the present 3D-NLFEA and NLSA for (a) undamaged pier, (b) stage 1 of corrosion, (c) stage 2 of corrosion, (d) stage 3 of corrosion, (e) level 1 of combined damage, (f) level 2 of combined damage, and (g) level 3 of combined damage

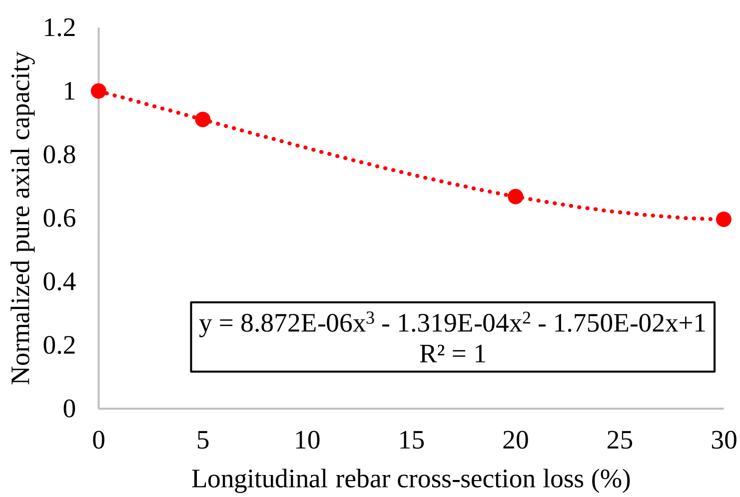

(a)

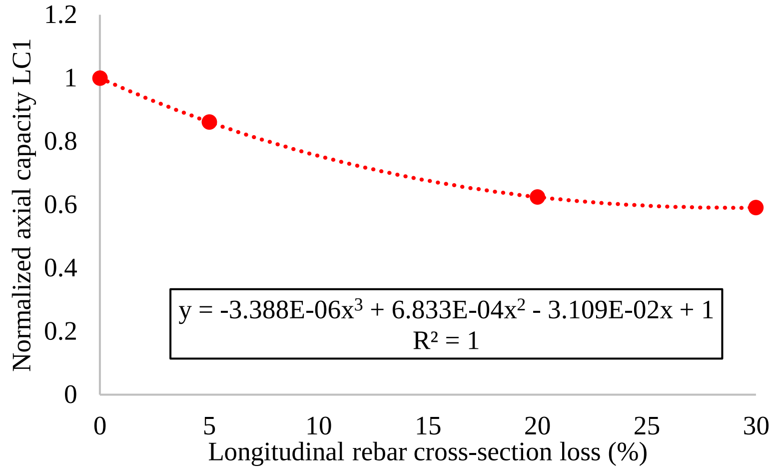
1.2
1
0.8
0.6
0.4
0.2
0
Normalized axial capacity LC1
y = -3.388E-06x3 + 6.833E-04x2 - 3.109E-02x + 1
R² = 1
0 5 10 15 20 25 30
Longitudinal rebar cross-section loss (%)
(b)

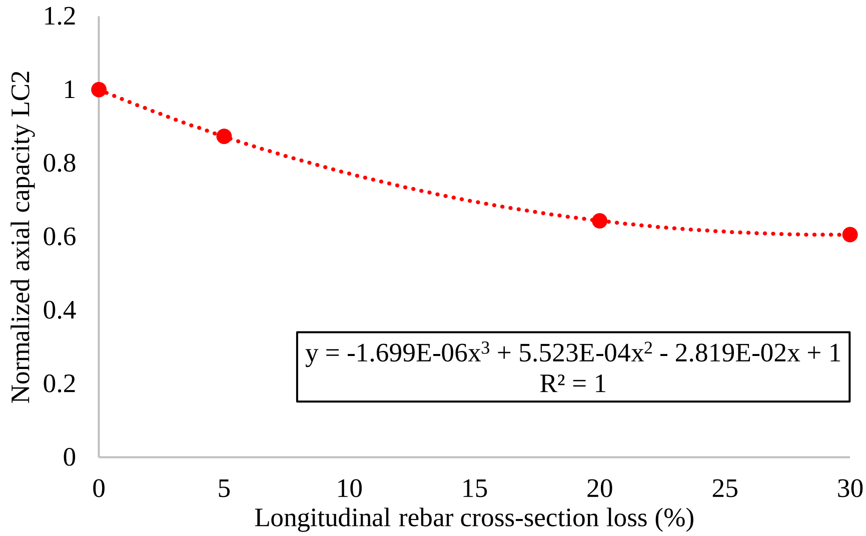
1.2
1
0.8
0.6
0.4
0.2
0
Normalized axial capacity LC2
y = -1.699E-06x3 + 5.523E-04x2 - 2.819E-02x + 1
R² = 1
0 5 10 15 20 25 30
Longitudinal rebar cross-section loss (%)
(c)

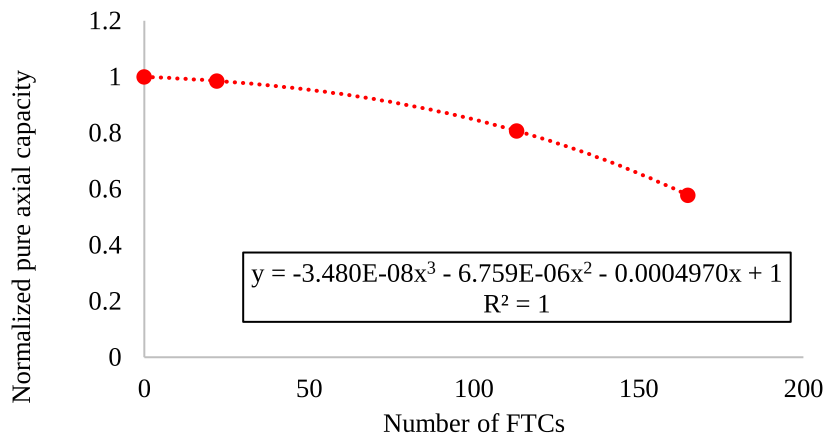
1.2
1
0.8
0.6
0.4
0.2
0
Normalized pure axial capacity
y = -3.480E-08x3 - 6.759E-06x2 - 0.0004970x + 1
R² = 1
0 50 100 150 200
Number of FTCs
(d)

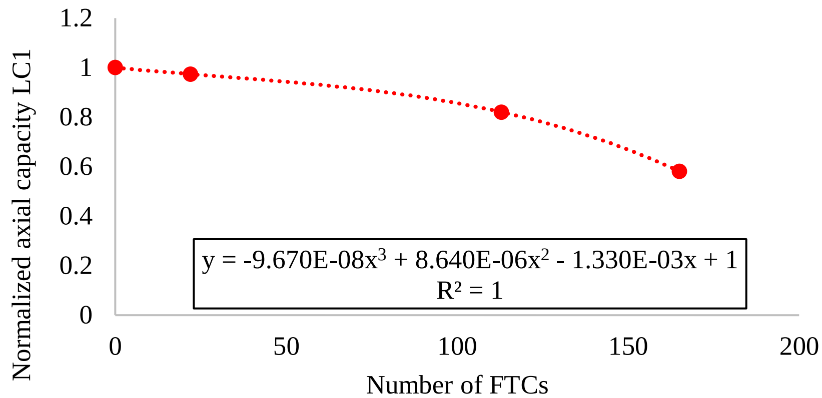

(e)

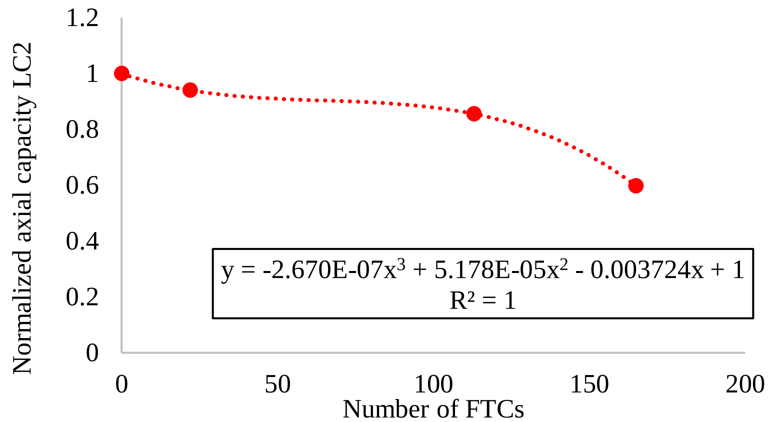

(f)

Figure 6-3 Prediction equations of (a) axial capacity of the pier under the combined effect of pure axial load and corrosion as a function of rebar cross-section loss (%), (b) axial capacity of the pier under the combined effect of axial load with an eccentricity of 30 mm (LC1) and corrosion as a function of rebar cross-section loss (%), (c) axial capacity of the pier under the combined effect of axial load with an eccentricity of 75 mm (LC2) and corrosion as a function of rebar cross-section loss (%), (d) axial capacity of the pier under the combined effect of pure axial load, corrosion and FTCs as a function of the number of FTCs, (e) axial capacity of the pier under the combined effect of axial load with an eccentricity of 30 mm (LC1), corrosion and FTCs as a function of the number of FTCs, (f) axial capacity of the pier under the combined effect of axial load with an eccentricity of 75 mm (LC2), corrosion and FTCs as a function of the number of FTCs

6.4 Advantages/limitations of the proposed modelling framework

The present study has intended to numerically assess the structural performance of a RC bridge pier subjected to stage-based corrosion, FTCs, and the combined effects of corrosion, FTCs, and service load over a service life of 60 years, during which no repair/rehabilitation intervention had occurred. To this aim, a comprehensive stage-based 3D-NLFEA is conducted to estimate the residual capacity and capture the failure pattern of the damaged bridge pier over its service life. In addition, an NLSA is conducted to verify the reliability of the proposed 3D-NLFEA. A good agreement between the generated interaction diagrams based on both methods proposes the validity of the 3D-NLFEA. The author is aware of the limitations of the 3D-NLFEA imposed by the assumptions of damage accumulation over time by both corrosion and frost damage. The validity of results strongly depends on the assumptions made in this methodology, although attempts have been made to make reasonable assumptions based on the state-of-the-art and field observations. The present simplified NLSA method is deemed to propose a more efficient methodology to the engineering community that can successfully estimate the residual capacity of a damaged pier; however, it is also dependent on the validity of the assumptions and cannot predict the pier's post-peak response and failure behaviour. The use of 3D-NLFEA provides insights of affected bridge piers potential failure modes, post-peak deformation capacity and stress distribution in regions where environmentally-induced damage concentrates, and thus it is a valuable tool to gain knowledge on the structural behaviour of these members.

6.5 Future work

A literature review has shown a lack of field/laboratory data reporting RC bridge piers damage induced by both reinforcement corrosion and freezing/thawing cycles. A minimal number of experimental efforts on the deteriorating effects of FTCs or the combined effects of corrosion and FTCs on the structural performance of small-scale RC columns have relied on existing standard methods to test frost damage in small concrete/mortar samples, which cannot simulate the real deterioration propagation that occurs in actual RC members in service. On the other hand, these small-scale columns did not necessarily fail by the same expected pattern in real-scale piers. The research gaps identified in the literature review and the present research limitations propose the following potential future research lines:

- It would be very interesting to envision an experimental program to test real-scale RC piers subjected to FTCs or to the combined effects of corrosion, FTCs, and service load. A comparison between the results based on the proposed 3D-NLFEA and NLSA in the present study and the future experimental program could further validate the present methodology's reliability and efficiency and address the present study's limitations, as mentioned in the previous section. Once validated with experiment test results, the present quantitative pilot approach could be recommended as a reliable tool for assessment in engineering practice.

- Currently, there is a lack of comprehensive field reports describing the visualized deterioration patterns in aging infrastructures. The combination of reliable field input, experimental testing, and the present methodology is deemed to propose a reliable tool to study the structural performance of bridge piers subjected to stage-based damaging scenarios.
- As explained earlier, a stage-based analysis at specified damage stages is proposed in the present study due to a lack of reliable field input data, i.e., time-variant material properties during the bridge’s service life. The damage stages are defined based on limited field observations, not detailed reports. It is crucial to accurately define critical damage stages and incorporate them into practical time-dependent models to refine assessment procedures of ageing bridge piers.

6.6 References

Coronelli, D., and Gambarova, P. (2004). “Structural assessment of corroded reinforced concrete beams: Modeling guidelines.” Journal of Structural Engineering, 130(8), 1214–1224.

Kashani, M. M., Crewe, A. J., and Alexander, N. A. (2013). “Nonlinear stress-strain behaviour of corrosion-damaged reinforcing bars including inelastic buckling.” Engineering Structures, 48, 417–429.

Li, A., Xu, S., and Wang, Y. (2017). “Effects of frost-damage on mechanical performance of concrete.” Journal Wuhan University of Technology, Materials Science Edition, 32(1), 129–135.

Ontario Ministry of Transportation. (2008). Ontario Structure Inspection Manual (OSIM), Policy, planning & Standards division engineering standards branch bridge office;

Saatcioglu, M., and Razvi, S. R. (1992). “Strength and ductility of confined concrete.” Journal of Structural Engineering (ASCE), 118(6), 1590–1607.